# Collective dynamics of driven-dissipative atomic systems in optical cavities

Dissertation
zur Erlangung des Grades
des Doktors der Naturwissenschaften
der Naturwissenschaftlich-Technischen Fakultät
der Universität des Saarlandes

von

Simon Balthasar Jäger

Saarbrücken

2019

| | |
|---|---|
| Tag des Kolloquiums: | 01.10.2019 |
| Dekan: | Prof. Dr. Guido Kickelbick |
| Berichterstatter: | Prof. Dr. Giovanna Morigi |
| | Prof. Dr. Ludger Santen |
| | Prof. Dr. Helmut Ritsch |
| Vorsitz: | Prof. Dr. Michael Vielhaber |
| Akad. Mitarbeiter: | Dr. Adam Wysocki |

# Zusammenfassung

Diese Arbeit behandelt die theoretische Beschreibung von raumzeitlichen Strukturen in mit Licht wechselwirkenden atomaren Ensembles. Die Atome befinden sich in einem Resonator, werden von einem oder mehreren externen Lasern getrieben und emittieren Photonen in den Resonator. Geordnete Strukturen entstehen für Parameterbereiche, in denen die emittierten Photonen konstruktiv interferieren. Das Ausbilden von räumlichen Strukturen kann als Folge einer langreichweitigen Wechselwirkung zwischen den Atomen verstanden werden, welche durch die mehrfach gestreuten Photonen vermittelt wird. In dieser Doktorarbeit entwickeln wir Molekularfeldmodelle um die Nichtgleichgewichtsdynamik der Atome, unter Einbezug des Einsetzen, der vorübergehenden Dynamik und dem stationären Zustand der geordneten Strukturen, zu charakterisieren. Dabei identifizieren wir die Bedingungen für welche die ausbildenden dynamischen Phasen Eigenschaften von räumlicher Selbstorganisation und Synchronisation zeigen. Wir weisen darauf hin, dass diese Eigenschaften durch das von dem Resonator abgegebene Licht gemessen werden können. Schließlich argumentieren wir, dass die statistische Mechanik dieser getriebenen dissipativen Systeme Schlüsselerkenntnisse über die Dynamik von langreichweitig wechselwirkenden Systemen bereitstellt, welche bis heute weitgehend unerforscht sind.

# Abstract

This thesis reports the theoretical description of spatio-temporal pattern forming in atomic ensembles interacting with photons. The atoms are confined in a cavity, are driven by one or several external lasers, and scatter or emit light into the resonator. Ordered structures emerge in parameter ranges where the emitted photons constructively interfere. The formation of spatial patterns can be understood as a consequence of long-range interactions between the atoms mediated by the multiple-scattered cavity photons. In this thesis we develop mean-field models to characterize the out-of-equilibrium dynamics of the atoms including the onset, the transient, and the stationary state of the ordered structures. Here, we identify the conditions for which the emerging dynamical phases exhibit features of spatial self-organization and synchronization. We point out that these features can be measured by observing the light at the cavity output. Finally, we argue that the statistical mechanics of this driven-dissipative systems provides key insights into the dynamics of long-range interacting systems, which is to date largely unexplored.

# Contents

# Introduction

Collective dynamics in nature cannot be fully understood in terms of the sum of the dynamics of the individual constituents. Prominent examples are the evolution of galaxy clusters emerging from gravitational interactions [1], the formation of flocks of birds or schools of fish [2] and the Hopfield network that describes an associative memory with collective computational abilities [3]. In quantum optics one of the most prominent examples is superradiant emission. Here an ensemble of particles interacts with a common mode of the electromagnetic field and quantum interference leads to a speed up of the emission process and to an anisotropic modification of the emission pattern [4, 5]. The quantum interference appears in the emission amplitudes and gives rise to a macroscopic build up of coherence in the atomic ensemble.

Typically the atomic cloud undergoes superradiant emission for a sufficiently high optical density. In free space this can be achieved if the interparticle distance is smaller than the optical wavelength [4, 5]. Another possibility is to trap the light in confined geometries, such as fibers and optical cavities [5, 6]. In this thesis we consider the case when many atoms couple to an optical cavity.

An optical cavity typically consists of two mirrors that trap the light while the finite transmittivity of the cavity mirrors leads to dissipation [7, 8]. To avoid that all cavity photons are eventually lost one can balance the losses by pumping the cavity with external lasers through the mirrors or indirectly by driving the atoms that scatter light into it.

Every scattering process of a photon by an atom is accompanied by a change of the photon's amplitude and an optomechanical force acting on the atom. Since the cavity photons normally undergo multiple scattering events, they transfer information and mediate interactions between the atoms. For a sufficiently strong interactions this can lead to spatio-temporal pattern formation such as self-organization [9–13] or synchronization [14–19]. The onset and stability of these patterns are the object of this thesis.

The coupling between the particles is usually well-described by a long- or even infinite-range interaction. This draws a connection to the physics of long-range interactions and allows us to study cavity systems with powerful concepts developed in the framework of long-range interactions [20–23]. On the other hand an atomic ensemble inside of an optical cavity provides a promising platform to investigate features of long-range interactions that are usually not observed in short-range interacting systems, such as ensemble inequivalence, negative specific heat, slow relaxation, and broken ergodicity [23–28].

In a cavity system, moreover, noise and dissipation give rise to long-range friction and diffusion [29, 30]. These incoherent sources can be tailored such that the atomic ensemble reaches an out-of-equilibrium steady state in a driven-dissipative setting [13, 31]. Remarkably, even if the cavity decay rate determines the fastest timescale, we will show that coherences remain for a long time in the ensemble of particles [32, 33].

Among a rich variety of phenomena and realizations, we focus on the dynamics of atomic ensembles interacting with an optical resonator, where the mechanical effects of light can give rise to cooling and formation of spatio-temporal pattern such as self-organized and synchronized structures.

**Content of the thesis**

In this thesis we investigate theoretically the collective dynamics of particles confined in an optical cavity, focusing on the regime in which superradiant photon scattering establishes long-range interactions between the constituents. This includes the coherent and dissipative dynamics of the particles. We study the out-of-equilibrium dynamics and the steady state of the particles' ensemble and characterize the emerging phases of the system. This dissertation consists of three chapters.

In **Chapter 1** we review the basic concepts at the basis of the theoretical models we analyze in this thesis. In particular, we discuss the optomechanical forces a single atom experiences when it interacts with laser light and an optical cavity and discuss basic properties of superradiant emission by an ensemble of dipoles in an optical resonator.

**Chapter 2** is devoted to the theoretical characterization of spatial density patterns which spontaneously form when polarizable particles interact with the cavity. We determine the statistical mechanics of these spatial patterns and study relaxation into them after quenches of the laser parameters. The original contributions to this chapter are presented in five publications in different subsections where we present a list of the authors' contributions. In subsection 2.2.2 we include the preprint [34] of the original publication.

*2.2.1 Thermodynamics and dynamics of atomic self-organization in an optical cavity*
S. Schütz, S. B. Jäger, and G. Morigi, Phys. Rev. A **92**, 063808 (2015).

*2.2.2 Phases of cold atoms interacting via photon-mediated long-range forces*
T. Keller, S. B. Jäger, and G. Morigi, J. Stat. Mech. **6**, 064002 (2017).

*2.3.1 Mean-field theory of atomic self-organization in optical cavities*
S. B. Jäger, S. Schütz, and G. Morigi, Phys. Rev. A **94**, 023807 (2016)

*2.3.2 Dissipation-Assisted Prethermalization in Long-Range Interacting Atomic Ensembles*
S. Schütz, S. B. Jäger, and G. Morigi, Phys. Rev. Lett. **117**, 083001 (2016).

*2.3.3 Quenches across the self-organization transition in multimode cavities*
T. Keller, V. Torggler, S. B. Jäger, S. Schütz, H. Ritsch, and G. Morigi, New J. Phys. **20**, 025004 (2018).

In **Chapter 3** we extend the dynamics of the previous chapter by including the incoherently driven atomic pseudospins. We explore the onset of superradiant emission and the coherent and dissipative effects on the atomic motion. The last section of this chapter consists of two publications in subsections where we also report the authors' contributions.

*3.3.1 Supercooling of Atoms in an Optical Resonator*
M. Xu, S. B. Jäger, S. Schütz, J. Cooper, G. Morigi, and M. J. Holland, Phys. Rev. Lett. **116**, 153002 (2016).

*3.3.2 Semiclassical theory of synchronization-assisted cooling*
S. B. Jäger, M. Xu, S. Schütz, M. J. Holland, and G. Morigi, Phys. Rev. A **95**, 063852 (2017).

In the end of the thesis we provide some concluding remarks with an outlook.

# Chapter 1

# Polarizable particles interacting with light

In this chapter we discuss basic concepts for the description of interactions between polarizable particles and light. Our focus is on the mechanical effects of light on atoms or molecules. In the first section we introduce the model describing the interaction of a single particle with a laser, for the purpose of trapping and cooling with optical radiation. In the second section we investigate the mechanical effects that arise from the coupling of a dipolar transition of an atom to a single resonator mode. We then discuss coherent and dissipative forces of light on the atom. In the last section we analyze superradiance of an ensemble of spins inside an optical cavity.

Section 1.1

# MECHANICAL EFFECTS OF LIGHT ON A SINGLE ATOM

In this section we provide the underlying concepts of the dynamics of the atoms due to the mechanical effects of atom-photon interactions. In the end of this section we discuss the dynamics in terms of light forces and how mechanical effects of light can be used to trap and cool the particle's motion [35].

## 1.1.1 A polarizable particle interacting with a laser

### The particle degrees of freedom

We consider a single particle with mass $m$ whose relevant internal degrees of freedom constitute a dipolar, two-level transition [8] with ground and excited state $|g\rangle$ and $|e\rangle$, respectively. The Hamiltonian governing the dynamics of the internal and external degrees of freedom reads

$$\hat{H}_{\rm at} = \hbar\omega_a \hat{\sigma}^\dagger \hat{\sigma} + \frac{\hat{\mathbf{p}}^2}{2m}, \tag{1.1.1}$$

with energy gap $\omega_a$ between the internal states and kinetic energy $\hat{\mathbf{p}}^2/2m$. Here, $\hat{\sigma} = |g\rangle\langle e|$ is the transition matrix from excited to ground state, the operator $\hat{\mathbf{p}} = (\hat{p}_x, \hat{p}_y, \hat{p}_z)^T$ is the momentum and $\hat{\mathbf{r}} = (\hat{r}_x, \hat{r}_y, \hat{r}_z)^T$ the position operator of the particle's center of mass. They fulfill the canonical commutation relations $[\hat{r}_i, \hat{p}_j] = i\hbar\delta_{i,j}$ where $\delta_{i,j}$ is the Kronecker delta and $i, j = x, y, z$.

We assume that the transition from the electronic excited state $|e\rangle$ to the ground state $|g\rangle$ is a dipole transition. In this case the electric dipole operator $\hat{\mathbf{d}}$ can be written as

$$\hat{\mathbf{d}} = \mathbf{d}_{eg}\hat{\sigma}^\dagger + \mathbf{d}_{ge}\hat{\sigma}, \tag{1.1.2}$$

where $\mathbf{d}_{eg} = \mathbf{d}^*_{ge} = \langle e|\hat{\mathbf{d}}|g\rangle$ is the transition matrix element between the electronic ground and excited state.

### Interaction between the electric dipole and the electromagnetic field

The atom and the electromagnetic field are assumed to be confined within the volume $V$. The interaction between the particle's dipole $\hat{\mathbf{d}}$ and the electric field $\hat{\mathbf{E}}(\hat{\mathbf{r}})$ is described in the electric-dipole approximation [1] [8]. The Hamiltonian describing the interaction takes the form

$$\hat{H}_{\rm int} = -\hat{\mathbf{d}} \cdot \hat{\mathbf{E}}(\hat{\mathbf{r}}), \tag{1.1.3}$$

[1] This is valid when the size of the bound state of the electron $l$ is sufficiently small compared to optical wavelength $\lambda$ of the dipole transition. For atoms interacting with light this is often a good approximation considering typical values for the size of the bound state $l \sim 10^{-10}$ m and for the optical wavelength $\lambda \sim 10^{-7}$ m.

where the electric field operator is here quantized and evaluated at the position of the atom's center of mass $\hat{\mathbf{r}}$:

$$\hat{\mathbf{E}}(\hat{\mathbf{r}}) = \sum_m \sqrt{\frac{\hbar\omega_m}{2\epsilon_0 V}} \boldsymbol{\epsilon}_m f_m(\hat{\mathbf{r}}) \hat{a}_m + \text{H.c.} \tag{1.1.4}$$

The sum in Eq. (1.1.4) runs over all modes of the electromagnetic field indexed by $m = (\mathbf{k}_m, \boldsymbol{\epsilon}_m)$ that consist of a wave vector $\mathbf{k}_m$ and a polarization $\boldsymbol{\epsilon}_m$ with $\boldsymbol{\epsilon}_m \perp \mathbf{k}_m$. We also introduced the frequency of the $m$th mode $\omega_m$ with the dispersion relation $\omega_m = c|\mathbf{k}_m|$, the dielectric constant $\epsilon_0$, the quantization volume $V$ and the mode function $f_m(\mathbf{r})$. The operators $\hat{a}_m$ and $\hat{a}_m^\dagger$ annihilate and create a photon in the $m$th mode. They fulfill the canonical commutation relation $[\hat{a}_m, \hat{a}_{m'}^\dagger] = \delta_{m,m'}$. The energy of the electromagnetic field is given by

$$\hat{H}_{\text{field}} = \sum_m \hbar\omega_m \hat{a}_m^\dagger \hat{a}_m, \tag{1.1.5}$$

where we dropped the contribution of the vacuum state since it is not relevant in this work [36, 37].

Using Eq. (1.1.2) and Eq. (1.1.4) in Eq. (1.1.3) and then applying the rotating wave approximation[2] [8] the interaction Hamiltonian takes the form

$$\hat{H}_{\text{int}} = -\sum_m \hbar g_m(\mathbf{r}) \hat{a}_m^\dagger \hat{\sigma} + \text{H.c.}, \tag{1.1.6}$$

where we have introduced the coupling strength

$$g_m(\mathbf{r}) = \sqrt{\frac{\omega_m}{2\hbar\epsilon_0 V}} f_m(\mathbf{r})^* (\mathbf{d}_{ge} \cdot \boldsymbol{\epsilon}_m^*), \tag{1.1.7}$$

that has the dimension of a frequency.

### Master equation formalism for the description of the particle's dynamics

For the description of the evolution of the coupled field and particle dynamics we use the master equation formalism. The master equation is a differential equation for the density matrix $\hat{\varrho}$ that describes the temporal state of particle and field. When the dynamics is purely Hamiltonian, its dynamics is governed by the von Neumann equation [38, 39]

$$\frac{\partial \hat{\varrho}}{\partial t} = \frac{1}{i\hbar} \left[\hat{H}, \hat{\varrho}\right]. \tag{1.1.8}$$

For the dynamics we consider, where $\hat{\varrho}$ is the density matrix of the atomic internal and external degrees of freedom as well as of the electromagnetic field, $\hat{H}$ is given by the sum

$$\hat{H} = \hat{H}_{\text{at}} + \hat{H}_{\text{field}} + \hat{H}_{\text{int}}, \tag{1.1.9}$$

where the individual operators on the right-hand side are described in Eqs. (1.1.1), (1.1.5), and (1.1.6).

[2] This is valid in the regime when the effective coupling between field and dipole is sufficiently small. This needs that the inequality $|\omega_a + \omega_m| \gg |\omega_a - \omega_m|$ must be fulfilled in order to neglect the counter rotating terms. For optical frequencies this is usually fulfilled since we consider detunings up to $|\omega_a - \omega_m| \sim 10^{11}\text{s}^{-1}$ while $|\omega_a + \omega_m| \sim 10^{15}\text{s}^{-1}$ is orders of magnitude larger.

We now present an effective description for the density matrix of the atomic degrees $\hat{\rho} = \mathrm{Tr}_{\mathrm{field}}(\hat{\varrho})$, where $\mathrm{Tr}_{\mathrm{field}}(\,.\,)$ denotes the trace over the electromagnetic field degrees of freedom. In quantum optics the effective description is given by a Born-Markov master equation [3] [38, 39], that reads

$$\frac{\partial \hat{\rho}}{\partial t} = \frac{1}{i\hbar}\left[\hat{H}_{\mathrm{eff}}, \hat{\rho}\right] + \gamma \mathcal{L}[\hat{\sigma}]\hat{\rho}, \tag{1.1.10}$$

where the term $\mathcal{L}[\hat{\sigma}]$ is the relaxation superoperator and takes the form

$$\mathcal{L}[\hat{O}]\hat{\rho}_{\mathrm{sys}} = -\frac{1}{2}\left(\hat{O}^{\dagger}\hat{O}\hat{\rho}_{\mathrm{sys}} + \hat{\rho}_{\mathrm{sys}}\hat{O}^{\dagger}\hat{O} - 2\hat{O}\hat{\rho}_{\mathrm{sys}}\hat{O}^{\dagger}\right). \tag{1.1.11}$$

In Eq. (1.1.10) $\mathcal{L}[\hat{\sigma}]$ describes the incoherent process of spontaneous emission with rate $\gamma$ of the atom.[4] Spontaneous emission eventually leads the particle to the ground state in absence of external excitation. In presence of a laser, the corresponding Hamiltonian is given by

$$\hat{H}_{\mathrm{eff}} = \hat{H}_{\mathrm{at}} + \hat{H}_{L}, \tag{1.1.12}$$

where $\hat{H}_{\mathrm{at}}$ is shown in Eq. (1.1.1) and the laser-atom interaction takes the form

$$\hat{H}_{\mathrm{L}} = \hbar\Omega_{L}(\hat{\mathbf{r}}, t)^{\dagger}\hat{\sigma} + \mathrm{H.c.}. \tag{1.1.13}$$

This description is based on assuming that the laser corresponds to a coherent state of radiation [41]. The frequency $\Omega_L(\hat{\mathbf{r}}, t)$ includes the information of the spatial dependence of the intensity and the phase of the coherent light field. For the case of a monochromatic laser with frequency $\omega_L$, $\Omega_L$ can be written as $\Omega_L(\hat{\mathbf{r}}, t) = \Omega\cos(\mathbf{k}_L \cdot \mathbf{r})e^{-i\omega_L t}$ for a standing wave laser field or $\Omega_L(\hat{\mathbf{r}}, t) = \Omega e^{-i\mathbf{k}_L\cdot\hat{\mathbf{r}}}e^{-i\omega_L t}$ for a running wave laser field. Here $\Omega$ is the Rabi frequency and $\mathbf{k}_L$ is the wave vector that fulfills the dispersion relation $k_L = |\mathbf{k}_L| = \omega_L/c$ with $c$ the speed of light.

### 1.1.2 Elimination of the excited state

In this subsection we derive the steady state of the optical dipole in the regime where the excited state can be eliminated from the dynamics. This will allow us to describe the atomic dipole by its classical polarizability and derive a closed equation for the particle's mechanical motion.

#### The steady state of the dipole

In the following we consider the case of a free particle in one dimension driven by a standing wave laser with frequency $\omega_L$. The master equation for the atomic state $\hat{\rho}'$ reads

$$\frac{\partial \hat{\rho}'}{\partial t} = \frac{1}{i\hbar}\left[\hat{H}', \hat{\rho}'\right] + \gamma \mathcal{L}[\hat{\sigma}]\hat{\rho}' \tag{1.1.14}$$

[3] The Born-Markov approximation is valid for the coupling of the particle to the electromagnetic field in free space while it usually does not apply for atom-cavity interactions, that we consider in the following sections and chapters.

[4] The rate $\gamma$ is the Einstein coefficient and can be calculated using Fermi's golden rule [40]. In general there would also be the absorption process of a thermal photon that we do not include in our description since for an optical transition this effect is negligible. At room temperature the energy of a photon $\hbar\omega_a \approx 10^{-19}$ J exceed by orders of magnitude the thermal energy $\beta^{-1} = k_B T \approx 4 \times 10^{-21}$ J.

and the Hamiltonian is given by

$$\hat{H}' = \hbar\omega_a\hat{\sigma}^\dagger\hat{\sigma} + \frac{\hat{p}^2}{2m} + \hbar\Omega\cos(k\hat{x})(\hat{\sigma}e^{i\omega_L t} + \hat{\sigma}^\dagger e^{-i\omega_L t}), \tag{1.1.15}$$

where $\hat{p}$ is the conjugate momentum operator to the position operator $\hat{x}$. We describe the system in the frame rotating with the laser frequency $\omega_L$ defined by the transformation

$$\hat{\rho} = e^{i\omega_L t\hat{\sigma}^\dagger\hat{\sigma}}\hat{\rho}' e^{-i\omega_L t\hat{\sigma}^\dagger\hat{\sigma}}. \tag{1.1.16}$$

In this reference frame the corresponding master equation for $\hat{\rho}$ reads

$$\frac{\partial\hat{\rho}}{\partial t} = \frac{1}{i\hbar}\left[\hat{H},\hat{\rho}\right] + \gamma\mathcal{L}[\hat{\sigma}]\hat{\rho}, \tag{1.1.17}$$

where the Hamiltonian takes the form

$$\hat{H} = -\hbar\Delta_a\hat{\sigma}^\dagger\hat{\sigma} + \frac{\hat{p}^2}{2m} + \hbar\Omega\cos(k\hat{x})(\hat{\sigma} + \hat{\sigma}^\dagger), \tag{1.1.18}$$

and where $\Delta_a = \omega_L - \omega_a$ is the detuning between the laser frequency and the atomic frequency.

The dynamics for $\hat{\rho}_{ij} = \langle i|\hat{\rho}|j\rangle$, with $i,j \in \{e,g\}$, is governed by the optical Bloch equations. The equations of motion of the matrix elements of $\hat{\rho}$ are given by

$$\frac{\partial\hat{\rho}_{eg}}{\partial t} = \left(i\Delta_a - \frac{\gamma}{2}\right)\hat{\rho}_{eg} + \frac{1}{i\hbar}\left[\frac{\hat{p}^2}{2m},\hat{\rho}_{eg}\right] - i\Omega\cos(k\hat{x})\hat{\rho}_{gg} + i\Omega\hat{\rho}_{ee}\cos(k\hat{x}), \tag{1.1.19}$$

$$\frac{\partial\hat{\rho}_{gg}}{\partial t} = \gamma\hat{\rho}_{ee} + \frac{1}{i\hbar}\left[\frac{\hat{p}^2}{2m},\hat{\rho}_{gg}\right] - i\Omega\cos(k\hat{x})\hat{\rho}_{eg} + i\Omega\hat{\rho}_{ge}\cos(k\hat{x}), \tag{1.1.20}$$

$$\frac{\partial\hat{\rho}_{ee}}{\partial t} = -\gamma\hat{\rho}_{ee} + \frac{1}{i\hbar}\left[\frac{\hat{p}^2}{2m},\hat{\rho}_{ee}\right] - i\Omega\cos(k\hat{x})\hat{\rho}_{ge} + i\Omega\hat{\rho}_{eg}\cos(k\hat{x}). \tag{1.1.21}$$

We first neglect the particle's motion. In this case the kinetic energy term is dropped and we treat $\hat{x}$ as parameter $x$ of the system. The steady state of the internal degrees of freedom satisfies $\partial\rho_{ij}/\partial t = 0$ and is given by [5]

$$\rho_{eg} = \frac{s}{1+2|s|^2}, \tag{1.1.22}$$

$$\rho_{gg} = \frac{1+|s|^2}{1+2|s|^2}, \tag{1.1.23}$$

$$\rho_{ee} = \frac{|s|^2}{1+2|s|^2}. \tag{1.1.24}$$

It solely depends on the parameter $s$, which reads

$$s = \frac{\Omega\cos(kx)}{\Delta_a + i\frac{\gamma}{2}} \tag{1.1.25}$$

and where $|s|^2$ is called the saturation parameter [8].

For sufficiently small laser power $\Omega \ll |\Delta_a + i\gamma/2|$, therefore $|s| \ll 1$, the excited state population scales with $|s|^2$. It is negligible in first order in $s$ while the coherence $\hat{\rho}_{eg} \propto s$. The low saturation limit is thus characterized by a dipole proportional to the electric field, like in the classical Lorentz oscillator model of a bound electron [42, 43].

In this limit we will analyze the mechanical effect of light on the center of mass motion of the particle.

[5] In this case we write $\rho_{ij}$ instead of $\hat{\rho}_{ij}$ since it is not an operator of the external degrees.

### 1.1.3 Light forces

We derive the equations of motion in the frame moving with the particle

$$\tilde{\rho} = \exp\left(\frac{i}{\hbar}\frac{\hat{p}^2}{2m}t\right)\hat{\rho}\exp\left(-\frac{i}{\hbar}\frac{\hat{p}^2}{2m}t\right).$$

In this frame and in the low saturation limit, Eq. (1.1.19) can be approximated by

$$\frac{\partial\tilde{\rho}_{eg}}{\partial t} = \left(i\Delta_a - \frac{\gamma}{2}\right)\tilde{\rho}_{eg} - i\Omega\cos\left(k\hat{x}(t)\right)\tilde{\rho}_{gg} + \mathrm{O}(|s|^2), \tag{1.1.26}$$

with $k\hat{x}(t) = k\hat{x} + \hat{\delta}t$ where the Doppler shift is $\hat{\delta} = k\hat{p}/m$. Integrating Eq. (1.1.26) we obtain

$$\begin{aligned}\tilde{\rho}_{eg}(t) =& e^{\left(i\Delta_a - \frac{\gamma}{2}\right)t}\tilde{\rho}_{eg}(0) - i\Omega\int_0^t d\tau e^{\left(i\Delta_a - \frac{\gamma}{2}\right)(t-\tau)}\cos\left(k\hat{x}(\tau)\right)\tilde{\rho}_{gg}(\tau) + \mathrm{O}(|s|^2)\\ =& e^{\left(i\Delta_a - \frac{\gamma}{2}\right)t}\tilde{\rho}_{eg}(0) - i\Omega\int_0^t d\tau e^{\left(i\Delta_a - \frac{\gamma}{2}\right)\tau}\cos\left(k\hat{x}(t) - \hat{\delta}\tau\right)\tilde{\rho}_{gg}(t-\tau) + \mathrm{O}(|s|^2).\end{aligned} \tag{1.1.27}$$

We may now expand $\tilde{\rho}_{gg}(t-\tau) = \tilde{\rho}_{gg}(t) - \tau\partial_t\tilde{\rho}_{gg}(t) + ...$ in the integrand in Eq. (1.1.27). Then, using Eq. (1.1.20), $\partial_t\tilde{\rho}_{gg} \sim \mathrm{O}(\Omega)$ therefore in the low saturation limit we may approximate $\tilde{\rho}_{gg}(t-\tau) \approx \tilde{\rho}_{gg}(t)$ in Eq. (1.1.27). We obtain

$$\tilde{\rho}_{eg}(t) \approx - i\Omega\int_0^t d\tau e^{\left(i\Delta_a - \frac{\gamma}{2}\right)\tau}\cos\left(k\hat{x}(t) - \hat{\delta}\tau\right)\tilde{\rho}_{gg}(t), \tag{1.1.28}$$

where we assumed that $\tilde{\rho}_{eg}(0) = 0$. To solve the integral in Eq. (1.1.28) we first rewrite

$$\cos(k\hat{x}(t) - \hat{\delta}\tau) = \frac{e^{i(k\hat{x}(t) - \hat{\delta}\tau)} + e^{-i(k\hat{x}(t) - \hat{\delta}\tau)}}{2}.$$

Then, using that

$$\frac{e^{i(k\hat{x}(t) - \hat{\delta}\tau)} + e^{-i(k\hat{x}(t) - \hat{\delta}\tau)}}{2} = \frac{e^{ik\hat{x}(t)}e^{-i(\hat{\delta}+\omega_R)\tau} + e^{-ik\hat{x}(t)}e^{i(\hat{\delta}-\omega_R)\tau}}{2}$$

with the definition of the recoil frequency

$$\omega_R = \frac{\left[k\hat{x}, \hat{\delta}\right]}{2} = \frac{\hbar k^2}{2m} \tag{1.1.29}$$

we can solve the integral in Eq. (1.1.28) and obtain

$$\tilde{\rho}_{eg}(t) = \left[\frac{e^{ik\hat{x}(t)}}{2}\frac{\Omega}{\Delta_a - \hat{\delta} - \omega_R + i\frac{\gamma}{2}} + \frac{e^{-ik\hat{x}(t)}}{2}\frac{\Omega}{\Delta_a + \hat{\delta} - \omega_R + i\frac{\gamma}{2}}\right]\tilde{\rho}_{gg}(t), \tag{1.1.30}$$

where we assumed times $t$ such that $\gamma t \gg 1$.

We consider now the case where the recoil frequency is much smaller then the detuning, the spontaneous emission rate

$$\omega_R \ll |\Delta_a|, \gamma, \tag{1.1.31}$$

and as the standard deviation of the Doppler shift

$$\omega_R \ll \frac{k\Delta p}{m}, \tag{1.1.32}$$

with

$$\Delta p = \sqrt{\langle(\hat{p} - \langle\hat{p}\rangle)^2\rangle}. \tag{1.1.33}$$

In this case we can drop the dependence on $\omega_R$ in Eq. (1.1.30).[6] The regime where the inequality (1.1.32) holds is called the semiclassical regime where the single particle momentum width exceeds the single photon recoil by orders of magnitude

$$\hbar k \ll \Delta p. \tag{1.1.34}$$

In this case the single-photon recoil can be treated as infinitesimal momentum step for the particle's momentum distribution [44, 45].

In the semiclassical limit Eq. (1.1.30) takes the form

$$\tilde{\rho}_{eg}(t) = \left[\frac{\Omega e^{ik\hat{x}(t)}}{2(\Delta_a - \hat{\delta}) + i\gamma} + \frac{\Omega e^{-ik\hat{x}(t)}}{2(\Delta_a + \hat{\delta}) + i\gamma}\right]\tilde{\rho}_{gg}(t). \tag{1.1.35}$$

In the following we will derive the force on the atom by using the result of Eq. (1.1.35). The force acting on the particle is the derivative of the mean particle momentum $\langle\hat{p}\rangle = \mathrm{Tr}(\hat{p}\tilde{\rho})$. Using Eq. (1.1.17) this reads

$$\frac{d\langle\hat{p}\rangle}{dt} = \frac{1}{i\hbar}\mathrm{Tr}\left([\hat{p}, \hbar\Omega\cos(k\hat{x}(t))]\left(\tilde{\rho}_{eg}(t) + \tilde{\rho}_{ge}(t)\right)\right) = \hbar k\Omega\mathrm{Tr}\left(\sin(k\hat{x}(t))(\tilde{\rho}_{eg}(t) + \tilde{\rho}_{ge}(t))\right).$$

We can cast the right-hand side as the expectation value of an operator $\hat{F}$, that we denote by force operator. Using Eq. (1.1.35) we can explicitly derive the form of $\hat{F}$ that we split into two components $\hat{F}_1$ and $\hat{F}_2$ with

$$\hat{F} = \hat{F}_1 + \hat{F}_2 \tag{1.1.36}$$

where[7]

$$\hat{F}_1 = \hbar k\Omega\sin(k\hat{x}(t))\cos(k\hat{x}(t))\left[\frac{(\Delta_a - \hat{\delta})\Omega}{(\Delta_a - \hat{\delta})^2 + \frac{\gamma^2}{4}} + \frac{(\Delta_a + \hat{\delta})\Omega}{(\Delta_a + \hat{\delta})^2 + \frac{\gamma^2}{4}}\right], \tag{1.1.37}$$

$$\hat{F}_2 = \hbar k\Omega\sin^2(k\hat{x}(t))\left[\frac{\gamma\Omega}{(\Delta_a - \hat{\delta})^2 + \frac{\gamma^2}{4}} - \frac{\gamma\Omega}{(\Delta_a + \hat{\delta})^2 + \frac{\gamma^2}{4}}\right]. \tag{1.1.38}$$

[6] As a consequence of this approximation the operators $e^{ik\hat{x}(t)}$ and $\Omega/(\Delta_a - \hat{\delta} + i\gamma/2)$ commute. This can be seen using the relation

$$e^{ik\hat{x}(t)}\frac{\Omega}{\Delta_a - \hat{\delta} - \omega_R + i\frac{\gamma}{2}} = \frac{\Omega}{\Delta_a - \hat{\delta} + \omega_R + i\frac{\gamma}{2}}e^{ik\hat{x}(t)}$$

and then applying the approximations

$$e^{ik\hat{x}(t)}\frac{\Omega}{\Delta_a - \hat{\delta} - \omega_R + i\frac{\gamma}{2}} \approx e^{ik\hat{x}(t)}\frac{\Omega}{\Delta_a - \hat{\delta} + i\frac{\gamma}{2}}$$

as well as

$$\frac{\Omega}{\Delta_a - \hat{\delta} + \omega_R + i\frac{\gamma}{2}}e^{ik\hat{x}(t)} \approx \frac{\Omega}{\Delta_a - \hat{\delta} + i\frac{\gamma}{2}}e^{ik\hat{x}(t)}.$$

[7] These formulas are semiclassical and are only valid in the limit where we can drop $\omega_R$. The operators $\hat{F}$, $\hat{F}_1$, and $\hat{F}_2$ are hermitian since we can commute the operators depending on $\hat{p}$ and $\hat{x}$ because the corresponding commutator would be of higher order in $\omega_R/\Delta_a$, $\omega_R/\gamma$, and $\omega_R/\sqrt{\langle\hat{\delta}^2\rangle}$.

We denote $\hat{F}_1$ by dipole and $\hat{F}_2$ by cooling force, respectively, as it will become clear later on.

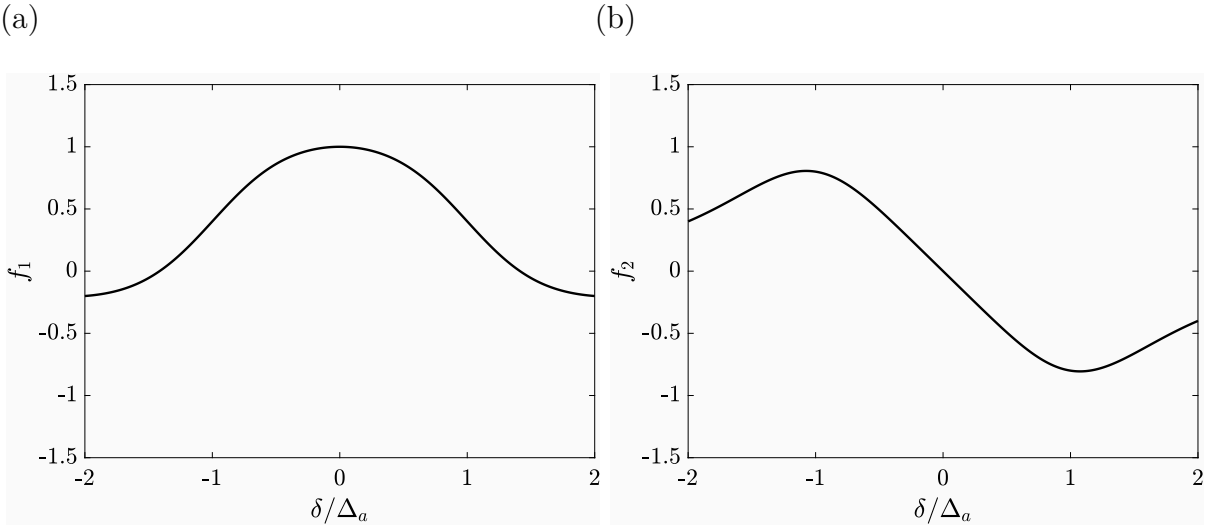


Figure 1.1: (a) The function $f_1$, Eq. (1.1.40), and (b) $f_2$ ,Eq. (1.1.45), as a function of $\delta$ in units of $\Delta_a$. We have chosen the parameter $\Delta_a = -\gamma/2$.

### Dipole force

The dipole force reads

$$\hat{F}_1 = \hbar k \sin(k\hat{x}(t)) \cos(k\hat{x}(t)) \frac{\Omega^2}{\Delta_a} f_1(\hat{\delta}), \tag{1.1.39}$$

where $f_1(\delta)$ contains the dependence on the Doppler shift and reads

$$f_1(\delta) = \frac{1 - \frac{\delta}{\Delta_a}}{\left(1 - \frac{\delta}{\Delta_a}\right)^2 + \frac{\gamma^2}{4\Delta_a^2}} + \frac{1 + \frac{\delta}{\Delta_a}}{\left(1 + \frac{\delta}{\Delta_a}\right)^2 + \frac{\gamma^2}{4\Delta_a^2}}. \tag{1.1.40}$$

This function is plotted in Fig. 1.1(a) for $\Delta_a = -\gamma/2$. It is symmetric in $\delta/\Delta_a$. For small values of $|\delta/\Delta_a|$ it is positive while for larger values of $|\delta/\Delta_a|$ it becomes negative and then converges to zero.

We analyze $f_1$ in the limit $|\delta| \ll |\Delta_a|, \gamma$ where the Doppler shift is much smaller than the detuning.[8] In this limit we expand $f_1$ in the lowest order $\delta/\Delta_a$ and obtain[9]

$$f_1(\delta) \approx \frac{2}{1 + \frac{\gamma^2}{4\Delta_a^2}}, \tag{1.1.41}$$

[8]This is the limit where the particles momentum width is already sufficiently small such that the internal degrees of freedom evolve much faster than the external degrees of freedom. If we consider a linewidth $\gamma \sim 10^7$ s$^{-1}$ and a recoil energy $\omega_R \sim 10^4$ s$^{-1}$ this consideration is justified for a momentum width of $\Delta p \ll 10^3 \hbar k$. We want to remark that this still allows the inequality $\Delta p \gg \hbar k$ to be fulfilled that is important for the semiclassical approximation.

[9]The first order in $\delta/\Delta_a$ vanishes since $f_1$ is an even function.

that is independent of $\delta$ and positive. This allows us to rewrite the force as derivative of the standing-wave potential $\hat{V}$ with

$$\hat{F}_1 = -\left.\frac{\partial \hat{V}(x)}{\partial x}\right|_{x=\hat{x}(t)}, \tag{1.1.42}$$

where $\hat{V}$ is given by

$$\hat{V}(\hat{x}) = \frac{\hbar\Delta_a\Omega^2}{\Delta_a^2 + \frac{\gamma^2}{4}}\cos^2(k\hat{x}(t)). \tag{1.1.43}$$

The motion due to $\hat{F}_1$ is hence conservative in this limit. The sign of this force depends on the detuning $\Delta_a$ that determines whether this force is attractive at the antinodes or nodes of the laser field. For red detuning $\Delta_a < 0$ the minima of the potential are the maxima of field intensity (high-field seeker) while for blue detuning $\Delta_a > 0$ the minima of the potential are also the minima of the intensity (low-field seeker).

### Cooling force

We now discuss the motion due to $\hat{F}_2$. This force reads

$$\hat{F}_2 = \hbar k \sin^2(k\hat{x}(t))\frac{\Omega^2}{\Delta_a} f_2(\hat{\delta}), \tag{1.1.44}$$

where

$$f_2(\delta) = \frac{\frac{\gamma}{2\Delta_a}}{\left(1-\frac{\delta}{\Delta_a}\right)^2 + \frac{\gamma^2}{4\Delta_a^2}} - \frac{\frac{\gamma}{2\Delta_a}}{\left(1+\frac{\delta}{\Delta_a}\right)^2 + \frac{\gamma^2}{4\Delta_a^2}}. \tag{1.1.45}$$

The function $f_2$ defined in Eq. (1.1.45) is shown in Fig. 1.1(b) for $\Delta_a = -\gamma/2$. It is odd in $\delta$: $f_2$ is positive for $\delta < 0$ and negative for $\delta > 0$.

In the limit $|\delta| \ll |\Delta_a|$ we can expand $f_2$ up to first order in $|\delta/\Delta_a|$:

$$\hat{F}_2 \approx \hbar k \sin^2(k\hat{x}(t))\frac{2\Delta_a\gamma\Omega^2}{\left(\Delta_a^2 + \frac{\gamma^2}{4}\right)^2}\hat{\delta}. \tag{1.1.46}$$

In this limit $\hat{F}_2$ is proportional to $\hat{\delta}$ and therefore to the velocity of the particle. For the case of red detuning $\Delta_a < 0$ it is a damping force, while for blue detuning it leads to heating.[10]

### Doppler limit

We now consider the dynamics due to the mechanical forces and consider the equation of motion for the kinetic energy

$$\frac{d\langle\hat{p}^2\rangle}{dt} = \hbar k\Omega \mathrm{Tr}\left([\hat{p}\sin(k\hat{x}(t)) + \sin(k\hat{x}(t))\hat{p}](\tilde{\rho}_{eg} + \tilde{\rho}_{ge})\right) \tag{1.1.47}$$

[10]For an increasing momentum width non-linear terms of the Doppler shift in Eq. (1.1.44) become important and the description by Eq. (1.1.46) becomes invalid.

in the low saturation limit and the semiclassical regime. Using now the form of $\hat{\rho}_{eg}$ given in Eq. (1.1.35) we may write

$$\frac{d\langle\hat{p}^2\rangle}{dt} = \left\langle \hat{p}(\hat{F}_1 + \hat{F}_2) + (\hat{F}_1 + \hat{F}_2)\hat{p} \right\rangle + \langle \hat{D} \rangle \tag{1.1.48}$$

with

$$\hat{D} \approx \frac{(\hbar k)^2 \Omega^2 \gamma}{\Delta_a^2 + \frac{\gamma^2}{4}} \sin^2(k\hat{x}(t)) \tag{1.1.49}$$

in zeroth order[11] in $\hat{\delta}$ and where $\hat{F}_1$ and $\hat{F}_2$ are defined in Eqs. (1.1.37), (1.1.38). The term $\hat{D}$ is a diffusion operator that is here position dependent. In absence of a well defined phase relation between the counter-propagating lasers, the $\sin^2(k\hat{x}(t))$ is approximated by its ergodic average, $\langle \sin^2(k\hat{x}(t)) \rangle \sim 1/2$, while the dipole force vanishes. This gives

$$\frac{d\langle\hat{p}^2\rangle}{dt} \approx \frac{4\omega_r \Delta_a \gamma \Omega^2}{\left(\Delta_a^2 + \frac{\gamma^2}{4}\right)^2} \langle \hat{p}^2 \rangle + \frac{(\hbar k)^2}{2} \frac{\Omega^2 \gamma}{\Delta_a^2 + \frac{\gamma^2}{4}}. \tag{1.1.50}$$

The steady state reads then

$$\frac{\langle \hat{p}^2 \rangle}{2m} = \frac{\hbar(\Delta_a^2 + \frac{\gamma^2}{4})}{-8\Delta_a}. \tag{1.1.51}$$

Using $\langle \hat{p}^2 \rangle/(2m) = k_B T/2$, with the Boltzmann constant $k_B$, we obtain the temperature achieved by Doppler cooling

$$k_B T_D = \frac{\hbar(\Delta_a^2 + \frac{\gamma^2}{4})}{-4\Delta_a}. \tag{1.1.52}$$

It is minimal for $\Delta_a = -\gamma/2$ and is bounded from below by $k_B T_D \geq \hbar\gamma/4$.[12] This is the Doppler-cooling limit. This description requires that the inequalities

$$|\Delta_a|, \gamma \gg \frac{k\Delta p}{m} \gg \omega_R \tag{1.1.53}$$

hold. Therefore, we cannot use Eq. (1.1.52) if the linewidth $\gamma$ approaches the recoil frequency $\omega_R$ (Eq. (1.1.29)).

Doppler cooling has been first predicted in Refs. [50, 51]. It is nowadays commonly realized in labs and the first experimental realization has been reported in Ref. [52].

Laser cooling mechanisms that can reach temperatures that are below $\hbar\gamma/4$ are denoted by sub-Doppler cooling. The maybe most prominent example for sub-Doppler cooling is polarization gradient cooling. With this cooling method the particle can approach the recoil limit [53]. For their achievements and developments of methods to cool and trap atoms with laser light C. Cohen-Tannoudji, W. D. Phillips, and S. Chu were awarded with the Nobel price in physics [54–56].

Radiative cooling of motion can also be achieved by coherent scattering of photons. This is the case of cavity cooling. In the following we discuss the mechanical effects on a particle that arise from coherent scattering into a lossy cavity mode.

[11] A more general result can be found in Ref. [46] that predicts also non-Gaussian distributions such as Tsallis distributions [47–49].

[12] For the choice of a transition where $\gamma \sim 10^7$ s$^{-1}$ we obtain the temperature $T_D \sim 100$ $\mu$K. We want to mention that this is consistent with the assumption that the Doppler shift $k\Delta p/m$ is small compared to $|\Delta_a|$ and $\gamma$.

Section 1.2

# A polarizable particle coupling to a cavity mode

In this section we discuss the dynamics of a single cavity mode coupling to the dipole of a particle. We focus on the mechanical effects that arise from this interaction and we will show that coherent scattering of a polarizable particle in a lossy resonator can cool the particle's motion.

## 1.2.1 A polarizable particle interacting with an optical cavity

### The cavity degrees of freedom

An optical standing-wave cavity can be realized by two mirrors facing each other allowing the electromagnetic field to populate quantized modes [7]. The hard wall condition (for ideally parallel mirrors) provide a spectrum of modes where the frequency gap scales with $1/L$ where $L$ is the length of the resonator. For sufficiently small mode volume a single resonator mode couples quasi-resonantly to a dipole transition of a particle while all other modes are off resonant.[13] This is the typical scenario that we consider in the following.

For the purpose of modeling the cavity dynamics we thus assume a single harmonic oscillator. The frequency of the single resonator mode is given by $\omega_c$. The Hamiltonian describing this mode reads

$$\hat{H}_{\mathrm{cav}} = \hbar\omega_c \hat{a}^\dagger \hat{a}, \tag{1.2.1}$$

where $\hat{a}$ and $\hat{a}^\dagger$ are the annihilation and creation operator of a cavity photon that fulfill the canonical commutation relation $[\hat{a}, \hat{a}^\dagger] = 1$ and we discarded the contribution of the vacuum [36, 37].

The cavity mode couples to the free electromagnetic field external to the resonator via the finite mirror transmittance. This process can be described by the Hamiltonian [8]

$$\hat{H}_{\mathrm{cav-ff}} = \hbar \sum_m (c_m \hat{a}^\dagger \hat{a}_m + c_m^* \hat{a}_m^\dagger \hat{a}), \tag{1.2.2}$$

where $c_m$ is the coupling of the cavity mode to the mode $m$ of the free electromagnetic field, and $\hat{a}_m$ and $\hat{a}_m^\dagger$ are the annihilation and creation operator of a photon in mode $m$, see Eq. (1.1.5). The Hamiltonian in Eq. (1.2.2) describes the coherent processes that a cavity photon is annihilated and a photon in the electromagnetic field outside the cavity is created and vice versa.

Like in the case of spontaneous emission, the effect of the finite transmittance of the cavity mirrors can be described by means of an effective Born-Markov master equation. This effective master equation for the reduced density matrix $\hat{\rho}$, that now only describes the particle and cavity degrees of freedom, reads [8]

$$\frac{\partial \hat{\rho}}{\partial t} = \frac{1}{i\hbar}[\hat{H}_{\mathrm{eff}}, \hat{\rho}] + \gamma \mathcal{L}[\hat{\sigma}]\hat{\rho} + \kappa \mathcal{L}[\hat{a}]\hat{\rho}, \tag{1.2.3}$$

[13] For a cavity length $L \sim 10^{-2}$ cm [57, 58] the free spectral range is of the order $c/(2L) \sim 10^3$ GHz and for a cavity length of $L \sim 1$ cm [30, 59, 60] the free spectral range is of the order $c/(2L) \sim 10$ GHz.

where the dissipative parts are given by relaxation superoperators defined in Eq. (1.1.11).[14] The term $\gamma\mathcal{L}[\hat{\sigma}]$ describes spontaneous emission with rate $\gamma$ and the term $\kappa\mathcal{L}[\hat{a}]$ describes the losses of cavity photons through the cavity mirrors. The rate $\kappa$ is the linewidth of the cavity.

The coherent part of the master equation in Eq. (1.2.3) is given by the Hamiltonian $\hat{H}_{\text{eff}}$ that is now written as

$$\hat{H}_{\text{eff}} = \hat{H}_{\text{at}} + \hat{H}_L + \hat{H}_{\text{cav}} + \hat{H}_{L2} + \hat{H}_{JC}. \tag{1.2.4}$$

The Hamiltonian $\hat{H}_{\text{at}}$ describes the dynamics of the atomic degrees of freedom (Eq. (1.1.1)) while $\hat{H}_L$ describes the coupling of the laser to the atomic dipole (Eq. (1.1.13)). The cavity degrees of freedom evolve according to the Hamiltonian $\hat{H}_{\text{cav}}$ (Eq. (1.2.1)) and a possibly additional laser driving of the resonator mode [8]

$$\hat{H}_{L2} = \hbar(\eta(t)^*\hat{a} + \hat{a}^\dagger\eta(t)). \tag{1.2.5}$$

For a monochromatic laser field it is given by $\eta(t) = \eta e^{-i\omega_L t}$ where $\omega_L$ is the laser frequency and $|\eta|^2$ is proportional to the laser power.

**Jaynes-Cummings Hamiltonian**

The coupling between the cavity mode and the particle in the dipole approximation is described by the Hamiltonian in Eq. (1.1.3) where the electric field is now the electric field of the cavity. Using the rotating wave approximation [8], the Hamiltonian describing the coupling between cavity and particle takes the form

$$\hat{H}_{\text{JC}} = \hbar(g(\hat{\mathbf{r}})\hat{a}^\dagger\hat{\sigma} + g(\hat{\mathbf{r}})^\dagger\hat{\sigma}^\dagger\hat{a}), \tag{1.2.6}$$

that is the celebrated Jaynes-Cummings model [8]. Here $g(\hat{\mathbf{r}})$ is the coupling frequency of the cavity field to the particle and depends on the mode function of the cavity. For a standing wave along the $x$ axis it takes the form $g(\hat{\mathbf{r}}) = g\cos(k\hat{x})$ where $g$ is the vacuum Rabi frequency. This Hamiltonian describes the change of the particle's internal and external state by emitting or absorbing a cavity photon. [15]

## 1.2.2 Elimination of the internal degrees of freedom

We now aim at deriving a theoretical model for the description of the motion of the particle in the optical cavity. Our starting point is the Born-Markov master equation for the density matrix $\hat{\rho}'$ describing the particle's and the cavity degrees of freedom

$$\frac{\partial\hat{\rho}'}{\partial t} = \frac{1}{i\hbar}[\hat{H}', \hat{\rho}'] + \kappa\mathcal{L}[\hat{a}]\hat{\rho}' + \gamma\mathcal{L}[\hat{\sigma}]\hat{\rho}'. \tag{1.2.7}$$

The master equation includes the spontaneous decay of the particle's excited state with rate $\gamma$, the decay of cavity photons with rate $\kappa$, and the Hamiltonian

$$\begin{aligned}\hat{H}' =& \hbar\omega_a\hat{\sigma}^\dagger\hat{\sigma} + \frac{\hat{p}^2}{2m} + \hbar\omega_c\hat{a}^\dagger\hat{a} + \hbar g\cos(k\hat{x})(\hat{a}^\dagger\hat{\sigma} + \hat{\sigma}^\dagger\hat{a}) \\ &+ \hbar\Omega(\hat{\sigma}^\dagger e^{-i\omega_L t} + \hat{\sigma}e^{i\omega_L t}) + \hbar\eta(\hat{a}^\dagger e^{-i\omega_L t} + \hat{a}e^{i\omega_L t}).\end{aligned} \tag{1.2.8}$$

[14] Here, we have treated the electromagnetic modes coupling to the particle's dipole and to the cavity independently. This is only true if the resonator mode and the particle's dipole couple to different modes of the electromagnetic field.

[15] The Jaynes-Cummings model in Eq. (1.2.6) conserves the excitations in field and atom [8]. This means that it commutes with the operator $\hat{E} = \hat{a}^\dagger\hat{a} + \hat{\sigma}^\dagger\hat{\sigma}$.

The first line in the Hamiltonian (1.2.8) includes, from left to right, the energy splitting of the two-level system, the kinetic energy of the particle in one dimension, the energy of the cavity photons, and the Jaynes-Cummings coupling. The Jaynes-Cummings term includes the standing-wave mode function of the cavity field $\cos(kx)$, where we defined the cavity axis to be the $x$ axis. The laser pumps are shown in the second line of Eq. (1.2.8). The first term is a laser pump of the particle and the second term is a laser pump of the cavity. Here, we assumed that both lasers have the same frequency $\omega_L$. Furthermore, that the both lasers are phase locked. We note that the spatial mode of the laser pump is assumed to be constant. Figure 1.2 is a sketch of this physical setup.

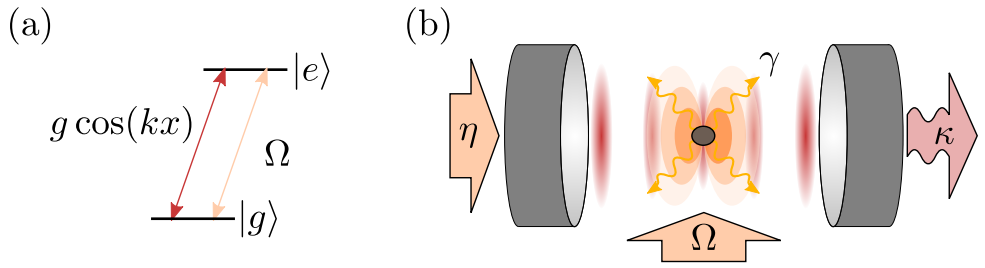


Figure 1.2: (a) The dipole of the particle with ground state $|g\rangle$ and excited state $|e\rangle$ that couples to the cavity with vacuum coupling $g\cos(kx)$ and is driven by a laser with Rabi frequency $\Omega$. (b) Sketch of the physical setup: the particle's dipole is transversally pumped by a laser with Rabi frequency $\Omega$ and couples to the cavity mode. The cavity is pumped by a second laser (arrow with label $\eta$). The model also includes losses of the cavity with rate $\kappa$ and spontaneous emission of the dipole with rate $\gamma$ into the modes external to the resonator.

In the frame oscillating with the laser frequency and defined by the transformation:

$$\hat{\rho} = e^{i\omega_L t[\hat{\sigma}^\dagger\hat{\sigma}+\hat{a}^\dagger\hat{a}]}\hat{\rho}' e^{-i\omega_L t[\hat{\sigma}^\dagger\hat{\sigma}+\hat{a}^\dagger\hat{a}]}, \tag{1.2.9}$$

we obtain the master equation for the density matrix in the rotating frame $\hat{\rho}$ that reads

$$\frac{\partial\hat{\rho}}{\partial t} = \frac{1}{i\hbar}[\hat{H},\hat{\rho}] + \kappa\mathcal{L}[\hat{a}]\hat{\rho} + \gamma\mathcal{L}[\hat{\sigma}]\hat{\rho}. \tag{1.2.10}$$

The new Hamiltonian is time independent and takes the form

$$\hat{H} = -\hbar\Delta_a\hat{\sigma}^\dagger\hat{\sigma} + \frac{\hat{p}^2}{2m} - \hbar\Delta_c\hat{a}^\dagger\hat{a} + \hbar g\cos(k\hat{x})(\hat{a}^\dagger\hat{\sigma} + \hat{\sigma}^\dagger\hat{a}) + \hbar\Omega(\hat{\sigma}^\dagger + \hat{\sigma}) + \hbar\eta(\hat{a}^\dagger + \hat{a}). \tag{1.2.11}$$

Here, we introduced the detuning between the laser and the atomic frequency $\Delta_a = \omega_L - \omega_a$ as well as the detuning between the laser and the cavity frequency $\Delta_c = \omega_L - \omega_c$.

### Coherent scattering

We will focus in the regime where the detuning $\Delta_a$ is much larger than any other characteristic frequency in determining the dynamics in the reference frame of the laser. In this case the scattering processes of the atom are prevailing coherent. We now use this assumption and derive the Hamiltonian that is at the basis of our studies in chapter 2.

To simplify Eq. (1.2.10) we derive the equation of motion for $\hat{\rho}_{eg} = \langle e|\hat{\rho}|g\rangle$

$$\frac{\partial \hat{\rho}_{eg}}{\partial t} \approx \left(i\Delta_a - \frac{\gamma}{2}\right)\hat{\rho}_{eg} + \frac{1}{i\hbar}\left[\frac{\hat{p}^2}{2m}, \hat{\rho}_{eg}\right] - i(\Omega + g\hat{a}\cos(k\hat{x}))\hat{\rho}_{gg} + i\hat{\rho}_{ee}(\Omega + g\hat{a}\cos(k\hat{x})). \tag{1.2.12}$$

For this case we can estimate the saturation parameter for a given mean intracavity photon number $\bar{n}$, and it reads

$$|s| \approx \frac{|\Omega| + |g|\sqrt{\bar{n}}}{|\Delta_a + i\frac{\gamma}{2}|}. \tag{1.2.13}$$

For the parameter choice where $\Delta_a$ exceeds the other characteristic frequencies, $|s| \ll 1$. We can then drop $\hat{\rho}_{ee}$ in Eq. (1.2.12). In this limit Equation (1.2.12) can be formally integrated to obtain as a final result

$$\hat{\rho}_{eg} \approx \frac{\Omega + g\hat{a}\cos(k\hat{x})}{\Delta_a}\hat{\rho}_{gg}. \tag{1.2.14}$$

Using this result, one can derive a master equation for the reduced density matrix, obtained by tracing out the internal degrees of freedom, that reads

$$\frac{\partial \hat{\rho}_{\mathrm{red}}}{\partial t} = \frac{1}{i\hbar}[\hat{H}_{\mathrm{red}}, \hat{\rho}_{\mathrm{red}}] + \kappa\mathcal{L}[\hat{a}]\hat{\rho}_{\mathrm{red}}, \tag{1.2.15}$$

with the effective Hamiltonian [13]

$$\hat{H}_{\mathrm{red}} = \frac{\hat{p}^2}{2m} - \hbar(\Delta_c - U_0\cos^2(k\hat{x}))\hat{a}^\dagger\hat{a} + \hbar S\cos(k\hat{x})(\hat{a}^\dagger + \hat{a}) + \hbar\eta(\hat{a}^\dagger + \hat{a}). \tag{1.2.16}$$

Here $S = \Omega g/\Delta_a$ is the coherent scattering rate of laser photons into the resonator.[16] The quantity $U_0 = g^2/\Delta_a$ scales the dynamical AC Stark shift of the ground state. Both describe a coupling between the particle's external state and the cavity field which we denote by optomechanical coupling.

The term proportional to $U_0$ shifts the resonance of the cavity field depending on the position of the particle and, in turn, it is an optical lattice for the particle whose depth is a quantum variable. For a laser frequency that is red detuned to the atomic frequency ($\Delta_a < 0$) it lowers the cavity resonance frequency if the particle localizes at the antinodes of the cavity mode function $\cos(kx)$. Therefore if the laser is also red detuned with respect to the cavity frequency $\Delta_c < 0$ a localization at the antinodes shifts the cavity frequency towards resonance.

When $S \neq 0$, the corresponding term describes a pump of the cavity field whose amplitude depend on the particle's position. The effective scattering rate $|S\cos(kx)|$ is maximal if the particle is at an antinode of the cavity mode.

### 1.2.3 Elimination of the cavity field

The dynamics described by Eq. (1.2.15) has been studied in Ref. [61] numerically using a semiclassical approximation for the field and the particle motion. In the following we want to derive analytical relations in the case where the cavity degrees of freedom can be eliminated. This will allow us to derive effective light-mediated forces acting on the particle.

[16] The coherent scattering rate is usually given in the form $S = \Omega g\Delta_a/(\Delta_a^2 + \gamma^2/4)$ that simplifies for large detuning to $S = \Omega g/\Delta_a$. The incoherent scattering rate $S_{\mathrm{inc}} = \Omega g\gamma/[2(\Delta_a^2 + \gamma^2/4)]$ is of the order $\gamma/|\Delta_a|$ smaller than $S$ and can therefore be neglected.

**Steady-state of the field**

We calculate now the master equation for the reduced density matrix $\hat{\rho}_{\rm par} = {\rm Tr}_{\rm cav}(\hat{\rho}_{\rm red})$ where we defined the trace over the cavity degrees of freedom as ${\rm Tr}_{\rm cav}(\hat{\rho}) = \sum_{n=0}^{\infty}\langle n|\hat{\rho}|n\rangle$, with the Fock states $|n\rangle$ that fulfill $\hat{a}|n\rangle = \sqrt{n}|n-1\rangle$ for $n = 1, 2, ....$ This is done using Eq. (1.2.15) and tracing over the cavity variables. The resulting equation reads

$$\frac{\partial\hat{\rho}_{\rm par}}{\partial t} = \frac{1}{i\hbar}\left[\frac{\hat{p}^2}{2m}, \hat{\rho}_{\rm par}\right] + \frac{1}{i\hbar}\left[\hbar U_0\cos^2(k\hat{x}), \left\langle\hat{a}^\dagger\hat{a}\right\rangle_{\rm cav}\right] + \frac{1}{i\hbar}\left[\hbar S\cos(k\hat{x}), \left\langle\hat{a}^\dagger + \hat{a}\right\rangle_{\rm cav}\right], \tag{1.2.17}$$

where in the reduced Hilbert space of the atom the cavity relaxation term vanishes. We defined here $\langle\hat{O}\rangle_{\rm cav} = {\rm Tr}_{\rm cav}(\hat{O}\hat{\rho}_{\rm red})$, where the time evolution of the operators $\left\langle\hat{a}^\dagger\hat{a}\right\rangle_{\rm cav}$ and $\left\langle\hat{a}^\dagger + \hat{a}\right\rangle_{\rm cav}$ is governed by the equation of motion derived from Eq. (1.2.15) [17]

$$\begin{aligned}\frac{\partial\left\langle\hat{a}\right\rangle_{\rm cav}}{\partial t} =& \left(i[\Delta_c - U_0\cos^2(k\hat{x})] - \frac{\kappa}{2}\right)\left\langle\hat{a}\right\rangle_{\rm cav} - i(\eta + S\cos(k\hat{x}))\hat{\rho}_{\rm par} \\ &+ \frac{1}{i\hbar}\left[\frac{\hat{p}^2}{2m}, \left\langle\hat{a}\right\rangle_{\rm cav}\right] + \frac{1}{i\hbar}\left[\hbar U_0\cos^2(k\hat{x}), \left\langle\hat{a}^\dagger\hat{a}\hat{a}\right\rangle_{\rm cav}\right] \\ &+ \frac{1}{i\hbar}\left[\hbar S\cos(k\hat{x}), \left\langle\left(\hat{a} + \hat{a}^\dagger\right)\hat{a}\right\rangle_{\rm cav}\right], \end{aligned} \tag{1.2.18}$$

$$\begin{aligned}\frac{\partial\left\langle\hat{a}^\dagger\hat{a}\right\rangle_{\rm cav}}{\partial t} =& -\kappa\left\langle\hat{a}^\dagger\hat{a}\right\rangle_{\rm cav} - i(\eta + S\cos(k\hat{x}))\left\langle\hat{a}^\dagger - \hat{a}\right\rangle_{\rm cav} \\ &+ \frac{1}{i\hbar}\left[\frac{\hat{p}^2}{2m}, \left\langle\hat{a}^\dagger\hat{a}\right\rangle_{\rm cav}\right] + \frac{1}{i\hbar}\left[\hbar U_0\cos^2(k\hat{x}), \left\langle(\hat{a}^\dagger\hat{a})^2\right\rangle_{\rm cav}\right] \\ &+ \frac{1}{i\hbar}\left[\hbar S\cos(k\hat{x}), \left\langle\left(\hat{a} + \hat{a}^\dagger\right)\hat{a}^\dagger\hat{a}\right\rangle_{\rm cav}\right]. \end{aligned} \tag{1.2.19}$$

Now, $\left\langle\hat{a}\right\rangle_{\rm cav}$ and $\left\langle\hat{a}^\dagger\hat{a}\right\rangle_{\rm cav}$ are operators defined over the particle's Hilbert space. If we first treat the position $x$ as a time-independent parameter and we calculate the stationary state, providing $\partial\left\langle\hat{a}\right\rangle_{\rm cav}/\partial t = 0$ and $\partial\left\langle\hat{a}^\dagger\hat{a}\right\rangle_{\rm cav}/\partial t = 0$, we obtain

$$\langle\hat{a}\rangle_{\rm cav} = \frac{\eta + S\cos(kx)}{\Delta_c - U_0\cos^2(kx) + i\frac{\kappa}{2}}, \tag{1.2.20}$$

$$\langle\hat{a}^\dagger\hat{a}\rangle_{\rm cav} = \frac{[\eta + S\cos(kx)]^2}{[\Delta_c - U_0\cos^2(kx)]^2 + \frac{\kappa^2}{4}}. \tag{1.2.21}$$

In the following we use these expression to eliminate the cavity degrees of freedom. We assume $U_0, \eta, S \ll \Delta_c, \kappa$, such that $\langle\hat{a}\rangle_{\rm cav} \ll 1$, and the population of the cavity field mode $\langle\hat{a}^\dagger\hat{a}\rangle_{\rm cav}$ can be discarded.

### 1.2.4 Optomechanical dynamics

We now include the particle's motion. Following the procedure as in subsection 1.1.3, we move to the reference frame moving with the particle

$$\tilde{\rho}_{\rm red} = \exp\left(\frac{i}{\hbar}\frac{\hat{p}^2}{2m}t\right)\hat{\rho}_{\rm red}\exp\left(-\frac{i}{\hbar}\frac{\hat{p}^2}{2m}t\right).$$

[17] Note that $\langle\hat{O}\rangle_{\rm cav}$ is an operator in the Hilbert space of the particle's external degrees of freedom.

In the following we will use the notations $\tilde{\rho}_{\rm par} = {\rm Tr}_{\rm cav}(\tilde{\rho}_{\rm red})$ and $\langle \tilde{O} \rangle_{\rm cav} = {\rm Tr}_{\rm cav}(\hat{O}\tilde{\rho}_{\rm red})$.

Formally integrating Eq. (1.2.18), we obtain

$$\begin{aligned}\langle \tilde{a} \rangle_{\rm cav}(t) \approx & e^{(i\Delta_c-\kappa)t}\langle \tilde{a} \rangle_{\rm cav}(0) - i\int_0^t d\tau e^{(i\Delta_c-\kappa)(t-\tau)}[\eta + S\cos(k\hat{x}(\tau))]\tilde{\rho}_{\rm par}(\tau) \\ & - i\int_0^t d\tau e^{(i\Delta_c-\kappa)(t-\tau)}U_0\cos^2(k\hat{x}(\tau))\langle \tilde{a} \rangle_{\rm cav}(\tau), \end{aligned} \tag{1.2.22}$$

where we discarded the second order in $\epsilon \sim (\eta, S, U_0)/(\Delta_c^2 + \kappa^2/4)^{1/2}$. In presence of a time scale separation between the typical timescale of the particle's external degrees of freedom and the timescale of the cavity degrees of freedom we get

$$\langle \tilde{a} \rangle_{\rm cav}(t) = \left[\frac{\eta}{\Delta_c + i\frac{\kappa}{2}} + \frac{e^{ik\hat{x}(t)}}{2}\frac{S}{\Delta_c - \hat{\delta} - \omega_R + i\frac{\kappa}{2}} + \frac{e^{-ik\hat{x}(t)}}{2}\frac{S}{\Delta_c + \hat{\delta} - \omega_R + i\frac{\kappa}{2}}\right]\tilde{\rho}_{\rm par}(t). \tag{1.2.23}$$

We focus on the semiclassical regime, where we discard higher powers of $\omega_R$ with respect to $\Delta_c, \kappa$ and the Doppler shift. Following the same procedure as in subsection 1.1.3 we write

$$\langle \tilde{a} \rangle_{\rm cav}(t) = \left[\frac{\eta}{\Delta_c + i\frac{\kappa}{2}} + \frac{Se^{ik\hat{x}(t)}}{2(\Delta_c - \hat{\delta}) + i\kappa} + \frac{Se^{-ik\hat{x}(t)}}{2(\Delta_c + \hat{\delta}) + i\kappa}\right]\tilde{\rho}_{\rm par}(t). \tag{1.2.24}$$

This term is almost equivalent to the term given in Eq. (1.1.35). The first term in Eq. (1.2.24) represents the coherent cavity field that is created by the laser pump of the cavity. This term does not include the coupling to motional degrees of the particle since it is a direct coupling of the laser with the cavity mode. Such a term is not present in Eq. (1.1.35). The two terms proportional to $S$ describe the scattering of the transversal light field into the cavity mode. The two terms belong to the different scattering directions with respect to the particle's motion. Therefore the scattering amplitude appears with Doppler-shifted frequencies. [18]

In analogy with the procedure shown in subsection 1.1.3 we can use $\langle \hat{p} \rangle = {\rm Tr}(\hat{p}\tilde{\rho}_{\rm par})$ to define a hermitian force operator $\hat{F}$ by

$$\frac{d\langle \hat{p} \rangle}{dt} = \langle \hat{F} \rangle. \tag{1.2.25}$$

It can be developed into two terms $\hat{F}_1$ and $\hat{F}_2$ with

$$\hat{F} = \hat{F}_1 + \hat{F}_2, \tag{1.2.26}$$

which correspond now to the adiabatic and retarded response of the cavity field and read

$$\hat{F}_1 = \hbar k S\sin(k\hat{x}(t))\left\{\frac{2\Delta_c\eta}{\Delta_c^2 + \frac{\kappa^2}{4}} + \cos(k\hat{x}(t))\left[\frac{(\Delta_c - \hat{\delta})S}{(\Delta_c - \hat{\delta})^2 + \frac{\kappa^2}{4}} + \frac{(\Delta_c + \hat{\delta})S}{(\Delta_c + \hat{\delta})^2 + \frac{\kappa^2}{4}}\right]\right\}, \tag{1.2.27}$$

$$\hat{F}_2 = \hbar k S\sin^2(k\hat{x}(t))\left[\frac{\kappa S}{(\Delta_c - \hat{\delta})^2 + \frac{\kappa^2}{4}} - \frac{\kappa S}{(\Delta_c + \hat{\delta})^2 + \frac{\kappa^2}{4}}\right]. \tag{1.2.28}$$

In order to gain insight into the dynamics, we discuss in the following the limit where the Doppler shift is small compared to $\Delta_c$ and $\kappa$.

[18] The AC Stark shift $U_0$ is neglected here that is only valid for small cavity photon numbers and for a small value of $U_0/\Delta_c$. The AC Stark shift can be used for trapping and cooling of particles [30, 61] while its effect is suppressed in the regime that we use.

**Small Doppler-shift limit**

In this limit Eq. (1.1.42) takes the form

$$\hat{F}_1 \approx \hbar k S \sin(k\hat{x}(t)) \frac{2\Delta_c[\eta + S\cos(k\hat{x}(t))]}{\Delta_c^2 + \frac{\kappa^2}{4}}, \tag{1.2.29}$$

which is here reported up to first order in the expansion in $\hat{\delta}/(\Delta_c^2 + \kappa^2)^{1/2}$. This force is conservative since it can be written as

$$\hat{F}_1 \approx -\left.\frac{\partial \hat{V}(x)}{\partial x}\right|_{x=\hat{x}(t)}, \tag{1.2.30}$$

with

$$\hat{V}(\hat{x}) = \frac{\hbar\Delta_c(2\eta S\cos(k\hat{x}) + S^2\cos^2(k\hat{x}))}{\Delta_c^2 + \frac{\kappa^2}{4}}. \tag{1.2.31}$$

This potential has an additional term $\cos(k\hat{x})$ with respect to the potential derived in Eq. (1.1.43). This is due to the direct laser pump of the cavity that interferes with the laser photons that are scattered by the particles into the resonator.

The component due to the non-adiabatic corrections takes the form

$$\hat{F}_2 \approx \hbar k \sin^2(k\hat{x}(t)) \frac{2\Delta_c \kappa S^2}{\left(\Delta_c^2 + \frac{\kappa^2}{4}\right)^2}\hat{\delta}, \tag{1.2.32}$$

up to first order in $\hat{\delta}/(\Delta_c^2 + \kappa^2)^{1/2}$. It vanishes at the antinode of the cavity field intensity. Because of its linear dependence on the momentum of the particle it can be considered to be a friction force in the case of red detuning ($\Delta_c < 0$) and a heating force in the case of blue detuning ($\Delta_c > 0$).

The resulting dynamics of the kinetic energy takes the same form as Eq. (1.1.48), where $\hat{F}_1$ and $\hat{F}_2$ are now given by Eq. (1.2.29) and Eq. (1.2.32), respectively, and the diffusion coefficient takes the form

$$\hat{D} \approx \frac{(\hbar k)^2 S^2 \kappa}{\Delta_c^2 + \frac{\kappa^2}{4}} \sin^2(k\hat{x}(t)). \tag{1.2.33}$$

This equation allows for a steady state for $\Delta_c < 0$. In our case the stationary value of the kinetic energy reads

$$\frac{\langle \hat{p}^2 \rangle}{2m} = \frac{\hbar(\Delta_c^2 + \frac{\kappa^2}{4})}{-8\Delta_c}, \tag{1.2.34}$$

and for the choice of $\Delta_c = -\kappa/2$ it reaches its minimum value $\langle \hat{p}^2 \rangle / 2m = \hbar\kappa/8$.

Cavity cooling of a two-level system has first been predicted in Ref. [29]. Since cavity cooling relies on coherent scattering of photons it has been pointed out to be applicable to cool molecules, which typically do not have closed transitions [30, 62]. Cooling of particles by means of coherent scattering inside a resonator has been realized for a single atom [57], a single ion [63], atomic clouds [9, 10, 64], and nanoparticles [65, 66].

Section 1.3

# SUPERRADIANCE IN AN OPTICAL CAVITY

Superradiance, in quantum optics, describes the collective emission of $N$ emitters interacting with a common mode of the electromagnetic field. It relies on quantum interference of the emission amplitudes and gives rise to a macroscopic coherence in the atomic ensemble. As originally predicted by Dicke [4] superradiance appears for a sufficiently high optical density that can be realized if the interparticle distance of the atomic cloud is smaller than the optical wavelength [4, 5].

Superradiance can also be observed if dipoles couple to a common single mode of an resonator that confines the light [5, 33, 67]. This is the setup that we consider in this section.

## 1.3.1 Dipoles coupling to a single cavity mode

We study the model of $N$ identical dipoles interacting with a single resonator mode. The dynamics of the system is given by the Tavis-Cummings model [68, 69] [19]

$$\hat{H} = \hbar\omega_c \hat{a}^\dagger \hat{a} + \hbar\omega_a \sum_{j=1}^{N} \hat{\sigma}_j^\dagger \hat{\sigma}_j + \hbar g \sum_{j=1}^{N} (\hat{a}^\dagger \hat{\sigma}_j + \hat{\sigma}_j^\dagger \hat{a}). \tag{1.3.1}$$

Here $\omega_c$ is the frequency of the cavity mode, $\omega_a$ is the dipolar transition frequency, and $g$ is the vacuum Rabi frequency. The operators $\hat{a}$, $\hat{a}^\dagger$ are the cavity annihilation and creation operators and $\hat{\sigma}_j = |g\rangle_j\langle e|$ is the transition matrix from the excited state $|e\rangle_j$ to the ground state $|g\rangle_j$ of the $j$th atom. We assume that there is no inhomogeneous broadening of the transition frequency and that the coupling between cavity mode and particle $g$ is independent of the particle's position. In a cavity this is realizable by trapping the atoms at the antinodes of a standing-wave mode function $\cos(kx)$ [72].

### Collective spin

We now cast the Hamiltonian (1.3.1) in terms of collective spin operators. For this purpose we introduce $\hat{\sigma}_j^x = (\hat{\sigma}_j^\dagger + \hat{\sigma}_j)/2$, $\hat{\sigma}_j^y = (\hat{\sigma}_j^\dagger - \hat{\sigma}_j)/(2i)$, and $\hat{\sigma}_j^z = (\hat{\sigma}_j^\dagger\hat{\sigma}_j - \hat{\sigma}_j\hat{\sigma}_j^\dagger)/2$. The collective spin operators are given by

$$\hat{S}^x = \sum_{j=1}^{N} \hat{\sigma}_j^x, \tag{1.3.2}$$

$$\hat{S}^y = \sum_{j=1}^{N} \hat{\sigma}_j^y, \tag{1.3.3}$$

$$\hat{S}^z = \sum_{j=1}^{N} \hat{\sigma}_j^z. \tag{1.3.4}$$

[19] The Tavis-Cummings model is the Dicke model in the rotating wave approximation. The Dicke model is known for the Dicke phase transition between a normal and a superradiant phase [70, 71].

They fulfill the commutation relation [73]

$$[\hat{S}^n, \hat{S}^m] = \sum_{l=x,y,z} i\epsilon_{nml}\hat{S}^l, \tag{1.3.5}$$

where $n, m = x, y, z$ and $\epsilon_{nml}$ is the Levi-Civita Symbol. We can rewrite the Hamiltonian in Eq. (1.3.1) as

$$\hat{H} = \hbar\omega_c\hat{a}^\dagger\hat{a} + \hbar\omega_a\hat{S}^z + \hbar g(\hat{a}^\dagger\hat{S}^- + \hat{S}^+\hat{a}), \tag{1.3.6}$$

that is reported apart from the constant term $\hbar\omega_a/2$. Here, we used the raising and lowering operators $\hat{S}^\pm = \hat{S}^x \pm i\hat{S}^y$.

We will now choose a basis that will allow us to calculate explicitly transition amplitudes of $\hat{H}$. Using Eq. (1.3.5) one can show that the squared spin operator $\hat{\mathbf{S}}^2 = (\hat{S}^x)^2 + (\hat{S}^y)^2 + (\hat{S}^z)^2$ commutes with $\hat{S}^z$. Hence, one can find a common eigenbasis that we denote by $|s, m_s\rangle$[73]. The eigenvalues of $\hat{\mathbf{S}}^2$ and $\hat{S}^z$ corresponding to $|s, m_s\rangle$ are given by

$$\hat{\mathbf{S}}^2|s, m_s\rangle = s(s+1)|s, m_s\rangle, \tag{1.3.7}$$

$$\hat{S}^z|s, m_s\rangle = m_s|s, m_s\rangle, \tag{1.3.8}$$

where $-s \leq m_s \leq s$ and $s = N/2 - \lfloor N/2 \rfloor, N/2 - \lfloor N/2 \rfloor + 1, ..., N/2$. Here, $\lfloor x \rfloor$ is the floor function that maps $x$ to the greatest integer less or equal to $x$. With this definition one can verify that

$$\hat{S}^\pm|s, m_s\rangle = \sqrt{s(s+1) - m_s(m_s \pm 1)}|s, m_s \pm 1\rangle. \tag{1.3.9}$$

The Hamiltonian $\hat{H}$ commutes with $\hat{\mathbf{S}}^2$ and $\hat{E} = \hat{S}^z + \hat{a}^\dagger\hat{a}$. Therefore, the length of the collective Bloch vector $\langle\hat{\mathbf{S}}^2\rangle$ and the total number of excitations $\langle\hat{E}\rangle$ are constants of motion. As a result a state of the form $|s, m_s; n_{\text{ph}}\rangle = |s, m_s\rangle \otimes |n_{\text{ph}}\rangle$, where $|n_{\text{ph}}\rangle$ is the Fock state of the cavity mode corresponding to the photon number $n_{\text{ph}}$, can only couple to states where $|s', m'_s; n'_{\text{ph}}\rangle$ with $s' = s$, $m_s + n_{\text{ph}} = m'_s + n'_{\text{ph}}$.

### Collective emission rate

We consider now the case where the collective Bloch vector $\langle\hat{\mathbf{S}}\rangle$ points along $z$ direction [20] with $\langle\hat{S}^z\rangle = N/2$ and the cavity mode is in the vacuum, such that $\langle\hat{E}\rangle = N/2$. Therefore, the initial state reads $|s = N/2, m_s = N/2; n_{\text{ph}} = 0\rangle$. In this state photon emission leads to a decrease of the number of particles in the excited states according to $\langle\hat{S}^z\rangle = N/2 - \langle\hat{a}^\dagger\hat{a}\rangle$.

The superradiant enhancement of the emission rate is visible in the scaling with $N$ of the transition amplitude describing the emission of one photon

$$\langle m_s = N/2 - 1; n_{\text{ph}} = 1|\hat{H}|m_s = N/2; n_{\text{ph}} = 0\rangle = g\sqrt{N}. \tag{1.3.10}$$

We note that $|s = N/2, m_s = N/2 - 1\rangle$ is a coherent superposition of atomic excitations:

$$|s = N/2, m_s = N/2 - 1\rangle = \frac{1}{\sqrt{N}}\left(|g, e, e, ..., e\rangle + |e, g, e, ..., e\rangle + ... + |e, e, e, ..., g\rangle\right) \tag{1.3.11}$$

[20] We assume that all particles are in the excited state.

### 1.3.2 Superradiant emission in a bad cavity

We now introduce the effect of cavity decay into the dynamics. The master equation for the density matrix $\hat{\rho}$ describing the particles' internal and the cavity degrees of freedom can be written as

$$\frac{\partial \hat{\rho}}{\partial t} = \frac{1}{i\hbar}[\hat{H}, \hat{\rho}] + \kappa \mathcal{L}[\hat{a}]\hat{\rho}, \tag{1.3.12}$$

where $\hat{H}$, given by Eq. (1.3.1), describes the coherent effects and $\kappa\mathcal{L}[\hat{a}]$, shown in Eq. (1.1.11), describes the dissipation of the cavity mode with rate $\kappa$.[21]

Now, we consider the bad cavity regime, namely the regime when

$$\sqrt{N}g \ll \kappa,$$

hence the dipoles cannot absorb the photon. This parameter regime allows us to eliminate the cavity degrees of freedom and the evolution can be cast in a Born-Markov master equation for the reduced density matrix $\hat{\rho}_{\rm red}$, describing the dipoles' degrees of freedom, that reads[22]

$$\frac{\partial \hat{\rho}_{\rm red}}{\partial t} = \frac{1}{i\hbar}\left[\hat{H}_{\rm eff}, \hat{\rho}_{\rm eff}\right] + \Gamma_c \mathcal{L}[\hat{S}^-]\hat{\rho}_{\rm eff}, \tag{1.3.13}$$

with

$$\hat{H}_{\rm eff} = -\frac{\Delta}{\kappa/2}\frac{\hbar\Gamma_c}{2}\hat{S}^+\hat{S}^-, \tag{1.3.14}$$

and the single-particle decay rate

$$\Gamma_c = \frac{g^2\kappa}{\Delta^2 + \frac{\kappa^2}{4}}. \tag{1.3.15}$$

Details of the derivation are reported in App. A.1. Both, the Hamiltonian (1.3.14) and the dissipator $\mathcal{L}[\hat{S}^-]$, include coupling terms of the form $\hat{\sigma}_i^\dagger\hat{\sigma}_j$ that describe the dipole-dipole coupling mediated by the cavity field.

Using Eq. (1.3.13) we can derive

$$\frac{d\langle \hat{S}^z\rangle}{dt} = -\Gamma_c\left\langle \hat{S}^+\hat{S}^-\right\rangle = -\Gamma_c\left[\left\langle \hat{\mathbf{S}}^2\right\rangle - \left\langle (\hat{S}^z)^2\right\rangle + \left\langle \hat{S}^z\right\rangle\right]. \tag{1.3.16}$$

This equation of motion describes the dynamics of $\langle \hat{S}^z\rangle$. It couples to the second moment $\langle (\hat{S}^z)^2\rangle$. The equation for the second moment of $\hat{S}^z$ in turn, couples it to higher moments. In order to solve this hierarchy of equations, we make the mean-field approximation $\langle (\hat{S}^z)^2\rangle \approx \langle \hat{S}^z\rangle^2$. In this case we can solve Eq. (1.3.16) using the separation of variables and obtain

$$\int_{\langle \hat{S}^z(t_0)\rangle}^{\langle \hat{S}^z(t)\rangle} \frac{dx}{(s+x)(s+1-x)} = -\Gamma_c(t-t_0),$$

that can be rewritten after elementary transformation as

$$\frac{s + \langle \hat{S}^z(t)\rangle}{s+1-\langle \hat{S}^z(t)\rangle} = \frac{s + \langle \hat{S}^z(t_0)\rangle}{s+1-\langle \hat{S}^z(t_0)\rangle} e^{-\Gamma_c(2s+1)(t-t_0)}. \tag{1.3.17}$$

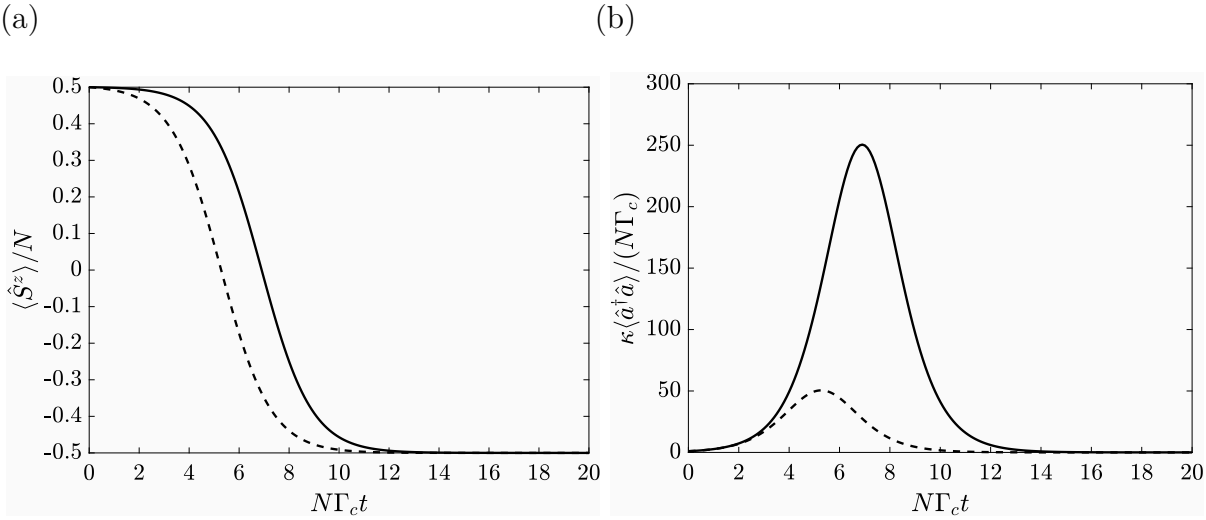


Figure 1.3: The projection of the Bloch vector on the $z$ axis $\langle\hat{S}^z\rangle$ (a) and the intracavity photon number $\langle\hat{a}^\dagger\hat{a}\rangle$ (c) as function of time $t$ (in units of $(N\Gamma_c)^{-1}$). The dashed lines correspond to $N = 200$ and the solid line to $N = 1000$. We have chosen $s = N/2$ for both curves and $\langle\hat{S}^z(t_0)\rangle = s/2$, $t_0 = 0$. The curves are derived under the assumption $\langle(\hat{S}^z)^2\rangle = \langle\hat{S}^z\rangle^2$ using Eq. (1.3.17) and Eq. (1.3.20).

The solution $\langle\hat{S}^z(t)\rangle$ of Eq. (1.3.17) is shown in Fig. 1.3(a) as a function of time. At $t = 0$ the particles are initialized in the state where all particles are in the excited state $\langle\hat{S}^z\rangle = N/2$. The steady state of the system is reached after sufficient long time $t \gg 1/(N\Gamma_c)$. The time axis is rescaled with $N$ such that the decay appears approximately in the same time interval. However, the two curves for $N = 1000$ and $N = 200$ are slightly displaced. This can be understood by solving Eq. (1.3.17) in the limit $N \gg 1$. The solution reads

$$\langle\hat{S}^z\rangle \approx \frac{N}{2}\left[\frac{Ne^{-\Gamma_c N t} - 1}{Ne^{-\Gamma_c N t} + 1}\right] = \frac{N}{2}\tanh\left[\frac{N\Gamma_c}{2}(t - t_D)\right], \tag{1.3.18}$$

where [5]

$$t_D = \frac{\log(N)}{N\Gamma_c}. \tag{1.3.19}$$

This time $t_D$ scales the duration of the superradiant emission process and explains the deviation of both curves in Fig. 1.3(a).

Figure 1.3(b) shows the intracavity field photon number $\langle\hat{a}^\dagger\hat{a}\rangle$ as function of time. This curve has been calculated using Eq. (1.3.12) where we extract the solution

$$\langle\hat{a}^\dagger\hat{a}\rangle \approx \frac{\Gamma_c}{\kappa}\langle\hat{S}^+\hat{S}^-\rangle \tag{1.3.20}$$

in the limit $\kappa \gg \sqrt{N}g$. We observe an exponential increase of the photon number, after which it reaches its maximum value at time $t = t_D$ and decreases to zero. The maximum of the intracavity photon correlates with the collective Bloch vector pointing in the $x, y$ plane. This orientation supports superradiant emission into the cavity field.

[21] Although this is a dissipative system it conserves the length of the Bloch vector. However, it does not conserve the total number of excitations.

[22] This is a special case of the master equation for superradiance [5].

# Chapter 2

# Self-organization of particles in an optical cavity

In this chapter we investigate the formation and the properties of self-organized spatial structures interacting with an optical cavity. It is divided into three sections. Section 2.1 contains an introduction to self-organization of particles in optical cavities. The theoretical description is based on a semiclassical model, which is used to simulate the dynamics. In section 2.2 we discuss steady-state properties of self-organized systems. Section 2.3 treats the relaxation dynamics of the system into the stationary state. The concluding section 2.4 summarizes the chapter.

Section 2.1

# SEMICLASSICAL DESCRIPTION OF SELF-ORGANIZATION OF PARTICLES IN OPTICAL CAVITIES

In this section we present the semiclassical model for the description of transversally pumped particles inside a cavity. We will introduce the theoretical tools that are used throughout this chapter to describe and simulate self-organization of particles which optomechanically couple to a standing wave mode of a high-finesse cavity. In the end of this section we provide a short overview of work that is related to this chapter and the recent work that is done in this field.

## 2.1.1 The model of single-mode self-organization

We consider $N$ polarizable particles with mass $m$ in an optical resonator that are transversally pumped by a laser and coherently scatter photons into a single cavity mode. For the case of red detuning $\Delta_c = \omega_L - \omega_c < 0$ when the laser frequency $\omega_L$ is smaller than the frequency of the cavity mode $\omega_c$ the particles undergo superradiant scattering for a sufficiently high driving-laser intensity. This superradiant scattering occurs when the atoms form a Bragg grating. The Bragg grating, on the other hand, can be stabilized by the mechanical effects of light of the intracavity field. Superradiance can then lead to the spontaneous formation of spatially ordered structures which support, in turn, superradiant scattering into the cavity mode. This effect is referred to as atomic self-organization in optical cavities [9] and is analyzed by means of a semiclassical description in this chapter.

### Master equation

The dynamics of the system can be described by means of a master equation

$$\frac{\partial \hat{\rho}}{\partial t} = \frac{1}{i\hbar}[\hat{H}, \hat{\rho}] + 2\kappa \mathcal{L}[\hat{a}]\hat{\rho}, \tag{2.1.1}$$

where we used the definition of Eq. (1.1.11). The Hamiltonian $\hat{H}$ in Eq. (2.1.1) describes the coherent dynamics[1] and is given by

$$\hat{H} = \sum_{j=1}^{N} \frac{\hat{p}_j^2}{2m} - \hbar\Delta_c \hat{a}^\dagger \hat{a} + \sum_{j=1}^{N} \hbar S \cos(k\hat{x}_j)(\hat{a}^\dagger + \hat{a}). \tag{2.1.2}$$

Here $\hat{p}_j$ and $\hat{x}_j$ are the momentum and position operator of the $j$th particle with mass $m$ fulfilling the commutation relation $[\hat{x}_j, \hat{p}_j] = 1$. The operators $\hat{a}$ and $\hat{a}^\dagger$ are the cavity mode annihilation and creation operator with the commutation relation $[\hat{a}, \hat{a}^\dagger] = 1$. The mode function of the cavity mode is here $\cos(kx)$ where $k = 2\pi/\lambda$ is the wavenumber of the scattered photons, $\lambda$ is the wavelength, and $S$ is the coherent scattering rate. The

[1] This is the many-atom version of the Hamiltonian presented in Eq. (1.2.16), where we neglect here the dynamical AC Stark shift and we do not consider a direct pump of the cavity mode [13].

model is described in a frame rotating with the laser frequency $\omega_L$ where $\Delta_c = \omega_L - \omega_c$ is the detuning between the laser frequency $\omega_L$ and the frequency of the cavity mode $\omega_c$. The incoherent dynamics is governed by the cavity decay process $2\kappa\mathcal{L}[\hat{a}]\hat{\rho}$ where $\kappa$ is the linewidth of the cavity mode.

In the following subsection we will specify the parameter regime that we are working with. This will allow us to derive a semiclassical picture where the cavity degrees of freedom are eliminated. For details we refer the reader to Ref. [74], where this derivation has been first reported.

### 2.1.2 Elimination of the cavity degrees of freedom and semiclassical dynamics

We consider the parameter regime where the cavity degrees of freedom evolve much faster than the particles degrees of freedom. This is the case when the cavity detuning $\Delta_c$ and decay rate $\kappa$ are by far the largest frequencies in the coupled system that have to be much larger than the average Doppler shift $k\Delta p/m$ and the recoil frequency $\omega_R = \hbar k^2/2m$:

$$|\Delta_c + i\kappa| \gg \frac{k\Delta p}{m}, \omega_R. \tag{2.1.3}$$

In our approach we consider that the single particle momentum width $\Delta p$ exceeds the single photon recoil $\hbar k$ such that

$$\Delta p \gg \hbar k. \tag{2.1.4}$$

The regime of validity of this inequality corresponds to the semiclassical approximation for the particles' motion [45, 75].

The inequalities (2.1.3) and (2.1.4) are not completely independent from each other but they are consistent in the case where the following inequality holds[2]

$$\omega_R \ll \frac{k\Delta p}{m} \ll |\Delta_c + i\kappa|.$$

#### Wigner representation and Fokker-Planck equation

In order to derive an equation of motion for the semiclassical limit, we use a phase-space representation for the external degrees of freedom. The density matrix in Wigner representation reads

$$\hat{W}(\mathbf{x}, \mathbf{p}) = \frac{1}{(2\pi\hbar)^N} \int d\boldsymbol{\xi} e^{-\frac{i}{\hbar}\mathbf{p}\cdot\boldsymbol{\xi}} \langle \mathbf{x} + \boldsymbol{\xi}/2|\hat{\rho}|\mathbf{x} - \boldsymbol{\xi}/2\rangle,$$

where $\mathbf{p} = (p_1, ..., p_N)$, $\mathbf{x} = (x_1, ..., x_N)$, $\boldsymbol{\xi} = (\xi_1, .., \xi_N)$ and $\mathbf{p}\cdot\boldsymbol{\xi}$ is the standard scalar product in $\mathbb{R}^n$. Note that we adopt the convention $\int d\boldsymbol{\xi} = \int_{-\infty}^{\infty} d\xi_1 ... \int_{-\infty}^{\infty} d\xi_N$. The Wigner transformation is applied to both sides of the master equation in Eq. (2.1.1). Particularly interesting is the transformation of the position-dependent operators. They give

$$\frac{\int d\boldsymbol{\xi} e^{-\frac{i}{\hbar}\mathbf{p}\cdot\boldsymbol{\xi}} \langle \mathbf{x} + \boldsymbol{\xi}/2| \cos(k\hat{x}_i)\hat{\rho}|\mathbf{x} - \boldsymbol{\xi}/2\rangle}{(2\pi\hbar)^N} = \frac{e^{ikx_i}\hat{W}\left(\mathbf{x}, \mathbf{p} - \frac{\hbar k}{2}\mathbf{e}_i\right) + e^{-ikx_i}\hat{W}\left(\mathbf{x}, \mathbf{p} + \frac{\hbar k}{2}\mathbf{e}_i\right)}{2}. \tag{2.1.5}$$

[2]For typical setups we consider $\kappa$, $|\Delta_c|$ is of the order of $10^6$ s$^{-1}$ [58], the Doppler shift is of the order of $10^5$ s$^{-1}$ and the recoil frequency of the order of $10^4$ s$^{-1}$. In that case all frequencies differ by an order of magnitude.

Here $\mathbf{e}_i$ denote the $N$ dimensional unit vector whose $i$th entry is equal to one while all other entries are equal to zero.

The semiclassical approximation (see Eq. (2.1.4)) for the operator in Eq. (2.1.5) can be understood as a coarse graining of the momentum axis where we can treat the change in the momentum variable $\mathbf{p}$ by $\hbar k/2$ as infinitesimal since it is much smaller than the momentum width $\Delta p$ of the distribution. This allows to approximate

$$\hat{W}\left(\mathbf{x},\mathbf{p}-\frac{\hbar k}{2}\mathbf{e}_i\right)\approx\hat{W}\left(\mathbf{x},\mathbf{p}\right)-\frac{\hbar k}{2}\frac{\partial}{\partial p_i}\hat{W}\left(\mathbf{x},\mathbf{p}\right)+\frac{(\hbar k)^2}{8}\frac{\partial^2}{\partial p_i^2}\hat{W}\left(\mathbf{x},\mathbf{p}\right), \tag{2.1.6}$$

where we neglect terms with an order of magnitude larger than $(\hbar k/\Delta p)^2$. We use Eq. (2.1.5) and Eq. (2.1.6) and obtain

$$\begin{aligned}\frac{\partial\hat{W}}{\partial t}=&\frac{1}{i\hbar}\left[-\hbar\Delta_c\hat{a}^\dagger\hat{a}+\hbar S\sum_{j=1}^{N}\cos(kx_j)(\hat{a}+\hat{a}^\dagger),\hat{W}\right]+2\kappa\mathcal{L}[\hat{a}]\hat{W}\\&+\mathcal{L}_{\text{kin}}\hat{W}-\left[\frac{\hbar k}{2}S\sum_{j=1}^{N}\sin(kx_j)(\hat{a}+\hat{a}^\dagger)\frac{\partial\hat{W}}{\partial p_j}+\text{H.c.}\right]\\&-\frac{i\hbar k^2}{8}S\sum_{j=1}^{N}\left[\cos(k\hat{x}_j)(\hat{a}+\hat{a}^\dagger),\frac{\partial^2\hat{W}}{\partial p_j^2}\right],\end{aligned} \tag{2.1.7}$$

and the kinetic term

$$\mathcal{L}_{\text{kin}}\hat{W}=-\sum_j\frac{p_j}{m}\frac{\partial\hat{W}}{\partial x_j}. \tag{2.1.8}$$

The next step is to use the separation of timescales that allows us to eliminate the cavity degrees of freedom from the equations of motion of the atoms and to derive an effective equation of motion for the particles' external degrees of freedom. For this purpose we describe the dynamics of the atoms on a coarse-grained timescale with timesteps $\Delta t$ where we derive an effective evolution that is governed by a Fokker-Planck equation for the particles' Wigner function $f(\mathbf{x},\mathbf{p})$.

For this purpose we choose the timestep $\Delta t$ sufficiently long compared to the typical relaxation time of the cavity degrees of freedom $T_C\sim|\Delta_c+i\kappa|^{-1}$ but sufficiently short compared to the typical timescale of the particles motion $T_S\sim(k\Delta p/m)^{-1}$. This corresponds to assuming

$$T_C\ll\Delta t\ll T_S. \tag{2.1.9}$$

The Fokker-Planck equation for the particles' Wigner function can than be derived by integrating Eq. (2.1.7) on the timesteps $\Delta t$. To do this we consider the frame that moves with the particles' velocities in the time interval $[t_0,t_0+\Delta t]$

$$\hat{\tilde{W}}(\mathbf{x},\mathbf{p})=e^{\mathcal{L}_{\text{kin}}\tau}\hat{W}=\hat{W}(\mathbf{x}+\mathbf{p}\tau/m,\mathbf{p}), \tag{2.1.10}$$

where $\tau=t-t_0<\Delta t$ and $t_0$ is an arbitrary instant of time. Using $T_S\gg\Delta t$ we can expand $\cos(kx_j+kp_j\tau/m)$ and $\sin(kx_j+kp_j\tau/m)$ to find the following equations of motion

$$\frac{\partial\hat{\tilde{W}}}{\partial t}=\mathcal{L}_0\hat{\tilde{W}}+\mathcal{L}_1(t)\hat{\tilde{W}}+\mathcal{L}_2\hat{\tilde{W}}. \tag{2.1.11}$$

Here the individual terms are defined as

$$\mathcal{L}_0\hat{\tilde{W}}_t = \frac{1}{i\hbar}\left[-\hbar\Delta_c\hat{a}^\dagger\hat{a} + \hbar S\sum_{j=1}^{N}\cos(kx_j)(\hat{a}+\hat{a}^\dagger), \hat{W}\right] + 2\kappa\mathcal{L}[\hat{a}], \tag{2.1.12}$$

$$\mathcal{L}_1(t)\hat{\tilde{W}}_t = \frac{i}{\hbar}\tau\sum_{j=1}^{N}\left[\frac{p_j}{m}\hat{F}_j, \hat{\tilde{W}}_t\right] - \frac{1}{2}\sum_{j=1}^{N}\left[\left(\frac{\partial}{\partial p_j} - \frac{\tau}{m}\frac{\partial}{\partial x_j}\right)\hat{\tilde{W}}_t, \hat{F}_j\right]_+, \tag{2.1.13}$$

$$\mathcal{L}_2\hat{\tilde{W}}_t = \frac{i\hbar}{8}\sum_{j=1}^{N}\left[\frac{\partial^2}{\partial p_j^2}\hat{\tilde{W}}_t, \frac{\partial}{\partial x_j}\hat{F}_j\right], \tag{2.1.14}$$

where $\hat{F}_j = \hbar k S\sin(kx_j)(\hat{a}+\hat{a}^\dagger)$ is the force operator, $[\hat{A},\hat{B}]_+ = \hat{A}\hat{B}+\hat{B}\hat{A}$ is the anticommutator, and $\mathcal{L}_i$ collects the terms at order $\epsilon^i$ with $\epsilon \sim \hbar k/\Delta p, k\Delta p\Delta t/m$ and $i = 0, 1, 2$.

The stationary state $\hat{W}_0$ of $\mathcal{L}_0$ satisfies $\mathcal{L}_0\hat{W}_0 = 0$. It can be calculated analytically

$$\hat{W}_0 = \tilde{f}(\mathbf{x},\mathbf{p})|\alpha(\mathbf{x})\rangle\langle\alpha(\mathbf{x})|, \tag{2.1.15}$$

where function $\tilde{f}(\mathbf{x},\mathbf{p})$ is the Wigner function of the particles' degrees of freedom and $|\alpha(\mathbf{x})\rangle$ is a coherent state of the cavity field with amplitude

$$\alpha(\mathbf{x}) = \frac{NS}{\Delta_c + i\kappa}\Theta(\mathbf{x}) \tag{2.1.16}$$

and

$$\Theta(\mathbf{x}) = \frac{1}{N}\sum_{j=1}^{N}\cos(kx_j). \tag{2.1.17}$$

We now use perturbation theory in order to derive a closed equation for the Wigner function $\tilde{f}(\mathbf{x},\mathbf{p})$. For this purpose, we split the Wigner operator into the sum

$$\hat{\tilde{W}} = \hat{W}_0 + \hat{\xi}, \tag{2.1.18}$$

where $\hat{\tilde{\xi}} = \hat{\tilde{W}} - \hat{W}_0$ is the correction to $\hat{W}_0$ (Eq. (2.1.15)). The equation of motion for $\tilde{f}(\mathbf{x},\mathbf{p})$ at $t = t_0$ can then be derived applying the trace over the cavity degrees of freedom $\mathrm{Tr}_{\mathrm{cav}}$ on Eq. (2.1.11). This delivers the equation

$$\left.\frac{\partial\tilde{f}}{\partial t}\right|_{t=t_0} = \mathrm{Tr}_{\mathrm{cav}}(\mathcal{L}_1(t_0)(\hat{W}_0(t_0) + \hat{\xi}(t_0))) + \mathrm{Tr}_{\mathrm{cav}}(\mathcal{L}_2(t_0)\hat{W}_0(t_0)). \tag{2.1.19}$$

The formal integration of Eq. (2.1.11) over the time interval $[t_0, t_0+\Delta t]$ [3] allows us to identify the form of the operator $\hat{\xi}(t_0)$:

$$\hat{\xi}(t_0) = \int_0^\infty d\tau\left[e^{\mathcal{L}_0\tau}\mathcal{L}_1(t_0-\tau)\hat{W}_0(t_0) - \mathrm{Tr}_{\mathrm{cav}}(e^{\mathcal{L}_0\tau}\mathcal{L}_1(t_0-\tau)\hat{W}_0(t_0)\right]. \tag{2.1.20}$$

Using Eq. (2.1.20) in Eq. (2.1.19) and

$$\frac{\partial\tilde{f}}{\partial t} = \frac{\partial f}{\partial t} + \sum_{j=1}^{N}\frac{p_j}{m}\frac{\partial f}{\partial x_j},$$

[3] Notice that the form of $\mathcal{L}_1$ given in Eq. (2.1.13) can be used since the timescale $\Delta t$ is very long compared to $T_C$. Therefore the action of $e^{\mathcal{L}_0\tau}$ on $\mathcal{L}_1(t_0-\tau)\hat{W}_0(t_0)$ will be practically zero for longer times $\tau > \Delta t$. This is a result of the timescale separation (2.1.9).

we get the Fokker-Planck equation (FPE) of the Wigner function $f(\mathbf{x}, \mathbf{p})$ at the instant of time $t_0$. This FPE describe the dynamics of the Wigner function on a coarsed grained timescale and reads

$$\frac{\partial f}{\partial t} + \{f, H\} = -\bar{n}\Gamma \sum_{j=1}^{N} \frac{\partial}{\partial p_j} \sum_{l=1}^{N} \sin(kx_j)\sin(kx_l) \left[ p_l + \frac{m}{\beta}\frac{\partial}{\partial p_l} + \frac{\bar{\eta}}{\beta}\frac{\partial}{\partial x_l} \right] f, \tag{2.1.21}$$

where $\{a, b\}$ denotes the Poisson bracket

$$\{a, b\} = \sum_{j=1}^{N} \left[ \frac{\partial a}{\partial x_j}\frac{\partial b}{\partial p_j} - \frac{\partial b}{\partial x_j}\frac{\partial a}{\partial p_j} \right]. \tag{2.1.22}$$

Here we have introduced the Hamilton function

$$H = \sum_{j=1}^{N} \frac{p_j^2}{2m} + \hbar\Delta_c \bar{n} N \Theta(\mathbf{x})^2 \tag{2.1.23}$$

and the quantity

$$\bar{n} = \frac{NS^2}{\Delta_c^2 + \kappa^2} \tag{2.1.24}$$

is the maximum mean intracavity photon number per particle.

The term on the right-hand side of Eq. (2.1.21) describe the dynamics which cannot be cast in a Poisson bracket. It is a term containing dissipative forces and diffusion. The coefficients read

$$\Gamma = \frac{8\omega_R \kappa \Delta_c}{\Delta_c^2 + \kappa^2}, \tag{2.1.25}$$

$$\beta = \frac{-4\Delta_c}{\hbar(\Delta_c^2 + \kappa^2)}, \tag{2.1.26}$$

$$\bar{\eta} = \frac{\kappa^2 - \Delta_c^2}{\kappa(\Delta_c^2 + \kappa^2)}. \tag{2.1.27}$$

The coefficient $\bar{\eta}$ is also reported in Refs. [75].

### Coherent dynamics

If we neglect the dissipative part, Eq. (2.1.21) reduces to

$$\frac{\partial f}{\partial t} + \{f, H\} = 0. \tag{2.1.28}$$

For Eq. (2.1.28) the energy is conserved and any function of the form

$$f(\mathbf{x}, \mathbf{p}) = \bar{f}(H(\mathbf{x}, \mathbf{p})) \tag{2.1.29}$$

is a stationary solution.

We consider the case of red detuning where $\Delta_c$ is negative therefore the potential term in Eq. (2.1.23) is negative and to minimize the system's energy we need to maximize $\Theta(\mathbf{x})^2$. The value of $\Theta(\mathbf{x})^2$, that we also call magnetization, is large if the system reaches one of the configurations where either $\cos(kx_j) \lesssim 1$ or $\cos(kx_j) \gtrsim -1$ for all $j = 1, ..., N$. In that case the particles order in a Bragg grating $kx_j \approx 2\pi n_j$ or $kx_j \approx 2\pi n_j + \pi$ with $n_j \in \mathbb{N}$, such that $|x_j - x_l| \approx (n_j - n_l)\lambda$. This spatial structure supports constructive interference of scattered photons that leads to superradiant scattering into the resonator.

**Steady state**

We now analyze the stationary state of the FPE including dissipation. We observe that $\bar{f}$ fulfills $\partial\bar{f}/(\partial t) = 0$ assuming $\bar{\eta} = 0$ and

$$0 = \sum_{j=1}^{N} \frac{\partial}{\partial p_j} \sum_{l=1}^{N} \sin(kx_j)\sin(kx_l) \left[ p_l \bar{f}(H) + \frac{m}{\beta} \frac{\partial H}{\partial p_l} \frac{\partial \bar{f}}{\partial H} \right]. \tag{2.1.30}$$

Using that

$$\bar{f}(H) + \frac{1}{\beta} \frac{\partial \bar{f}}{\partial H} = 0$$

we get as stationary solution a Maxwell-Boltzmann distribution

$$f(\mathbf{x}, \mathbf{p}) = Z^{-1} e^{-\beta H}, \tag{2.1.31}$$

where the width $\beta^{-1}$ is defined in Eq. (2.1.26) and

$$Z = \int d\mathbf{x} \int d\mathbf{p}\, e^{-\beta H}$$

is the partition function. Even though there is no proper thermal bath, the steady state has the form of a thermal state whose temperature $1/(k_B\beta)$, with Boltzmann constant $k_B$, is controlled by the cavity detuning $\Delta_c$ and the linewidth $\kappa$.

### 2.1.3 Generalization to multimode cavities

In this subsection we show how the assumptions and methods that we used to describe the semiclassical dynamics of particles interacting with a single cavity mode can be generalized to the coupling of the particles to several modes of a cavity.

**Master equation**

We consider a generalization of the master equation (2.1.1) that reads

$$\frac{\partial \hat{\rho}}{\partial t} = \frac{1}{i\hbar}[\hat{H}, \hat{\rho}] + \sum_{n=1}^{M} 2\kappa_n \mathcal{L}[\hat{a}_n]\hat{\rho}. \tag{2.1.32}$$

The Hamiltonian $\hat{H}$ in Eq. (2.1.32) describes the coherent dynamics and is given by

$$\hat{H} = \sum_{j=1}^{N} \frac{\hat{p}_j^2}{2m} - \sum_{n=1}^{M} \hbar\Delta_n \hat{a}^\dagger \hat{a} + \sum_{n=1}^{M} \sum_{j=1}^{N} \hbar S_n \cos(k_n \hat{x}_j)(\hat{a}_n^\dagger + \hat{a}_n). \tag{2.1.33}$$

Here we consider $M$ modes with annihilation and creation operator $\hat{a}_n$ and $\hat{a}_n^\dagger$, $n = 1, 2, ..., M$, with $[\hat{a}_n, \hat{a}_{n'}^\dagger] = \delta_{n,n'}$ where $\delta_{n,n'}$ is the Kronecker-delta. For the mode functions we consider here $\cos(k_n x)$[4] and $S_n$ is the single-particle coherent scattering into the $n$th mode. The frequency $\Delta_n$ is the detuning between the laser pump and the frequency of the $n$th mode and $\kappa_n$ scales the decay of this mode.

[4]The choice of the mode functions corresponds to orthogonal standing-wave longitudinal modes of the cavity.

**Fokker-Planck equation**

The derivation of a semiclassical theory where the cavity degrees are eliminated is very similar and can be done following a similar approach as in the single mode case [26, 74]. The generalization of $\hat{W}_0$ in Eq. (2.1.15) in this case is

$$\hat{W}_0 = \tilde{f}(\mathbf{x},\mathbf{p})|\alpha_1(\mathbf{x}),\alpha_2(\mathbf{x}),...,\alpha_M(\mathbf{x})\rangle\langle\alpha_1(\mathbf{x}),\alpha_2(\mathbf{x}),...,\alpha_M(\mathbf{x})| \tag{2.1.34}$$

where $\alpha_n(\mathbf{x})$ corresponds to a coherent state in the $n$th mode with

$$\alpha_n(\mathbf{x}) = \frac{NS_n}{\Delta_n + i\kappa_n}\Theta_n(\mathbf{x}). \tag{2.1.35}$$

Here we defined the generalization of Eq. (2.1.17) that reads

$$\Theta_n(\mathbf{x}) = \frac{1}{N}\sum_{j=1}^{N}\cos(k_n x_j). \tag{2.1.36}$$

The Fokker-Planck equation for the Wigner function $f$ can then be derived in a similar way and reads

$$\frac{\partial f}{\partial t} + \{f,H\} = -\sum_{n=1}^{M}\bar{n}_n\Gamma_n\sum_{j=1}^{N}\frac{\partial}{\partial p_j}\sum_{l=1}^{N}\sin(k_n x_j)\sin(k_n x_l)\left[p_l + \frac{m}{\beta_n}\frac{\partial}{\partial p_l} + \frac{\bar{\eta}_n}{\beta_n}\frac{\partial}{\partial x_l}\right]f, \tag{2.1.37}$$

with the Hamilton function

$$H = \sum_{j=1}^{N}\frac{p_j^2}{2m} + \sum_{n=1}^{M}\hbar\Delta_n\bar{n}_n N\Theta_n(\mathbf{x})^2, \tag{2.1.38}$$

where we used the maximum intracavity photon number per particle in the $n$th mode

$$\bar{n}_n = \frac{NS_n^2}{\Delta_n^2 + \kappa_n^2}. \tag{2.1.39}$$

The dissipative dynamics is governed by the quantities

$$\Gamma_n = \frac{8\omega_{R,n}\kappa_n\Delta_n}{\Delta_n^2 + \kappa_n^2}, \tag{2.1.40}$$

$$\beta_n = \frac{-4\Delta_n}{\hbar(\Delta_n^2 + \kappa_n^2)}, \tag{2.1.41}$$

$$\bar{\eta}_n = \frac{\kappa_n^2 - \Delta_n^2}{\kappa_n(\Delta_n^2 + \kappa_n^2)}, \tag{2.1.42}$$

and $\omega_{R,n} = \hbar k_n^2/(2m)$. Equation (2.1.37) is the multimode version of Eq. (2.1.21) and includes as in the single-mode case beside the coherent dynamics governed by $H$ also incoherent processes governed by the right-hand side of Eq. (2.1.37). The coherent dynamics shows now $M$ magnetizations $\Theta_m$. These are, however, not independent quantities since they all depend on the particles' positions $\mathbf{x}$. [5]

[5]This can also be seen as a effective coupling between the cavity degrees of freedom that is mediated by the motional degrees of the particles.

### 2.1.4 Overview and state of the art

We will now present a short overview and a state of the art in self-organization. For a detailed review we refer to Ref. [13].

Self-organization was first theoretically predicted in Ref. [9] where a semiclassical theory for field and atomic motion is used. One year later self-organization was experimentally observed for a thermal ensemble [10, 76]. A theoretical derivation of the threshold in the semiclassical regime has been derived for the first time in Ref. [77] and experimentally confirmed in Ref. [78].

Already in the first description of self-organization the possible extension to a quantum theory was discussed Ref. [9] and the strong coupling of a Bose-Einstein condensate to a resonator has been realized in Ref. [58, 79]. Using a Gross-Pitaevskii-type equation self-organization for a Bose-Einstein condensate was theoretical predicted in Ref. [11]. This phase-transition was mapped to the Dicke quantum phase transition [80] and experimentally observed in Ref. [12]. Superradiance of fermions in a cavity has also been discussed in literature [81].

Many related theoretical as well as experimental extensions of these setups and theoretical models are recently studied. Several studies are focused on cavity setups for the quantum simulation of many-body phases [82, 83]. By loading a BEC in a 2D optical lattice inside a cavity different phases of matter have been realized. The physical model can be mapped to a Bose-Hubbard model with competing long- and short-range interactions [84]. In this case the gas can be in an Mott-insulating phase, a superfluid phase but also in the two self-organized phases of a charge density wave and a supersolid [85–91]. Further generalizations predict phases like Bose-glasses and Superglasses [84, 92].

The coupling of the atomic to several modes is used to achieve different interactions between the atoms. This can be done by using a crossed cavity setup [26, 93, 94] whereby supersolid formation is discussed in the literature [93–95]. Other experiments use different transversal modes to engineer almost arbitrary interactions [96] that might be useful to build a quantum simulator for spin models [97, 98].

Different studies, including a part of this thesis, are working on the description of metastable states in a long-range interacting system [22, 25, 27, 28, 99–102]. These systems can usually not be described by equilibrium statistical mechanics [23].

The coupling of a cloud of atoms or particles to one or several modes of the cavity is also used to create effective spin-spin interactions. This can be realized by including effective interactions between the particles' internal degrees of freedom. Here spin textures have been observed [103] and spinor self-ordering has been theoretically predicted and observed [104, 105]. In similar setups also topological phases have been predicted [106, 107].

Section 2.2

# Steady-state properties in self-organization

In this section we investigate the steady state of self-organized systems. In every subsection we provide the reference to the article and the contribution list of the authors.

## 2.2.1 Thermodynamics and dynamics of atomic self-organization in an optical cavity

Physical Review A **92**, 063808 (2015)

DOI: 10.1103/PhysRevA.92.063808

Authors: Stefan Schütz, Simon B. Jäger, and Giovanna Morigi

*Theoretische Physik, Universität des Saarlandes, D-66123 Saarbrücken, Germany*



**Author Contributions:**
S. Schütz and G. Morigi developed the theoretical model. Analytical calculations were performed by S. Schütz and S. B. Jäger. Numerical simulations were performed by S. Schütz. The calculations and results were checked and discussed by all authors. The article was written by all authors.

**Abstract:**
Pattern formation of atoms in high-finesse optical resonators results from the mechanical forces of light associated with superradiant scattering into the cavity mode. It occurs when the laser intensity exceeds a threshold value such that the pumping processes counteract the losses. We consider atoms driven by a laser and coupling with a mode of a standing-wave cavity and describe their dynamics with a Fokker-Planck equation, in which the atomic motion is semiclassical but the cavity field is a full quantum variable. The asymptotic state of the atoms is a thermal state, whose temperature is solely controlled by the detuning between the laser and the cavity frequency and by the cavity loss rate. From this result we derive the free energy and show that in the thermodynamic limit self-organization is a second-order phase transition. The order parameter is the field inside the resonator to which one can associate a magnetization in analogy to ferromagnetism, the control field is the laser intensity, but the steady state is intrinsically out of equilibrium. In the symmetry-broken phase, quantum noise induces jumps of the spatial density between two ordered patterns: We characterize the statistical properties of this temporal behavior at steady state and show that the thermodynamic properties of the system can be extracted by detecting the light at the cavity output. The results of our analysis are in full agreement with previous studies; we extend them by deriving a self-consistent theory which is valid also when the cavity field is in the shot-noise limit and elucidate the nature of the self-organization transition.

PHYSICAL REVIEW A **92**, 063808 (2015)

# Thermodynamics and dynamics of atomic self-organization in an optical cavity

Stefan Schütz, Simon B. Jäger, and Giovanna Morigi
*Theoretische Physik, Universität des Saarlandes, D-66123 Saarbrücken, Germany*
(Received 27 August 2015; published 7 December 2015)

Pattern formation of atoms in high-finesse optical resonators results from the mechanical forces of light associated with superradiant scattering into the cavity mode. It occurs when the laser intensity exceeds a threshold value such that the pumping processes counteract the losses. We consider atoms driven by a laser and coupling with a mode of a standing-wave cavity and describe their dynamics with a Fokker-Planck equation, in which the atomic motion is semiclassical but the cavity field is a full quantum variable. The asymptotic state of the atoms is a thermal state, whose temperature is solely controlled by the detuning between the laser and the cavity frequency and by the cavity loss rate. From this result we derive the free energy and show that in the thermodynamic limit self-organization is a second-order phase transition. The order parameter is the field inside the resonator to which one can associate a magnetization in analogy to ferromagnetism, the control field is the laser intensity, but the steady state is intrinsically out of equilibrium. In the symmetry-broken phase, quantum noise induces jumps of the spatial density between two ordered patterns: We characterize the statistical properties of this temporal behavior at steady state and show that the thermodynamic properties of the system can be extracted by detecting the light at the cavity output. The results of our analysis are in full agreement with previous studies; we extend them by deriving a self-consistent theory which is valid also when the cavity field is in the shot-noise limit and elucidate the nature of the self-organization transition.

DOI: 10.1103/PhysRevA.92.063808 PACS number(s): 37.30.+i, 42.65.Sf, 05.65.+b, 05.70.Ln

## I. INTRODUCTION

There is ample experimental evidence that electromagnetic fields can cool matter to ultralow temperatures [1–3]. This is achieved by tailoring scattering processes, so that the frequency of the emitted photon is, on average, larger than that of the absorbed one, the energy balance being warranted by the mechanical energy which is exchanged between matter and light [4,5]. When atoms or molecules interact with high-finesse optical resonators, these processes can be tailored using the strong coupling with the cavity field [6–13].

A peculiar aspect of light-matter interaction inside optical cavities consists of the long-range interactions between the atoms, which are mediated by multiple scattering of photons [14,15]. The onset of this behavior is observed when the system is driven by external pumps, whose strength overcomes the loss rate. Some prominent examples are optomechanical bistability [16,17], synchronization [18], and spontaneous spatial ordering [12,19–23]. Among several setups, spontaneous pattern formation in standing-wave and single-mode cavities has been the object of several theoretical and experimental studies [12]. This phenomenon occurs when the atoms are confined within the resonator and are transversally driven by a laser and consists of the formation of atomic gratings that maximize coherent scattering of laser photons into the cavity mode, as sketched in Figs. 1(a) and 1(b). These "Bragg gratings" are stably trapped by the mechanical effects of the light they scatter, provided that the laser compensates the cavity losses so that the number of intracavity photons is sufficiently large. It takes place when the laser intensity, pumping the atoms, exceeds a threshold value depending on, among other things, the rate of photon losses and the number of atoms [12,21]. This behavior was first predicted in Ref. [21] and experimentally demonstrated in several settings, which differ majorly from the initial temperature of the atomic ensemble: In Refs. [22,24] the atoms were cooled by the mechanical effects of the photons scattered into the resonator, while in Refs. [23,25] the atoms initially formed a Bose-Einstein condensate, and the mechanical effects of light were giving rise to conservative forces. As a consequence, matter-wave coherence was preserved during the experiment. In this regime, the transition to self-organization can be cast in terms of the Dicke phase transition [26].

In this work we theoretically analyze the dynamics leading to the formation of spatial structures and their properties at the asymptotics. Our analysis is based on a semiclassical treatment and specifically on a Fokker-Planck equation (FPE) derived when the atoms are classically polarizable particles and their center-of-mass motion is along one dimension [27]. The cavity field, instead, is a full quantum variable, which makes our treatment valid also in the shot-noise limit [27] and describes parameter regimes that are complementary to those of the model in Ref. [28], where the field is a semiclassical variable. Our formalism permits us, in particular, to consistently eliminate the cavity variables from the equations of motion of the atoms, and to analyze the properties of the cavity field across the self-organization threshold, where the intracavity field is characterized by large fluctuations.

This work extends and complements the study presented in Ref. [29]. In particular, we perform a detailed analysis of the stationary state and obtain an analytic expression, which allows us to determine the phase diagram of the transition as a function of the relevant parameters. Drawing from this result, in addition, we show that the onset of self-organization in spatially ordered patterns is a second-order phase transition, associated with a symmetry breaking in the phase of the intracavity field. This allows us to verify conjectures on the nature of the self-organization transition, previously discussed in Refs. [30–32]. We further analyze in detail the effects of the nature of the long-range interactions mediated by the photons and report on several features which are analogously found in the Hamiltonian Mean Field (HMF) model, the workhorse

 

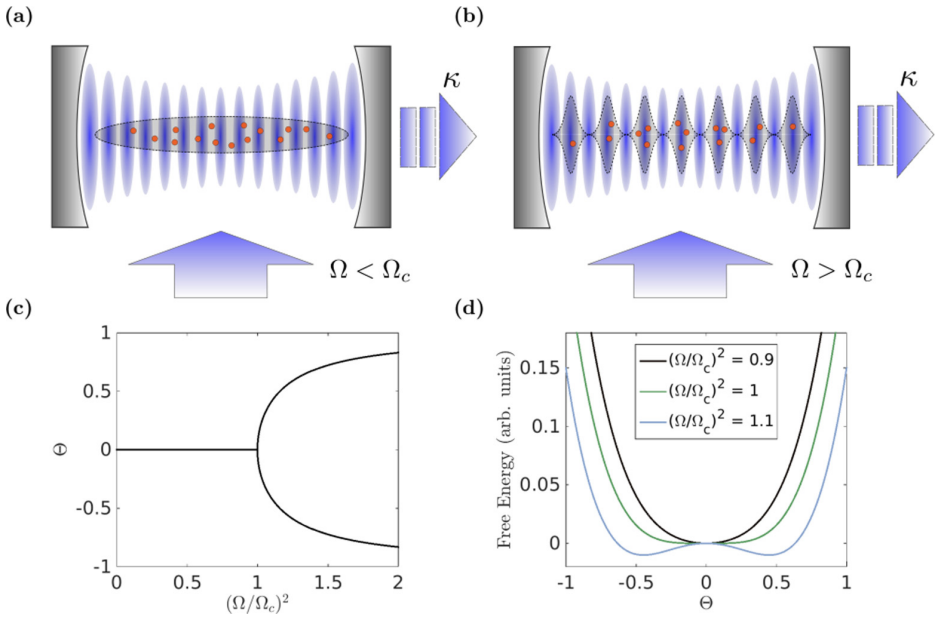


FIG. 1. (Color online) (a) Atoms in a standing-wave cavity and driven by a transverse laser can spontaneously form ordered patterns (b) when the laser intensity $\Omega$ exceeds a threshold value $\Omega_c$, which depends on the rate of photon losses, here due to cavity decay at rate $\kappa$. In this regime the atoms experience a long-range interaction mediated by the cavity photons and their motion becomes strongly correlated. (c) Spatial ordering of atoms is described by the parameter $\Theta$, which characterizes the localization of the atoms within the standing-wave mode of the cavity and is proportional to the cavity field. This parameter undergoes a bifurcation at $\Omega = \Omega_c$, corresponding to two different stable patterns. The values it takes are the minima of an effective Landau potential, displayed in (d) for some values of $\Omega$, demonstrating that self-organization is a second-order phase transition. See text for details.

of the statistical physics with long-range interactions [33]. This article is the first of a series of works devoted to the semiclassical theory of self-organization.

In the present work we analyze the thermodynamics of self-organization and the dynamics at the asymptotics, while in following articles we investigate the dynamics following sudden quenches across the phase transition [34] and compare our analysis with a mean-field model that discards some relevant effects of the long-range correlations [35]. This paper is organized as follows. In Sec. II the FPE at the basis of our analysis is reported and discussed. In Sec. III the stationary properties of the distribution function are characterized both analytically and numerically. In Sec. IV the correlation functions of the light at the cavity output are determined. The conclusions are drawn in Sec. V, while the Appendixes report details of analytical calculations and of the numerical program that is used to simulate the FPE.

## II. MODEL

The dynamics of $N$ atoms or molecules of mass $m$ inside a single-mode standing-wave cavity is analyzed when the particles are transversally illuminated by a laser field, as illustrated in Fig. 1(a). Laser and cavity couple to a dipole transition of the scatterers and are assumed to be sufficiently far-off resonance so that the coupling with the internal degrees of freedom is described by the particles polarizability. From now on we assume that the particles are atoms, but the treatment in this paper can be extended to any ensemble of linearly polarizable particle that can be confined within the optical resonator [36].

In this regime the atoms scatter all coherently and the cavity field $E_c$ is the sum of the fields that each atom scatters. We assume that the atoms' center-of-mass motion is confined along the cavity axis, which coincides with the $x$ axis (we disregard their motion in the transverse plane), and that the atoms are uniformly illuminated by the laser field. Denoting the atomic position by $x_j$ and the cavity-mode function by $\cos(kx)$, with $k$ the wave number, then $E_c \propto N\Theta$, where

$$\Theta = \frac{1}{N}\sum_j \cos(kx_j) \tag{1}$$

measures the ordering of the atoms within the cavity standing wave. For $N \gg 1$, when the atoms are uniformly distributed, $\Theta \sim 0$ and the field within the cavity vanishes. The intracavity intensity is maximal when the positions are such that $\cos(kx_j) = 1$ (even pattern) or $\cos(kx_j) = -1$ (odd pattern), namely, when the atoms form Bragg gratings; see Fig. 1(b). These gratings are the two possible stable configurations the atoms can form when the laser pump is above threshold, as shown in Fig. 1(c).

The formation and stability of the Bragg gratings is determined by the mechanical effects of photon scattering on the atoms. In this section we report the basic equations describing the dynamics of the coupled systems, as well as the assumptions that lead to a FPE governing the semiclassical trajectories of $N$ atoms inside the single-mode resonator [27]. The FPE is derived under the assumption that the atomic

motion is at all times in the semiclassical regime, while the cavity field adjusts quasi-instantaneously to the atomic density distribution. In this limit, using a perturbative treatment, the cavity field can be eliminated by the equations of motion of the atoms' external degrees of freedom [37]. Readers interested in the detailed derivation of the FPE from the full quantum master equation of atoms and cavity are referred to Refs. [27,37]. An alternative FPE, where fluctuations of the intracavity field are treated semiclassically but no time-scale separation between atoms and cavity dynamics is assumed, is derived in Ref. [28].

### A. The cavity field

In our treatment the cavity field is a quantum variable. We report its equation of motion in the limit in which the atoms constitute a nonsaturated medium and their internal atomic transitions are described by the polarizability. Our starting point is the Heisenberg-Langevin equation for operator $\hat{a}(t)$, which annihilates a cavity photon at frequency $\omega_c$ and wave number $k$. The equation is reported in the reference frame rotating at the laser frequency $\omega_L$ and reads [38]

$$\frac{\partial}{\partial t}\hat{a}(t) = -\{\kappa - i[\Delta_c - NU\hat{\mathcal{B}}(t)]\}\hat{a}(t) - iNS\hat{\Theta}(t) + \hat{\xi}(t), \tag{2}$$

where $\Delta_c = \omega_L - \omega_c$ is the detuning of the laser from the cavity frequency, $\hat{\xi}(t)$ is the Langevin force with $\langle\hat{\xi}(t')\hat{\xi}^{\dagger}(t)\rangle = 2\kappa\delta(t-t')$, and $\kappa$ is the cavity decay rate. The cavity field is a function of the two operators $\hat{\mathcal{B}}(t)$ and $\hat{\Theta}(t)$, which, in turn, are functions of the atomic positions $\hat{x}_j$ at time $t$. In detail, $U$ is a frequency, $U = g^2/\Delta_a$, where $g$ is the vacuum Rabi frequency at the antinodes of the cavity mode, $\Delta_a = \omega_L - \omega_a$ is the detuning of the laser frequency from the atomic transition resonance $\omega_a$, and operator $\hat{\mathcal{B}}$ is defined as

$$\hat{\mathcal{B}} = \frac{1}{N}\sum_j \cos^2(k\hat{x}_j) \tag{3}$$

and takes on values between 0 and 1. Its expectation value $B = \langle\hat{\mathcal{B}}\rangle$ is the so-called bunching parameter [12]. Operator $\hat{\Theta}(t)$ is the quantum variable corresponding to the order parameter in Eq. (1). In Eq. (2) it is scaled by the frequency $S = \Omega g/\Delta_a$, which is proportional to the laser Rabi frequency $\Omega$ and corresponds to the scattering amplitude of a laser photon into the cavity mode by an atom at an antinode, with $S/U = \Omega/g$. Equation (2) shows that the pump on the cavity is maximum when $\langle\hat{\Theta}\rangle = \pm 1$, corresponding to the situation in which the atoms form Bragg gratings. Self-organization occurs when these gratings are mechanically stable, namely, when the mechanical effects of the scattered light stabilize the atoms in ordered structures, which, in turn, generate the field. In order to determine these dynamics one would need to solve the coupled equations of cavity and atomic motion.

We can further simplify the problem by considering the regime in which the time scale over which the atomic motion evolves is much larger than the time scale determining the evolution of the cavity field. This is typically fulfilled when $k\bar{p}/m \ll |\kappa + i\Delta_c|$, where $\bar{p} = \sqrt{\langle\hat{p}^2\rangle}$ is the variance of the atomic momentum (the mean value vanishes), under the condition that the coupling between cavity and atomic motion is sufficiently weak. This latter condition requires that [39]

$$\sqrt{\omega_r}\sqrt{N}|S| \ll |\Delta_c + i\kappa|^{3/2}, \tag{4}$$

where $\omega_r = \hbar k^2/(2m)$ is the recoil frequency, scaling the exchange of mechanical energy between photons and atoms. At zero order in this expansion the cavity field operator depends on the instantaneous density and reads

$$\hat{a}_{\rm ad}(t) = \frac{NS\hat{\Theta}(t)}{\hat{\Delta}_c'(t) + i\kappa}, \tag{5}$$

where the subscript indicates the adiabatic limit and we omitted to report the noise term. Operator $\hat{\Delta}_c'$ is defined as

$$\hat{\Delta}_c' = \Delta_c - UN\hat{\mathcal{B}}. \tag{6}$$

Its mean value vanishes for certain density distributions, giving rise to resonances. For $|NU| > \kappa$ small changes of $\Delta_c$ about the resonance can induce large variations of the field, resulting in the appearance of optomechanical bistable behavior [16,17,40]. In this paper we focus on the regime in which $|NU| \ll \kappa$, and treat this as a small parameter on the same footing as the retardation term. In this limit, the field, including the diabatic corrections, reads

$$\hat{a}(t) = \frac{NS\hat{\Theta}(t)}{\Delta_c + i\kappa}\left[1 + \frac{NU}{\Delta_c + i\kappa}\hat{\mathcal{B}}(t)\right] + \hat{a}_{\rm ret}(t), \tag{7}$$

where

$$\hat{a}_{\rm ret}(t) = \frac{iNS}{(i\Delta_c - \kappa)^2}\dot{\hat{\Theta}} \tag{8}$$

accounts for retardation effects and depends on the time derivative of operator $\hat{\Theta}$, Eq. (1). The derivative, in particular, takes the form

$$\dot{\hat{\Theta}} = -\frac{1}{2N}\sum_j \left\{\sin[k\hat{x}_j(t)]\frac{k\hat{p}_j(t)}{m} + \frac{k\hat{p}_j(t)}{m}\sin[k\hat{x}_j(t)]\right\}$$

and shows that the diabatic correction scales with $(k\bar{p}/m)/|\kappa + i\Delta_c|$. When this parameter is small, then one can perform a coarse graining for the atomic motion, over which the cavity field fast relaxes.

It is also useful to discuss the mean number of photons inside the resonator. In the adiabatic limit it is given by

$$\langle\hat{n}\rangle_{t,\rm ad} = N\bar{n}\langle\hat{\Theta}^2\rangle_t, \tag{9}$$

which is valid in zero order in the delay time. For later convenience, we introduced the dimensionless quantity

$$\bar{n} = \frac{NS^2}{\Delta_c^2 + \kappa^2}, \tag{10}$$

such that $N\bar{n}$ gives the maximum intracavity photon number, corresponding to the value $\langle\Theta^2\rangle_t = 1$, namely, when the atoms form a perfectly ordered Bragg grating. The average photon number can be different from zero also when the field inside the resonator has vanishing mean expectation value, since in this case it is proportional to the fluctuations of the order parameter.

### B. Fokker-Planck equation for $N$ atoms

An equation for the motion of the $N$ atoms within the resonator is derived under the assumption that at all times the atomic momentum distribution has width $\Delta p = \bar{p}$, which is much larger than the quantum of linear momentum $\hbar k$ that the atom exchanges with the individual photons (but sufficiently small so that the atoms are within the velocity capture range [11]). This assumption is valid for cavities whose decay rate $\kappa$ exceeds the recoil frequency $\omega_r$: $\omega_r \ll \kappa$. In fact, we show that $\kappa$ determines the minimum stationary width of the momentum distribution. This regime is encountered in several existing experiments [17,22,24]. We note that, with this assumption, the requirement of time-scale separation between cavity and motion is fulfilled, since the inequality $k\bar{p}/m \ll \kappa$ is consistent with $\omega_r \ll \kappa$ after using $\bar{p}^2/2m = \hbar\kappa/2$.

Reference [27] reports the detailed steps that lead to the derivation of a FPE for the distribution $f(\boldsymbol{x},\boldsymbol{p},t)$ of the $N$ atoms positions and momenta $\boldsymbol{x} = (x_1, x_2, \ldots, x_N)$ and $\boldsymbol{p} = (p_1, p_2, \ldots, p_N)$. The FPE can be cast in the form

$$\frac{\partial f}{\partial t} = -\sum_i \frac{p_i}{m}\frac{\partial}{\partial x_i} f + S^2 L f, \tag{11}$$

where $f \equiv f(\boldsymbol{x},\boldsymbol{p},t)$. The right-hand side (RHS) separates the ballistic motion from the term proportional to the scattering rate $S$ and describes the dynamics due to the mechanical effects of light. This latter term specifically reads

$$\begin{aligned} L f = &-\sum_i \frac{\partial}{\partial p_i} F_0(\boldsymbol{x}) \sin(kx_i) f \\ &- \sum_{i,j} \frac{\partial}{\partial p_i} \Gamma_0(\boldsymbol{x}) \sin(kx_i)\sin(kx_j) p_j f \\ &+ \sum_{i,j} \frac{\partial^2}{\partial p_i \partial x_j} \eta_0(\boldsymbol{x}) \sin(kx_i)\sin(kx_j) f \\ &+ \sum_{i,j} \frac{\partial^2}{\partial p_i \partial p_j} D_0(\boldsymbol{x}) \sin(kx_i)\sin(kx_j) f \\ &+ \frac{\gamma'}{2}\sum_i \frac{\partial^2}{\partial p_i^2} \mathcal{D}^{\mathrm{sp}}(x_i) f. \end{aligned} \tag{12}$$

Here the first term on the RHS describes the dispersive force associated with scattering of laser photons into the resonator, where

$$F_0(\boldsymbol{x}) = (\hbar k)\frac{2\Delta_c'}{\Delta_c'^2 + \kappa^2}(1+\delta_F) N \Theta. \tag{13}$$

Its amplitude is proportional to the order parameter $\Theta$ [Eq. (1)], which is the Wigner representation of operator $\hat{\Theta}$ [27]. Its sign is also determined by the frequency shift of the cavity frequency $\Delta_c'(\boldsymbol{x})$ from the laser, which takes the same form as in Eq. (6), now with the corresponding Wigner form for operator $\hat{\mathcal{B}}$. Coefficient $\delta_F$ is a small correction for the parameter regime we consider; its general form is given in Appendix A. The same applies for the coefficients $\delta_j$ ($j = \Gamma, \eta, D$) appearing in the other terms we specify below.

The second term on the RHS of Eq. (12) describes the damping force due to retardation between the scattered field and the atomic motion. It depends on the atomic momentum and is scaled by the function

$$\Gamma_0(\boldsymbol{x}) = \omega_r \frac{8\Delta_c'\kappa}{\left(\Delta_c'^2 + \kappa^2\right)^2}(1+\delta_\Gamma). \tag{14}$$

The third summand is due to the anharmonicity of the cavity optical lattice. The function scaling this term has the form

$$\eta_0(\boldsymbol{x}) = 2\hbar\omega_r \frac{\left(-\Delta_c'^2 + \kappa^2\right)}{\left(\Delta_c'^2 + \kappa^2\right)^2}(1+\delta_\eta) \tag{15}$$

and vanishes when $\Delta_c' = \pm\kappa$.

The last two terms describe diffusion. In particular, the one scaled by the function

$$D_0(\boldsymbol{x}) = (\hbar k)^2 \frac{\kappa}{\Delta_c'^2 + \kappa^2}(1+\delta_D) \tag{16}$$

corresponds to the diffusion associated with global fluctuations of the cavity field and is characterized by long-range correlations, while the term with coefficient $\mathcal{D}^{\mathrm{sp}}(x_i)$ is instead due to spontaneous emission of a photon outside the resonator with $\gamma' = \gamma g^2/\Delta_a^2$, where $\gamma$ is the decay rate of the excited state. It is the sole term which acts locally, and the dynamics it implies does not establish correlations between the atoms. Its explicit form is reported in Appendix A.

### C. Dynamics away from the bistable regime

Equation (11) describes the coherent and dissipative dynamics associated with the mechanical effects of light on the atomic motion. In this work we assume that $\gamma'$ is much smaller than the other rates and discard the effect of spontaneous decay in the dynamics, so that losses are due to cavity decay. As far as it concerns the terms due to the cavity, we note their nonlinear dependence on the bunching parameter, which appears in the denominator of all coefficients and gives rise to bistable behavior. Here we focus on the regime in which $|NU| \ll \kappa$. In this regime the dispersive forces due to the mechanical effects of light in leading order are due to scattering of laser photons into the cavity. In this limit, we choose detunings $|\Delta_c| \sim \kappa$ so that the motion is efficiently cooled, as we show below. Correspondingly, the coefficients of the functional in Eq. (12) are modified so that $\Delta_c' \simeq \Delta_c$ and the functions $\delta_F, \delta_\eta, \delta_\Gamma, \delta_D \approx 0$. More precisely, we perform an expansion in first order in $N|U|/\kappa$. In this limit, the FPE, Eq. (11), can be cast in the form

$$\begin{aligned} &\partial_t f + \{f, H\} + \bar{n}\frac{NU}{\Delta_c} L_1 f \\ &\quad = -\bar{n}\Gamma \sum_i \sin(kx_i)\partial_{p_i}\frac{1}{N} \\ &\qquad \times \sum_j \sin(kx_j)\left(p_j + \frac{m}{\beta}\partial_{p_j} + \frac{\bar{\eta}}{\beta}\partial_{x_j}\right) f, \end{aligned} \tag{17}$$

where all terms due to the coupling with the light scale with $\bar{n}$, given in Eq. (10). In detail, the left-hand side (LHS) collects the Hamiltonian terms, expressed in terms of Poisson brackets

with Hamiltonian

$$H = \sum_j \frac{p_j^2}{2m} + \hbar \Delta_c \bar{n} N \Theta^2, \tag{18}$$

as well as the terms scaling with $U$, summarized in the functional $L_1$, whose detailed form is given in Appendix A. The RHS reports terms of different origin, which can be classified as damping, diffusion, and a third term which scales cross derivatives in position and momentum. In the order of this list, they are scaled by the coefficients

$$\Gamma = 8\omega_r \kappa \Delta_c / \left(\Delta_c^2 + \kappa^2\right), \tag{19}$$

$$\beta = -4\Delta_c / \hbar / \left(\Delta_c^2 + \kappa^2\right), \tag{20}$$

$$\bar{\eta} = \frac{\kappa^2 - \Delta_c^2}{\kappa\left(\Delta_c^2 + \kappa^2\right)}. \tag{21}$$

We remark that the term in the FPE scaled by parameter $\bar{\eta}$ was already found in the derivation of Ref. [37]. While its effect is to date not well understood, we checked that for the parameters we consider it gives rise to small corrections in the quantities we evaluate. In the mean-field treatment it can be cast in terms of a correction of the effective mean-field potential the atoms experience. In that limit it induces a shift to the critical value of the pump strength at the self-organization transition [35].

### D. Long-range correlations

Let us now make some preliminary remarks on the FPE discussed this far. We first focus on the Hamiltonian term, Eq. (18). In addition to the kinetic energy this contains the cavity-mediated potential, which has been obtained in zero order in the retardation time. Its sign is determined by the sign of the detuning $\Delta_c$: When $\Delta_c < 0$, the formation of Bragg gratings, which maximizes the value of $|\Theta|$, is energetically favored. Thus, Eq. (18) summarizes in a compact way a property which was observed in several previous works [21,22,29,30].

We note that the Hamiltonian in Eq. (18) exhibits several analogies with the HMF model [33], whose Hamiltonian reads

$$H_{\mathrm{MF}} = \sum_j \frac{p_j^2}{2m} + \frac{J}{2N} \sum_{i \neq j} [1 - \cos(\theta_i - \theta_j)], \tag{22}$$

where $\theta_i$ are angle variables that in our case would correspond to $\theta_i = k x_i$. The analogy becomes explicit in Eq. (18) by using

$$\Theta^2 = \sum_{i,j} \{\cos[k(x_i + x_j)] + \cos[k(x_i - x_j)]\}/(2N^2).$$

Like Hamiltonian $H_{\mathrm{MF}}$, also Hamiltonian $H$ is extensive as it satisfies the Kac prescription [33] for the thermodynamic limit we choose, which keeps $\bar{n}$ fixed for $N \to \infty$ (see the next section). In a canonical ensemble, for $J > 0$ the HMF exhibits a second-order phase transition from a paramagnetic to a ferromagnetic phase controlled by the temperature, where the order parameter is the magnetization $M = (M_x, M_y)$, with $M_x = \sum_j \cos\theta_j / N$ and $M_y = \sum_j \sin\theta_j / N$. This suggests that $\Theta$ identifies with the $x$ component of a two-dimensional magnetization and creates an expectation of a transition to order for negative values of the detunings, $\Delta_c < 0$, for which a nonvanishing interaction potential term tends to minimize the energy (we mention that the dynamics for $\Delta_c > 0$ has been recently studied in Ref. [41]).

Differing from the HMF model, the term $\cos[k(x_i + x_j)]$ in $\Theta^2$ originates from the underlying cavity standing-wave potential that breaks continuous translational invariance. Moreover, the cavity coupling at higher order in $|NU/\Delta_c|$ gives rise to deviations from the Hamiltonian dynamics due to further terms in the LHS of Eq. (17), which for larger values are responsible for bistable behavior [40] and only in certain limits can be cast in the form of conservative forces.

We further highlight that long-range correlations can also be established by the terms on the RHS of the FPE in Eq. (17), which are usually associated with incoherent processes. In fact, retardation effects in the scattering of one atom modify the intracavity potential which traps the whole atomic ensemble. Photon losses, in addition, give rise to sudden quenches of the global potential [11,42]. When the density is uniform, the terms in the RHS can be reduced to a form [27] which is analogous to the Brownian Mean Field model [43]. However, this mapping applies only when the system is deep in the paramagnetic phase. When the atoms form a Bragg grating, instead, damping and diffusion become smaller, the atoms being localized at the points where $\sin(k x_j) \sim 0$. Moreover, when several atoms are trapped in a Bragg grating, also damping and diffusion of atoms which are away from the nodes become smaller. These properties share some analogies with models constructed to simulate correlated damping [44] and suggest that incoherent dynamics can endorse coherent effects for transient but long times [29,34].

## III. PROPERTIES AT EQUILIBRIUM

We now discuss the existence and the form of the stationary state, namely, of the solution of Eq. (17) satisfying

$$\partial_t f_{\mathrm{S}} = 0.$$

It is simple to verify that the function of the form

$$f_{\mathrm{S}} = f_0 \exp(-\beta H) \tag{23}$$

is a stationary solution in zero order in the parameter $UN/\kappa$ and $\bar{\eta}$, where $f_0$ warrants normalization. Equation (23) describes a thermal state whose temperature $T$ is solely controlled by the detuning $\Delta_c$:

$$k_B T = 1/\beta = \frac{\hbar\left(\Delta_c^2 + \kappa^2\right)}{-4\Delta_c}. \tag{24}$$

We mention that this result has been reported in Ref. [29] and was also found in Refs. [30,31,45] using different theoretical approaches.

In this section, starting from Eq. (23) we analyze the properties of the system at steady state. We show that Eq. (23) makes it possible to identify the transition to self-organization and the corresponding critical value at which it occurs. By deriving the single-particle free energy in an appropriate thermodynamic limit, we demonstrate that the transition to self-organization is a second-order phase transition, whose order parameter is $\Theta$. We point out that the treatment here presented applies concepts of equilibrium thermodynamics

and is strictly valid at the steady state, because it is a thermal distribution.

This section contains analytical results, extracted from Eq. (23), and data of numerical simulations, obtained by integrating the stochastic differential equations (SDEs) which simulate the dynamics of Eq. (17). These equations have been reported in Ref. [27] and for completeness are also detailed in Appendix B . A single trajectory for $N$ atoms corresponds to integrating the set of coupled equations (B1) and (B2) for the variables $\{x_\ell(t); p_\ell(t)\}$ with $\ell = 1, \ldots, N$ and for a given initial condition. From this calculation, for instance, we find

$$\Theta(t) = \sum_{\ell=1}^{N} \cos[k x_\ell(t)]/N.$$

The mean values are numerically computed by taking the average over $n$ such trajectories, which statistically satisfy the initial conditions, and deliver quantities such as $\langle \Theta^2 \rangle_t = \sum_{i=1}^{n} \Theta_i(t)^2/n$, where $i$ now labels the trajectory, $i = 1, \ldots, n$.

In the simulations we assume an ensemble of $^{85}$Rb atoms with transition wavelength $\lambda = 780$ nm ($D_2$ line). This gives the recoil frequency $\omega_r = 2\pi \times 3.86$ kHz. The transition linewidth is $\gamma = 2\pi \times 6$ MHz and the linewidth of the resonator is $\kappa = 2\pi \times 1.5$ MHz. These parameters correspond to the ones of the experiment of Ref. [23]; they warrant the validity of our semiclassical treatment based on a time-scale separation.

### A. Self-organization as second-order phase transition

In order to characterize the thermodynamic properties of the self-organization transition, we first determine the free energy per particle. Our starting point is the definition of the free energy $F = -k_B T \ln \mathcal{Z}$, where $\mathcal{Z}$ is the partition function,

$$\mathcal{Z} = \frac{1}{\Delta^N} \int_{\boldsymbol{x}} d\boldsymbol{x} \int_{\boldsymbol{p}} d\boldsymbol{p} \exp(-\beta H), \tag{25}$$

and $\Delta$ is the unit phase space volume. For convenience, we have introduced the notation $\int_{\boldsymbol{x}} d\boldsymbol{x} \equiv \int_0^\lambda dx_1 \cdots \int_0^\lambda dx_N$ and $\int_{\boldsymbol{p}} d\boldsymbol{p} \equiv \int_{-\infty}^{\infty} dp_1 \cdots \int_{-\infty}^{\infty} dp_N$. After integrating out the momentum variables, Eq. (25) can be cast in the form

$$\mathcal{Z} = (Z_0 \lambda/\Delta)^N \int_{-1}^{1} d\Theta \Omega(\Theta) \exp(-N\beta\hbar\bar{n}\Delta_c \Theta^2). \tag{26}$$

Here $Z_0 = (2\pi m/\beta)^{1/2}$ is a constant which depends on the temperature. The functional $\Omega(\Theta)$ is the density of states at a given magnetization $\Theta$ and is defined as

$$\Omega(\Theta) = \int_{\boldsymbol{x}} \frac{d\boldsymbol{x}}{\lambda^N} \delta\left[\Theta - \frac{1}{N}\sum_{i=1}^{N} \cos(k x_i)\right]. \tag{27}$$

For identifying the transition to order, we consider $N \gg 1$. This requires an adequate thermodynamic limit. We choose a thermodynamic limit for which the amplitude $\bar{n}$ [Eq. (10)] remains constant as $N$ increases and warrants that Hamiltonian in Eq. (18) is extensive. In detail, it corresponds to scale the vacuum Rabi frequency as $g \sim 1/\sqrt{N}$, which is physically equivalent to scale up the cavity mode volume $V$ linearly with $N$, being the vacuum Rabi frequency $g \propto 1/\sqrt{V}$. It follows that the scattering rates characterizing the dynamics scale as $S \sim 1/\sqrt{N}$ and $U \sim 1/N$ as $N \to \infty$ (moreover, $S^2\eta_0 \sim 1/N$, but this contribution is here neglected). Such scaling has been applied in a series of theoretical works [30,38,40].

With this definition in mind, we determine an explicit form of the free energy as a function of $\Theta$ by using the method of the steepest descent. We identify the fixed point $\Theta^*$, which is given by the equation

$$\Theta^* = \frac{I_1(y\Theta^*)}{I_0(y\Theta^*)}, \tag{28}$$

with $y = 2\bar{n}/\bar{n}_c$ and $\bar{n}_c > 0$, while $I_1$ and $I_0$ are modified Bessel functions of the first kind [46] (the details of the calculations are reported in Appendix C). Depending on $y$, and thus on $\bar{n}$, Eq. (28) allows for either one or three solutions, where the two regimes are separated by the value $\bar{n} = \bar{n}_c$, with

$$\bar{n}_c = \frac{\kappa^2 + \Delta_c^2}{4\Delta_c^2}. \tag{29}$$

Using this result, the free energy per particle in the thermodynamic limit takes the form

$$\mathcal{F}(\Theta) \approx \mathcal{F}_0 + \frac{1}{\beta}\left[\left(1 - \frac{\bar{n}}{\bar{n}_c}\right)\Theta^2 + \frac{1}{4}\Theta^4\right], \tag{30}$$

with $\mathcal{F}_0 = -k_B T \ln(Z_0\lambda/\Delta)$. Equation (30) has the form of the Landau free energy [47], and shows that the transition to self-organization is continuous and of second order. Its form close to threshold for different values of the pump strength, and thus of $\bar{n}$, is sketched in Fig. 1(d), where $(\Omega/\Omega_c)^2 = \bar{n}/\bar{n}_c$. For $\bar{n} < \bar{n}_c$, thus, the order parameter vanishes: The atoms are uniformly distributed in space and one can denote this phase as paramagnetic invoking the analogy between $\Theta$ and a magnetization. For $\bar{n} > \bar{n}_c$, on the contrary, the order parameter takes a value different from zero, as shown in Fig. 1(c). By setting the first derivative of the free energy [Eq. (30)] to zero we also find an analytic expression for the order parameter above but close to the threshold: $\Theta = \pm\sqrt{2(\bar{n}/\bar{n}_c - 1)}$.

We remark that in Ref. [30] it was conjectured that self-organization in a standing-wave cavity is a second-order phase transition. In this section we have demonstrated that this conjecture is correct by performing an explicit mapping of the free energy into the form of a Landau model [47]. Our theoretical model demonstrates that the steady-state distribution is thermal; it further naturally delivers the steady-state temperature and the value of the critical pump strength, here cast in terms of the quantity $\bar{n}_c$. We observe that the critical value $\bar{n}_c$ is in agreement with the value determined in Ref. [30] by means of a mean-field model based on a phenomenological derivation. [This is visible after considering the definition in Eq. (10), which gives the critical pump strength value $\Omega_c$ after using $S_c = g\Omega_c/\Delta_a$ as a function of the critical value $\bar{n}_c$ of Eq. (29).] In Ref. [31] the self-organization threshold was estimated by means of a kinetic theory based on treating the cavity field semiclassically, finding a value consistent with our result.

We remark that the typical concept in second-order phase transition of spatial domains, whose average size increases with a power-law behavior as the critical value is approached,

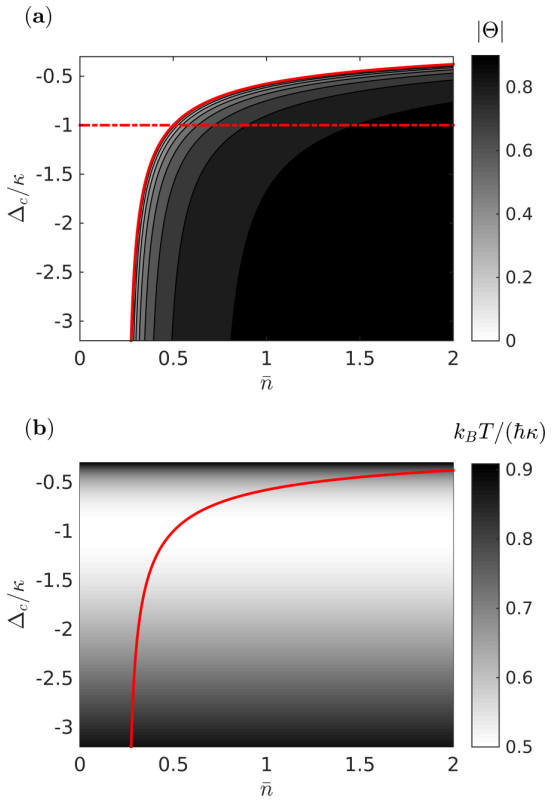


FIG. 2. (Color online) (a) Order parameter $|\Theta|$ and (b) steady-state temperature as a function of $\bar{n}$ and $\Delta_c$ (in units of $\kappa$). The red line denotes the value $\bar{n}_c$ as a function of $\Delta_c$, as reported in Eq. (29).

becomes now invalid: Their energetic cost scales with the system size due to the long-range cavity-mediated potential. This is simply understood as two domains with $\langle\Theta\rangle = +1$ and $\langle\Theta\rangle = -1$ generate fields which interfere destructively, resulting in a vanishing intracavity photon number. This example illustrates the nonadditivity of long-range interacting systems. We now analyze more in detail the behavior of the magnetization.

### B. Phase diagram

The magnetization of our model [Eq. (1)] is intrinsically related to the spatial order of the atoms within the cavity and thus determines the properties of the signal at the cavity output. Its stationary value depends on the various physical quantities, which can be summarized in terms of the single parameter $\bar{n}$ in Eq. (10). The detuning $\Delta_c$, which also enters in the definition of $\bar{n}_c$, determines the temperature of the steady state; see Eq. (24).

Figure 2(a) displays the phase diagram of the magnetization as a function of $\bar{n}$ and $\Delta_c$: The white region is the paramagnetic phase, the dark region the ferromagnetic one, and the scale of gray indicates the value of $|\Theta|$. We note that the lines at constant $\Delta_c$ correspond to constant asymptotic temperatures and to a well-defined threshold value of $\bar{n}_c(\Delta_c)$. Following one such line, the value of $|\Theta|$ is zero for $\bar{n} < \bar{n}_c$, while above $\bar{n}_c$ it grows monotonically until unity as $\bar{n} \to \infty$. The magnetization as a function of $\bar{n}$ and at $\Delta_c = -\kappa$ is shown in Fig. 1(c).

Keeping $\bar{n}$ fixed and varying $\Delta_c$ instead consists of varying the temperature. However, not for all values of $\bar{n}$ there is a temperature at which the transition to ferromagnetism is observed. In fact, if $\bar{n} < \min(\bar{n}_c) = 1/4$, the phase is paramagnetic for all values of $\Delta_c$. For $\bar{n} > 1/4$, instead, there exists a critical value of $\Delta_c(\bar{n})$ at which the transition to self-organization occurs. In this case, above threshold the magnetization monotonically grows with $\Delta_c$. The temperature of the atoms is shown in Fig. 2(b): Here it is clearly visible that the temperature is independent on $\bar{n}$ and is solely a function of $\Delta_c$. In particular, it reaches a minimum at $\Delta_c = -\kappa$, as one can verify using Eq. (24). The corresponding minimal temperature is $k_B T_{\min} = \hbar\kappa/2$.

### C. Dynamics of the magnetization at steady state

The mapping of the free energy to the Landau model allows one to draw an analogy between self-organization and ferromagnetism. Due to the long-range interactions, however, the symmetry-breaking transition does not occur through the spatial formation of magnetized domains of increasing size, rather through the observation of Bragg gratings during long periods of time, whose mean duration increases as the pump strength is increased above threshold. This property was already reported in Refs. [21,30] and is also found in the HMF [33]. The behavior close to threshold is instead to large extent unexplored, as it is characterized by large fluctuations of the cavity field and thus requires a theoretical model that treats the cavity field as a quantum variable, which our model does. Our analysis focuses on the statistical properties of these time intervals and, more generally, of the autocorrelation function of the magnetization across the transition. In this section we discuss this temporal behavior by analyzing trajectories of the magnetization evaluated by means of the SDE as in Appendix B . We set $\Delta_c = -\kappa$ and $N|U|/\kappa = 0.05$.

#### *1. Stationary magnetization for finite N*

In order to perform the numerical analysis, we first benchmark the statistical properties for a finite number of trajectories. Typical trajectories at the steady state are shown in Fig. 3 for different values of $\bar{n}$.

They show $\Theta(t)$, obtained by averaging over the instantaneous positions of 50 atoms within the resonator. Fluctuations about the mean value are visible: Their size increases below threshold as $\bar{n}$ is increased and depends on the number of atoms, as one can see in Fig. 4 (see below). In order to extract the order parameter from the numerical data, we thus need to estimate the size of the fluctuations about the mean value as a function of $N$. For this purpose we determine the probability distribution $P_N(\Theta_0)$ of finding $\Theta = \Theta_0$ at the stationary state, which we define as

$$P_N(\Theta_0) = \mathcal{P}_0 \int_{-1}^{1} d\Theta \delta(\Theta - \Theta_0) \Omega(\Theta) \exp(-\beta\hbar\Delta_c \bar{n} N \Theta^2), \tag{31}$$

where $\Omega(\Theta)$ is given in Eq. (27) and the parameter $\mathcal{P}_0 = (Z_0\lambda/\Delta)^N/\mathcal{Z}$ warrants normalization: $\int_{-1}^{1} d\Theta_0 P_N(\Theta_0) = 1$.

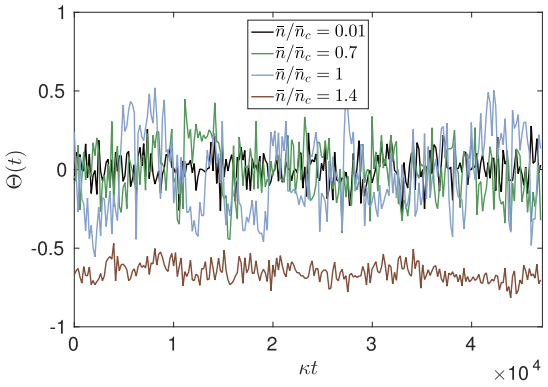


FIG. 3. (Color online) Order parameter as a function of time (in units of $\kappa^{-1}$) at the asymptotics of the dynamics and for different values of $\bar{n}$ (see inset). Each trajectory corresponds to a numerical simulation with $N = 50$ atoms.

For a given detuning $\Delta_c$ this probability distribution depends on $\bar{n}$ and on the atom number $N$. We determine $P_N(\Theta_0)$ using our analytical model and performing the integral by means of the Metropolis algorithm [48].

The results are displayed in Fig. 4 for different atom numbers $N$ and pumping strengths $\bar{n}$. The curves clearly show that the size of the fluctuations about the mean value decrease with $N$. We also observe that, for $N$ fixed, the fluctuations about the mean value increase with $\bar{n}$ as it approaches the threshold value from below. For atom numbers of the order of 50 and larger we verified that $P_N(\Theta_0)$ converges to the form $\exp(-N\,\Theta_0^4/4)$ for $\bar{n} = \bar{n}_c$, in agreement with the result found in the thermodynamic limit. Above threshold, on the contrary, the distribution exhibits two peaks whose centers converge towards the asymptotic values of Eq. (28) for large $N$ and whose widths decrease as $\bar{n}$ is increased. We compare these results with the data obtained after integrating the SDE (circles) and verify the convergence of the numerical results with increasing $N$ to the predictions at the thermodynamic limit.

Figure 5(a) displays $\Theta(t)$ as a function of time obtained by integrating the SDE for $N = 20$ atoms and $\bar{n} = 0.01\,\bar{n}_c$, thus well below threshold. The distribution $P_N(\Theta_0)$ that we extract after averaging over the time and over 100 trajectories of this sort is given by the circles in Fig. 5(b). The curve is in excellent agreement with a Gaussian distribution centered at $\Theta_0 = 0$ (dashed curve) whose explicit derivation is reported in Appendix D and which reads

$$P_N^{\text{theo}}(\Theta_0) = \frac{1}{\sqrt{2\pi\sigma_N^2}} \exp\left(-\frac{\Theta_0^2}{2\sigma_N^2}\right), \tag{32}$$

with

$$\sigma_N = 1/\sqrt{2N}. \tag{33}$$

From this result we identify the width $\sigma_N$ with the statistical uncertainty in determining the value of $\Theta_0$. Figure 5(c) displays a trajectory $\Theta(t)$ for $\bar{n} = 1.4\,\bar{n}_c$, thus above threshold; the corresponding distribution $P_N(\Theta_0)$ is given by the circles in Fig. 5(d). The trajectory exhibits jumps between the two values of the Bragg gratings, the duration of the time intervals during which the atoms are trapped in a Bragg grating determines the size of the fluctuations about the two peaks of the probability distribution, and the finite rate at which these jumps occur is the reason for the nonvanishing value of the probability at $\Theta_0 \sim 0$.

### 2. *Autocorrelation function*

We now analyze the autocorrelation function for the magnetization,

$$C(\tau) = \lim_{t\to\infty} \langle \Theta(t)\Theta(t+\tau)\rangle, \tag{34}$$

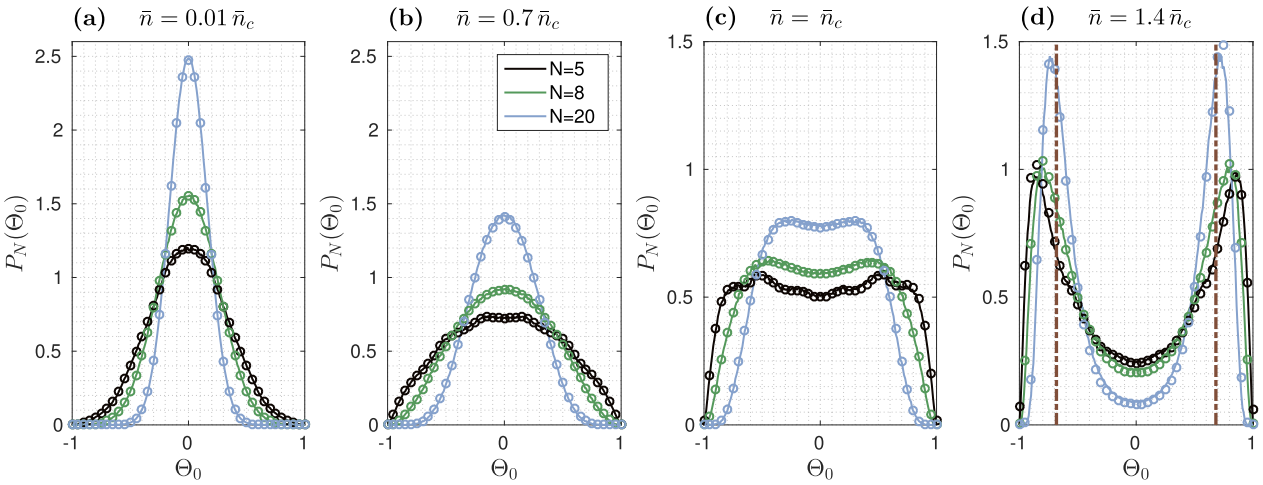


FIG. 4. (Color online) Probability distribution for the order parameter at steady state, $P_N(\Theta_0)$ as in Eq. (31), for $N = 5,8,20$ atoms with $\Delta_c = -\kappa$ and $\bar{n}/\bar{n}_c = 0.01, 0.7, 1, 1.4$ (from left to right). The dots correspond to the probability distribution $P_N(\Theta_0)$ extracted from numerical simulations at steady state, performed by means of the SDE. The dashed vertical lines in (d) indicate the asymptotic value $\Theta_0 = \pm\Theta^*$ [Eq. (28)] for $\bar{n} = 1.4\,\bar{n}_c$.

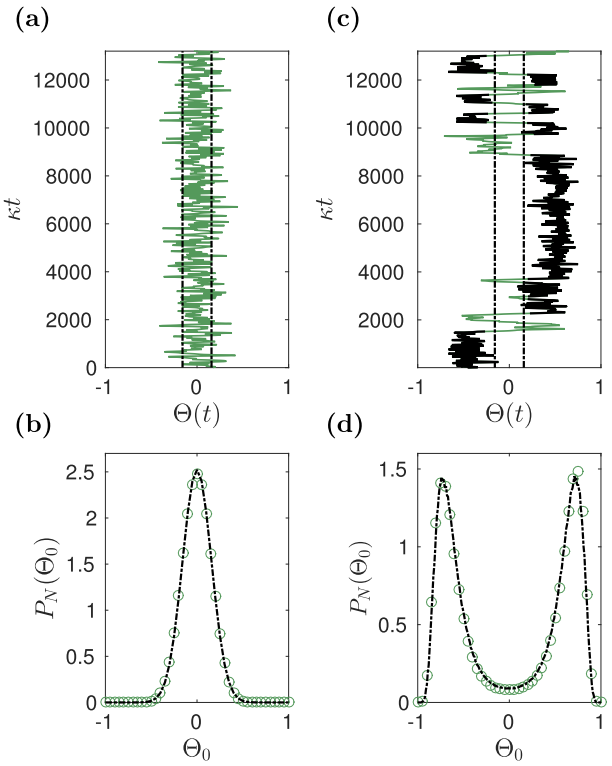


FIG. 5. (Color online) (Top panels) Magnetization $\Theta$ as a function of time (in units of $\kappa^{-1}$), obtained from a simulation of the SDE for $N = 20$, $\Delta_c = -\kappa$, and $\bar{n} = 0.01\,\bar{n}_c$ (a) and $\bar{n} = 1.4\,\bar{n}_c$ (c). The black dashed lines are located at $\pm\sigma_N = \pm\sqrt{1/(2N)}$ and indicate the statistical uncertainty in the determination of the value of $\Theta_0$. Subplots (b) and (d) display the corresponding probability distribution $P_N(\Theta_0)$ obtained after averaging over time and over 100 trajectories $\Theta(t)$ (circles). The dashed line in (b) is the theoretical prediction in Eq. (32). The dashed line in (d) corresponds to the distribution obtained by numerically integrating Eq. (31) using a Metropolis algorithm [48].

which we extract from the trajectories evaluated using the SDE. Figure 6 displays $C(\tau)$ for different values of $\bar{n}$. For all values of the pump strength a fast decaying component is always present whose temporal width seems to be independent of $\bar{n}$. One also notices the contribution of a slowly decaying component whose decay rate decreases as $\bar{n}$ increases.

In order to gain insight, we first analyze the autocorrelation function below threshold for $\bar{n} = 0.01\,\bar{n}_c$. For this case we can reproduce the numerical result by means of an analytical model, reported in Appendix D . This model assumes that the atoms are homogeneously distributed in space and form a thermal distribution at the temperature determined by Eq. (20), which corresponds to the stationary solution of the FPE in Eq. (17) well below threshold [27]. Starting from this state, their motion is assumed to be ballistic and is thus calculated after setting $\bar{n} = 0$ in Eq. (17). The resulting autocorrelation function reads

$$C_{\text{free}}(\tau) = \sigma_N^2 \exp\left[-\left(\tau/\tau_c^{\text{free}}\right)^2\right], \tag{35}$$

where the correlation time is

$$\tau_c^{\text{free}} = \sqrt{\hbar\beta/\omega_r}. \tag{36}$$

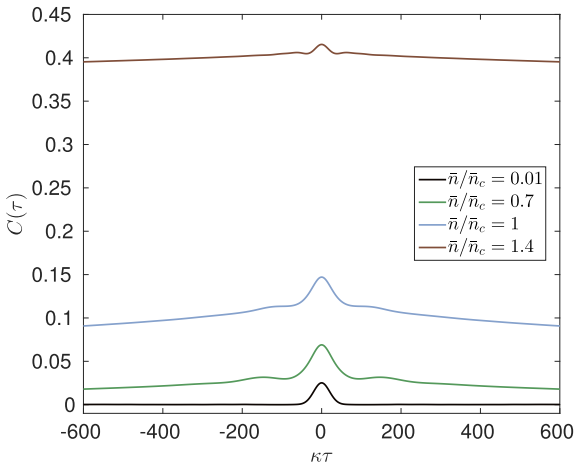


FIG. 6. (Color online) Autocorrelation function $C(\tau) = \lim_{t\to\infty}\langle\Theta(t)\Theta(t+\tau)\rangle$ [Eq. (34)] as a function of the time $\tau$ (in units of $\kappa^{-1}$) for $N = 20$ atoms, $\Delta_c = -\kappa$, and various values of $\bar{n}$ (see inset). The curves are obtained by determining $\Theta(t)$ with the numerical data (SDE).

Its excellent agreement with the numerics is visible in Fig. 7. This result shows that below threshold the fluctuations are mostly due to thermal motion, while the effect of the cavity forces, which tend to localize the atoms, is negligible. By considering the analogy between the different curves in Fig. 6, we conjecture that thermal fluctuations are responsible for the short-time behavior of the autocorrelation function.

We now turn to the long-time behavior of the autocorrelation function for increasing values of $\bar{n}$. Inspection of typical trajectories close and above threshold, shown in Figs. 3 and 5(c), shows that this is related to the time scales over which the atomic ensemble forms a Bragg grating. The system can take on values for the collective parameter $\Theta$ clearly exceeding the value of $\sigma_N$ for times which are orders of magnitude larger than

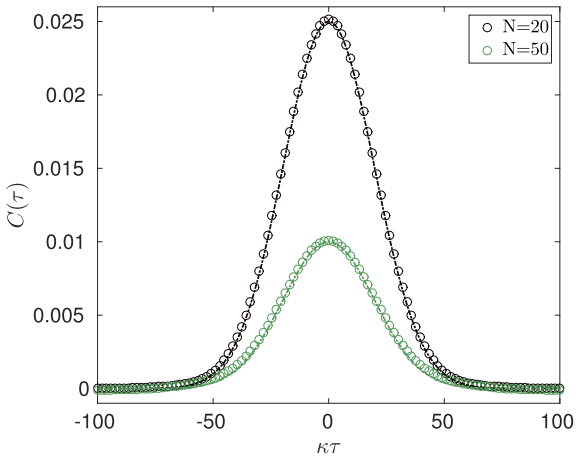


FIG. 7. (Color online) Autocorrelation function $C(\tau) = \lim_{t\to\infty}\langle\Theta(t)\Theta(t+\tau)\rangle$ as a function of the time $\tau$ (in units of $\kappa^{-1}$) for $N = 20$ and $N = 50$ atoms (see inset). The circles correspond to numerical simulations performed with $\bar{n} = 0.01\,\bar{n}_c$ and $\Delta_c = -\kappa$. The line shows the analytical estimate using Eq. (35).

the correlation time $\tau_c$ characteristic of thermal fluctuations, as visible in Fig. 5(c). We call these finite time intervals *trapping times*, corresponding to configurations in which (part of) the atoms are trapped in Bragg gratings.

In order to analyze the statistics of the trapping times, we first introduce the following criterion: the atoms are forming a Bragg grating when $|\Theta(t)| > \sigma_N$. This criterion alone, however, also includes fluctuations that can also happen well below threshold, as visible in Fig. 5(a). For this reason we set an infrared cutoff for the trapping times, such that they shall exceed $\tau_c^{\rm free}$. Herewith, we thus find a trapping time of length $\tau_{\rm trap}$ with starting point $t$ and end point $t+\tau_{\rm trap}$ if $|\Theta(t+t')| > \sigma_N$ for $t' \in [0,\tau_{\rm trap}]$ and $\tau_{\rm trap} > 10\,\tau_c^{\rm free}$. It is important to note that this sets a rather strict criterion on the trapping times as we explain now. In Fig. 5(c), one can see that even if the atoms seem to be trapped in a grating, the order parameter can take on values $|\Theta(t)| < \sigma_N$ for times of the order of $\tau_c^{\rm free}$. We choose to ignore these events when they are not associated with a sign change of $\Theta$. We perform the statistics of the trapping times by evaluating the probability density $P_{\rm trap}(\tau)$ of finding a trapping time of length $\tau$, and then using this quantity to determine the cumulative distribution $F(\tau_{\rm trap})$, defined as

$$F(\tau_{\rm trap}) = \int_{\tau_{\rm trap}}^{\infty} d\tau' P_{\rm trap}(\tau'). \tag{37}$$

Distribution $F(\tau_{\rm trap})$ thus gives the probability that the trapping time is larger than $\tau_{\rm trap}$. Figure 8 displays $F(\tau_{\rm trap})$, as we extracted it for $N = 20$ atoms and different values of $\bar{n}$: It is clearly visible that the trapping times are shifted towards higher values as $\bar{n}$ increases. The distribution exhibits long tails, which suggests that this dynamics is characterized by the existence of rare events with very long trapping times. In order to better understand this behavior, we determine the mean trapping time $\langle\tau_{\rm trap}\rangle_n$. This is numerically found for a given interval of time $t_{\rm tot}$, in which $n$ trapping intervals of length $\tau_{\rm trap}^{(i)}$ are counted ($i = 1,\ldots,n$), and reads

$$\langle\tau_{\rm trap}\rangle_n = \sum_{i=1}^{n} \tau_{\rm trap}^{(i)}/n. \tag{38}$$

In Fig. 8(b) we plot $\langle\tau_{\rm trap}\rangle_n$ as a function of the number of counts for $N = 20$ and various values of $\bar{n}$ above threshold. The mean trapping time $\langle\tau_{\rm trap}\rangle_n$, in particular, seems to converge to a finite value for sufficiently long integration times. We argue, however, that this can be an artifact of the finite integration time $t_{\rm tot}$, which we choose to be $t_{\rm tot} \approx 10^6\kappa^{-1}$: This conjecture is supported by the rather steep decay of the cumulative distribution at $t > 10^5\kappa^{-1}$ visible in Fig. 8(a). Hence, our results do not exclude the existence of a power-law decay of the distribution $F(\tau)$. This discussion clearly shows, nevertheless, that the trapping times are responsible for the long tails of the autocorrelation function.

We now study the statistics of the events which lead to jumps between two Bragg gratings. These events are visible, for instance, in Fig. 5(c) and are characterized by a time scale which we now analyze. We denote these finite times by *jumping times*. More precisely, we define a jump of time length $\tau_{\rm jump}$ as the interval of time $[0,\tau_{\rm jump}]$ within which $|\Theta(t+t')| < \sigma_N$ for $t' \in [0,\tau_{\rm jump}]$. We further impose that

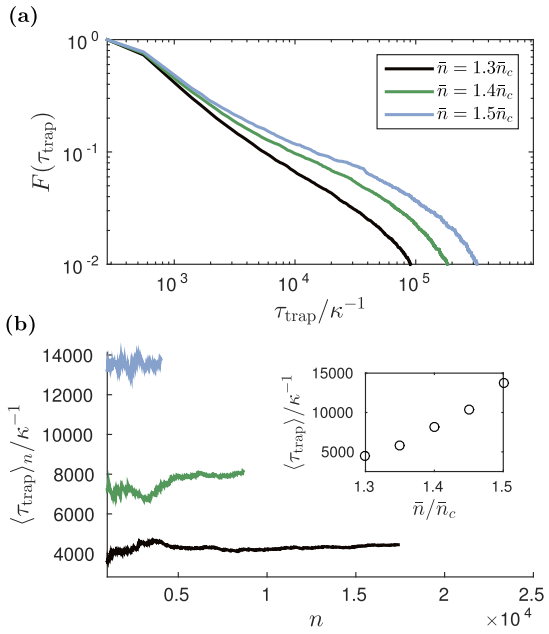


FIG. 8. (Color online) Statistics of the trapping times, evaluated numerically by averaging over 100 trajectories of $N = 20$, $\Delta_c = -\kappa$, and total evolution time $t_{\rm tot} \approx 10^6\kappa^{-1}$. The curves correspond to different values of $\bar{n}$ above threshold (see inset). (a) Cumulative distribution $F(\tau_{\rm trap})$ for the trapping times [Eq. (37)]. Higher pumping strengths lead to longer trapping times. Subplot (b) displays the mean trapping time $\langle\tau_{\rm trap}\rangle_n$ [Eq. (38)] as a function of the number of counts $n$. The inset shows the values of $\langle\tau_{\rm trap}\rangle$ as a function of $\bar{n}$, which we extrapolate from the curves, like the ones shown in the onset.

at the starting and the end points of the jumps the order parameter $\Theta$ has a different sign, such that the configuration has switched, for instance, from an even pattern ($\Theta > \sigma_N$) to an odd one ($\Theta < -\sigma_N$). We identify jump events in Fig. 5(c) with the green segments. An exception is the event at $\kappa t \sim 3000$, which does not fulfill the criteria we impose and thus does not qualify. We numerically determine the probability distribution $P_{\rm jump}(\tau_{\rm jump})$ for the jumping times at a given value of $\bar{n} > \bar{n}_c$. Figure 9(a) displays the probability distribution $P_{\rm jump}(\tau_{\rm jump})$ for $\bar{n} = 1.4\,\bar{n}_c$. We observe that it exhibits the features of exponential decay with time. Further information is extracted from the mean jumping time $\langle\tau_{\rm jump}\rangle_n$, which we evaluate as

$$\langle\tau_{\rm jump}\rangle_n = \sum_{i=1}^{n} \tau_{\rm jump}^{(i)}/n, \tag{39}$$

with $\tau_{\rm jump}^{(i)}$ the jumping time for the $i$th jump and $i = 1,\ldots n$. Figure 9(b) displays $\langle\tau_{\rm jump}\rangle_n$ for different pumping strengths. The mean values $\langle\tau_{\rm jump}\rangle_n$ do not differ much for different pumping strengths, in agreement with the conjecture that thermal fluctuations are responsible for the short-time behavior of the autocorrelation function. Nevertheless, we see indications that the mean jumping time decreases as $\bar{n}$ increases; thus, at large pump strengths the atoms reorganize in Bragg gratings over shorter time scales.

Insight into the dynamics underlying a jump in the order parameter can be gained by considering the corresponding

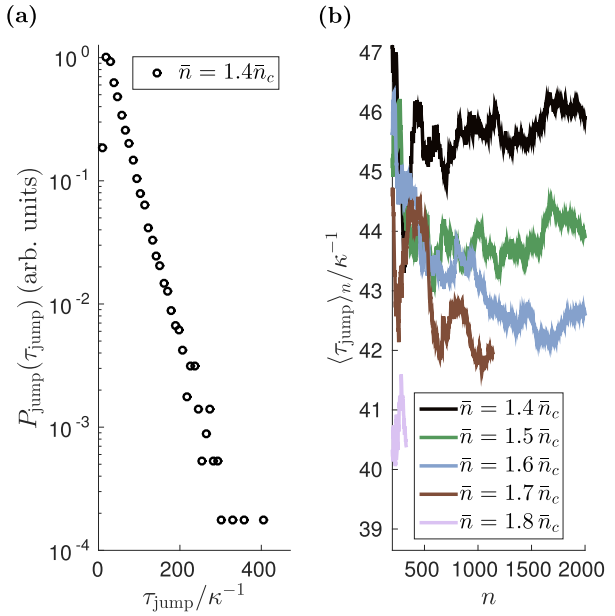


FIG. 9. (Color online) Statistics of the jumping times, evaluated numerically by averaging over 100 trajectories of $N = 20$, $\Delta_c = -\kappa$, total evolution time $t_{\rm tot} \approx 10^6\kappa^{-1}$. (a) Probability distribution $P_{\rm jump}(\tau_{\rm jump})$ for $\bar{n} = 1.4\,\bar{n}_c$. (b) Mean jumping time $\langle\tau_{\rm jump}\rangle_n$ [Eq. (39)] as a function of the number of counts $n$ and for several values of $\bar{n}$ above threshold (see inset).

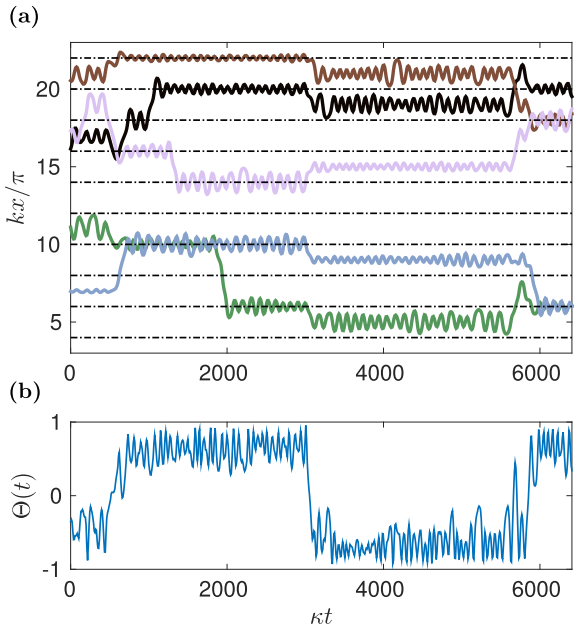


FIG. 10. (Color online) (a) Individual atomic trajectories and (b) corresponding order parameter as a function of time (in units of $\kappa^{-1}$) for $N = 5$ atoms, $\Delta_c = -\kappa$, and $\bar{n} = 1.4\,\bar{n}_c$. The black dashed horizontal lines in (a) indicate the position of the even sites of the cavity spatial mode function. The trajectories have been numerically evaluated taking the stationary state as the initial distribution.

individual atomic trajectories. A simulation for $N = 5$ atoms is shown in Fig. 10(a) for the choice of a pump strength above threshold $\bar{n} = 1.4\,\bar{n}_c$. At a given instant of time, the atomic positions are, in general, at distances which are integer multiples of the cavity wavelength, thus localized either at the even or the odd sites of the spatial mode function, thus forming one of the two possible Bragg gratings. When this occurs, the atoms perform oscillations about these positions. The amplitude of these oscillations does not remain constant, and one can observe an effective exchange of mechanical energy among the atoms. This can lead to a change of the potential that can untrap atoms. The onset of this behavior seems to be the precursor of the instability of the whole grating, as one can observe by comparing these dynamics with the one of the corresponding order parameter in subplot (b). The oscillations about the grating minima, moreover, are responsible for the damped oscillation observed in the autocorrelation function in Fig. 6 for values of $\bar{n}$ above threshold.

### 3. *Power spectrum*

Complementary information to the temporal behavior of the autocorrelation function can be gained by studying its Fourier transform. We thus numerically compute the power spectrum of $\Theta(t)$, which we define as

$$\tilde{S}(\omega) = \langle|\Theta(\omega)|^2\rangle, \tag{40}$$

where

$$\Theta(\omega) = \int_0^t d\tau\, \exp(-i\omega\tau)\Theta(\tau) \tag{41}$$

is the Fourier transform of the order parameter. Figure 11 displays the spectrum of the autocorrelation function for different values of $\bar{n}$ (a) below and (b) above threshold.

One clearly observes two different kinds of behavior, depending on whether $\bar{n}$ is below or above threshold: For $\bar{n} < \bar{n}_c$ we observe a rather broad spectrum about $\omega = 0$, whose breadth increases as $\bar{n}$ approaches the critical value from below. The emergence of a flat broad structure can be associated with the creation of (unstable) Bragg gratings and is related to the broadening of the distribution $P_N(\Theta_0)$ visible in Figs. 4(b) and 4(c). Above threshold, for $\bar{n} > \bar{n}_c$, the width of the component centered at zero frequency becomes dramatically narrower and narrows further with $\bar{n}$, indicating that the atoms become increasingly localized in a Bragg pattern. The width of this frequency component is determined by the inverse of the mean trapping time, namely, the rate at which jumps between different Bragg gratings occur.

Above threshold sidebands of the central peak appear, which correspond to the damped oscillations of the autocorrelation function. The central frequency of these sidebands increases for higher pumping strength, while their width decreases. We understand these features as the onset of oscillations about the minima of the Bragg grating, which one can also observe in the trajectories of Fig. 10(a). This conjecture is supported by a simple calculation of the oscillation frequency as a function of $\bar{n}$, assuming that the potential about their minima is approximated by harmonic oscillators. Even though the estimated frequency is higher, this estimate qualitatively reproduces the dependence of the sidebands' central frequency

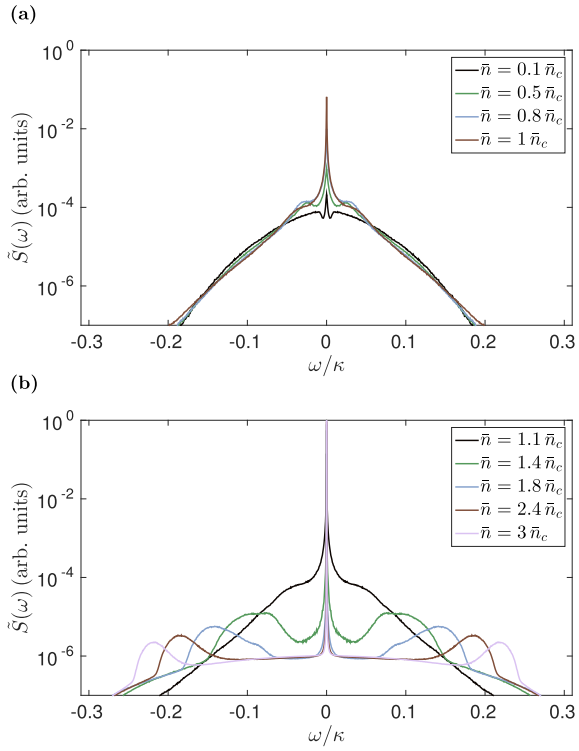


FIG. 11. (Color online) Spectrum of the autocorrelation function $\tilde{S}(\omega)$ [Eq. (40)] and in arbitrary units, as a function of the frequency (in units of $\kappa$) for different $\bar{n}$, and evaluated from the numerical data of $\Theta(t)$ for 100 trajectories of $N = 50$ atoms, $\Delta_c = -\kappa$, and evolution time $t_{\rm tot} = 10^4\kappa^{-1}$. The subplots show the spectrum for $\bar{n}$ below (a) and above (b) threshold (see insets).

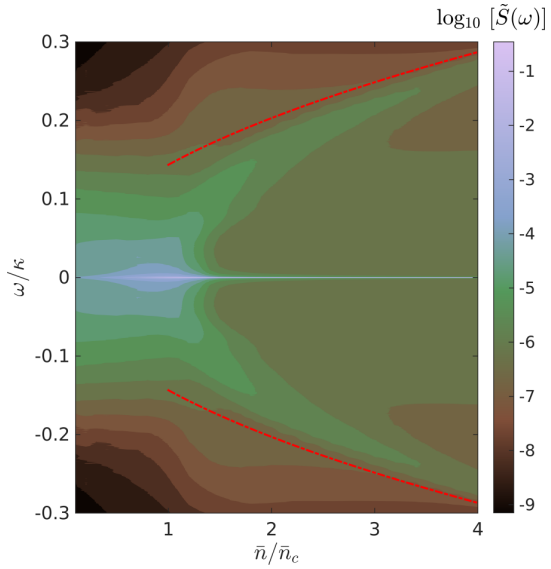


FIG. 12. (Color online) Contour plot of the spectrum of the autocorrelation function $\tilde{S}(\omega)$ [Eq. (40)] as a function of $\bar{n}$ and of the frequency (in units of $\kappa$). The other parameters are the same as in Fig. 11. The red dashed line corresponds to an estimate deep in the organized regime assuming the atoms are trapped in a harmonic potential with frequency $\tilde{\omega} = \sqrt{2\omega_r\kappa\bar{n}/\bar{n}_c}$.

with $\bar{n}$ above threshold, as visible in Fig. 12. This plot further shows that the behavior between the two parameter regions, below and above threshold, are qualitatively very different. The results of our simulations suggest that the transition in Fig. 12 at $\bar{n}_c$ becomes sharper as the atom number is increased.

## IV. PHOTON STATISTICS AND COHERENCE OF THE FIELD AT THE CAVITY OUTPUT

Since the photons scattered by the atoms into the resonator carry the information about the density of the atoms within the cavity spatial mode function, then detection of the light at the cavity output allows to monitor the state of the atoms during the dynamics. This is an established method in experiments with atoms and ions in cavities [22,49–52], and it is at the basis of proposals for detecting nondestructively the quantum phase of ultracold atoms [53,54].

Formally, the field at the cavity output $\hat{a}_{\rm out}(t)$ is directly proportional to the intracavity field $\hat{a}$ via the relation $\hat{a}_{\rm out}(t) = \sqrt{2\kappa}\hat{a} - \hat{a}_{\rm in}(t)$, where $\hat{a}_{\rm in}(t)$ is the input field, with zero mean value and $[\hat{a}_{\rm in}(t),\hat{a}_{\rm in}(t')^\dagger] = \delta(t-t')$ [55]. The intracavity field is, in turn, given by the solution of the coupled atoms-field dynamics, and under the assumption of time-scales separation it can be cast in the form given in Eq. (7), which expresses an effective operator resulting from the coarse-grained dynamics. Equation (7) shows that in leading order the intracavity field is proportional to the magnetization $\Theta(t)$; therefore, the features of the magnetization we identified thus far shall be visible also in the photon statistics at the cavity output. In addition, there is a retardation component, which gives rise to cooling and that in our parameter regime is a small correction. We now report the analysis of the intracavity photon number, and of the first- and second-order correlation functions as a function of the pump strength $\bar{n}$. Throughout this analysis we consider that the system has reached the stationary state at $\Delta_c = -\kappa$, corresponding to the minimum temperature of the atoms. Analytically, all averages are taken assuming the atomic distribution is stationary. Numerically, this consists of assuming that the trajectories are evolved starting from the stationary distribution.

### A. Intracavity photon number

The intensity of the emitted light is proportional to the mean intracavity photon number

$$n_{\rm cav} = \lim_{t\to\infty} \langle \hat{a}^\dagger(t)\hat{a}(t)\rangle. \tag{42}$$

Figure 13(a) displays $n_{\rm cav}$ as a function of $\bar{n}$ for different atom numbers. The circles correspond to the mean photon number evaluated by numerical simulations using Eq. (7), whereas the dot-dashed lines show the adiabatic solution, Eq. (9), evaluated with the steady-state solution of Eq. (23). For $\bar{n} < \bar{n}_c$ the mean photon number is below unity: Therefore, in this regime shot noise is dominant. Above threshold, $n_{\rm cav}$ rapidly increases with $N$ and $\bar{n}$. For the parameters we choose its value is essentially determined by the adiabatic component of the cavity field, while the contribution due to retardation is negligible (it is less than 0.1%). Thus, the intracavity photon number provides

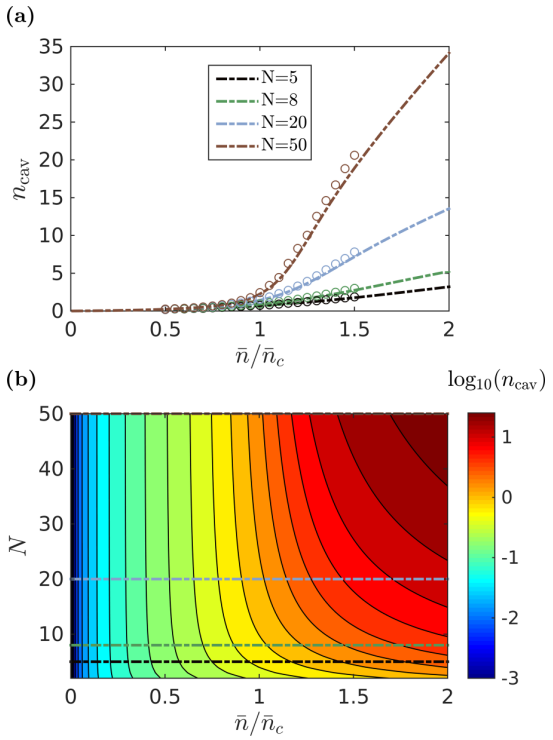


FIG. 13. (Color online) (a) The mean intracavity photon number $n_{cav}$ at steady state is displayed as a function of the pump strength $\bar{n}$ (in units of $\bar{n}_c$) and for different atom numbers (see inset). The circles correspond to the numerical data obtained by using Eq. (7) and integrating the SDE. The dot-dashed lines correspond to the adiabatic limit $n_{cav}|_{ad} = N\bar{n}\lim_{t\to\infty}\langle\Theta(t)^2\rangle$, where the average is performed over the stationary state in Eq. (23). (b) Contour plot of $n_{cav}|_{ad}$ as a function of $N$ and $\bar{n}$. The color code is in logarithmic scale. The horizontal lines correspond to the dot-dashed curves shown in subplot (a).

direct access to the autocorrelation function at zero-time delay, $\langle\Theta^2\rangle$. The numerical data, represented by the circles, follow very closely the curves corresponding to the adiabatic solution $n_{cav}|_{ad} = N\bar{n}\lim_{t\to\infty}\langle\Theta(t)^2\rangle$. The difference between the two curves is indeed small and due to the effect of the dynamical Stark shift scaling with the parameter $U$, which in the numerics is systematically taken into account. This nonlinear shift of the cavity frequency is maximum when the atoms are localized in a grating and for the chosen sign ($U < 0$) it tends to increase the value of $n_{cav}$.

Figure 13(b) displays the contour plot of $n_{cav}$ as a function of $\bar{n}$ and $N$ using the adiabatic solution [Eq. (9)] and the steady-state solution in Eq. (23). We observe that well below threshold $n_{cav}$ depends solely on $\bar{n}$ and is independent of $N$. In this regime, in fact, the atoms are homogeneously distributed; there is no collective effect in photon scattering and thus no superradiance. Using the assumption of a homogeneous spatial distribution and $\bar{n} \ll \bar{n}_c$ we can derive an analytical estimate of $n_{cav}$ which is independent of $N$ (see Appendix D ):

$$n_{cav}|_{\bar{n}\ll\bar{n}_c} \approx \bar{n}/2.$$

As $\bar{n}$ approaches and then exceeds the threshold value, instead, the dependence of the mean intracavity photon number on $N$ becomes evident.

### B. Spectrum of the emitted light

We now turn to the first-order correlation function at steady state, $g^{(1)}(\tau) = \lim_{t\to\infty}\langle\hat{a}^\dagger(t+\tau)\hat{a}(t)\rangle$. At zero-time delay, $\tau = 0$, it corresponds to the intracavity photon number. For finite delays $\tau$ it is proportional to the power spectrum of the autocorrelation function. In addition, it contains the nonlinear contribution of the cavity frequency shift and the retarded component of the cavity field. We discuss here the spectrum of $g^{(1)}(\tau)$,

$$S(\omega) = \lim_{t\to\infty}\frac{1}{2\pi}\int_{-\infty}^{\infty} d\tau e^{-i\omega\tau}\langle\hat{a}^\dagger(t+\tau)\hat{a}(t)\rangle, \qquad (43)$$

which we then compare with the result obtained for the power spectrum of the magnetization. The spectrum $S(\omega)$ is displayed in Fig. 14 for $N = 50$ atoms and different values of the pumping strength.

The behavior is very similar to the spectrum of the autocorrelation function of the magnetization in Fig. 11. Below threshold [Fig. 14(a)] we observe a broad frequency spectrum, while above threshold [Fig. 14(b)] we notice the emergence of sidebands whose frequency increases with $\bar{n}$. In general, the spectrum of the emitted light has the same form as the power spectrum of the magnetization and thus allows to extract information about the thermodynamics of self-organization. The contour plot is very similar to the corresponding one of the autocorrelation function, Fig. 12. A distinct feature is found in a small asymmetry between the red ($\omega < \omega_L$) and the blue ($\omega > \omega_L$) sidebands in Fig. 14(b). The asymmetry seems to be due to the contribution of the diabatic component of the cavity field, given in Eq. (8). Remarkably, the spectrum qualitatively agrees with the one observed in experiments analyzing self-organization of ultracold atoms in single-mode standing-wave resonators [52], thus outside the regime of validity of the semiclassical treatment. In particular, sideband asymmetry above threshold was also reported in Ref. [52].

### C. Intensity-intensity correlations

The intracavity photon number below and close to threshold is smaller than unity, and is thus characterized by large photon fluctuations. We now study the properties of these fluctuations by determining the intensity-intensity correlation function,

$$g^{(2)}(\tau) = \lim_{t\to\infty}\frac{\langle\hat{a}^\dagger(t)\hat{a}^\dagger(t+\tau)\hat{a}(t+\tau)\hat{a}(t)\rangle}{\langle\hat{a}^\dagger(t)\hat{a}(t)\rangle^2}. \qquad (44)$$

with $t \to \infty$ indicating the steady-state, and focus on its value at zero-time delay, $g^{(2)}(0)$, as a function of $\bar{n}$ for gaining insight in the photon statistics. Figure 15(a) displays the correlation function $g^{(2)}(0)$ as a function of $\bar{n}$ and for different atom numbers. The circles show $g^{(2)}(0)$ extracted from numerical simulations using Eq. (7), while the dot-dashed lines correspond to the adiabatic solution $g^{(2)}(0)|_{ad} = \langle\Theta^4\rangle/\langle\Theta^2\rangle^2$ using the steady-state solution in Eq. (23). Both curves are in good agreement. We observe a crossover from $g^{(2)}(0) \approx 3$ to $g^{(2)}(0) \approx 1$ when tuning the pumping strength from below to

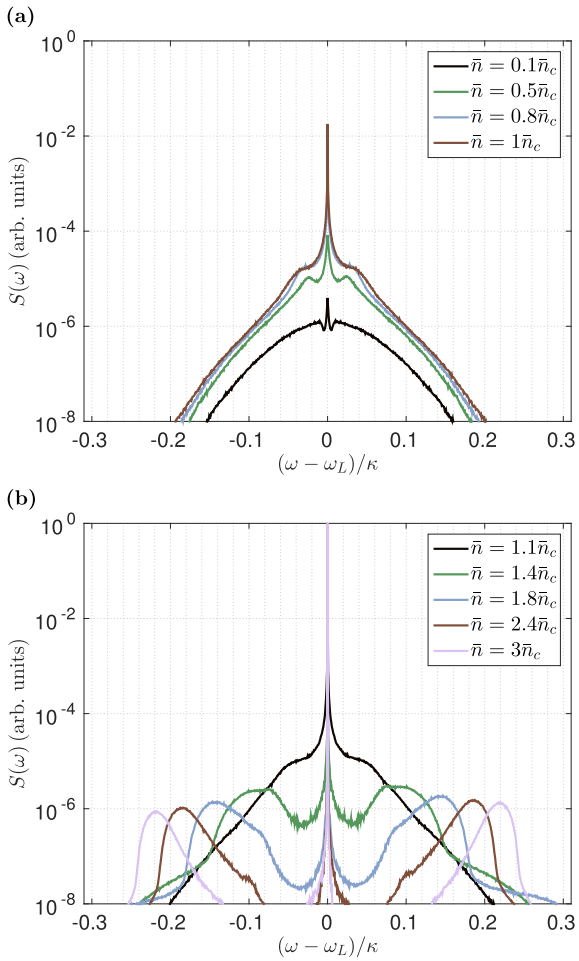


FIG. 14. (Color online) Spectrum of the intracavity field intensity $S(\omega)$ [Eq. (43)] and in arbitrary units at steady state. In (a) the curves correspond to values of $\bar{n} \leqslant \bar{n}_c$ and in (b) they correspond to values of $\bar{n} > \bar{n}_c$. The data have been numerically evaluated for $N = 50$ atoms and over the interval of time $(-10^4 : 1 : 10^4)\,\kappa^{-1}$.

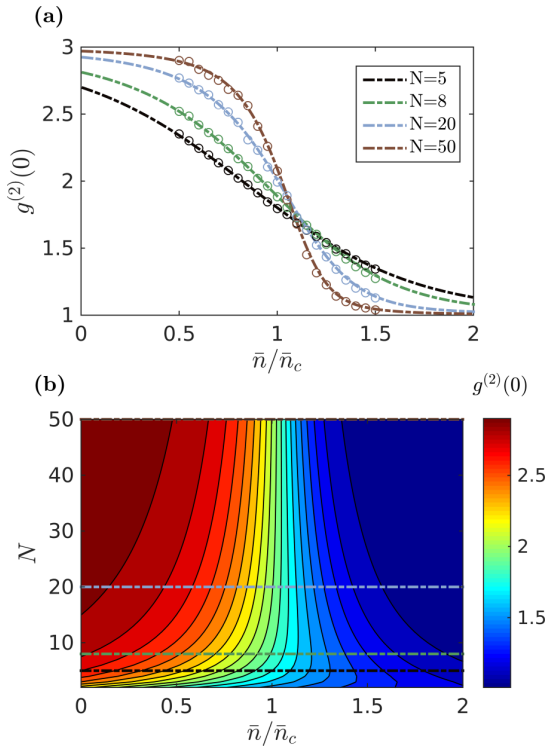


FIG. 15. (Color online) (a) The intensity-intensity correlation at zero-time delay $g^{(2)}(0)$ [Eq. (44)] is shown as a function of the pump strength $\bar{n}$ (in units of $\bar{n}_c$) and for different atom numbers $N$ (see inset). The circles correspond to the data extracted from numerical simulations, the dot-dashed lines are evaluated using the steady state in Eq. (23) and the adiabatic solution, where the field is proportional to the instantaneous value of the magnetization: $g^{(2)}(0)|_{\rm ad} = \langle\Theta^4\rangle/\langle\Theta^2\rangle^2$. (b) Contour plot of the adiabatic component of the intensity-intensity correlation function at zero-time delay $g^{(2)}(0)|_{\rm ad}$ vs $\bar{n}$ and $N$. The horizontal cuts correspond to the dot-dashed lines in subplot (a).

above the threshold, which sharpens as $N$ grows. The value above threshold is associated with coherent radiation, which is what one expects when the atoms are locked in a Bragg grating. The behavior below threshold can be reproduced by means of an analytical model valid for $\bar{n} \ll \bar{n}_c$, in the limit in which the atoms form a homogeneous distribution. In Appendix D we show that in this limit we can write

$$g^{(2)}(0) = 3 - 3/(2N), \tag{45}$$

which asymptotically tends to 3 as $N$ increases. This result qualitatively agrees with experimental measurements with ultracold atoms performed below threshold [52]. While this value is also found for squeezed states, in our case we could not find any squeezing in the field quadratures and thus attribute the behavior of $g^{(2)}(0)$ below threshold to thermal fluctuations.

Figure 15(b) displays $g^{(2)}(0)$ for different pumping strengths and number of atoms, evaluated using the adiabatic solution $g^{(2)}(0) = \langle\Theta^4\rangle/\langle\Theta^2\rangle^2$ and the steady state in Eq. (23). The dashed horizontal cuts correspond to the dot-dashed curves shown in subplot (a). One clearly observes the crossover from $g^{(2)}(0) \approx 3$ to $g^{(2)}(0) \approx 1$ when $\bar{n}$ exceeds $\bar{n}_c$, while the transition sharpens for increasing atom numbers.

## V. CONCLUSIONS

Atoms can spontaneously form spatially ordered structures in optical resonators when they are transversally driven by lasers. In this paper we have characterized the stationary solution, which emerges from the interplay between the coherent dynamics due to scattering of laser photons into the resonator and the incoherent effects associated with photon losses due to cavity decay. We assumed that these dynamics are characterized by a time-scale separation, such that the cavity field relaxes on a faster time scale to a local steady state depending on the atomic density. This assumption is valid when the cavity loss rate $\kappa$ exceeds the recoil energy $\omega_r$ scaling the mechanical effects of light, and it is fulfilled in several existing experiments [17,22,24]. Retardation effects are small, but important in order to establish the stationary state.

Starting from a FPE, which has been derived by means of an *ab initio* theoretical treatment [27], we have shown that the stationary state is thermal, with a temperature that is solely determined by the detuning between cavity and laser. From this result, we could determine the free energy and thus show that atomic self-organization in a standing-wave cavity mode is a second-order transition of Landau type. Our model allows us to determine the phase diagram for the self-organization transition and delivers the critical value of the pump strength in a self-consistent way. This value is in agreement with previous estimates [30,31]. An interesting further step is to connect this theory with quantum-field theoretical models which analyze self-organization in the ultracold regime [32,45,56], thus extending the validity of our model to the regime in which quantum fluctuations in the atomic motion cannot be treated within a semiclassical model.

We further remark that, while our analysis focuses on a one-dimensional model, we expect that from our predictions we can extrapolate the stationary behavior in two spatial dimensions. This can be calculated by means of a straightforward extension of the treatment in Ref. [27] to two dimensions. Differing from one dimension, in the symmetry-broken phase the atoms will form a checkerboard pattern as found in Ref. [23], as long as the atomic gas is uniformly illuminated by the laser and the coupling with the resonator can be treated in the paraxial approximation. The effect of the dimensionality can modify the specific form of friction and diffusion. Moreover, in two dimensions the effect of correlations is expected to be more relevant, so that the statistical properties will be modified.

Photodetection of the emitted light allows one to reveal the thermodynamic properties of the atoms. Our results show that they exhibit several remarkable analogies with experimental results obtained with ultracold atomic ensembles inside of resonators [52]. While our theory is not generally applicable to these systems, it is not surprising that the field at the cavity output does not depend on the presence (or absence) of matter-wave coherence, as it solely depends on the atomic density. Nevertheless, it would be interesting to identify observables for the cavity field output, if possible, that provide information about quantum coherent properties of matter, in the spirit of matter-wave homodyne detection discussed in Ref. [57]. This could be possible when the cavity spectroscopically resolves the many-body excitations, as is verified in the parameter regime of the experimental setup reported in Ref. [58].

This work is the first of a series analyzing the effect of the long-range cavity-mediated interaction. Here we focused on the dynamics at steady state. In Ref. [35] we will compare the results here reported with a mean-field solution, which is systematically derived from this treatment after making a mean-field ansatz, and discuss its validity in the perspective of developing a BBGKY hierarchy for self-organization in optical resonators [33]. In Ref. [34] we will analyze the dynamics of the full distribution after quenches across the phase transition, expanding on the results presented in Ref. [29].

## ACKNOWLEDGMENTS

The authors are grateful to R. Landig, G. Manfredi, C. Nardini, F. Piazza, and R. Shaebani for stimulating discussions and helpful comments. This work was supported by the German Research Foundation (DFG, DACH project "Quantum crystals of matter and light") and by the German Ministry of Education and Research (BMBF "Q.com").

## APPENDIX A: PARAMETERS OF THE FOKKER-PLANCK EQUATION

In this Appendix we give the explicit form of the parameters appearing in the coefficients of Eq. (12):

$$\delta_F = \frac{NU\Theta}{\Delta_c'}\cos(kx_i), \tag{A1}$$

$$\delta_\Gamma = \cos(kx_j)\frac{NU\Theta}{\Delta_c'}\frac{3\Delta_c'^2-\kappa^2}{\Delta_c'^2+\kappa^2} + \cos(kx_i)\frac{NU\Theta}{\Delta_c'} + 4\cos(kx_i)\cos(kx_j)\frac{(NU\Theta)^2}{\Delta_c'^2+\kappa^2}, \tag{A2}$$

$$\delta_\eta = \frac{(2NU\Theta)^2}{\Delta_c'^2+\kappa^2}\cos(kx_i)\cos(kx_j) + \frac{2NU\Theta\Delta_c'}{-\Delta_c'^2+\kappa^2}\left\{\frac{3\kappa^2-\Delta_c'^2}{\Delta_c'^2+\kappa^2}\cos(kx_j)-\cos(kx_i)\right\}, \tag{A3}$$

$$\delta_D = \frac{4NU\Theta}{\Delta_c'^2+\kappa^2}\cos(kx_j)[\Delta_c' + \cos(kx_i)NU\Theta]. \tag{A4}$$

The diffusion coefficient for the spontaneous decay term reads

$$\mathcal{D}^{\rm sp}(x_i) = (\hbar k)^2\left\{\frac{N^2S^2\Theta^2}{\Delta_c'^2+\kappa^2}[\sin^2(kx_i)+\overline{u^2}\cos^2(kx_i)] + s\overline{u^2}\left[\frac{2NS\Theta\Delta_c'}{\Delta_c'^2+\kappa^2}\cos(kx_i)+s\right]\right\},$$

where $s=\Omega/g$ and $\overline{u^2}$ determines the momentum diffusion due to spontaneous emission recoils projected on the cavity axis (dipole pattern of radiation).

Finally, the correction scaling with $NU/\kappa$ in Eq. (17) reads

$$L_1 f = 2\hbar k\Delta_c\Theta\sum_i \sin(kx_i)\left[\frac{\Delta_c^2-\kappa^2}{\Delta_c^2+\kappa^2}\mathcal{B}+\Theta\cos(kx_i)\right]\partial_{p_i} f \tag{A5}$$

and is systematically taken into account in our calculations.

## APPENDIX B: STOCHASTIC DIFFERENTIAL EQUATIONS

The FPE given in Eq. (17) for $|NU| \ll |\Delta_c|$ can be simulated by SDEs, which in our case read

$$dx_j = \frac{p_j}{m}dt + dX_j, \tag{B1}$$

$$dp_j = \hbar k\frac{2S^2\Delta_c}{\Delta_c^2+\kappa^2}\sin(kx_j)\left[\sum_{i=1}^N\cos(kx_i)\right]\delta_U dt + \frac{8\omega_r S^2\Delta_c\kappa}{\left(\Delta_c^2+\kappa^2\right)^2}\sin(kx_j)\left[\sum_{i=1}^N\sin(kx_i)p_i\right]dt + dP_j, \tag{B2}$$

with

$$\delta_U = 1 + \frac{NU}{\Delta_c}\left[\frac{\Delta_c^2 - \kappa^2}{\Delta_c^2 + \kappa^2}\mathcal{B} + \Theta\cos(kx_j)\right], \tag{B3}$$

where $j = 1, \ldots, N$ labels the atoms and $dP_j$ denote the momentum noise terms, which are simulated by means of Wiener processes. In particular, $\langle dP_j\rangle = 0$ and $\langle dP_i dP_j\rangle = 2D_{ij}dt$, with

$$D_{ij} = (\hbar k)^2 S^2 \frac{\kappa}{\Delta_c^2 + \kappa^2}\sin(kx_i)\sin(kx_j) \tag{B4}$$

the element of the diffusion matrix when spontaneous emission is neglected.

For $\Delta_c \neq -\kappa$, we additionally take into account position noise $dX_i$, which shows cross-correlations with momentum diffusion $\langle dP_j dX_\ell\rangle = \eta_{j\ell}dt$, with

$$\eta_{j\ell} = 2\hbar\omega_r S^2 \sin(kx_j)\sin(kx_\ell)\frac{\kappa^2 - \Delta_c^2}{\left(\Delta_c^2 + \kappa^2\right)^2}. \tag{B5}$$

These terms can only be simulated when adding terms as $\langle dX_i dX_j\rangle \neq 0$ to the FPE.

For the numerical simulations, we use the Heun method [59], which is a second-order Runge-Kutta scheme with a Euler predictor.

## APPENDIX C: DETERMINATION OF THE FREE ENERGY

The equilibrium state reads

$$f(\boldsymbol{x},\boldsymbol{p}) = \frac{1}{\mathcal{Z}\Delta^N}\exp(-\beta H), \tag{C1}$$

where $\mathcal{Z}$ is the partition function, $\Delta$ is the unit phase space volume, and Hamiltonian $H$ is given in Eq. (18). The canonical partition function $\mathcal{Z}$ takes the form

$$\begin{aligned}\mathcal{Z} &= \left(\frac{\lambda}{\Delta}\right)^N \int_{-1}^{1} d\Theta\Omega(\Theta)\int_{-\infty}^{\infty} dp_1\cdots\int_{-\infty}^{\infty} dp_N \exp(-\beta H)\\ &= \left(\frac{Z_0\lambda}{\Delta}\right)^N \int_{-1}^{1} d\Theta\Omega(\Theta)\exp(-\beta\hbar\Delta_c\bar{n}N\Theta^2),\end{aligned} \tag{C2}$$

with $Z_0 = \sqrt{2m\pi/\beta}$ and

$$\Omega(\Theta) = \frac{N}{2\pi}\int_{-\infty}^{\infty} d\omega \exp\left(i\omega N\Theta\right)J_0(\omega)^N, \tag{C3}$$

where $J_n(w) = 1/(i^n\lambda)\int_0^\lambda dx\cos(nkx)\exp[i\omega\cos(kx)]$ is the $n$th-order Bessel function [46]. In order to compute Eq. (C3), we rewrite it as

$$\Omega(\Theta) = \frac{N}{2\pi}\int_{-\infty}^{\infty} d\omega \exp\left[Nh(\omega)\right], \tag{C4}$$

where we introduced the function

$$h(\omega) = i\omega\Theta + \ln\left[J_0(\omega)\right]. \tag{C5}$$

We can now compute the integral in Eq. (C4) using the method of steepest descent. For this purpose, we derive the stationary condition for Eq. (C5). This reads

$$i\Theta - \frac{J_1(\omega_0)}{J_0(\omega_0)} = 0,$$

which we can rewrite as

$$\Theta = q(\gamma_0) = \frac{I_1(\gamma_0)}{I_0(\gamma_0)} \tag{C6}$$

after defining $\omega_0 = i\gamma_0$ and using that $\frac{J_1(\omega_0)}{J_0(\omega_0)} = i\frac{I_1(\gamma_0)}{I_0(\gamma_0)}$. The function $q : \mathbb{R} \to (-1,1)$ with $y \mapsto \frac{I_1(y)}{I_0(y)}$ is bijective, such that there is a unique solution satisfying the equation

$$\gamma_0 = q^{-1}(\Theta). \tag{C7}$$

With the method of steepest descent, we get

$$\begin{aligned}\Omega(\Theta) &\sim \frac{N}{2\pi}\sqrt{\frac{2\pi}{N|h''(\omega_0)|}}\exp[Nh(\omega_0)]\\ &= \sqrt{\frac{N}{2\pi}}C(\Theta)\exp(N\{\ln[I_0(q^{-1}(\Theta))] - q^{-1}(\Theta)\Theta\}),\end{aligned} \tag{C8}$$

with

$$C(\Theta) = \left|\Theta^2 - \frac{I_0(q^{-1}(\Theta)) + I_2(q^{-1}(\Theta))}{2I_0(q^{-1}(\Theta))}\right|^{-\frac{1}{2}}.$$

Using Eq. (C8) in Eq. (C2), at leading order in $N$ we can cast the canonical partition function into the form

$$\mathcal{Z} = \left(\frac{Z_0\lambda}{\Delta}\right)^N \int_{-1}^{1} d\Theta\sqrt{\frac{N}{2\pi}}C(\Theta)\exp[-\beta N\mathcal{F}(\Theta)],$$

where $\mathcal{F}(\Theta)$ is the free energy per particle,

$$\beta[\mathcal{F}(\Theta) - \mathcal{F}_0] = \beta\hbar\Delta_c\bar{n}\Theta^2 + q^{-1}(\Theta)\Theta - \ln[I_0(q^{-1}(\Theta))], \tag{C9}$$

and $-\beta N\mathcal{F}_0 = N\ln(Z_0\lambda/\Delta)$. After performing a Taylor expansion of Eq. (C9) for small values of the order parameter, close to $\Theta = 0$, we obtain

$$\beta[\mathcal{F}(\Theta) - \mathcal{F}_0] \approx (1 - \bar{n}/\bar{n}_c)\Theta^2 + \tfrac{1}{4}\Theta^4, \tag{C10}$$

which shows that close to the instability the free energy can be cast into the form of a Landau potential [47]. This shows that the system undergoes, in the considered limit, a second-order phase transition at the critical value $\bar{n} = \bar{n}_c$ with

$$\bar{n}_c = \frac{\kappa^2 + \Delta_c^2}{4\Delta_c^2}. \tag{C11}$$

We use the method of steepest descent to minimize $\mathcal{F}(\Theta)$ in Eq. (C9) and find that the free energy is stationary if the order parameter solves the equation

$$\Theta = q\left(2\frac{\bar{n}}{\bar{n}_c}\Theta\right). \tag{C12}$$

## APPENDIX D: ANALYTICAL ESTIMATES

Several quantities of relevance can be analytically determined in the limit of small pumping strength, specifically when $\bar{n} \ll \bar{n}_c$. In this limit we assume that the atoms move ballistically and their spatial distribution is homogeneous. The

steady state then reads

$$f_s(\boldsymbol{x},\boldsymbol{p}) = \frac{1}{\lambda^N}\left(\frac{\beta}{2\pi m}\right)^{N/2} \exp\left(-\beta\sum_i \frac{p_i^2}{2m}\right),$$

which is a homogeneous distribution for the atoms, while the momentum distribution is thermal with $\beta$ defined in Eq. (20). The mean value of the order parameter for this distribution vanishes $\langle\Theta\rangle = 0$, while fluctuations scale as

$$\langle\Theta^2\rangle = \int d\boldsymbol{x}\int d\boldsymbol{p}\, f_s(\boldsymbol{x},\boldsymbol{p})\Theta^2 = \frac{1}{2N}. \tag{D1}$$

Here we used that the cross terms in $\Theta^2 = \sum_{i,j}\cos(kx_i)\cos(kx_j)/(N^2)$ vanish for a homogeneous distribution. For the standard deviation $\Delta\Theta = (\langle\Theta^2\rangle - \langle\Theta\rangle^2)^{1/2}$ we thus find

$$\Delta\Theta = \sqrt{\frac{1}{2N}}, \tag{D2}$$

which shows that the width $\Delta\Theta_0$ for the distribution function $P_N(\Theta_0)$ in Eq. (31) decreases with $N^{-1/2}$ for very low pumping strengths. We checked that for $\bar{n} \ll \bar{n}_c$ the Gaussian assumption is a good approximation for low values of $|\Theta_0|$ and sufficiently large atom number. This result is reported in Eq. (32).

In Sec. IV cavity field properties such as mean photon number $\langle\hat{a}^\dagger\hat{a}\rangle$ and intensity-intensity correlations at zero-time delay $g^{(2)}(0)$ are discussed. By adiabatically eliminating the cavity field, i.e., using Eq. (9), and neglecting the dynamical Stark shift, we can give the following estimate for the mean photon number

$$\langle\hat{a}^\dagger\hat{a}\rangle = N\bar{n}\langle\Theta^2\rangle = \bar{n}/2 = \frac{\bar{n}_c}{2}\frac{\bar{n}}{\bar{n}_c} \tag{D3}$$

under the assumption of a homogeneous spatial distribution. As long as the spatial distribution remains homogeneous, the mean photon number thus scales with the ratio $\bar{n}/\bar{n}_c$ independent on the atom number $N$. This result is discussed in Sec. IV A and gets evident in Fig. 13(b). Under the same conditions, far below threshold, we get

$$\begin{aligned}\langle\Theta^4\rangle &= \int d\boldsymbol{x}\int d\boldsymbol{p}\, f_s(\boldsymbol{x},\boldsymbol{p})\left[\sum_i \cos(kx_i)/N\right]^4 \\ &= \frac{1}{N^4}\left[N\frac{I_{(4)}}{2\pi} + 3N(N-1)\frac{I_{(2)}^2}{(2\pi)^2}\right] = \frac{3(N-1)}{8N^3},\end{aligned} \tag{D4}$$

with $I_{(2)} = \int_0^{2\pi} d\tilde{x}\cos^2(\tilde{x})$ and $I_{(4)} = \int_0^{2\pi} d\tilde{x}\cos^4(\tilde{x})$. For the intensity-intensity correlations at zero-time delay

$$g^{(2)}(0) = \langle\Theta^4\rangle/\langle\Theta^2\rangle^2, \tag{D5}$$

using Eqs. (D1) and (D4), we thus find

$$\lim_{\bar{n}\to 0} g^{(2)}(0) = 3 - \frac{3}{2N}. \tag{D6}$$

This function tends towards the value of 3 for increasing atom numbers, as can be seen in Fig. 15.

When assuming ballistic expansion, which is justified whenever the forces on the atoms due to cavity backaction are small, i.e., far below threshold, we can also derive an analytical estimate for the correlation function $C(\tau) = \langle\Theta(t)\Theta(t+\tau)\rangle$ at steady state,

$$\begin{aligned}&\lim_{\bar{n}\to 0}\langle\Theta(t)\Theta(t+\tau)\rangle \\ &= \langle\Theta^2\rangle_t\left(\frac{\beta}{2\pi m}\right)^{1/2}\int dp\exp\left(-\beta\frac{p^2}{2m}\right)\cos\left(k\frac{p}{m}\tau\right) \\ &= \langle\Theta^2\rangle_t\exp\left(-\frac{\omega_r}{\hbar\beta}\tau^2\right) = \langle\Theta^2\rangle_t\exp\left[-\left(\tau/\tau_c^{\text{free}}\right)^2\right],\end{aligned} \tag{D7}$$

with $\tau_c^{\text{free}} = \sqrt{(\hbar\beta/\omega_r)}$, where $\beta$ is the inverse temperature defined in Eq. (20) and $\langle\Theta^2\rangle_t = \frac{1}{2N}$ according to Eq. (D1). The result is reported in Eq. (35).

[1] S. Chu, Rev. Mod. Phys. **70**, 685 (1998); C. N. Cohen-Tannoudji, *ibid.* **70**, 707 (1998); W. D. Phillips, *ibid.* **70**, 721 (1998).
[2] R. Kaiser, A. Kastberg, and G. Morigi, J. Opt. Soc. Am. B **20**, 883 (2003).
[3] M. Aspelmeyer, T. J. Kippenberg, and F. Marquardt, Rev. Mod. Phys. **86**, 1391 (2014).
[4] D. J. Wineland and W. M. Itano, Phys. Rev. A **20**, 1521 (1979).
[5] S. Stenholm, Rev. Mod. Phys. **58**, 699 (1986).
[6] P. Horak, G. Hechenblaikner, K. M. Gheri, H. Stecher, and H. Ritsch, Phys. Rev. Lett. **79**, 4974 (1997).
[7] P. W. H. Pinkse, T. Fischer, P. Maunz, and G. Rempe, Nature (London) **404**, 365 (2000).
[8] C. J. Hood, T. W. Lynn, A. C. Doherty, A. S. Parkins, and H. J. Kimble, Science **287**, 1447 (2000).
[9] V. Vuletić and S. Chu, Phys. Rev. Lett. **84**, 3787 (2000).
[10] P. Maunz, T. Puppe, I. Schuster, N. Syassen, P. W. H. Pinkse, and G. Rempe, Nature (London) **428**, 50 (2004).
[11] P. Domokos and H. Ritsch, J. Opt. Soc. Am. B **20**, 1098 (2003).
[12] H. Ritsch, P. Domokos, F. Brennecke, and T. Esslinger, Rev. Mod. Phys. **85**, 553 (2013).
[13] T. Kampschulte, W. Alt, S. Manz, M. Martinez-Dorantes, R. Reimann, S. Yoon, D. Meschede, M. Bienert, and G. Morigi, Phys. Rev. A **89**, 033404 (2014).
[14] D. H. J. O'Dell, S. Giovanazzi, and G. Kurizki, Phys. Rev. Lett. **90**, 110402 (2003).
[15] P. Münstermann, T. Fischer, P. Maunz, P. W. H. Pinkse, and G. Rempe, Phys. Rev. Lett. **84**, 4068 (2000).
[16] B. Nagorny, Th. Elsässer, and A. Hemmerich, Phys. Rev. Lett. **91**, 153003 (2003); S. Gupta, K. L. Moore, K. W. Murch, and D. M. Stamper-Kurn, *ibid.* **99**, 213601 (2007).
[17] S. Ritter, F. Brennecke, K. Baumann, T. Donner, C. Guerlin, and T. Esslinger, Appl. Phys. B **95**, 213 (2009).

[18] C. von Cube, S. Slama, D. Kruse, C. Zimmermann, Ph. W. Courteille, G. R. M. Robb, N. Piovella, and R. Bonifacio, Phys. Rev. Lett. **93**, 083601 (2004).
[19] G. Labeyrie, E. Tesio, P. M. Gomes, G.-L. Oppo, W. J. Firth, G. R. M. Robb, A. S. Arnold, R. Kaiser, and T. Ackemann, Nat. Photonics **8**, 321 (2014); G. R. M. Robb, E. Tesio, G.-L. Oppo, W. J. Firth, T. Ackemann, and R. Bonifacio, Phys. Rev. Lett. **114**, 173903 (2015).
[20] D. E. Chang, J. I. Cirac, and H. J. Kimble, Phys. Rev. Lett. **110**, 113606 (2013).
[21] P. Domokos and H. Ritsch, Phys. Rev. Lett. **89**, 253003 (2002).
[22] A. T. Black, H. W. Chan, and V. Vuletić, Phys. Rev. Lett. **91**, 203001 (2003).
[23] K. Baumann, C. Guerlin, F. Brennecke, and T. Esslinger, Nature (London) **464**, 1301 (2010).
[24] K. J. Arnold, M. P. Baden, and M. D. Barrett, Phys. Rev. Lett. **109**, 153002 (2012).
[25] R. Mottl, F. Brennecke, K. Baumann, R. Landig, T. Donner, and T. Esslinger, Science **336**, 1570 (2012).
[26] D. Nagy, G. Kónya, G. Szirmai, and P. Domokos, Phys. Rev. Lett. **104**, 130401 (2010).
[27] S. Schütz, H. Habibian, and G. Morigi, Phys. Rev. A **88**, 033427 (2013).
[28] P. Domokos, P. Horak, and H. Ritsch, J. Phys. B **34**, 187 (2001).
[29] S. Schütz and G. Morigi, Phys. Rev. Lett. **113**, 203002 (2014).
[30] J. K. Asbóth, P. Domokos, H. Ritsch, and A. Vukics, Phys. Rev. A **72**, 053417 (2005).
[31] W. Niedenzu, T. Grießer, and H. Ritsch, Europhys. Lett. **96**, 43001 (2011).
[32] Emanuele G. Dalla Torre, S. Diehl, M. D. Lukin, S. Sachdev, and P. Strack, Phys. Rev. A **87**, 023831 (2013).
[33] A. Campa, T. Dauxois, and S. Ruffo, Phys. Rep. **480**, 57 (2009).
[34] S. Schütz, S. B. Jäger, and G. Morigi (unpublished).
[35] S. B. Jäger, master's thesis, Saarland University, 2015; S. B. Jäger, S. Schütz, and G. Morigi (unpublished).
[36] A. Vukics and P. Domokos, Phys. Rev. A **72**, 031401(R) (2005).
[37] J. Dalibard and C. Cohen-Tannoudji, J. Phys. B **18**, 1661 (1985).
[38] S. Fernández-Vidal, G. De Chiara, J. Larson, and G. Morigi, Phys. Rev. A **81**, 043407 (2010).
[39] More specifically, the condition reads $\omega_r N S^2 \ll (\kappa^2 + \Delta_c^2)^2/(4|\Delta_c|)$ and reduces to the form in Eq. (4) when $|\Delta_c| \sim \kappa$.
[40] J. Larson, B. Damski, G. Morigi, and M. Lewenstein, Phys. Rev. Lett. **100**, 050401 (2008); J. Larson, S. Fernández-Vidal, G. Morigi, and M. Lewenstein, New J. Phys. **10**, 045002 (2008).
[41] F. Piazza and H. Ritsch, Phys. Rev. Lett. **115**, 163601 (2015).
[42] K. Murr, P. Maunz, P. W. H. Pinkse, T. Puppe, I. Schuster, D. Vitali, and G. Rempe, Phys. Rev. A **74**, 043412 (2006).
[43] P. H. Chavanis, J. Vatteville, and F. Bouchet, Eur. Phys. J. B **46**, 61 (2005); P. H. Chavanis, *ibid.* **87**, 120 (2014).
[44] B. Olmos, I. Lesanovsky, and J. P. Garrahan, Phys. Rev. Lett. **109**, 020403 (2012).
[45] F. Piazza and P. Strack, Phys. Rev. A **90**, 043823 (2014).
[46] M. Abramowitz and I. Stegun (editors), *Handbook of Mathematical Functions* (Dover, New York, 1968).
[47] L. D. Landau and E. M. Lifshitz, *Statistical Physics* (Pergamon, Oxford, U.K., 1958).
[48] N. Metropolis, A. W. Rosenbluth, M. N. Rosenbluth, A. H. Teller, and E. Teller, J. Chem. Phys. **21**, 1087 (1953).
[49] K. Baumann, R. Mottl, F. Brennecke, and T. Esslinger, Phys. Rev. Lett. **107**, 140402 (2011).
[50] N. Brahms, T. Botter, S. Schreppler, D. W. C. Brooks, and D. M. Stamper-Kurn, Phys. Rev. Lett. **108**, 133601 (2012).
[51] A. Dantan, J. P. Marler, M. Albert, D. Guénot, and M. Drewsen, Phys. Rev. Lett. **105**, 103001 (2010).
[52] F. Brennecke, R. Mottl, K. Baumann, R. Landig, T. Donner, and T. Esslinger, Proc. Natl. Acad. Sci. USA **110**, 11763 (2013); R. Landig, F. Brennecke, R. Mottl, T. Donner, and T. Esslinger, Nat. Commun. **6**, 7046 (2015).
[53] I. B. Mekhov, C. Maschler, and H. Ritsch, Nat. Phys. **3**, 319 (2007); I. B. Mekhov and H. Ritsch, Phys. Rev. Lett. **102**, 020403 (2009).
[54] S. Rist, C. Menotti, and G. Morigi, Phys. Rev. A **81**, 013404 (2010).
[55] C. W. Gardiner and M. J. Collett, Phys. Rev. A **31**, 3761 (1985).
[56] M. Buchhold, P. Strack, S. Sachdev, and S. Diehl, Phys. Rev. A **87**, 063622 (2013).
[57] S. Rist and G. Morigi, Phys. Rev. A **85**, 053635 (2012).
[58] M. Wolke, J. Klinner, H. Keßler, and A. Hemmerich, Science **337**, 75 (2012).
[59] W. Rümelin, SIAM J. Numer. Anal. **19**, 604 (1982).

### 2.2.2 Phases of cold atoms interacting via photon-mediated long-range forces

Journal of Statistical Mechanics: Theory and Experiment **6**, 064002 (2017)

DOI: https://doi.org/10.1088/1742-5468/aa71d7

Authors: Tim Keller, Simon B. Jäger, and Giovanna Morigi

*Theoretische Physik, Universität des Saarlandes, D-66123 Saarbrücken, Germany*

**Author Contributions:**
The theoretical model was developed by all authors. Analytical calculations were performed by T. Keller and S. B. Jäger. The numerical simulations were performed by T. Keller. The results were checked and discussed by all authors. The article was written by all authors.

**Abstract:**
Atoms in high-finesse optical resonators interact via the photons they multiply scatter into the cavity modes. The dynamics is characterized by dispersive and dissipative optomechanical long-range forces, which are mediated by the cavity photons, and exhibits a steady state for certain parameter regimes. In standing- wave cavities the atoms can form stable spatial gratings. Moreover, their asymptotic distribution is a Maxwell-Boltzmann whose effective temperature is controlled by the laser parameters. In this work we show that in a two-mode standing-wave cavity the stationary state possesses the same properties and phases of the Generalized Hamiltonian Mean Field model in the canonical ensemble. This model has three equilibrium phases: a paramagnetic, a nematic, and a ferromagnetic one, which here correspond to different spatial orders of the atomic gas and can be detected by means of the light emitted by the cavities. We further discuss perspectives for investigating in this setup the ensemble inequivalence predicted for the Generalized Hamiltonian Mean Field model.

**Remark:**
In this thesis we embedded a preprint version of the article with reference arXiv:1702.07653 [34].

# Phases of cold atoms interacting via photon-mediated long-range forces

**Tim Keller**[1] **, Simon B. Jäger**[1]**, and Giovanna Morigi**[1]

[1] Theoretische Physik, Saarland University, D-66123 Saarbruecken, Germany



**Abstract.** Atoms in high-finesse optical resonators interact via the photons they multiply scatter into the cavity modes. The dynamics is characterized by dispersive and dissipative optomechanical long-range forces, which are mediated by the cavity photons, and exhibits a steady state for certain parameter regimes. In standing-wave cavities the atoms can form stable spatial gratings. Moreover, their asymptotic distribution is a Maxwell-Boltzmann whose effective temperature is controlled by the laser parameters. In this work we show that in a two-mode standing-wave cavity the stationary state possesses the same properties and phases of the Generalized Hamiltonian Mean Field model in the canonical ensemble. This model has three equilibrium phases: a paramagnetic, a nematic, and a ferromagnetic one, which here correspond to different spatial orders of the atomic gas and can be detected by means of the light emitted by the cavities. We further discuss perspectives for investigating in this setup the ensemble inequivalence predicted for the Generalized Hamiltonian Mean Field model.

## 1. Introduction

Atomic ensembles in optical resonators offer a promising platform for studying the physics of long-range interacting systems [1]. The long-range interaction here originates from multiple scattering of cavity photons, which carry the information about the positions of the scattering atoms and thus mediate an optomechanical interparticle potential [2]. In a single-mode cavity the photons are coherent over the cavity mode volume, which makes the interaction range as large as the system size. Therefore, the energy is non-additive like in gravitational and Coulomb systems in two or more dimensions [1, 3, 4].

In equilibrium statistical mechanics, consequences of non-additivity are for instance the super-linear scaling of thermodynamic quantities with the system size and the inequivalence of the statistical ensembles [4], one manifestation of which are negative specific heats in the microcanonical ensemble [4, 5, 6]. Differing from these systems, however, the dynamics of atomic gases in optical cavities is typically dissipative and non-trivial effects can only be observed if either the atoms or the cavity are pumped by light [2, 7]. The steady state, when it exists, results from the dynamical interplay between drive and losses and its properties thus depend on the drive and on the cavity parameters. It is therefore often not possible to draw a direct connection with equilibrium statistical mechanics of long-range interacting systems.

In this context it is remarkable that for some parameter regimes the dynamics of atoms' spatial selforganization in an optical resonator can be mapped to long-range interacting systems at equilibrium [2, 8, 9]. Selforganization of the atomic gas in ordered spatial patterns occurs in a single-mode standing-wave resonator when the atoms are driven by lasers whose intensity exceeds a threshold value, which depends also on the cavity decay rate [2, 8, 9, 10, 11]. By suitably tuning the laser frequency, moreover, a stationary state exists which is characterised by a Maxwell-Boltzmann distribution of the atomic momentum. In Ref. [11] it was shown that the stationary dynamics can be mapped to the one of the Hamiltonian-Mean-Field model in a canonical ensemble [4, 12] and in particular that the transition to spatial order can be described in terms of a Landau second-order phase transition. The dynamics leading to equilibrium, moreover, exhibits a slow relaxation that is due to the interplay between the conservative and dissipative cavity-mediated long-range forces [7].

In this paper we extend the model of Ref. [11] and consider a gas of cold atoms that interact with two cavity modes and are transversally driven by lasers. A possible setup is illustrated in Fig. 1. We determine the parameter regimes where the dynamics asymptotically tends to a stationary state and show that its phase diagram as a function of the lasers' and of the cavity parameters can be mapped to the one of the Generalized Hamiltonian Mean Field model (GHMF) in a canonical ensemble [13, 14, 15]. This model describes the dynamics of $N$ particles with canonically conjugated variables $p_j$, $\theta_j$ constrained on a circle that interact via competing long-range forces. In the form

studied in Ref. [13, 15] its Hamiltonian reads

$$H = \sum_j \frac{p_j^2}{2} + \frac{1}{2N} \sum_{i,j} \left(1 - \Delta \cos\theta_{ij} - (1-\Delta)\cos 2\theta_{ij}\right) , \tag{1}$$

where $\theta_{ij} = \theta_i - \theta_j \in [0, 2\pi)$ and $\Delta$ is a dimensionless parameter that can vary continuously in the interval $[0, 1]$. The phase diagram as a function of the temperature and $\Delta$ is characterised by (i) a paramagnetic, (ii) a nematic, and (iii) a ferromagnetic phase, with first and second-order transitions. In our case the phases correspond to density modulations of the atoms at different periodicity and can be detected through the light emitted by the cavity. Our motivation draws from ongoing experimental investigations [16]. Theoretical studies of this system focused on the dynamics leading to equilibrium and reported the existence of several metastable states [17]. These properties are at the basis of proposals for using these systems to simulate a quantum Hopfield associative memory scheme [18, 19]. The determination of the condition for a stationary state of the setup in Fig. 1 and the analysis of the corresponding phase diagram is the main result of the present manuscript. The mapping to the GHMF model shows that Cavity Quantum Electrodynamics (CQED) setups offer a versatile platform for studying the statistical mechanics of systems with long-range interactions.

This article is organised as follows. In Sec. 2 we introduce the physical model and sketch the derivation of a Fokker-Planck equation governing the dynamics of the atoms' external variables in the semiclassical limit. We then determine the parameters' regime for which the Fokker-Planck equation allows for a stationary state which is a Maxwell-Boltzmann distribution. In Sec. 3 we define the free energy, which we can associate to the stationary state, and introduce an appropriate thermodynamic limit. We then show that the free energy can be mapped to the one of the GHMF model. We determine the phase diagram as a function of the system's parameters and identify the observables which allow one to measure the predicted phases. In Sec. 4 we discuss possible implementations of the setup which could correspond to the realization of the microcanonical ensemble of the GHMF model, for which ensemble inequivalence has been predicted [15], and identify the parameters regimes for which it could be measured.

## 2. Semiclassical dynamics of an atomic gas in an optical cavity

The system we consider consists of a gas of $N$ cold atoms of mass $m$, whose motion is confined to occur along one dimension parallel to the unit vector $\mathbf{e}_x$. We denote by $\hat{x}_j$ and $\hat{p}_j$ the canonically conjugated position and momentum operators ($j = 1, \ldots, N$), such that $[\hat{x}_i, \hat{p}_j] = i\hbar\delta_{ij}$. The atoms experience the optomechanical forces due to the interaction with the lasers and with the quantized fields of two high-finesse cavities in the setup of Fig. 1. Specifically, the axes of the two cavities are in the $x - y$ plane, the wave vector $\mathbf{k}_1$ of cavity 1 forms an angle $\varphi$ with the $x$-axis and thus the force the atoms experience is the projection of the mechanical force along $x$, while the wave vector $\mathbf{k}_2$ of cavity 2 is parallel to $\mathbf{e}_x$. The laser fields are linearly polarised and propagate in

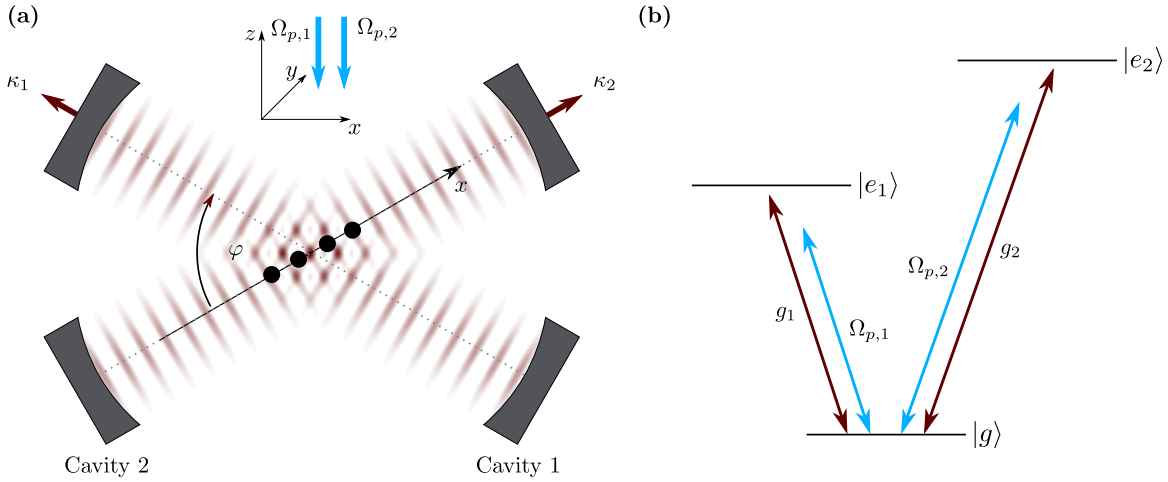


**Figure 1. (a)** A gas of cold atoms is confined to move along the $x$-axis and interacts with the modes of two optical cavities, whose wave vectors form the angle $\varphi$. The cavities emit photons at rate $\kappa_1$ and $\kappa_2$, respectively, and are pumped via coherent scattering of laser photons by the atoms. The atoms, in turn, experience the optical potential and the dissipative forces which result from the mechanical effects of the two cavity fields. Inset: Linearly-polarized lasers propagate along the direction orthogonal to the plane defined by the two cavity wave vectors. We assume that cavity 1(2) couples with the electronic transition $|g\rangle \to |e_1\rangle$ ($|g\rangle \to |e_2\rangle$), as illustrated in subplot **(b)**. The electronic transitions are also driven by the laser fields at Rabi frequency $\Omega_{p,j}$ ($j = 1, 2$). The cavity and laser fields are far-off resonance from the dipolar transition they couple to and quasi resonant with each other. In this limit the scattering is prevailingly coherent.

the direction orthogonal to the plane, they pump the cavity fields by means of coherent scattering via the atoms. The amplitude of coherent scattering, in turn, is maximal when the atoms form Bragg gratings, whose stability depends on the mechanical forces of the cavity light. As we will show, a nematic phase corresponds to a stable Bragg grating which supports the build-up of the field of only one cavity mode. In the ferromagnetic phase, instead, the atoms form stable Bragg gratings for both modes.

Below we describe the setup in detail and introduce the master equation for the density matrix $\hat{\rho}$ of atoms and cavity fields which governs the system's dynamics. We then sketch the derivation of a Fokker-Planck equation for the motion of the atoms' external degrees of freedom, which is valid when the atomic variables can be treated as semiclassical variables and the cavity fields can be eliminated from the equations of motion in a coarse-grained time scale. We finally determine the stationary state of the atoms and identify the regime in which it is a thermal state.

### *2.1. Master equation*

The state of the atoms' external degrees of freedom and of the cavity modes is described by the density operator $\hat{\rho}$, whose dynamics is governed by a Born-Markov master

equation of the form:

$$\frac{\partial}{\partial t}\hat{\rho} = \frac{1}{i\hbar}\left[\hat{H}_0, \hat{\rho}\right] - \sum_{n=1,2} \kappa_n \left(\hat{a}_n^\dagger \hat{a}_n \hat{\rho} + \hat{\rho}\hat{a}_n^\dagger \hat{a}_n - 2\hat{a}_n \hat{\rho} \hat{a}_n^\dagger\right) , \tag{2}$$

where $\hat{H}_0$ is the Hamiltonian of the system, which we introduce below, and the second term of the right-hand side describes photon emission by the cavity modes at rate $\kappa_n$ ($n = 1, 2$). Here, $\hat{a}_n^\dagger$ and $\hat{a}_n$ denote the creation and annihilation operators of a photon of the standing-wave cavity mode $n$ ($n = 1, 2$), with wave vector $\mathbf{k}_n$, frequency $\omega_{c,n} = c|\mathbf{k}_n|$, and linear polarization in the $x - y$ plane. The commutation relations are $\left[\hat{a}_i, \hat{a}_j^\dagger\right] = \delta_{ij}$.

Hamiltonian $\hat{H}_0$ describes the optomechanical coupling between atoms' degrees of freedom and cavity modes. It is an effective Hamiltonian derived in the limit where the atoms' internal degrees of freedom can be adiabatically eliminated, such that the scattering processes are coherent and the relevant parameters of the atomic internal structure is the atoms' polarizability [20]. Here, cavity mode $n$ couples with the electronic transition $|g\rangle \to |e_n\rangle$ at frequency $\omega_{a,n}$ with vacuum Rabi frequency $g_n$. We further assume that the coupling of mode 1 (2) with $|g\rangle \to |e_2\rangle$ ($|g\rangle \to |e_1\rangle$) is off-resonance by orders of magnitude and can be discarded (nonetheless, the wave numbers are assumed to be $|\mathbf{k}_1| \approx |\mathbf{k}_2| = k$). In this limit cavity $n$ is pumped by coherent scattering of the laser, which couples to the transition $|g\rangle \to |e_n\rangle$ with Rabi frequency $\Omega_{p,n}$ and frequency $\omega_{p,n}$. The condition for adiabatic elimination of the internal excited state is given by the inequality $|\omega_{a,n} - \omega_{p,n}|, |\omega_{a,n} - \omega_{c,n}| \gg \Omega_{p,n}, g_n\sqrt{\bar{n}_{c,n}}, |\Delta_n|$, where $\bar{n}_{c,n}$ is the mean intracavity photon number in cavity $n$ and $\Delta_n = \omega_{p,n} - \omega_{c,n}$ is the detuning of the laser from the cavity mode it pumps [3]. In this regime $\hat{H}_0$ reads:

$$\begin{aligned}\hat{H}_0 = \sum_{i=1}^{N} \frac{\hat{p}_i^2}{2m} - \hbar \sum_{n=1,2} \left(\Delta_n - U_n \sum_{i=1}^{N} \cos^2(k_n \hat{x}_i)\right) \hat{a}_n^\dagger \hat{a}_n \\ + \hbar \sum_{n=1,2} S_n \sum_{i=1}^{N} \cos(k_n \hat{x}_i) \left(\hat{a}_n^\dagger + \hat{a}_n\right) ,\end{aligned} \tag{3}$$

and is here reported in the frame where each atomic transition and cavity mode rotates at the corresponding laser frequency. Beside the kinetic energy of the atoms, it contains the resonators' energy, which is shifted by the dynamical Stark shift with amplitude $U_n$ induced by the coupling between cavity mode and the atoms at the position $x_i$ within the cavity spatial mode function $\cos(k_n \hat{x}_i)$. This term is also a periodic potential for the atoms whose depth is a dynamical variable. The last term on the right-hand side, finally, describes coherent scattering by the atoms between laser and cavity mode with coupling strength $S_n = g_n \Omega_{p,n}/(\omega_{p,n} - \omega_{a,n})$. It is an effective pump of the resonator whose amplitude is maximal when the atoms form Bragg gratings maximizing the expectation value of the operator $\sum_{i=1}^{N} \cos(k_n \hat{x}_i)$.

Note that in Eq. (3) we introduced the notation $k_1 \equiv |\mathbf{k}_1 \cdot \mathbf{e}_x| = k \cos\varphi$ and $k_2 \equiv |\mathbf{k}_2 \cdot \mathbf{e}_x| = k$. In the following we will set $\varphi = \pi/3$, thus $k_1 = k/2$.

*2.2. Fokker-Planck equation for the atoms' external variables*

We now discuss the assumptions at the basis of the derivation of a Fokker-Planck equation (FPE) for the dynamics of the atomic external variables. A semiclassical description of the atoms' center-of-mass motion is justified when the width $\Delta p$ of the single-atom momentum distribution is much larger than the linear momentum $\hbar k$ carried by a cavity photon $\Delta p \gg \hbar k$ [21]. In this limit it is convenient to use the Wigner function $f_{\rm tot}(\mathbf{x}, \mathbf{p}, t)$ for the atomic variables $\mathbf{x} = (x_1, \ldots, x_N)$, $\mathbf{p} = (p_1, \ldots, p_N)$:

$$f_{\rm tot}(\mathbf{x}, \mathbf{p}, t) = \int \frac{d^N y}{(2\pi\hbar)^N} \, \mathrm{e}^{-\frac{i}{\hbar}\mathbf{y}\cdot\mathbf{p}} \, \mathrm{Tr} \left\{ |\mathbf{x} - \frac{1}{2}\mathbf{y}\rangle \, \langle \mathbf{x} + \frac{1}{2}\mathbf{y}| \, \hat{\rho}(t) \right\} , \tag{4}$$

with $\mathbf{y} = (y_1, \ldots, y_N)$. We further assume that the cavity field relaxes very fast to a local steady state depending on the atomic distribution, which is verified when the inequality $k\Delta p/m \ll |\kappa_n + i\Delta_n|$ is fulfilled, namely, when the dimensionless parameter

$$\varepsilon = \frac{k\Delta p/m}{|\kappa_n + i\Delta_n|} \tag{5}$$

is small. This allows us to identify a coarse-grained time scale $\Delta t$ that is infinitesimal for the external degrees of freedom but over which the cavity degrees of freedom can be eliminated from the equations of the atomic dynamics. In particular, $f_{\rm tot}(\mathbf{x}, \mathbf{p}, t) = f(\mathbf{x}, \mathbf{p}, t) + f_{\rm na}(\mathbf{x}, \mathbf{p}, t)$, where $f(\mathbf{x}, \mathbf{p}, t)$ is the term in zero order in the retardation effect, corresponding to the cavity field following adiabatically the atomic motion, and $f_{\rm na}(\mathbf{x}, \mathbf{p}, t)$ represents the non-adiabatic corrections scaling with $\varepsilon$. The latter can be expressed in terms of $f(\mathbf{x}, \mathbf{p}, t)$ using perturbation theory [22, 23]. The derivation is lengthy but is also a straightforward extension of the derivation for a single-mode cavity, which is extensively reported in Ref. [23]. We thus refer the interested reader to this work and present here the resulting FPE, which reads

$$\begin{aligned} &\frac{\partial}{\partial t} f(\mathbf{x}, \mathbf{p}, t) + \{ f(\mathbf{x}, \mathbf{p}, t), H(\mathbf{x}, \mathbf{p}) \} = \\ &\sum_{i,j=1}^{N} \sum_{n=1,2} \frac{\partial}{\partial p_i} \left[ \sin(k_n x_i) \sin(k_n x_j) \left( D_n \frac{\partial f(\mathbf{x}, \mathbf{p}, t)}{\partial p_j} - \Gamma_n p_j f(\mathbf{x}, \mathbf{p}, t) \right) \right] \\ &+ \sum_{i,j=1}^{N} \sum_{n=1,2} \frac{\partial}{\partial p_j} \left[ \eta_n \sin(k_n x_i) \sin(k_n x_j) \frac{\partial}{\partial x_i} f(\mathbf{x}, \mathbf{p}, t) \right] . \end{aligned} \tag{6}$$

In detail, Hamiltonian (7) results from the adiabatic component of the dynamics and describes coherent long-range, two-body interactions which are mediated by the cavity photons:

$$H(\mathbf{x}, \mathbf{p}) = \sum_{i=1}^{N} \frac{p_i^2}{2m} - N \sum_{n=1,2} \gamma_n \Theta_n^2 , \tag{7}$$

where $\gamma_n$ is a scalar and

$$\Theta_1 = \frac{1}{N} \sum_{i=1}^{N} \cos(k x_i/2) \, ; \, \Theta_2 = \frac{1}{N} \sum_{i=1}^{N} \cos(k x_i) \, . \tag{8}$$

The quantities $\Theta_n$ are order parameters for spatial selforganization. In fact, they vanish for homogeneous spatial distributions, they are both different from zero when the atomic density forms spatial gratings with periodicity $4\pi/k$, while $\Theta_1 = 0$ and $\Theta_2 \neq 0$ when the spatial grating has periodicity $2\pi/k$, as illustrated in Fig. 2. The cavity mode field amplitudes $\mathcal{E}_n = \langle \hat{a}_n \rangle$, in turn, are proportional to $\Theta_n$ and in leading order in the expansion in $\varepsilon$ read [11]

$$\mathcal{E}_n = \frac{N S_n \Theta_n}{\Delta_n + i\kappa_n} \,. \tag{9}$$

The Bragg gratings can be stable provided that $\gamma_n > 0$. The sign of $\gamma_n$ is here controlled by the detuning $\Delta_n$, and hence by the frequency of the pumping laser. For later convenience we write $\gamma_n = \alpha_n/\beta_n$ with

$$\alpha_n = \frac{4N S_n^2 \Delta_n^2}{(\Delta_n^2 + \kappa_n^2)^2} \,, \tag{10}$$

$$\beta_n = \frac{-4\Delta_n}{\hbar(\Delta_n^2 + \kappa_n^2)} \,. \tag{11}$$

Friction and diffusion are instead due to retardation effects between atoms and cavity dynamics and describe cross-correlations between the atoms, which can play a relevant role in stabilizing the system in non-thermal metastable states [7]. Their coefficients take the form

$$D_n = (\hbar k_n)^2 S_n^2 \frac{\kappa_n}{\Delta_n^2 + \kappa_n^2} \,, \tag{12}$$

$$\Gamma_n = \frac{\hbar k_n^2}{m} S_n^2 \frac{4\Delta_n \kappa_n}{(\Delta_n^2 + \kappa_n^2)^2} \,, \tag{13}$$

$$\eta_n = \frac{(\hbar k_n)^2}{m} S_n^2 \frac{\kappa_n^2 - \Delta_n^2}{(\Delta_n^2 + \kappa_n^2)^2} \,, \tag{14}$$

and are here reported in the limit $|\Delta_n| \gg N U_n$, where we neglected the contribution of the dynamical Stark shift to the dynamics.

### *2.3. Existence of a stationary state*

The FPE (6) allows for a stationary solution satisfying the condition $\partial_t f_{\rm st}(\mathbf{x}, \mathbf{p}, t) = 0$. We first consider two limiting cases, in which only one cavity mode is pumped. These situations correspond to the dynamics of atoms in a single-mode standing-wave cavity investigated in Refs. [3, 11, 23, 24].

Let us first assume that $S_1 = 0$ but $S_2 \neq 0$. In this case a stationary state exists provided that $\Delta_2 < 0$ and the stationary distribution reads $f_{\rm st} = C_2 \exp(-\beta_2 H|_{\gamma_1 = 0})$, with normalization constant $C_2$ and $\beta_2 = -\frac{m\Gamma_2}{D_2}$ given in Eq. (11) ‡. Vice versa, when $S_1 \neq 0$, $S_2 = 0$, and $\Delta_1 < 0$, the stationary state is $f_{\rm st} = C_1 \exp(-\beta_1 H|_{\gamma_2 = 0})$ with $\beta_1 = -\frac{m\Gamma_1}{D_1}$ from Eq. (11).

‡ In this discussion we neglect the terms of Eq. (6) that scale with $\eta_n$. This is exact if $\Delta_n = -\kappa_n$. In general, these terms give rise to corrections to the coherent dynamics that scale with $1/N$ in the thermodynamic limit we use in Sec. 3, see Ref. [24] for details.

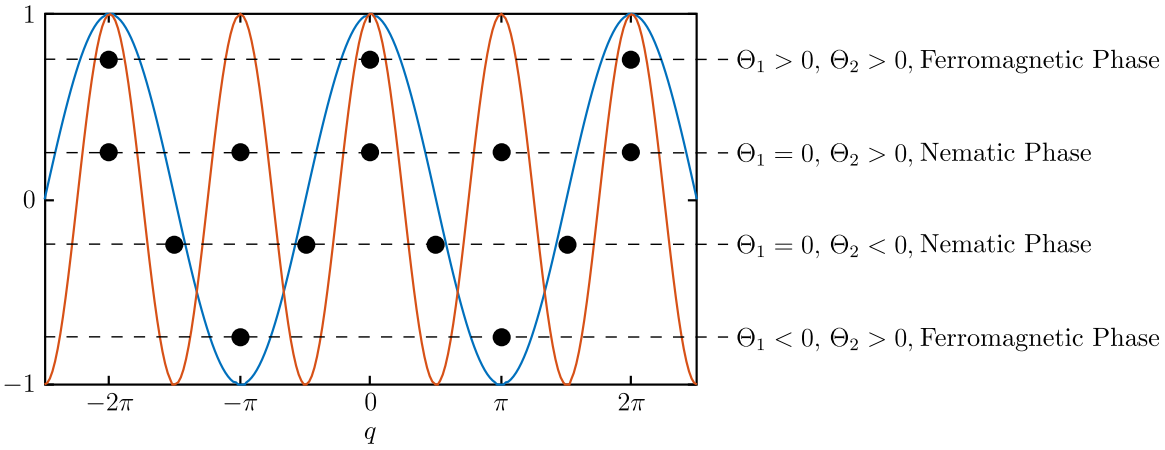


**Figure 2.** Periodic potential of cavity 1 (blue line) and cavity 2 (red line) along the $x$-axis and as a function of $q = kx/2$. The spatial configurations leading to non-vanishing values of $\Theta_1$ and/or $\Theta_2$ are illustrated by the bullet points along each horizontal line. As we show below, configurations where $\Theta_1 = 0$ while $\Theta_2 \neq 0$ correspond to the nematic phase of the GHMF. Configurations where both $\Theta_1, \Theta_2 \neq 0$ are ferromagnetic phases. Each configuration gives rise to different cavity field amplitudes and can thus be detected by monitoring the fields at the cavities' outputs.

When both resonators are pumped, a stationary solution can be found provided that $\Delta_1, \Delta_2$ are negative and $\beta_1 = \beta_2$, namely:

$$\frac{\Delta_1}{\Delta_1^2 + \kappa_1^2} = \frac{\Delta_2}{\Delta_2^2 + \kappa_2^2}\,. \tag{15}$$

This is the situation we consider in the following. In particular, $\beta_1 = \beta_2 = \beta$, where

$$\beta^{-1} = \frac{\hbar(\Delta_n^2 + \kappa_n^2)}{-4\Delta_n}\,. \tag{16}$$

The detunings and cavity loss rates thus determine an effective temperature $T_{\text{eff}} = k_B/\beta$ characterizing the stationary state. The stationary state is given by

$$f_{\text{st}} = C\exp(-\beta H)\,. \tag{17}$$

## 3. Mapping to the generalized Hamiltonian Mean Field model

We now consider the stationary state of Eq. (17) and draw a formal analogy to a canonical ensemble at equilibrium. For this purpose we define the thermodynamic limit, according to which $\alpha_n \propto NS_n^2$ is constant. This assumption warrants that the energy is extensive, it is thus equivalent to Kac scaling [4] and physically corresponds to scaling the cavity mode volume linearly with the number of particles [10, 25]. In this thermodynamic limit we obtain an explicit expression of the free energy per particle which allows us to perform a mapping of the steady state in Eq. (17) to the canonical ensemble realization of the GHMF.

We determine the free energy per particle $\mathcal{F}$ using the relation $\mathcal{F} = -\ln(Z)/(N\beta)$, where $Z$ is the "canonical" partition function and reads:

$$Z = \frac{1}{h^N}\int_0^\lambda dx_1 \ldots \int_0^\lambda dx_N \int_{-\infty}^{\infty} dp_1 \ldots \int_{-\infty}^{\infty} dp_N e^{-\beta H(\mathbf{x},\mathbf{p})}, \tag{18}$$

with $\lambda = 4\pi/k$. We integrate over the momenta $\mathbf{p}$ and apply the Hubbard-Stratonovich transformation to eliminate $\Theta_n^2(\mathbf{x})$, obtaining

$$Z = \frac{N\sqrt{\alpha_1\alpha_2}}{\pi\left(\pi\hbar\omega_r\beta\right)^{\frac{N}{2}}}\int_{-\infty}^{\infty} dy_1 \int_{-\infty}^{\infty} dy_2 \exp\left[-N\left\{\alpha_1 y_1^2 + \alpha_2 y_2^2 - \ln\left(\mathcal{I}(y_1,y_2)\right)\right\}\right] ,$$

with $q_i = kx_i/2$, $\omega_r = \hbar k^2/(2m)$, and

$$\mathcal{I}(y_1,y_2) = \int_0^{2\pi} dq \exp\left[2\left(\alpha_1 y_1 \cos(q) + \alpha_2 y_2 \cos(2q)\right)\right] . \tag{19}$$

In the thermodynamic limit $N \to \infty$ we perform a saddle-point approximation, which leads to the expression for the free energy

$$\mathcal{F}(y_1,y_2) = \frac{\ln\left(\pi\hbar\omega_{\mathrm{r}}\beta\right)}{2\beta} + \frac{1}{\beta}\inf_{y_1,y_2}\left\{\alpha_1 y_1^2 + \alpha_2 y_2^2 - \ln\left(\mathcal{I}(y_1,y_2)\right)\right\} . \tag{20}$$

This expression coincides, apart for irrelevant constants, with the mean free energy of the GHMF model in the canonical ensemble [15]. In particular, the extrema $y_n^*$ of the free energy fulfill the relation

$$y_n^* = \frac{\int_0^{2\pi} dq \cos(nq)\exp\left[2(\alpha_1 y_1^* \cos(q) + \alpha_2 y_2^* \cos(2q))\right]}{\int_0^{2\pi} dq \exp\left[2(\alpha_1 y_1^* \cos(q) + \alpha_2 y_2^* \cos(2q))\right]} , \tag{21}$$

their values lie in the interval $y_n^* \in [-1,1]$ and they can be identified with the variables $\Theta_n$: $y_n^* = \langle \cos nq \rangle$. This shows that $\Theta_1, \Theta_2$ are analogous to the magnetization in the GHMF model. By means of this mapping, moreover, we connect the lasers and cavity parameters with the dimensionless parameter $\Delta$ of the GHMF in Eq. (1): $\alpha_1/\beta \to \Delta$ and $\alpha_2/\beta \to (1-\Delta)$. Therefore, varying the lasers' amplitudes would allow one to span over the values of $\Delta$ in Eq. (1), while the effective temperature can be tuned varying the detunings $\Delta_1$ and $\Delta_2$, and thus the lasers' frequencies (provided condition (15) is fulfilled).

The phase diagram is obtained following the same analysis as in Ref. [15] and it is illustrated in Fig. 3. The system exhibits second and first order phase transitions (see Appendix A for details), which are found for the same corresponding values of the phase diagram as in Ref. [15]. The phases can be measured by monitoring the amplitude and the phase of the fields at the cavity output, since these are proportional to the order parameters $\Theta_1$ and $\Theta_2$, as visible in Eq. (9).

## 4. Discussion and outlook

The mapping of the stationary dynamics of Eq. (6) to the canonical GHMF shows that cavity QED can be a versatile platform for studying equilibrium statistical mechanics of long-range interacting systems. In this perspective it is important to identify the

*Phases of cold atoms interacting via photon-mediated long-range forces* 10

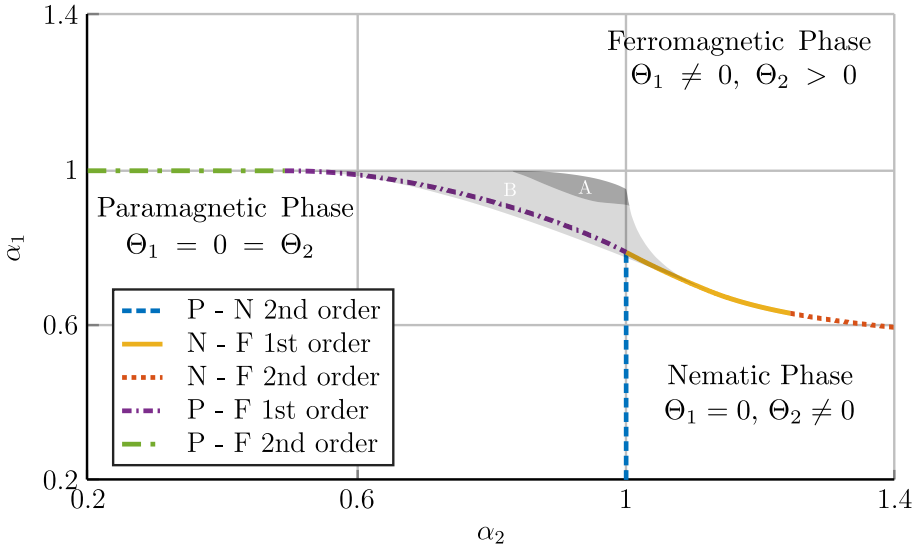


**Figure 3.** Canonical phase diagram as a function of $\alpha_1$ and $\alpha_2$. The phases are identified by numerically determining the global minima of the free energy of Eq. (20). The system shows second-order and first-order phase transitions (see inset). In the inset: P denotes paramagnetic, F ferromagnetic, and N nematic phase. The dark and light gray areas, labeled by A and B, respectively, indicate the parameter regions where ensemble inequivalence is expected. In A (B) the microcanonical ensemble exhibits three (two) phases [15].

parameter regimes for which this setup could simulate the microcanonical GHMF model. This would allow one to experimentally investigate the ensemble inequivalence that has been predicted for the GHMF [15].

Within the validity of the semiclassical description, the microcanonical GHMF could be realised in the regime where the parameter $\varepsilon$, Eq. (5), becomes smaller than the small parameter $\hbar k/\Delta p$ of the semiclassical expansion. This would require one to choose the detunings $|\Delta_n| \gg \kappa_n$ [25]. In this limit there is a well defined time scale over which the dynamics is coherent and solely dominated by Hamiltonian (7), while the right-hand side of the FPE (6), which scales with $\varepsilon$, can be discarded. Moreover, in order to prepare the system in a microcanonical ensemble, the atomic gas shall be in the asymptotic Boltzmann-Gibbs distribution of the corresponding Hamiltonian dynamics [4, 14]. By identifying the mean energy per particle in the canonical ensemble $\langle E/N\rangle = \partial(\beta\mathcal{F})/\partial\beta$ with the constant energy $\epsilon$ in the microcanonical ensemble, we obtain the relation

$$\epsilon = \frac{1}{2\beta} - \frac{1}{\beta}\left(\alpha_1\Theta_1^2 + \alpha_2\Theta_2^2\right), \tag{22}$$

which allows us to directly compare the results obtained in both ensembles. Ensemble inequivalence is predicted in the regions where the three phases meet and is indicated by the shaded area in Fig. 3. In an experimental realization it would become evident by detecting different phases in the canonical and microcanonical realizations for the same values of $\alpha_1$ and $\alpha_2$ [15]. It would be interesting to identify observables of this system which provide a measure of the specific heat, thus allowing one to determine whether it

may become negative in the microcanonical ensemble. This is an open question which we will address in future work.

The authors acknowledge discussions with Shamik Gupta, Julian Léonard, Stefan Schütz, Valentin Torggler, and Tobias Donner. This work was supported by the German Research Foundation (DFG DACH "Quantum crystals of matter and light") and by the European Commission (ITN network "ColOpt").

## Appendix A. Determination of the canonical phase diagram

For the calculation of the phase diagram in Fig. A1 we numerically calculated the global minimum of the free energy, Eq. (20), for each pair $\boldsymbol{\alpha} = (\alpha_1, \alpha_2)$. The global minimum describes a paramagnetic phase when $\Theta_1(\boldsymbol{\alpha}) = \Theta_2(\boldsymbol{\alpha}) = 0$. The phase is nematic when $\Theta_1(\boldsymbol{\alpha}) = 0$ and $\Theta_2(\boldsymbol{\alpha}) \neq 0$ and ferromagnetic when $\Theta_1, \Theta_2 \neq 0$. A phase transition occurs where the properties of the minimum change by varying $\boldsymbol{\alpha}$. The order of the transition is determined by calculating numerically the first derivatives of $\mathcal{F}(\boldsymbol{\alpha})$ with respect to $\alpha_1$ and $\alpha_2$: If they are discontinuous at the phase transition the transition is of first order, while if they are continuous the transition is of second order. This determines the phase diagram in Fig. A1.

We also checked our results by analytically calculating the Hessian matrix of the free energy, Eq. (20), at the extrema where Eq. (21) is fulfilled. We note that $\Theta_1 = \Theta_2 = 0$ is always a solution of Eq. (21). It is a minimum when the following inequalities hold:

$$\alpha_1 < 1\,, \qquad \alpha_2 < 1\,. \tag{A.1}$$

The thin black dashed line in Fig. A1 delimitates the region $\alpha_1, \alpha_2 < 1$, where the paramagnetic phase is a local minimum of the free energy. We now consider the nematic phase, set $\Theta_1 = 0$ in Eq. (21) and obtain the equation for $\Theta_2$:

$$\Theta_2 = \frac{I_1\left(2\alpha_2\Theta_2\right)}{I_0\left(2\alpha_2\Theta_2\right)}\,, \tag{A.2}$$

where $I_n(x)$ is the modified Bessel function of order $n$. The Hessian matrix is positive definite when the following inequalities are fulfilled:

$$\alpha_1 < \frac{1}{1+\Theta_2}\,, \tag{A.3}$$

$$1 < \alpha_2 < \frac{1}{1-\Theta_2^2}\,. \tag{A.4}$$

One can show that imposing $\Theta_2 \neq 0$ in Eq. (A.2) is equivalent to Eq. (A.4). Inequality (A.3) determines an upper threshold $\alpha_{1,c} = 1/(1+\Theta_2)$ on $\alpha_1$ above which the nematic configuration is no longer a minimum of the free energy. The thin black solid line in Fig. A1 shows $\alpha_{1,c}$ in the $\boldsymbol{\alpha}$-plane. Note that $\alpha_{1,c} < 1$ ($\alpha_{1,c} > 1$) for $\Theta_2 > 0$ ($\Theta_2 < 0$). In the limit $\alpha_2 \to \infty$, Eq. (A.2) delivers $\Theta_2 \to 1$ and $\Theta_2 \to -1$, giving $\alpha_{1,c} \to 1/2$ and $\alpha_{1,c} \to \infty$, respectively.

We note that the conditions we determine analytically do not overlap for all values of

$\alpha_1, \alpha_2$ with the numerically calculated phase transition lines (see Fig. A1). For instance there is an area where the inequalities (A.1) hold but the global minimum is in the ferromagnetic phase. Moreover the condition in Eq. (A.3) predicts a parameter region where the nematic phase with $\Theta_2 < 0$ is a local minimum but the global minimum is a ferromagnetic phase.

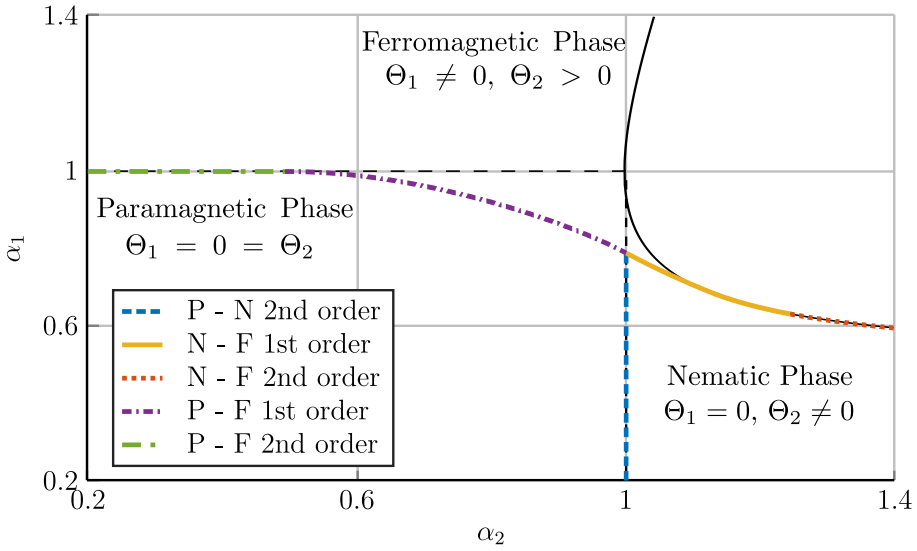


**Figure A1.** The canonical phase diagram as in Fig. 3 and the results of our analytical analysis. The dashed black lines delimitate the region determined by the inequality Eq.(A.1), where a paramagnetic phase ($\Theta_1 = 0 = \Theta_2$) is a local minimum of the free energy. The area below the solid black line (determined by the inequality Eq.(A.3) ) is the region where a nematic phase ($\Theta_1 = 0$, $\Theta_2 \neq 0$) is a local minimum of the free energy.

## References


[1] R. Bachelard, T. Manos, P. de Buyl, F. Staniscia, F. S. Cataliotti, G. De Ninno, D. Fanelli, and N. Piovella, J. Stat. Mech. (2010) P06009.
[2] H. Ritsch, P. Domokos, F. Brennecke, and T. Esslinger, Rev. Mod. Phys. **85**, 553 (2013).
[3] S. Schütz and G. Morigi, Phys. Rev. Lett. **113**, 203002 (2014).
[4] A. Campa, T. Dauxois, and S. Ruffo, Phys. Rep. **480**, 57 (2009).
[5] P.Hertel, W.Thirring, Ann. Phys. (N.Y.) **63**, 520 1971.
[6] J. Barré, D. Mukamel, and S. Ruffo, Phys. Rev. Lett. **87**, 030601 (2001).
[7] S. Schütz, S. B. Jäger, and G. Morigi, Phys. Rev. Lett. **117**, 083001 (2016).
[8] P. Domokos and H. Ritsch, Phys. Rev. Lett. **89**, 253003 (2002).
[9] A. T. Black, H. W. Chan, and V. Vuletić, Phys. Rev. Lett. **91**, 203001 (2003).
[10] J. K. Asbóth, P. Domokos, H. Ritsch, and A. Vukics, Phys. Rev. A **72**, 053417 (2005).
[11] S. Schütz, S. B. Jäger, and G. Morigi, Phys. Rev. A **92**, 063808 (2015).
[12] M. Antoni and S. Ruffo, Phys. Rev. E **52**, 2361 (1995).
[13] T. N. Teles, F. P. C. Benetti, R. Pakter, and Y. Levin, Phys. Rev. Lett. **100**, 230601 (2012).
[14] Y. Levin, R. Pakter, F. B. Rizzato, T. Teles, and F. P. C. Benetti, Phys. Rep. **535**, 1 (2014).
[15] A. Pikovsky, S. Gupta, T. N. Teles, F. P. C. Benetti, R. Pakter, Y. Levin, S. Ruffo, Phys. Rev. E, **90**, 062141 (2014).

[16] J. Léonard, A. Morales, P. Zupancic, T. Esslinger, and T. Donner, arXiv:1609.09053 (2016).
[17] S. Kraemer and H. Ritsch, Phys. Rev. A **90**, 033833 (2014).
[18] V. Torggler and H. Ritsch, Optica **1**, 336 (2014).
[19] V. Torggler, S. Kraemer, and H. Ritsch, preprint arXiv:1609.06250 (2016).
[20] A. Vukics and P. Domokos, Phys. Rev. A **72**, 031401(R) (2005).
[21] S. Stenholm, Rev. Mod. Phys. **58**, 699 (1986).
[22] J. Dalibard and C. Cohen-Tannoudji, J. Phys. B **18**, 1661 (1985).
[23] S. Schütz, H. Habibian, and G. Morigi, Phys. Rev. A **88**, 033427 (2013).
[24] S. B. Jäger, S. Schütz, and G. Morigi, Phys. Rev. A **94**, 023807 (2016).
[25] S. Fernández-Vidal, G. De Chiara, J. Larson, and G. Morigi, Phys. Rev. A **81**, 043407 (2010).

Section 2.3

# Out-of-equilibrium dynamics in self-organization

This section deals with the dynamics and relaxation of the system when it is driven across the self-organization phase transition. Every subsection starts with a reference to the peer-reviewed article and the contribution list of the authors.

## 2.3.1 Mean-field theory of atomic self-organization in optical cavities

Physical Review A **94**, 023807 (2016)

DOI: 10.1103/PhysRevA.94.023807

Authors: Simon B. Jäger, Stefan Schütz, and Giovanna Morigi

*Theoretische Physik, Universität des Saarlandes, D-66123 Saarbrücken, Germany*



**Author Contributions:**
The theoretical model was developed by all authors. Analytical calculations were performed by S. B. Jäger. Numerical simulations were performed by S. Schütz and S. B. Jäger. The results were checked and discussed by all authors. The article was written by all authors.

**Abstract:**
Photons mediate long-range optomechanical forces between atoms in high-finesse resonators, which can induce the formation of ordered spatial patterns. When a transverse laser drives the atoms, the system undergoes a second-order phase transition that separates a uniform spatial density from a Bragg grating maximizing scattering into the cavity and is controlled by the laser intensity. Starting from a Fokker-Planck equation describing the semiclassical dynamics of the N -atom distribution function, we systematically develop a mean-field model and analyze its predictions for the equilibrium and out-of-equilibrium dynamics. The validity of the mean-field model is tested by comparison with the numerical simulations of the N -body Fokker-Planck equation and by means of a Bogoliubov-Born-Green-Kirkwood-Yvon (BBGKY) hierarchy. The mean-field theory predictions well reproduce several results of the N -body Fokker-Planck equation for sufficiently short times and are in good agreement with existing theoretical approaches based on field-theoretical models. The mean field, on the other hand, predicts thermalization time scales which are at least one order of magnitude shorter than the ones predicted by the N -body dynamics. We attribute this discrepancy to the fact that the mean-field ansatz discards the effects of the long-range incoherent forces due to cavity losses.

PHYSICAL REVIEW A **94**, 023807 (2016)

# Mean-field theory of atomic self-organization in optical cavities

Simon B. Jäger, Stefan Schütz, and Giovanna Morigi
*Theoretische Physik, Universität des Saarlandes, D-66123 Saarbrücken, Germany*
(Received 16 March 2016; published 1 August 2016)

Photons mediate long-range optomechanical forces between atoms in high-finesse resonators, which can induce the formation of ordered spatial patterns. When a transverse laser drives the atoms, the system undergoes a second-order phase transition that separates a uniform spatial density from a Bragg grating maximizing scattering into the cavity and is controlled by the laser intensity. Starting from a Fokker-Planck equation describing the semiclassical dynamics of the $N$-atom distribution function, we systematically develop a mean-field model and analyze its predictions for the equilibrium and out-of-equilibrium dynamics. The validity of the mean-field model is tested by comparison with the numerical simulations of the $N$-body Fokker-Planck equation and by means of a Bogoliubov-Born-Green-Kirkwood-Yvon (BBGKY) hierarchy. The mean-field theory predictions well reproduce several results of the $N$-body Fokker-Planck equation for sufficiently short times and are in good agreement with existing theoretical approaches based on field-theoretical models. The mean field, on the other hand, predicts thermalization time scales which are at least one order of magnitude shorter than the ones predicted by the $N$-body dynamics. We attribute this discrepancy to the fact that the mean-field ansatz discards the effects of the long-range incoherent forces due to cavity losses.

DOI: 10.1103/PhysRevA.94.023807

## I. INTRODUCTION

Optically dense atomic ensembles offer a formidable framework to study collective effects induced by atom-photon interactions [1–3]. Correlations are established by multiple-photon scattering [4,5], which can give rise to phenomena such as synchronization [6,7], optomechanical bistability [8,9], and spontaneous spatial ordering [2,3,10–12]. Envisaged applications for these systems range from sensors [13] to quantum-enhanced metrology [14] and quantum simulators [12,15].

Single-mode cavities, furthermore, mediate strong long-range interactions between the atoms [16–18], similar to gravitational and Coulomb potential in two or more dimensions [19]. In view of this analogy, it is relevant to study the dynamics of these systems at and out of equilibrium to test in a laboratory conjectures and predictions, such as ensemble inequivalence and the existence of quasistationary states [16]. The realization in quantum optical setups, like the one sketched in Fig. 1(a), brings additional peculiar features. In fact, these systems are intrinsically lossy, so that nontrivial dynamics can be observed only in the presence of a pump. On the one hand, the conservative potential mediated by the cavity photons shares several analogies with the one of the Hamiltonian Mean Field model [17,19–21], of which several features are well reproduced by a mean-field description [19,20]. On the other hand, cavity losses give rise to damping and diffusion, which are characterized by a spatial structure, thus establishing long-range correlations between the atoms [17,22]. These correlations, in turn, cannot be captured by a mean-field description.

In this work we systematically develop a mean-field model for cold atoms in a standing-wave resonator in the setup illustrated in Fig. 1(a) and test its validity by comparing its predictions with the ones of the Fokker-Planck equation for the $N$-atom distribution [22]. This work completes a series of papers which analyze the equilibrium and out-of-equilibrium dynamics of spatial self-organization of atomic ensembles in a single-mode resonator. Our analysis is based on a semiclassical treatment, specifically on a Fokker-Planck equation (FPE) for the $N$-atom distribution, derived when the atoms are classically polarizable particles and their center-of-mass motion is confined to one dimension [22]. The cavity field, instead, is a full quantum variable. This makes our treatment applicable also in the shot-noise limit [22] and gives access to regimes that are complementary to those based on the model in Ref. [23], where the field is a semiclassical variable.

Our formalism permits us to consistently eliminate the cavity variables from the equations of motion of the atoms and to investigate the properties of the cavity field across the self-organization threshold, where the intracavity field is characterized by large fluctuations. Starting from this model in Ref. [21] we analyzed the stationary state of the $N$-body FPE and showed that (i) this is a thermal state whose temperature is determined by the linewidth of the resonator and (ii) the transition to self-organization is a Landau-type second-order phase transition, as illustrated in Figs. 1(b) and 1(c). In Ref. [21] we also determined the corresponding phase diagram as a function of the physical parameters and predicted the corresponding features in the light emitted by the resonator. In Ref. [24] we investigated the dynamics following sudden quenches across the phase transition and found that the interplay between long-range conservative and dissipative forces gives rise to prethermalization dynamics, where the long-range nature of dissipation plays an essential role.

In this work we derive a mean-field treatment from our $N$-atom FPE. We then benchmark the limits of validity of the mean-field ansatz by means of numerical simulations using the full $N$-body FPE and by means of a Bogoliubov-Born-Green-Kirkwood-Yvon (BBGKY) hierarchy. The results we obtain are compared with existing literature on spatial self-organization in single-mode cavities for both the semiclassical treatment [25–28] and the case in which the atomic quantum statistics is assumed to be relevant [15,28–33].

This work is organized as follows. In Sec. II the Fokker-Planck equation at the basis of our analysis is reported, and the corresponding mean-field equation is derived. In

 

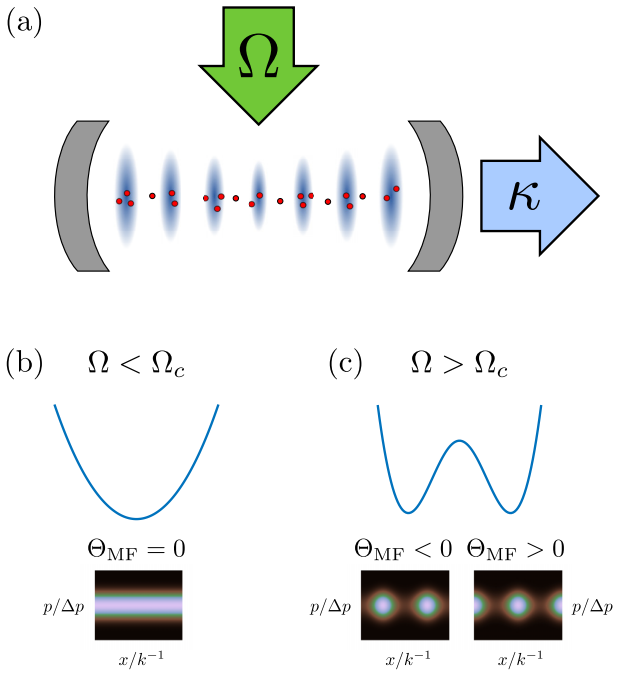


FIG. 1. (a) Atoms in a standing-wave cavity and driven by a transverse laser can spontaneously form ordered patterns when the amplitude of the laser coupling $\Omega$ exceeds a threshold value $\Omega_c$, which depends on the rate of photon losses, here due to cavity decay at rate $\kappa$. In this regime the system undergoes a second-order phase transition which is characterized by the parameter $\Theta$, indicating spatial ordering of the atoms in Bragg gratings and defined in Eq. (4). Its expectation value in the mean-field description is denoted as $\Theta_{\rm MF}$. (b) and (c) The thermodynamic potential below and above threshold. The bottom panels are schematic pictures of the single-particle density distribution $f_1(x,p)$ in phase space with $x$ in units of the inverse wave number $k^{-1}$ and $p$ in units of the width $\Delta p$ of the momentum distribution. In (b) the atomic density is uniform; in (c) it is localized at the even or odd sites of the cavity standing wave, [$\cos(kx) = 1$ or $-1$, respectively]. In this work we derive and discuss a mean-field theory for the dynamics of $f_1(x,p)$.

Sec. III the stationary properties of the mean-field FPE distribution function are analytically determined. The mean-field predictions are compared with the ones of the $N$-body FPE and with further existing theoretical works. In Sec. IV the Vlasov equation, which describes the short-time dynamics of the mean-field FPE, is derived. Its predictions are then determined by means of a stability analysis, and the analytical results are compared with the numerical simulations of the mean-field FPE. Section V reports a critical analysis of the limits of validity of the mean-field treatment. In Sec. VI the conclusions are drawn, while in the Appendix calculations are reported that complement the material presented in Sec. III.

## II. DERIVATION OF THE MEAN-FIELD MODEL

In this section we derive the mean-field model starting from the FPE describing the dynamics of an atomic ensemble in the optical potential of a high-finesse resonator of Ref. [22]. The atoms are $N$ and have mass $m$, and their motion is assumed to be confined along the $x$ axis, which also coincides with the axis of a high-finesse cavity within whose mirrors the atoms are spatially trapped. In the following we denote their canonically conjugated positions and momenta by $x_j$ and $p_j$ ($j = 1,\ldots,N$). The atomic dipole strongly couples to one cavity mode and is transversally driven by a laser, as sketched in Fig. 1(a). The parameter regime is such that the atoms coherently scatter photons into the cavity mode, and their external motion is determined by the light forces associated with these processes. The light forces are periodic, and their period is determined by the cavity-mode standing wave, whose spatial mode function is $\cos(kx)$, with $k$ being the cavity-mode wave number.

### A. Basic assumptions

Before reporting the FPE which governs the dynamics of the $N$-body distribution function, we summarize the main approximations behind its derivation and the corresponding physical parameters.

One basic assumption of our model is that the only relevant scattering processes are coherent. This regime can be reached when the cavity mode and laser frequencies are tuned far off resonance from the atomic transition [34,35]. We denote by $\Delta_a = \omega_L - \omega_0$ the detuning between laser ($\omega_L$) and atomic ($\omega_0$) frequencies and assume that this is the largest parameter of the problem. It is thus larger than the coupling strengths for the interaction between the dipole and fields. It is also larger than the detuning $\Delta_c = \omega_L - \omega_c$ between laser and cavity-mode frequencies, whose wave numbers are, to good approximation, denoted by the same parameter $k$. This allows us to eliminate the internal degrees of freedom of the atoms by a perturbative expansion in the lowest order of the small parameter $1/|\Delta_a|$.

The cavity field is treated as a quantum-mechanical variable, and the dynamics can be cast as an optomechanical coupling between atomic motion and cavity field [10,23]. The parameter regime we assume gives rise to a time-scale separation, such that the cavity degrees of freedom evolve on a faster time scale than the motion. This is warranted when the cavity linewidth $\kappa$, which determines the relaxation rate of the resonator state, is much larger than the recoil frequency $\omega_r = \hbar k^2/(2m)$, which scales the exchange of mechanical energy between light and atoms. In this limit the cavity field is eliminated from the equations of motion of the atomic external degrees of freedom in a perturbative expansion to first order in the small parameter $1/\kappa$, implementing a procedure first applied in Ref. [36]. The hierarchy of time scales is set by the inequalities $|\Delta_a| \gg \kappa \gg \omega_r$. This is also consistent with a semiclassical treatment since the kinetic energy of the atoms at steady state scales with $\hbar\kappa$, thus warranting that the width $\Delta p$ of the single-atom momentum distribution is large in comparison to the linear momentum $\hbar k$ carried by each photon [10,17,21].

### B. Collective motion of $N$ atoms in a cavity field

The approximations discussed above are at the basis of the theoretical procedure which connects the master equation of atoms in a quantized cavity field with the FPE for the Wigner function $f_N = f_N(x_1,\ldots,x_N;p_1,\ldots,p_N;t)$ describing the

positions and momenta of the $N$ atoms at time $t$. The derivation is detailed in Ref. [22], and the resulting FPE reads

$$\frac{\partial f_N}{\partial t} = -\sum_{i=1}^{N} \frac{\partial}{\partial x_i}\frac{p_i}{m} f_N + S^2 L[f_N], \tag{1}$$

where the second summand on the right-hand side (RHS) is due to mechanical effects of the cavity field on the atoms and scales like $S^2$. Here, $S = \Omega g/\Delta_a$ is the scattering amplitude between the laser and cavity mode, and it is proportional to the laser strength $\Omega$ and to the cavity vacuum Rabi frequency $g$, which scale the interaction between the dipole and laser and between the dipole and cavity, respectively. Operator $L[f_N]$ takes the form

$$S^2 L[f_N] = \frac{\partial f_N}{\partial p_i}\frac{\partial V(x_1,\ldots,x_N)}{\partial x_i} \tag{2a}$$

$$- S^2 \sum_{i,j} \frac{\partial}{\partial p_i}\Gamma_0 \sin(kx_i)\sin(kx_j) p_j f_N \tag{2b}$$

$$+ S^2 \sum_{i,j} \frac{\partial^2}{\partial p_i \partial p_j} D_0 \sin(kx_i)\sin(kx_j) f_N \tag{2c}$$

$$+ S^2 \sum_{i,j} \frac{\partial^2}{\partial p_j \partial x_i} \eta_0 \sin(kx_i)\sin(kx_j) f_N\,. \tag{2d}$$

Each line on the RHS of Eq. (2) has a physical meaning. The first term describes the dynamics due to the conservative potential

$$V(x_1,\ldots,x_N) = \frac{\hbar\Delta_c}{\kappa^2+\Delta_c^2} S^2 N^2 \Theta(x_1,\ldots,x_N)^2, \tag{3}$$

where

$$\Theta(x_1,\ldots,x_N) = \frac{1}{N}\sum_{j=1}^{N}\cos(kx_j), \tag{4}$$

so that the potential mediates long-range interactions between the atoms. Parameter $\langle|\Theta|\rangle_N$ is the order parameter of self-organization, where $\langle\cdot\rangle_N$ denotes the expectation value taken over the normalized distribution $f_N$. Specifically, when the atoms form Bragg grating, then $\langle|\Theta|\rangle_N \to 1$, and the potential depth is maximal. When the atoms are instead uniformly distributed in space, then $\langle|\Theta|\rangle_N \simeq 0$, and the potential vanishes. We note that the Bragg gratings minimize the potential when $\Delta_c < 0$; otherwise, the uniform distribution is energetically favored. We will here denote $\langle|\Theta|\rangle_N$ by magnetization due to the mapping of the self-organization transition to a ferromagnetic model [21].

For later convenience, we define the parameter

$$F_0 = (\hbar k)\frac{2\Delta_c}{\kappa^2+\Delta_c^2}, \tag{5}$$

such that $V = F_0(NS\Theta)^2/(2k)$.

The second term on the RHS [Eq. (2b)] describes a dissipative force and is scaled by the coefficient $\Gamma_0$:

$$\Gamma_0 = \omega_r \frac{8\Delta_c\kappa}{\left(\kappa^2+\Delta_c^2\right)^2}\,. \tag{6}$$

This term is due to nonadiabatic corrections in the dynamics of the cavity field.

The term in (2c) corresponds to diffusion due to fluctuations of the cavity field associated with losses. The diffusion matrix is the dyadic product of the vector $(\sin(kx_1),\ldots,\sin(kx_N))$ with itself and scales with the coefficient

$$D_0 = (\hbar k)^2 \frac{\kappa}{\kappa^2+\Delta_c^2}. \tag{7}$$

Therefore, besides the diffusion due to the diagonal elements, which is a single-particle effect, we also expect that term (2c) establishes long-range correlations.

The last line, (2d), contains cross derivatives and scales with the coefficient

$$\eta_0 = 2\hbar\omega_r \frac{\kappa^2-\Delta_c^2}{\left(\kappa^2+\Delta_c^2\right)^2}, \tag{8}$$

whose sign depends on whether the ratio $|\Delta_c/\kappa|$ is smaller or larger than unity, while it vanishes for $|\Delta_c/\kappa| = 1$. An analogous term has also been reported in the semiclassical description of cold atoms in optical lattices [36], where it has been neglected under the assumption of uniform spatial densities. Such an assumption cannot be applied in the self-organized regime; nevertheless, we will show that this term can be consistently discarded in the thermodynamic limit we apply, which warrants Kac's scaling [19].

### C. Mean-field ansatz

To derive a mean-field FPE we assume that the Wigner function is factorized into single-particle distribution functions according to the prescription

$$f_N(x_1,\ldots,x_N;p_1,\ldots,p_N;t) = \prod_{i=1}^{N} f_1(x_i,p_i;t), \tag{9}$$

where $f_1(x_i,p_i;t)$ denotes the distribution for particle $i$ at time $t$ and is thus defined on the phase space of this particle. We use then Eq. (9) in the FPE (1) and integrate out all particles' variables but one. In this way we derive the mean-field FPE, which reads

$$\frac{\partial f_1}{\partial t} = -\frac{\partial}{\partial x}\frac{p}{m} f_1 + S^2 \mathfrak{L}[f_1] \tag{10}$$

and has same structure as the FPE in Eq. (1). Operator $\mathfrak{L}$ describes, as $L$, the mechanical effects of light. However, it is now a nonlinear operator of $f_1$ and takes the form

$$\mathfrak{L}[f_1] = -\frac{\partial}{\partial p} F_0\{\cos(kx) + (N-1)\Theta_{\mathrm{MF}}[f_1]\}\sin(kx) f_1 \tag{11a}$$

$$- \frac{\partial}{\partial p}\Gamma_0\{\sin(kx)p + (N-1)\Xi_{\mathrm{MF}}[f_1]\}\sin(kx) f_1 \tag{11b}$$

$$+ \frac{\partial^2}{\partial^2 p} D_0 \sin^2(kx) f_1 \tag{11c}$$

$$+ \frac{\partial^2}{\partial p \partial x}\eta_0 \sin^2(kx) f_1, \tag{11d}$$

where we have introduced the functionals

$$\Theta_{\rm MF}[f_1] = \frac{1}{\lambda}\int_0^\lambda dx \int_{-\infty}^{\infty} dp\, \cos(kx) f_1, \tag{12}$$

$$\Xi_{\rm MF}[f_1] = \frac{1}{\lambda}\int_0^\lambda dx \int_{-\infty}^{\infty} dp\, \sin(kx) p f_1. \tag{13}$$

The mean-field order parameter $\Theta_{\rm MF}$ is the expectation value $\langle\cos(kx)\rangle$, where $\langle\cdot\rangle$ indicates the average taken over the single-particle distribution function $f_1(x,p)$. The terms on the RHS in (11a) and (11b) have a different origin but a similar structure, which can be recognized by analyzing the form of the two summands within the respective inner brackets. The first summand in each line describes the interaction of the atom with itself, mediated by the cavity field. The second summand in each line emerges from the interaction between the atom and all other $N-1$ atoms.

We further notice that the term in (11a) can be cast in terms of a conservative force originating from the potential

$$V_1[f_1](x) = \frac{F_0}{2k} S^2[\cos^2(kx) + 2(N-1)\Theta_{\rm MF}[f_1]\cos(kx)] + \frac{\Gamma_0}{k}(N-1)S^2\Xi_{\rm MF}[f_1]\cos(kx) \tag{14}$$

and contains a term whose corresponding term in Eq. (1) has dissipative nature [see (2b)]. Using this result, we can rewrite Eq. (11) in the compact form

$$\mathfrak{L}[f_1] = \frac{\partial V_1}{\partial x}\frac{\partial f_1}{\partial p} - \frac{\partial}{\partial p}\left(\Gamma_0 p - \frac{\partial}{\partial p}D_0 - \frac{\partial}{\partial x}\eta_0\right)\sin^2(kx) f_1,$$

which allows us to simply read out the physical meaning of the other terms; they are, in fact, the diagonal component of friction, diffusion, and the cross-derivative term in Eq. (1).

## III. STATIONARY STATE OF THE MEAN-FIELD EQUATION

The stationary properties of the mean-field distribution are analyzed by means of the single-particle distribution $f_{\rm st}(x,p)$ that solves Eq. (10) with

$$\partial_t f_{\rm st}(x,p) = 0. \tag{15}$$

In the following we determine $f_{\rm st}(x,p)$ and then analyze its predictions for relevant physical quantities.

### A. Derivation of the steady-state solution

In order to solve Eq. (15) we consider the ansatz

$$f_{\rm st}(x,p) = f_0 \exp[a(x) + b(p)],$$

where $a(x)$ and $b(p)$ are functions which depend only on position and momentum, respectively, and $f_0$ is the normalization constant. Using this ansatz in Eq. (10), we obtain differential equations for $a(x)$ and $b(p)$, whose solutions read $b(p) = -\beta p^2/(2m)$ and

$$a(x) = (Y/2-1)\ln[1+Z\sin^2(kx)] - (N-1)Y\Theta_{\rm MF}[f_{\rm st}] \times \sqrt{\frac{Z}{1+Z}}\,\mathrm{arctanh}\left(\sqrt{\frac{Z}{1+Z}}\cos(kx)\right), \tag{16}$$

with $Y = F_0/(k\eta_0)$, $Z = \beta\eta_0 S^2$, and

$$\beta = -\frac{\Gamma_0 m}{D_0} = \frac{-4\Delta_c}{\hbar(\kappa^2+\Delta_c^2)}. \tag{17}$$

Therefore,

$$f_{\rm st}(x,p) = \mathcal{F}(\cos kx)\exp\left(-\beta\frac{p^2}{2m}\right), \tag{18}$$

with $\mathcal{F}(\cos kx) = f_0\exp[a(x)]$. Equation (18) describes a thermal distribution provided that $\Delta_c < 0$: In this limit parameter $\beta$, Eq. (17), plays the role of an inverse temperature at steady state. This temperature coincides with the value found by solving the steady state of the $N$-body FPE, Eq. (1), as shown in Refs. [17,21].

We note that the function $\mathcal{F}(\cos kx)$ depends on $\Theta_{\rm MF}[f_{\rm st}]$, which leads to the fixed-point equation

$$\Theta_{\rm MF} \equiv \langle\cos(kx)\rangle = \sqrt{\frac{2\pi m}{\beta}}\frac{1}{\lambda}\int_0^\lambda dx\cos(kx)\mathcal{F}(\cos kx). \tag{19}$$

Its solution is, in general, not transparent, but it gets simpler in an appropriately defined thermodynamic limit. This consists of scaling the coupling strength $g \sim 1/\sqrt{N}$ as the number of atoms is increased, leading to the scaling relation $S \propto 1/\sqrt{N}$ [37,38]. In this limit function $a(x)$, Eq. (16), can be cast into the form

$$a(x) = 2\frac{\bar{n}}{\bar{n}_c}\Theta_{\rm MF}\cos(kx), \tag{20}$$

with

$$\bar{n} = \frac{NS^2}{\kappa^2+\Delta_c^2} \tag{21}$$

and

$$\bar{n}_c = \frac{\kappa^2+\Delta_c^2}{4\Delta_c^2}. \tag{22}$$

This leads to a compact form of the stationary distribution in the mean-field limit:

$$f_{\rm st}(x,p) = f_0\exp\left[-\beta\left(\frac{p^2}{2m} + \hbar\Delta_c\bar{n}\Theta_{\rm MF}\cos(kx)\right)\right], \tag{23}$$

with

$$f_0^{-1} = \sqrt{\frac{2m\pi}{\beta}} I_0\left(2\frac{\bar{n}}{\bar{n}_c}\Theta_{\rm MF}\right),$$

where $I_j$ is the modified Bessel function of $j$th order [39].

We thus see that in the thermodynamic limit the effect of the cross derivatives vanishes. For finite $N$, parameter $\eta_0$ is small but finite, and in the stationary state it gives rise to a correction to the effective potential term, as seen in Eq. (16).

### B. Stationary properties in the thermodynamic limit

The mean-field distribution, Eq. (23), allows one to analytically determine several properties of the steady state. First, functional $\Theta_{\rm MF}$ in the exponent has to be determined

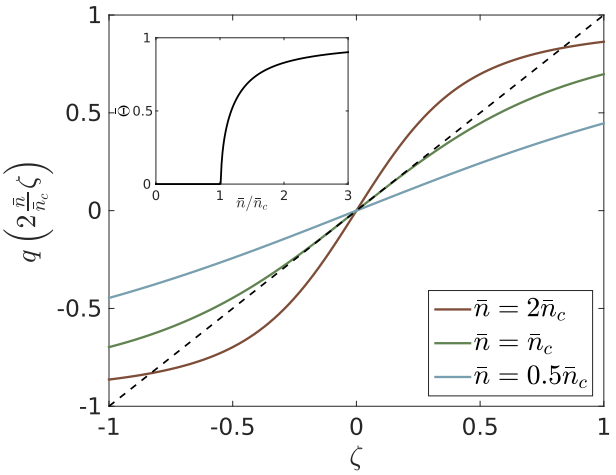


FIG. 2. Plot of $q(2\bar{n}\zeta/\bar{n}_c)$, Eq. (25), as a function of $\zeta$ and for different values of $\bar{n}$. The intersection points with the curve $y = \zeta$ (dashed line) give the solutions of Eq. (24). Stable points are at the crossing where $q' < \bar{n}_c/(2\bar{n})$ and are the equilibrium values of the order parameter $\Theta_{\rm MF}$. Inset: The resulting stable solution $\bar{\Theta} \geqslant 0$ as a function of $\bar{n}$ (in units of $\bar{n}_c$).

self-consistently. Using Eq. (20) in Eq. (19) gives the relation

$$\Theta_{\rm MF} = q\left(2\frac{\bar{n}}{\bar{n}_c}\Theta_{\rm MF}\right), \tag{24}$$

where $q$ is a function of the form

$$q\left(2\frac{\bar{n}}{\bar{n}_c}\zeta\right) = \frac{I_1\left(2\frac{\bar{n}}{\bar{n}_c}\zeta\right)}{I_0\left(2\frac{\bar{n}}{\bar{n}_c}\zeta\right)} \tag{25}$$

and is plotted in Fig. 2 for values of $\bar{n}$ below, at, and above $\bar{n}_c$. The solutions of Eq. (24) are the crossing between the curve $y = \zeta$ and $y = q(2\bar{n}\zeta/\bar{n}_c)$ [see Eq. (25)]. For $\bar{n} < \bar{n}_c$ this equation allows for one solution, corresponding to $\Theta_{\rm MF} = 0$. For $\bar{n} > \bar{n}_c$, there are three solutions, two of which are stable and one of which is unstable. The stable solutions give $\Theta_{\rm MF} = \pm\bar{\Theta}$, with $0 \leqslant \bar{\Theta} < 1$, and correspond to the self-organized state. Close to, but above, the critical point the value $\bar{\Theta}$ can be analytically determined and reads

$$\bar{\Theta} = \sqrt{2(\bar{n}/\bar{n}_c - 1)}. \tag{26}$$

The value $\bar{n} = \bar{n}_c$, with $\bar{n}_c$ defined in Eq. (22), hence determines a critical point at which the transition to self-organization occurs and that is controlled by the detuning from the cavity field and the cavity loss rate for the thermodynamic limit we chose. The results we have obtained so far for the stationary mean-field distribution are in full agreement with the ones found for the stationary distribution of Eq. (1) (see Ref. [21]). The stationary mean-field distribution in Eq. (23) corresponds to the one that is found from the stationary $N$-particle distribution after integrating out the other $N-1$ position and momentum variables and then taking the thermodynamic limit. The equation for the order parameter, Eq. (24), agrees with the one obtained for the $N$-particle case and obtained by means of a saddle-point approximation. This agreement is found also for the critical value of Eq. (22) and for the temperature of Eq. (17). Hence, the mean-field model predicts the same phase diagram as the $N$-body FPE.

It is also instructive to consider the value of the bunching parameter $\mathcal{B}$ as a function of $\bar{n}$. This is defined as

$$\mathcal{B} = \langle \cos^2(kx) \rangle \tag{27}$$

and gives a measure of localization of the particles at the minima of the mechanical potential [21,25]. Using Eq. (20), we obtain

$$\mathcal{B} = \begin{cases} 1/2, & \bar{n} \leqslant \bar{n}_c, \\ 1 - \bar{n}_c/(2\bar{n}), & \bar{n} > \bar{n}_c, \end{cases} \tag{28}$$

in the stationary state. Therefore, below threshold the atoms are uniformly distributed, while above threshold they increasingly localize at the minima of the Bragg potential. In particular, when the atoms are tightly bound at the minima, the above-threshold expression in Eq. (28) delivers the amplitude of the fluctuations, namely,

$$k^2\langle x^2 \rangle \approx \frac{\bar{n}_c}{2\bar{n}}, \tag{29}$$

showing that these are inversely proportional to the laser intensity.

### C. Comparison with existing literature

The results obtained so far by means of the mean-field model show a remarkable agreement with the predictions of the stationary solution of the $N$-particle FPE, Eq. (1). It is further worthwhile to compare the results derived here with the results obtained in the literature by means of different approaches.

We first discuss Ref. [25], where, among other studies, a mean-field approach is developed based on plausible conjectures. Here, the mean-field potential is calculated, and the threshold of self-organization is determined by (i) assuming that the stationary state is thermal, with temperature given by the linewidth of the cavity, and (ii) performing a stability analysis of the uniform density distribution. By means of this study a threshold value for self-organization is identified, which agrees with the prediction in Eq. (22), which becomes evident after defining the threshold amplitude $S_c$ such that

$$\frac{N S_c^2}{\Delta_c^2 + \kappa^2} \equiv \bar{n}_c.$$

In particular, the quantity $\eta^*$ in [25] is in our notations $S_c\Delta_a/g$ calculated for the case $\Delta_c = -\kappa$.

The stationary state of self-organization was first derived in Refs. [26,27] by means of a FPE as a function of the atomic and field variables. This description assumes that the field fluctuations are small and thus cannot reliably reproduce the field correlation functions below and at threshold. It predicts, nevertheless, that the atoms' steady state is thermal and its temperature coincides with the inverse of Eq. (17), apart from corrections of the order $\omega_r/\kappa$ that are systematically neglected in our approach because they are of higher order. It further predicts the same behavior of the order parameter as in Eq. (26) above, but close to, the threshold.

It is also interesting to compare our results with a series of other theoretical studies which focus on self-organization of

ultracold atomic ensembles in cavities but discard retardation effects: In these works only the conservative part of the cavity potential is considered, while the temperature at steady state is due to the coupling to an external heat bath [15,28–33]. Even though the conditions seem quite different from our case, remarkable agreement is found in the appropriate limits. References [15,29] analyze the self-organization transition of an ultracold gas of bosonic atoms and derive the mapping to the Dicke model. Here, the recoil energy plays a role analogous to the temperature, and the threshold which is derived agrees with the threshold in Eq. (22) after setting

$$NS_c^2 = \frac{1}{\beta}\frac{\kappa^2+\Delta_c^2}{-\Delta_c}, \tag{30}$$

with $\beta = 4/\hbar\omega_r$. By means of this prescription, the threshold also agrees with the one calculated in Ref. [28]. Furthermore, it also coincides with the one evaluated in Ref. [33] when using the Boltzmann distribution for the atoms statistics.

Another quantity which has been determined in these works is the photon flux, which corresponds to the intracavity photon number in our treatment. In Refs. [28–31] the photon flux scales as $1/|\bar{n}-\bar{n}_c|$ below threshold, while at threshold it diverges as $\sqrt{N}$. These predictions are in perfect agreement with the results we find when taking the stationary distribution of Eq. (1) [see Eqs. (A4) and (A5)]. In particular, the intracavity photon number at threshold, Eq. (A5), coincides with the one calculated in Ref. [28] after substituting in their equation $\omega_z = (\omega_0^2+\kappa^2)/\omega_0$ for the temperature, with $\omega_0 = -\Delta_c$. The result for the intensity-intensity correlations at zero time delay and below threshold, Eq. (A11), further agrees with the result derived in Refs. [30,31].

## IV. MEAN-FIELD DYNAMICS

We now study the dynamics predicted by the mean-field FPE. We focus on the Vlasov equation, which we derive from Eq. (10) by taking the thermodynamic limit, according to our prescription. The Vlasov equation for our problem reads

$$\frac{\partial f_1}{\partial t} + \frac{p}{m}\frac{\partial f_1}{\partial x_1} - \frac{\partial V_0[f_1](x)}{\partial x}\frac{\partial f_1}{\partial p} = 0, \tag{31}$$

with

$$V_0[f_1](x) = 2\hbar\Delta_c\bar{n}\cos(kx)\Theta_{\rm MF}[f_1] - \frac{\hbar^2 k}{m}\bar{n}\beta\kappa\cos(kx)\Xi_{\rm MF}[f_1], \tag{32}$$

and it corresponds to the potential in Eq. (14) after neglecting the self-reaction term, which is of order $1/N$. Therefore, the validity of the predictions we will extract is limited to sufficiently short time scales for which the corrections can be discarded. We will quantify this statement in the next section.

### A. Preliminary considerations: Energy conservation

We first analyze whether Eq. (31) warrants energy conservation. We consider a class of functions for which $\Xi_{\rm MF}[f_1] = 0$. This includes the stationary solution of Eq. (23). For these solutions, the energy of one particle takes the form

$$\epsilon(t) = \frac{\langle p^2\rangle}{2m} + \hbar\Delta_c\bar{n}\Theta_{\rm MF}^2. \tag{33}$$

In order to determine $\dot{\epsilon}(t)$ we thus calculate $\dot{\Theta}_{\rm MF}$ and $\langle\dot{p^2}\rangle$. This gives

$$\dot{\Theta}_{\rm MF} = -\frac{k}{m}\Xi_{\rm MF},$$
$$\frac{\langle\dot{p^2}\rangle}{2m} = 2\frac{\hbar}{m}\bar{n}(k\Delta_c\Theta_{\rm MF} - \omega_r\kappa\beta\Xi_{\rm MF})\Xi_{\rm MF},$$

and therefore, we get for the derivative of the energy

$$\dot{\epsilon} = -2\frac{\hbar}{m}\bar{n}\omega_r\kappa\beta\Xi_{\rm MF}^2.$$

These derivatives hence vanish when $\Xi_{\rm MF} = 0$, and thus, for the class of distribution fulfilling this condition, energy, with the potential term given in Eq. (33), is conserved. Fluctuations, on the other hand, can give rise to finite values of $\Xi_{\rm MF}$. The purpose of the next section is to analyze the stability and short-time dynamics of solutions of the Vlasov equation, Eq. (31), after quenches of the laser parameters.

### B. Stability analysis of spatially homogeneous distributions

We now analyze the short-time dynamics described by Eq. (31), assuming that at $t = 0$ the distribution is thermal and has uniform spatial density; thus, $f_1(x,p,0) = f_1(p,0)$ and $\Theta_{\rm MF}|_{t=0^-} = 0$, with

$$f_1(p,0) = \left(\frac{2m\pi}{\beta_0}\right)^{-\frac{1}{2}}\exp\left(-\beta_0\frac{p^2}{2m}\right), \tag{34}$$

where $\beta_0$ is the inverse temperature. This distribution is a stable solution of the Vlasov equation after setting $\bar{n} = 0$. At $t = 0$ the laser strength is quenched above threshold, so that parameter $\bar{n}$ takes a finite value larger than $\bar{n}_c$. We then let evolve the distribution of Eq. (34) by taking this value $\bar{n}$ in Eq. (31). Figure 3 shows the results of the numerical integration of Eq. (31) for different values of $\bar{n}$. We analyze these results, keeping in mind that they are strictly valid for short times since the Vlasov equation discards effects, such as diffusion, which are crucial in determining the stationary state. In Fig. 3(a) the order parameter evolves from zero to a finite value, about which it oscillates. This value is smaller than the one predicted by the stationary solution of the mean-field FPE. It is reached after an initial dynamics characterized by an exponential increase, whose slope is steeper the larger $\bar{n}$ is. Figures 3(b) and 3(c) display the corresponding evolution of the quantities $\Xi_{\rm MF}^2$ [see Eq. (13)]. This quantity emerges from the retardation effects of the dynamics; it is thus a signature of memory effects and mathematically corresponds to the buildup correlations between momentum and position that cannot be factorized. The initial distribution, Eq. (34), is chosen so that $\Xi_{\rm MF} = 0$, and we observe that the dynamics give rise to a buildup of a finite value of $\Xi_{\rm MF}^2$, with an exponential increase that leads to a maximum where the curve for $\Theta_{\rm MF}$ reaches the plateau. Then, it oscillates like $\Theta_{\rm MF}$ (one can well understand the behavior of these oscillations observing that $\Xi_{\rm MF}$ is proportional to the time derivative of $\Theta_{\rm MF}$) and is exponentially damped to zero. In the initial phase, the exponential growth of $\Xi_{\rm MF}^2$ increases with $\bar{n}$; as in the second phase of the dynamics, where $\Theta_{\rm MF}$ oscillates about a finite mean value, the amplitude of the oscillations of $\Xi_{\rm MF}^2$ is also larger the larger $\bar{n}$ is.

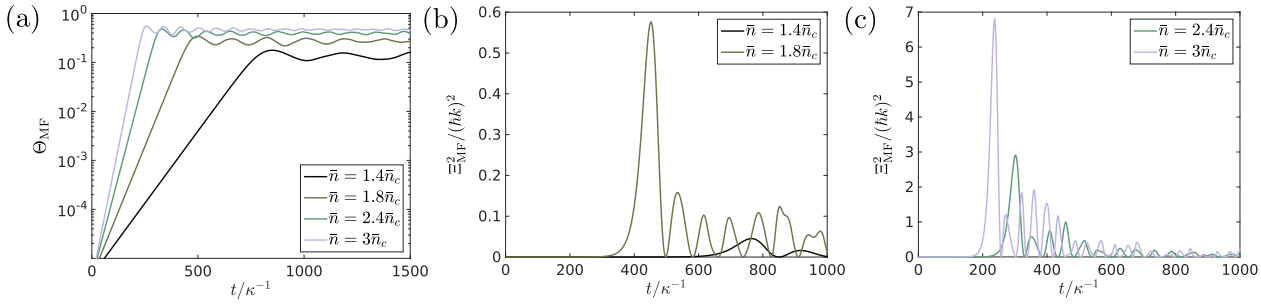


FIG. 3. Time evolution of (a) the order parameter $\Theta_{\rm MF}$, Eq. (12), and (b) and (c) parameter $\Xi^2_{\rm MF}$, Eq. (13), calculated by numerical integration of the Vlasov equation (31) for different values of $\bar{n}$ and for $\Delta_c = -\kappa$. The initial distribution is given in Eq. (34) with $\beta_0 = 2/(\hbar\kappa)$.

We now analyze the initial exponential increase, which is in the regime where the Vlasov equation is a reliable approximation of the full dynamics, as we also verified in Ref. [24]. In order to do so, we use a standard procedure, which is also detailed in Refs. [19,40]. For short times $t$ after the quench, we write the distribution as

$$f_1(x,p,t) = f_1(p,0) + \delta f_1(x,p,t), \tag{35}$$

where $\delta f_1$ describes small fluctuations which can be due to the finite size of the system and thus scale with $1/\sqrt{N}$. Using Eq. (35) in the Vlasov equation (31) and neglecting the terms of order $1/N$, we obtain the linearized Vlasov equation

$$\frac{\partial \delta f_1}{\partial t} + \frac{p}{m}\frac{\partial \delta f_1}{\partial x} - \frac{\partial \delta V}{\partial x}\frac{\partial f_1(p,0)}{\partial p} = 0, \tag{36}$$

where $\delta V = V[\delta f_1(x,p,t)]$ and we dropped the argument of function $\delta f_1$. We look for solutions of Eq. (36) by means of the ansatz of Fourier waves with frequency $\omega$ and wave number $k$:

$$\delta f_1 = g_1(p)e^{i(\omega t - kx)} + g_{-1}(p)e^{i(\omega t + kx)}, \tag{37}$$

$$\delta V = 2A\cos(kx)e^{i\omega t}, \tag{38}$$

where $A \propto 1/\sqrt{N}$ is some constant and the amplitudes $g_1(p)$ and $g_{-1}(p)$ are sole functions of the momentum $p$. The dispersion relation $\omega = \omega(k)$ can be derived after using Eqs. (37) and (38) in the linearized Vlasov equation (36). By equating the coefficients of $\exp(ikx)$ and $\exp(-ikx)$ we get expressions for the functions $g_1(p)$ and $g_{-1}(p)$. With those expressions one finds the dispersion relation by using the definition $\delta V = V[\delta f_1]$ and Eqs. (32) and (38):

$$0 = 1 + \left(\hbar\Delta_c + i\frac{\hbar\kappa}{2}\hbar\omega\beta\right)\bar{n}\frac{1}{2} \times \int_{-\infty}^{\infty} dp \left(\frac{-k}{\frac{pk}{m}+\omega} + \frac{-k}{\frac{pk}{m}-\omega}\right)\partial_p f_1(p,0). \tag{39}$$

This relation holds for any initial distribution that describes a uniform spatial density. We now use the Gaussian distribution in Eq. (34) and obtain

$$0 = 1 + \left(\hbar\Delta_c + i\frac{\hbar\kappa}{2}\hbar\omega\beta\right)\bar{n}\beta_0 \times \left[1 - \bar{a}\exp(-\bar{a}^2)\left(i\sqrt{\pi} - 2\int_0^{\bar{a}} du\exp(u^2)\right)\right], \tag{40}$$

where we defined $\bar{a} = \sqrt{\beta_0/(2m)}(m\omega/k)$. We then introduce $\bar{b} = i\bar{a}$ and

$$\gamma = i\omega$$

and cast Eq. (40) in the form

$$0 = 1 + \left(\hbar\Delta_c + \frac{\hbar\kappa}{2}\hbar\gamma\beta\right)\bar{n}\beta_0 \times \left[1 - \bar{b}\exp(\bar{b}^2)\left(\sqrt{\pi} - \int_{-\bar{b}}^{\bar{b}} du\exp(-u^2)\right)\right], \tag{41}$$

where $\bar{b} \propto \gamma$. It can be shown that parameter $\gamma$, which solves Eq. (41), is a real number. Therefore, $\omega$ is an imaginary number. In particular, if $\gamma < 0$, both Eqs. (37) and (38) describe fluctuations which are exponentially damped, and therefore, $f_1(x,p,t)$ will tend to the initial distribution, which is stable. If, instead, the solution of Eq. (40) gives $\gamma > 0$, the initial distribution is unstable against fluctuations. The value $\gamma = 0$ separates the two regimes. After setting $\gamma = 0$ in Eq. (41), we thus get the critical condition

$$1 = -\hbar\Delta_c\bar{n}\beta_0, \tag{42}$$

which connects $\Delta_c$, $\bar{n}$, and the initial temperature $1/\beta_0$, which is an external parameter. If $\beta_0$ coincides with the value in Eq. (17), then Eq. (42) corresponds to the same relation as in Eq. (22), which defines the critical value of $\bar{n}$ for self-organization. For the values of the parameters for which $\gamma > 0$, the uniform distribution is unstable and tends to form a grating at the wave vector $k$ of the resonator with exponential increase, giving rise to a violent relaxation. Parameter $\gamma$ gives the rate at which the amplitude of this density modulation grows.

Figure 4 compares the value of $\gamma$ extracted by fitting the exponential increase of $\Theta_{\rm MF}$ in the first phase of the dynamics of Fig. 3 and for different values of $\bar{n}$ with the one determined by Eq. (41), showing very good agreement. In particular, we note that in the limit $|\Delta_c| \gg |\gamma|$, Eq. (41) can be reduced to the form [41]

$$\gamma = \omega_0(1 - p\chi)\frac{\ln\left(\frac{\chi}{1.135}\right) - \ln(1-p\chi)}{1.4(1-p\chi) + \hbar\kappa\beta\omega_0/(2|\Delta_c|)}, \tag{43}$$

with $\chi = \hbar|\Delta_c|\bar{n}\beta_0 = (\bar{n}/\bar{n}_c)(\beta_0/\beta)$, $\omega_0 = \sqrt{2\omega_r/(\hbar\beta_0)}$, and $p = 27/227$.

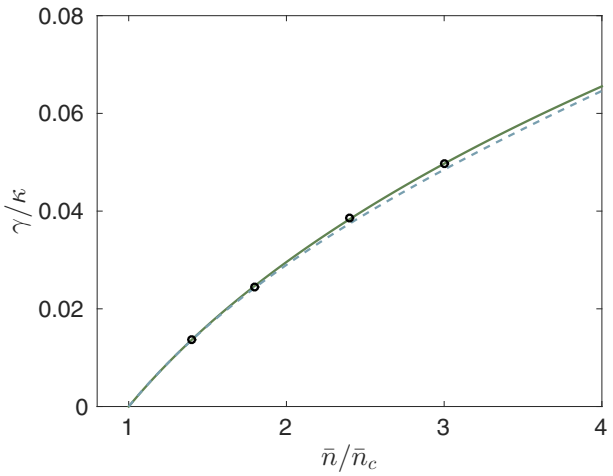


FIG. 4. Slope $\gamma$ of the initial increase of $\Theta_{\rm MF}$. The dots are extracted by fitting the curve obtained from the numerical simulations in Fig. 3, the dashed line is the value predicted by Eq. (43), which agrees well with Eq. (41) (solid line). For these parameters the threshold for the Vlasov stability, Eq. (42), reads $1 = \bar{n}/\bar{n}_c$.

## V. VALIDITY OF THE MEAN-FIELD ANSATZ

The mean-field treatment is based on the assumption that the distribution function for the $N$ particles can be approximated by the product of the single-particle distribution. This ansatz thus discards interparticle correlations which emerge from the photon-mediated interactions: the factorized ansatz is very different from the form of the distributions one obtains from the full $N$-particle FPE [17,21]. Nevertheless, the assumption still captures essential features of the short-time dynamics of distributions, which initially have the form of Eq. (9). We will follow the procedure illustrated in Refs. [19,42] and study the validity of the mean-field ansatz within a BBGKY hierarchy, which we derive from the $N$-particle FPE, Eq. (1). We will particularly focus on the dynamics of two-particle correlations and determine the characteristic time scale of their dynamics.

For convenience, we introduce the vectors $\mathbf{x} = (x_1,\ldots,x_N)^T$ and $\mathbf{p} = (p_1,\ldots,p_N)^T$, and define $f_N(\mathbf{x};\mathbf{p};t) \equiv f_N(x_1,\ldots,x_N;p_1,\ldots,p_N;t)$.

### A. BBGKY hierarchy of the photon-mediated Fokker-Planck equation

For the derivation of the BBGKY hierarchy we assume that the energy of the system is finite. This corresponds to assuming that the following limit holds,

$$\lim_{|\mathbf{p}|\to\infty} f_N(\mathbf{x};\mathbf{p};t) = 0, \tag{44}$$

where $|\mathbf{p}| = \sqrt{\sum_{i=1}^N p_i^2}$, and that expectation values of all moments exist. Furthermore, $f_N$ is periodic with wavelength $\lambda$ in every $x_i$, which implies

$$f_N(\mathbf{x}+\lambda\mathbf{z};\mathbf{p};t) = f_N(\mathbf{x};\mathbf{p};t) \tag{45}$$

for every $\mathbf{z}\in\mathbb{Z}^N$. The distribution function $f_N$ is invariant under particle exchange, which we can express by means of the permutation matrix $\mathbf{P}$, such that

$$f_N(\mathbf{Px};\mathbf{Pp};t) = f_N(\mathbf{x};\mathbf{p};t), \tag{46}$$

where each row and column of $\mathbf{P}$ contain only one entry different from zero and equal to 1.

In order to derive the BBGKY hierarchy of the FPE in Eq. (1) we first define the $l$-particle distribution function:

$$f_l = \int_0^\lambda \frac{dx_{l+1}}{\lambda}\int_{-\infty}^\infty dp_{l+1}\cdots\int_0^\lambda \frac{dx_N}{\lambda}\int_{-\infty}^\infty dp_N f_N, \tag{47}$$

where $f_l$ inherits the three properties in Eqs. (44), (45), and (46) from $f_N$. Index $l$ takes the value $l = 1,\ldots,N$, such that for $l = 1$ the distribution $f_l$ is the single-particle phase-space function, and for $l = N$ it describes the $N$-particle state. The evolution of $f_l$ is found from Eq. (1) after integrating out the other $N-l$ particle variables and can be cast in the form

$$\frac{\partial f_l}{\partial t} = \sum_{j=1}^l \left(\mathcal{L}_j^{(l)} f_l + \mathcal{G}_j^{(l)}[f_{l+1}]\right), \tag{48}$$

where the first operator on the RHS solely depends on the variables of the $l$ particles and reads

$$\begin{aligned}\mathcal{L}_j^{(l)} f_l = &-\frac{\partial}{\partial x_j}\frac{p_j}{m} f_l \\ &- S^2\frac{\partial}{\partial p_j}\sum_{i=1}^l [F_0\cos(kx_i)+\Gamma_0\sin(kx_i)p_i]\sin(kx_j) f_l \\ &+ S^2\frac{\partial}{\partial p_j}\sum_{i=1}^l\left(D_0\frac{\partial}{\partial p_i}+\eta_0\frac{\partial}{\partial x_i}\right)\sin(kx_i)\sin(kx_j) f_l.\end{aligned} \tag{49}$$

The second operator, instead, depends nonlinearly on the $(l+1)$-particle distribution function. This term vanishes when $l = N$, while for $l < N$ it describes the dynamics of correlations, which are established by the interparticle potential. It reads

$$\begin{aligned}\mathcal{G}_j^{(l)}[f_{l+1}] = &-S^2(N-l)\frac{\partial}{\partial p_j}\sin(kx_j) \\ &\times (F_0\Theta_l[f_{l+1}]+\Gamma_0\Xi_l[f_{l+1}]),\end{aligned} \tag{50}$$

where

$$\Theta_l[f_{l+1}] = \int_0^\lambda \frac{dx_{l+1}}{\lambda}\int_{-\infty}^\infty dp_{l+1}\cos(kx_{l+1}) f_{l+1}, \tag{51}$$

$$\Xi_l[f_{l+1}] = \int_0^\lambda \frac{dx_{l+1}}{\lambda}\int_{-\infty}^\infty dp_{l+1}\sin(kx_{l+1}) p_{l+1} f_{l+1}, \tag{52}$$

while $\Theta_0[f_1] = \Theta_{\rm MF}$ and $\Xi_0[f_1] = \Xi_{\rm MF}$. Note that when the factorization ansatz of Eq. (9) holds, $\Theta_1[f_2] = \Theta_{\rm MF} f_1$ and $\Xi_1[f_2] = \Xi_{\rm MF} f_1$. A closed set of equations for $f_l$ can thus be strictly obtained for $l = N$, giving Eq. (1), or for $S = 0$, hence in the absence of the cavity field.

### B. The Lenard-Balescu equation

For $l = 2$ we can generally decompose the distribution function into two terms:

$$f_2(x_1,x_2,p_1,p_2) = f_1(x_1,p_1)f_1(x_2,p_2) + g_2(x_1,x_2,p_1,p_2), \tag{53}$$

where the first term on the RHS is the mean-field term and the second term describes all corrections beyond mean field. When at $t = 0$ the distribution function is factorized in a form like Eq. (9), the dynamics beyond mean field will tend to build correlations which are described by $g_2$. We obtain the mean-field FPE, Eq. (10), by performing the approximation $\mathcal{G}_1^{(1)}[f_2] \to \mathcal{G}_1^{(0)}[f_1]f_1$. In the following we analyze the regime in which this approximation is justified by studying the equation describing the evolution of the function $g_2$ under some approximation, which permits us to truncate the BBGKY hierarchy to second order. This equation is known in the literature as the Lenard-Balescu equation [19], and it will allow us to identify a time scale where the mean-field treatment provides reliable predictions. In order to derive the Lenard-Balescu equation we first consider the distribution function for $l = 3$. Using the same type of decomposition as in Eq. (53), this can be written as

$$\begin{aligned} f_3(x_1,x_2,x_3,p_1,p_2,p_3) &= f_1(x_1,p_1)f_1(x_2,p_2)f_1(x_3,p_3) \\ &+ \sum_{i,j,k=1}^{3} |\epsilon_{ijk}| f_1(x_i,p_i)g_2(x_j,p_j,x_k,p_k) \\ &+ g_3(x_1,x_2,x_3,p_1,p_2,p_3), \end{aligned}$$

where $\epsilon_{ijk}$ is the Levi-Civita tensor and $g_3$ describes all three-body correlations which cannot be written as a function of $f_1$ and/or $f_2$. We assume now that $g_3$ is of higher order (from the treatment below we will see that $g_3 \propto 1/N^2$) and drop $g_3$ in the equation describing the dynamics of $f_2$, Eq. (48). By means of this assumption we obtain two coupled equations for $f_1$ and $f_2$, which can then be cast into the Lenard-Balescu equations for $f_1$ and $g_2$ using Eq. (53) and read

$$\frac{\partial f_1}{\partial t} = \mathcal{L}^{(1)} f_1 + \mathcal{G}^{(1)}[f_1]f_1 + \mathcal{G}^{(1)}[g_2], \tag{54a}$$

$$\begin{aligned} \frac{\partial g_2}{\partial t} = &- \frac{\partial}{\partial x_1}\frac{p_1}{m}g_2 - \frac{\partial}{\partial x_2}\frac{p_2}{m}g_2 - S^2\sum_{j=1}^{2}\sum_{i\neq j}\frac{\partial}{\partial p_j}F_0\sin(kx_j)\{\cos(kx_i) - \Theta_{\mathrm{MF}}[f_1]\}f_1 f_1 \\ &- S^2\sum_{j=1}^{2}\sum_{i\neq j}\frac{\partial}{\partial p_j}\Gamma_0\sin(kx_j)\{\sin(kx_i)p_i - \Xi_{\mathrm{MF}}[f_1]\}f_1 f_1 + S^2\sum_{j=1}^{2}\sum_{i\neq j}\frac{\partial}{\partial p_j}\sin(kx_j)\left(D_0\frac{\partial}{\partial p_i} + \eta_0\frac{\partial}{\partial x_i}\right)\sin(kx_i)f_1 f_1 \\ &- NS^2F_0\sum_{j=1}^{2}\sum_{i\neq j}\frac{\partial}{\partial p_j}\sin(kx_j)\{\Theta_1[g_2]_i f_1(x_j,p_j) + \Theta_{\mathrm{MF}}[f_1]g_2\} - NS^2\Gamma_0\sum_{j=1}^{2}\sum_{i\neq j}\frac{\partial}{\partial p_j}\sin(kx_j)\{\Xi_1[g_2]_i f_1(x_j,p_j) \\ &+ \Xi_{\mathrm{MF}}[f_1]g_2\}, \end{aligned} \tag{54b}$$

where we specified the arguments when necessary and introduced the notation $\Theta_1[g_2]_i$ and $\Xi_1[g_2]_i$ to indicate that these are functions of $(x_i, p_i)$.

The validity of the mean-field FPE, Eq. (10), relies on whether one can discard the term $\mathcal{G}^{(1)}[g_2]$ on the RHS of Eq. (54a). Let us recall the thermodynamic limit for which $S^2 \sim 1/N$. If we now assume that $g_2$ is of order $1/N$ with respect to $f_1$, then the term $\mathcal{G}^{(1)}[g_2]$ is of order $1/N$ with respect to $\mathcal{G}^{(1)}[f_1]f_1$. A detailed analysis of Eq. (54b) shows that, if $g_2 \sim 1/N$ at $t = 0$, this scaling is preserved by the dynamics. In fact, (i) the first two terms on the RHS of Eq. (54b) give a scaling with $1/N$ because they are proportional to $g_2$, while all other quantities are independent of $N$; (ii) the last term in the first line and the terms in the second line are all proportional to $S^2 \sim 1/N$, and (iii) the last two lines scale with $NS^2g_2 \sim 1/N$. Therefore, for sufficiently short times the contribution of $g_2$ to the dynamics in the mean-field equation can be neglected.

We note that in Eq. (54a) the term $\mathcal{L}^{(1)}f_1$ also has components which scale with $1/N$. If one consistently neglects all terms scaling with $1/N$, then Eq. (54a) reduces to the Vlasov equation (31) and therefore also neglects the diffusion processes leading to equilibrium. Figure 5 illustrates the order of magnitude of the corrections to the Vlasov and Lenard-Balescu equations, as well as the types of correlations that these describe.

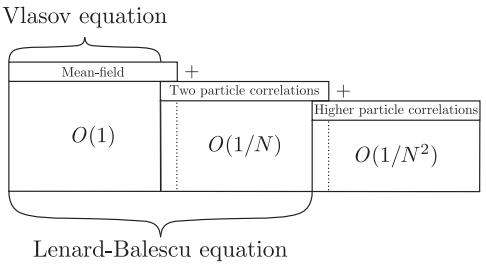


FIG. 5. Illustration of the order of magnitude of the corrections of the Vlasov and of the Lenard-Balescu equations and of which type of correlations they include.

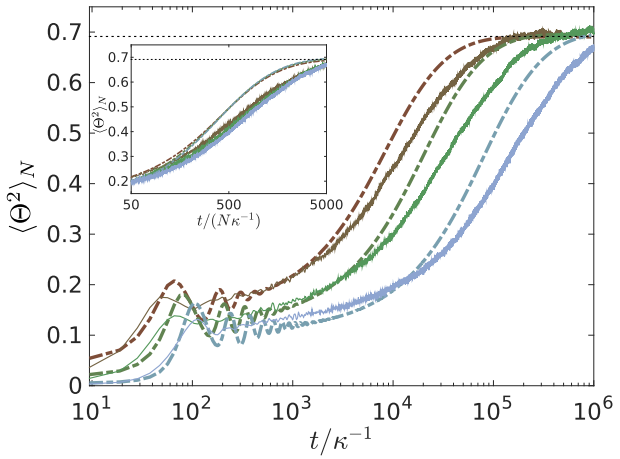


FIG. 6. Time evolution of the squared order parameter evaluated by numerically simulating the mean-field FPE, Eq. (10) (dash-dotted lines), and the $N$-particle FPE of Eq. (1) (solid lines). The curves correspond to different particle numbers $N = 20$ (top two brown curves), $N = 50$ (middle two green curves), and $N = 200$ (bottom two blue curves) and are calculated taking $\Delta_c = -\kappa$ and $\bar{n} = 2\bar{n}_c$. The number $\mathcal{T}$ of trajectories taken for the $N$-body FPE is $\mathcal{T} = 1000$ for $N = 20$, $\mathcal{T} = 500$ for $N = 50$, and $\mathcal{T} = 100$ for $N = 200$ (see Refs. [21,22] for details on the simulations). The horizontal dotted line indicates the asymptotic value of the squared order parameter. The inset shows the curves of the onset with the time axis rescaled by $N$. Note that the initial distribution of the full $N$-body FPE is the one which statistically corresponds to a spatially uniform distribution with the same temperature as the asymptotic one. Therefore, the value of $\langle\Theta^2\rangle_N$ at $t = 0$ does not vanish due to finite-size effects. In order to compare these dynamics with the mean-field FPE, we have taken into account these finite-size effects in the initial mean-field distribution given by $\tilde{f}_0(x,p) = [1 + \delta_N \cos(kx)] f_1(p,0)$, where $f_1$ is given in Eq. (34) and $\delta_N$ is a spatial modulation depending on $N$.

### C. Mean-field versus full $N$-atom dynamics

In order to complete our analysis of the limits of validity of the mean-field ansatz, we now compare its predictions with the ones obtained by numerical simulations of the $N$-particle FPE of Eq. (1). The latter are performed by means of stochastic differential equations (see Refs. [21,22] for details). We focus now on the evolution of the expectation value of $\Theta^2$, which explicitly depends on two-particle correlations and scales the strength of the conservative many-body potential. We recall the definition $\langle\cdot\rangle_N$ in order to indicate the mean value of an $N$-particle observable taken over the $N$-particle distribution $f_N$.

Figure 6 compares the $N$-particle description where the evolution of $f_N$ is governed by FPE (1) (solid line) and the mean-field description, where $f_N(\mathbf{x};\mathbf{p};t) = f_1(x_1,p_1;t)\cdots f_1(x_N,p_N;t)$ and the evolution of $f_1$ is governed by the mean-field FPE (10) (dash-dotted line). The curves are plotted as a function of time and for different particle numbers, $N = 20,50,200$, where the parameter $S^2$ has been rescaled according to our thermodynamic limit to warrant a threshold $\bar{n}_c$ which is independent of $N$. The parameters have been fixed so that, initially, the distribution is spatially uniform, while the momentum distribution is a Gaussian whose width coincides with the asymptotic temperature of the dynamics, Eq. (17). The strength of the field is such that $\bar{n} = 2\bar{n}_c$; therefore, the asymptotic spatial distribution is a Bragg grating with $|\Theta_{\rm MF}| \sim 0.83$. The dynamics we observe is the one which leads to the formation of the Bragg gratings starting from a uniform spatial distribution and exhibit three stages, which have been extensively discussed in Ref. [24]: a violent relaxation, a prethermalized phase, and a slow approach to equilibrium. The solid lines are simulations of the full FPE, and the dash-dotted lines are the corresponding mean-field prediction, which indeed qualitatively reproduces the three-stage dynamics.

The violent relaxation is a stage of the dynamics where there is good agreement between the mean-field and $N$-body FPEs. This is the short-time regime where the Vlasov equation, Eq. (31), is valid, and the behavior of the $N$-body FPE is reproduced by the one observed by numerically integrating the Vlasov equation [see Fig. 3(a)]. This has also been verified in Ref. [24]. The prethermalized regime is also predicted by the Vlasov equation [see Fig. 3(a)]. The mean-field FPE, however, provides a more accurate description and qualitatively reproduces the $N$-body FPE. Nevertheless, a clear difference between mean-field and $N$-body dynamics is found at the onset of the prethermalized stage: In fact, the oscillations are damped at a faster rate in the $N$-body FPE. Apart from this difference, there is a qualitative agreement between the mean-field and $N$-body FPEs also for this stage.

While both mean-field and $N$-body FPEs agree in the asymptotic value, we observe a striking difference between the two results in the relaxation to equilibrium after prethermalization. This is the stage where the role of dissipation and diffusion becomes relevant, as shown in Ref. [24] by comparing this behavior with the one where the dynamics is due to only the Hamiltonian term. In particular, the relaxation time scale predicted by the full simulation is about one order of magnitude larger than the corresponding mean-field prediction. This becomes even more evident by plotting the curves rescaling the time axis with $N$, which is visible in the inset. The curves of the mean-field FPE collapse to one curve, whereas the ones of the $N$-body FPE collapse to a significantly different curve.

Let us now summarize these results. First, the short-time behavior of the fluctuations of the order parameter are well described by the mean-field equation, in particular by the Vlasov equation. This is well understood in terms of the typical contributions to the dynamics: For short times the dominant contributions are indeed the terms of Eq. (31), and interparticle correlations are small, as we argued in the previous section. Discrepancies are due to finite-size effects. The prethermalized regime, moreover, exhibits good agreement between mean-field and full dynamics. This regime is dominated by the Hamiltonian dynamics, and the results show that Hamiltonian dynamics with long-range interactions is well reproduced by the mean-field description. Big deviations instead appear for long times, where the mean-field ansatz is expected to fail, and at the time scales dominated by relaxation to the stationary state.

## VI. CONCLUSIONS

In this work we have systematically developed a mean-field description of the self-organization dynamics of atoms in a

high-finesse cavity. The predictions of the mean-field model have been explored at equilibrium and out of equilibrium; its limits of validity have been tested by comparing them with those of the $N$-body FPE. We have found that the mean-field equation provides an excellent description of the dynamics when the latter is prevailingly Hamiltonian. It further describes the equilibrium properties of single-particle observables, including the asymptotic temperature and the order parameter. It fails, however, to reproduce the long-time out-of-equilibrium dynamics.

Despite these differences, this analysis shows that from the mean-field model one can analytically extract several predictions of the system dynamics. It is, indeed, remarkable that several predictions reproduce in the corresponding limits the ones obtained by means of other theoretical treatments, some of which start from a fully quantum mechanical treatment of the atoms. This, on the one hand, leads us to conjecture that quantum fluctuations play a marginal role in determining the steady-state properties of the cavity field. It further urges one to develop a full quantum kinetic theory, analogous to the full $N$-body semiclassical theory, which will overcome all limitations of simplifying theoretical assumptions performed so far. Only such a model, in fact, can give full access to the dynamical interplay between matter waves and cavity photons.

## ACKNOWLEDGMENTS

The authors are grateful to G. Manfredi, C. Nardini, S. Gupta, and S. Ruffo for insightful discussions. This work was supported by the German Research Foundation (DFG, DACH project "Quantum crystals of matter and light").

## APPENDIX: CAVITY-FIELD CORRELATION FUNCTION AT STEADY STATE

Experimentally accessible quantities are the correlation functions of the field at the cavity output, which allows one to monitor the atoms' state and is proportional to the intracavity field. In our formalism, the intracavity field is closely connected to the atomic state by the relation $E_{\rm cav} \propto \sqrt{N\bar{n}}\Theta$; therefore, the correlation functions of the cavity field are proportional to the correlation functions of the magnetization $\Theta$ [21,22]. In the following we determine the autocorrelation function of the magnetization, which can be detected by means of the first-order correlation function of the field and the fourth-moment of the magnetization $\langle\Theta^4\rangle_N$. As we showed in Ref. [21], in fact, $\langle\Theta^4\rangle_N$ delivers the value of the intensity-intensity correlation of the field at zero-time delay and at zero order in the retardation effects.

### 1. Field intensity across the transition

We first determine the intracavity photon number $n_{\rm cav}$ at steady state for $\bar{n}$ below, at, and above threshold. For this purpose we use the relation [21,22]

$$n_{\rm cav} = N\bar{n}\langle\Theta^2\rangle_N, \tag{A1}$$

which, by introducing $\alpha = \bar{n}/\bar{n}_c$, can be cast in the form (see also the Sec. A 3)

$$n_{\rm cav} = \frac{1}{2}\bar{n}_c + \bar{n}\frac{\partial}{\partial\alpha}\mathcal{G}(\alpha), \tag{A2}$$

where

$$\mathcal{G}(\alpha) = \ln\left(\int_{-\infty}^{\infty} dy\, \exp\{-N\{\alpha y^2 - \ln[I_0(2\alpha y)]\}\}\right). \tag{A3}$$

We then analyze the prediction of this expression close to threshold for $\bar{n} \sim \bar{n}_c$ and thus $\alpha \sim 1$. For this purpose we expand the exponent of $\mathcal{G}(\alpha)$ about the value $y = 0$ and consider the behavior of $n_{\rm cav}$ for $\alpha \to 1^-$ and hence for $\bar{n} < \bar{n}_c$ but sufficiently close to the transition point that the truncation of the expansion is valid. In this limit we find

$$n_{\rm cav} \approx \frac{\bar{n}_c^2/2}{\bar{n}_c - \bar{n}}, \tag{A4}$$

where the details of the derivation are reported in Sec. A 3. The value at the transition point is reported at leading order in $N$ and reads (see Sec. A 3)

$$n_{\rm cav} \approx 2\sqrt{N}\bar{n}_c\frac{\Gamma\left[\frac{3}{4}\right]}{\Gamma\left[\frac{1}{4}\right]}, \tag{A5}$$

where $\Gamma[x]$ denotes the gamma function [39].

The value of the intracavity photon number above threshold is found after observing that the exponent of function $\mathcal{G}(\alpha)$ has two minima that are given by the nonvanishing solutions of the fixed-point equation (24), which we denote by $\Theta_{\rm MF} = \pm\bar{\Theta}$, with $\bar{\Theta}$ given in Eq. (26). Therefore, it holds that

$$n_{\rm cav} = N\bar{n}\bar{\Theta}^2 \approx 2N(\bar{n} - \bar{n}_c),$$

sufficiently close to the critical point. In particular, the mean number of photons increases linearly with $\bar{n}$. We analyze now some properties of the first-order correlation function of the intracavity field, $g^{(1)}(\tau) = \lim_{t\to\infty}{\rm Re}\langle E_{\rm cav}(t+\tau)E_{\rm cav}(t)\rangle_N$. This function has been extensively studied in Ref. [21] by numerically solving the $N$-particle FPE. Here, we will use the mean-field ansatz in order to better understand the two sidebands of its Fourier transform, at which it exhibits maxima above threshold. For this purpose we first notice that the correlation function is proportional to the autocorrelation function $C(\tau)$ of the magnetization by the relation $g^{(1)}(\tau) = N\bar{n}C(\tau)$ and

$$C(\tau) = \lim_{t\to\infty}\langle\Theta(t)\Theta(t+\tau)\rangle_N. \tag{A6}$$

We want to derive $C(\tau)$ in the mean field, and hence, the mean value now has to be taken over the factorized distribution as in Eq. (9) with the stationary mean-field distribution given in Eq. (23). We calculate $C(\tau)$ by solving the equations of the mathematical pendulum

$$\begin{aligned}\dot{x} &= \frac{p}{m},\\ \dot{p} &= 2\hbar k\Delta_c\bar{n}\bar{\Theta}\sin(kx),\end{aligned} \tag{A7}$$

with initial conditions $x(0) = x_0$ and $p(0) = p_0$. The value $\bar{\Theta}$ is here the positive stable solution of Eq. (24). In the limit of small oscillations, these equations describe harmonic motion

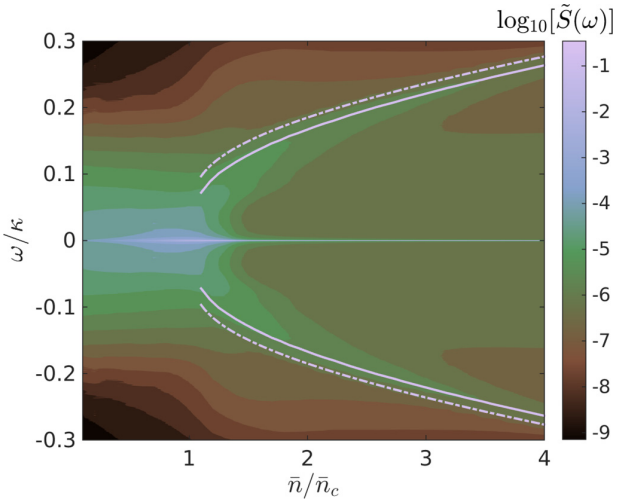


FIG. 7. Contour plot of the spectrum of the autocorrelation function $\tilde{S}(\omega)$ as a function of $\bar{n}$ and of the frequency (in units of $\kappa$) evaluated from the numerical data of $\Theta(x_1,\ldots,x_N)$, Eq. (4), by integrating the $N$-particle FPE, Eq. (1), for 100 trajectories of $N = 50$ atoms, $\Delta_c = -\kappa$, and evolution time $t_{\rm tot} = 10^4\kappa^{-1}$ (see Ref. [21]). The lines are analytical estimates of the spectrum maximum for $\bar{n} > \bar{n}_c$. The dashed line corresponds to the frequency of the corresponding harmonic oscillator in Eq. (A8). The solid line is at the frequency extracted by solving Eq. (A7) for a mathematical pendulum and in good agreement with the peak position of the numerically evaluated spectra.

at the frequency

$$\omega_0 = \sqrt{-4\omega_r \Delta_c \bar{n}\bar{\Theta}}. \tag{A8}$$

The mean frequency, however, is the result of the possible trajectories of the mathematical pendulum weighted by the probability density function $f_{\rm st}(x_0, p_0)$. For $x_0 \neq 0$ and $p_0 \neq 0$ the oscillation period turns out to be larger than $2\pi/\omega_0$, and this prediction fits quite well the maximum found numerically by integrating the coupled equations of $N$ particles, as shown in Fig. 7.

### 2. Intensity-intensity correlations at zero time delay

The intensity-intensity correlation function at zero time delay $g^{(2)}(0)$ provides a direct measurement of the fourth moment of the magnetization when retardation effects are sufficiently small [21]:

$$g^{(2)}(0) = \langle\Theta^4\rangle_N / \langle\Theta^2\rangle_N^2. \tag{A9}$$

Above threshold $\langle\Theta^n\rangle_N = \bar{\Theta}^n + O(1/N)$, with $\bar{\Theta}$ being the solution of Eq. (24). Therefore, for $\bar{n} > \bar{n}_c$ we obtain

$$g^{(2)}(0)_{\bar{n}>\bar{n}_c} = 1, \tag{A10}$$

which corresponds to coherent light and is valid at leading order, with an error that scales with $1/N$. In the mean field for the factorized distribution, Eq. (9), we get

$$\langle\Theta^2\rangle_N = \frac{1}{N}\mathcal{B} + \frac{N-1}{N}\bar{\Theta}^2$$

and

$$\langle\Theta^4\rangle_N = \frac{N(N-1)(N-2)(N-3)}{N^4}\bar{\Theta}^4 + \frac{6N(N-1)(N-2)}{N^4}\bar{\Theta}^2\mathcal{B} + \frac{3N(N-1)}{N^4}\mathcal{B}^2 + \frac{4N(N-1)}{N^4}\bar{\Theta}\langle\cos^3(x)\rangle + \frac{N}{N^4}\langle\cos^4(x)\rangle.$$

Notice that above threshold for $\bar{\Theta} \neq 0$ we can again write $\langle\Theta^4\rangle_N = \bar{\Theta}^4 + O(1/N)$. Hence, we get the same value for $g^{(2)}(0) = 1$ (above threshold) in the thermodynamic limit $N \to \infty$. Below threshold, in Sec. A 3 we show that the expression takes the value

$$g^{(2)}(0)_{\bar{n}<\bar{n}_c} = 3, \tag{A11}$$

which corresponds to super-Poissonian light. Corrections scale with $1/N$. This also holds for the calculation with the factorized ansatz. Below threshold we get

$$\langle\Theta^2\rangle_N = \frac{1}{N}\mathcal{B}$$

and

$$\langle\Theta^4\rangle_N = \frac{3}{N^2}\mathcal{B}^2 + O\left(\frac{1}{N}\right)$$

and therefore the same value of $g^{(2)}(0) = 3$ (below threshold) as for the $N$-particle description. Finally, at threshold we obtain

$$g^{(2)}(0)_{\bar{n}=\bar{n}_c} \approx \frac{1}{4}\left(\frac{\Gamma\left[\frac{1}{4}\right]}{\Gamma\left[\frac{3}{4}\right]}\right)^2, \tag{A12}$$

with corrections scaling with $1/\sqrt{N}$, thus giving a slower convergence than the one found for the values above and below threshold. We want to mention here that the mean-field description cannot reproduce the value in Eq. (A12). Figure 8 displays the mean-field predictions for $g^{(2)}(0)$ at the thermodynamic limit and as a function of $\bar{n}$. These curves are compared with the mean-field calculation at finite $N$ and with the corresponding one of the $N$-particle FPE. Even though the mean-field curve at finite $N$ is tendentially closer to the thermodynamic limit than the $N$-particle FPE prediction, they both converge to the values of Eqs. (A10), (A12), and (A11), depending on whether $\bar{n} <, =, > \bar{n}_c$ for $N \to \infty$.

### 3. Useful relations

In order to demonstrate Eq. (A2) we first consider the relation

$$\int_{-\infty}^{\infty} dy \exp\left[-\alpha N\left(y - \frac{1}{N}\sum_{i=1}^{N}\cos(kx_i)\right)^2\right] = \sqrt{\frac{\pi}{\alpha N}}$$

and cast it into the form

$$\int_{-\infty}^{\infty} dy e^{-\alpha N y^2} \exp\left(2\alpha N y \frac{1}{N}\sum_{i=1}^{N}\cos(kx_i)\right) = \sqrt{\frac{\pi}{\alpha N}}\exp[\alpha N \Theta(\mathbf{x})^2].$$

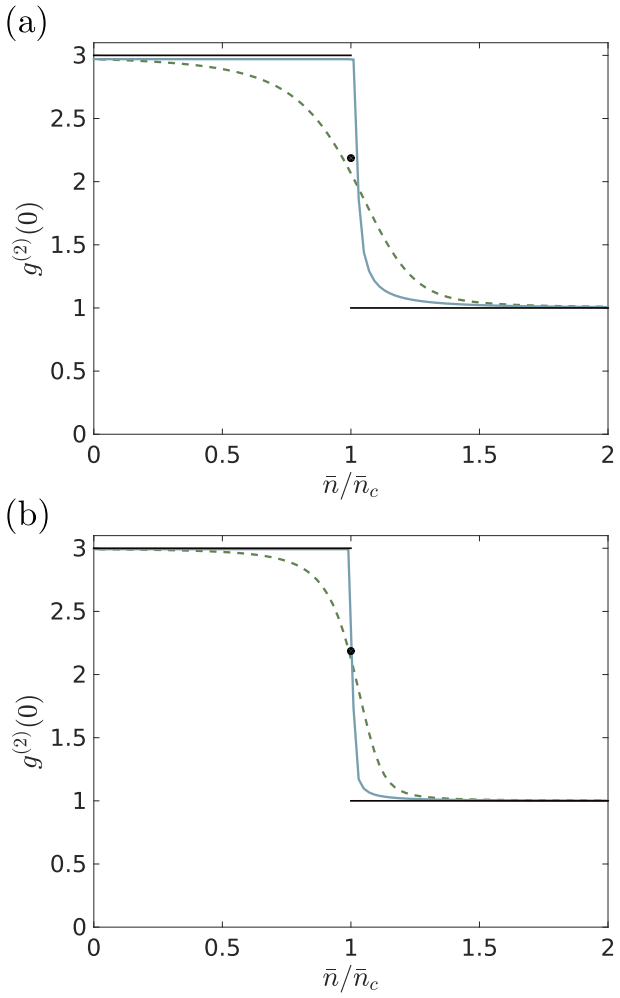


FIG. 8. Intensity-intensity correlation function at zero time delay $g^{(2)}(0)$, Eq. (A9), as a function of $\bar{n}$ for (a) $N = 50$ atoms and (b) $N = 200$ atoms. The solid blue lines are the curves evaluated using in Eq. (A9) the mean-field steady state (23). The dashed lines are calculated for the corresponding full $N$-particle distribution given in [17]. The horizontal black solid lines are the values at the thermodynamic limit given at $\bar{n} < \bar{n}_c$ by Eq. (A11) and at $\bar{n} > \bar{n}_c$ by Eq. (A10). The point at $\bar{n} = \bar{n}_c$ is at the value of Eq. (A12). The discrepancy between the mean-field curve and the full $N$-particle predictions decreases as $N \to \infty$, where they both converge to the value given by the thermodynamic limit.

From these relations, it follows

$$\ln\left\{\frac{1}{\lambda^N}\int d\mathbf{x}\exp[\alpha N\Theta(\mathbf{x})^2]\right\} = \frac{1}{2}\ln\left(\frac{N}{\pi}\alpha\right) + \ln\left(\int_{-\infty}^{\infty} dy\exp\left\{-N\{\alpha y^2 - \ln[I_0(2\alpha y)]\}\right\}\right).$$

We use it for evaluating expression (A1) and obtain

$$n_{\rm cav} = \bar{n}\frac{\partial}{\partial\alpha}\ln\left\{\frac{1}{\lambda^N}\int d\mathbf{x}\exp[\alpha N\Theta(\mathbf{x})^2]\right\} = \bar{n}\left(\frac{1}{2\alpha} + \frac{\frac{\partial}{\partial\alpha}\int_{-\infty}^{\infty} dy\exp\left\{-N\{\alpha y^2 - \ln[I_0(2\alpha y)]\}\right\}}{\int_{-\infty}^{\infty} dy\exp\left\{-N\{\alpha y^2 - \ln[I_0(2\alpha y)]\}\right\}}\right), \tag{A13}$$

which leads to Eq. (A2) by using definition (A3).

In order to determine the intracavity photon number close to threshold, we expand the exponent of Eq. (A3) about $y = 0$ to fourth order:

$$\alpha y^2 - \ln[I_0(2\alpha y)] = \alpha(1-\alpha)y^2 + \frac{\alpha^4}{4}y^4 + O(y^6).$$

For $\bar{n} < \bar{n}_c$, the coefficient of the quadratic term is positive, and we thus discard the fourth-order term. Expression (A2) takes the form

$$n_{\rm cav} \approx \bar{n}\left(\frac{1}{2\alpha} + \frac{\frac{\partial}{\partial\alpha}\int_{-\infty}^{\infty} dy\exp\left[-N\alpha(1-\alpha)y^2\right]}{\int_{-\infty}^{\infty} dy\exp\left[-N\alpha(1-\alpha)y^2\right]}\right) = \bar{n}\left(\frac{1}{2\alpha} + \frac{2\alpha-1}{2\alpha(1-\alpha)}\right) = \frac{\bar{n}}{2(1-\alpha)}.$$

Using the explicit value of $\alpha$,

$$n_{\rm cav} = \frac{\bar{n}\bar{n}_c}{2(\bar{n}_c - \bar{n})} \approx \frac{\bar{n}_c^2/2}{\bar{n}_c - \bar{n}}, \tag{A14}$$

which thus gives Eq. (A4).

At the transition point $\bar{n} = \bar{n}_c$ the integral in Eq. (A2) diverges in the limit $N \to \infty$. We determine its value for finite $N$ and keep the leading order. Moreover, since the coefficient of the quadratic term in the expansion in $y$ vanishes, we include the fourth order and evaluate the integral at $\alpha = 1$, obtaining

$$n_{\rm cav} \approx \bar{n}_c\left(\frac{1}{2} + \frac{\int_{-\infty}^{\infty} dy(Ny^2 - Ny^4)\exp\left[-\frac{N}{4}y^4\right]}{\int_{-\infty}^{\infty} dy\exp\left[-\frac{N}{4}y^4\right]}\right) \approx \bar{n}_c\frac{2\sqrt{N}\Gamma\left[\frac{3}{4}\right]}{\Gamma\left[\frac{1}{4}\right]},$$

which is the expression in Eq. (A5).

To calculate $g^{(2)}(0)$ below and at threshold we notice that

$$N^2\langle\Theta^4\rangle_N - N^2\langle\Theta^2\rangle_N^2 = \frac{\partial^2}{\partial\alpha^2}\ln\left\{\frac{1}{\lambda^N}\int d\mathbf{x}\exp[\alpha N\Theta(\mathbf{x})^2]\right\} = N\frac{\partial}{\partial\alpha}\langle\Theta^2\rangle_N$$

holds. Below threshold for $\alpha < 1$ we calculated in leading order that

$$\frac{\partial}{\partial\alpha}\frac{1}{2(1-\alpha)} = \frac{1}{2(1-\alpha)^2},$$

which then delivers the expression

$$g^{(2)}(0)_{\bar{n}<\bar{n}_c} = \frac{\frac{1}{2(1-\alpha)^2} + \frac{1}{4(1-\alpha)^2}}{\frac{1}{4(1-\alpha)^2}} = 3$$

and thus Eq. (A11). In order to calculate the value at threshold we use

$$N^2\langle\Theta^4\rangle_N - N^2\langle\Theta^2\rangle_N^2 \approx N - 4N\left(\frac{\Gamma\left[\frac{3}{4}\right]}{\Gamma\left[\frac{1}{4}\right]}\right)^2, \qquad \text{(A15)}$$

which is valid in leading order and which gives Eq. (A12).

[1] H. Ritsch, P. Domokos, F. Brennecke, and T. Esslinger, Rev. Mod. Phys. **85**, 553 (2013).
[2] G. Labeyrie, E. Tesio, P. M. Gomes, G.-L. Oppo, W. J. Firth, G. R. M. Robb, A. S. Arnold, R. Kaiser, and T. Ackemann, Nat. Photonics **8**, 321 (2014); G. R. M. Robb, E. Tesio, G.-L. Oppo, W. J. Firth, T. Ackemann, and R. Bonifacio, Phys. Rev. Lett. **114**, 173903 (2015).
[3] D. E. Chang, J. I. Cirac, and H. J. Kimble, Phys. Rev. Lett. **110**, 113606 (2013).
[4] D. H. J. O'Dell, S. Giovanazzi, and G. Kurizki, Phys. Rev. Lett. **90**, 110402 (2003).
[5] P. Münstermann, T. Fischer, P. Maunz, P. W. H. Pinkse, and G. Rempe, Phys. Rev. Lett. **84**, 4068 (2000).
[6] C. von Cube, S. Slama, D. Kruse, C. Zimmermann, Ph. W. Courteille, G. R. M. Robb, N. Piovella, and R. Bonifacio, Phys. Rev. Lett. **93**, 083601 (2004).
[7] B. Zhu, J. Schachenmayer, M. Xu, F. Herrera, J. G. Restrepo, M. J. Holland, and A. M. Rey, New J. Phys. **17**, 083063 (2015); J. M. Weiner, K. C. Cox, J. G. Bohnet, and J. K. Thompson, arXiv:1503.06464.
[8] B. Nagorny, Th. Elsässer, and A. Hemmerich, Phys. Rev. Lett. **91**, 153003 (2003); S. Gupta, K. L. Moore, K. W. Murch, and D. M. Stamper-Kurn, *ibid.* **99**, 213601 (2007).
[9] S. Ritter, F. Brennecke, K. Baumann, T. Donner, C. Guerlin, and T. Esslinger, Appl. Phys. B **95**, 213 (2009).
[10] P. Domokos and H. Ritsch, Phys. Rev. Lett. **89**, 253003 (2002).
[11] A. T. Black, H. W. Chan, and V. Vuletić, Phys. Rev. Lett. **91**, 203001 (2003).
[12] K. Baumann, C. Guerlin, F. Brennecke, and T. Esslinger, Nature (London) **464**, 1301 (2010).
[13] S. Schreppler, N. Spethmann, N. Brahms, T. Botter, M. Barrios, and D. M. Stamper-Kurn, Science **344**, 1486 (2014).
[14] F. Haas, J. Volz, R. Gehr, J. Reichel, and J. Estève, Science **344**, 180 (2014).
[15] D. Nagy, G. Kónya, G. Szirmai, and P. Domokos, Phys. Rev. Lett. **104**, 130401 (2010).
[16] R. Bachelard, T. Manos, P. de Buyl, F. Staniscia, F. S. Cataliotti, G. De Ninno, D. Fanelli, and N. Piovella, J. Stat. Mech. (2010) P06009.
[17] S. Schütz and G. Morigi, Phys. Rev. Lett. **113**, 203002 (2014).
[18] E. Tesio, G. R. M. Robb, G.-L. Oppo, P. M. Gomes, T. Ackemann, G. Labeyrie, R. Kaiser, and W. J. Firth, Philos. Trans. R. Soc. A **372**, 20140002 (2014).
[19] A. Campa, T. Dauxois, and S. Ruffo, Phys. Rep. **480**, 57 (2009).
[20] M. Antoni and S. Ruffo, Phys. Rev. E **52**, 2361 (1995).
[21] S. Schütz, S. B. Jäger, and G. Morigi, Phys. Rev. A **92**, 063808 (2015).
[22] S. Schütz, H. Habibian, and G. Morigi, Phys. Rev. A **88**, 033427 (2013).
[23] P. Domokos, P. Horak, and H. Ritsch, J. Phys. B **34**, 187 (2001).
[24] S. Schütz, S. B. Jäger, and G. Morigi, arXiv:1512.05243, Phys. Rev. Lett. (to be published).
[25] J. K. Asbóth, P. Domokos, H. Ritsch, and A. Vukics, Phys. Rev. A **72**, 053417 (2005).
[26] W. Niedenzu, T. Grießer, and H. Ritsch, Europhys. Lett. **96**, 43001 (2011).
[27] T. Grießer, W. Niedenzu, and H. Ritsch, New J. Phys. **14**, 053031 (2012).
[28] E. G. Dalla Torre, S. Diehl, M. D. Lukin, S. Sachdev, and P. Strack, Phys. Rev. A **87**, 023831 (2013).
[29] D. Nagy, G. Szirmai, and P. Domokos, Phys. Rev. A **84**, 043637 (2011).
[30] B. Öztop, M. Bordyuh, Ö. E. Müstecaplıoğlu, and H. E. Türeci, New J. Phys. **14**, 085011 (2012).
[31] M. Kulkarni, B. Öztop, and H. E. Türeci, Phys. Rev. Lett. **111**, 220408 (2013).
[32] F. Piazza, P. Strack, and W. Zwerger, Ann. Phys. (N.Y.) **339**, 135 (2013).
[33] F. Piazza and P. Strack, Phys. Rev. A **90**, 043823 (2014).
[34] P. Horak, G. Hechenblaikner, K. M. Gheri, H. Stecher, and H. Ritsch, Phys. Rev. Lett. **79**, 4974 (1997).
[35] V. Vuletic and S. Chu, Phys. Rev. Lett. **84**, 3787 (2000).
[36] J. Dalibard and C. Cohen-Tannoudji, J. Phys. B **18**, 1661 (1985).
[37] J. Larson, B. Damski, G. Morigi, and M. Lewenstein, Phys. Rev. Lett. **100**, 050401 (2008); J. Larson, S. Fernández-Vidal, G. Morigi, and M. Lewenstein, New J. Phys. **10**, 045002 (2008).
[38] S. Fernández-Vidal, G. De Chiara, J. Larson, and G. Morigi, Phys. Rev. A **81**, 043407 (2010).
[39] M. Abramowitz and I. Stegun, *Handbook of Mathematical Functions* (Dover, New York, 1968).
[40] T. Grießer, H. Ritsch, M. Hemmerling, and G. R. M. Robb, Eur. Phys. J. D **58**, 349 (2010).
[41] G. K. Karagiannidis and A. S. Lioumpas, IEEE Commun. Lett. **11**, 644 (2007).
[42] C. Nardini, Ph.D. thesis, École normale supérieure de Lyon and Università degli Studi di Firenze, 2013.

### 2.3.2 Dissipation-Assisted Prethermalization in Long-Range Interacting Atomic Ensembles

Physical Review Letters **117**, 083001 (2016)

DOI: 10.1103/PhysRevLett.117.083001

Authors: Stefan Schütz, Simon B. Jäger, and Giovanna Morigi

*Theoretische Physik, Universität des Saarlandes, D-66123 Saarbrücken, Germany*



**Author Contributions:**
The theoretical model was developed by S. Schütz and G. Morigi. Analytical calculations and numerical simulations were performed by S. Schütz and S. B. Jäger. The calculations were checked and discussed by all authors and the article was written by all authors.

**Abstract:**
We theoretically characterize the semiclassical dynamics of an ensemble of atoms after a sudden quench across a driven-dissipative second-order phase transition. The atoms are driven by a laser and interact via conservative and dissipative long-range forces mediated by the photons of a single-mode cavity. These forces can cool the motion and, above a threshold value of the laser intensity, induce spatial ordering. We show that the relaxation dynamics following the quench exhibits a long prethermalizing behavior which is first dominated by coherent long-range forces and then by their interplay with dissipation. Remarkably, dissipation-assisted prethermalization is orders of magnitude longer than prethermalization due to the coherent dynamics. We show that it is associated with the creation of momentum-position correlations, which remain nonzero for even longer times than mean-field predicts. This implies that cavity cooling of an atomic ensemble into the self-organized phase can require longer time scales than the typical experimental duration. In general, these results demonstrate that noise and dissipation can substantially slow down the onset of thermalization in long-range interacting many-body systems.

PRL 117, 083001 (2016) PHYSICAL REVIEW LETTERS week ending 19 AUGUST 2016

# Dissipation-Assisted Prethermalization in Long-Range Interacting Atomic Ensembles

Stefan Schütz, Simon B. Jäger, and Giovanna Morigi
*Theoretische Physik, Universität des Saarlandes, D-66123 Saarbrücken, Germany*

(Received 16 December 2015; revised manuscript received 11 May 2016; published 15 August 2016)

We theoretically characterize the semiclassical dynamics of an ensemble of atoms after a sudden quench across a driven-dissipative second-order phase transition. The atoms are driven by a laser and interact via conservative and dissipative long-range forces mediated by the photons of a single-mode cavity. These forces can cool the motion and, above a threshold value of the laser intensity, induce spatial ordering. We show that the relaxation dynamics following the quench exhibits a long prethermalizing behavior which is first dominated by coherent long-range forces and then by their interplay with dissipation. Remarkably, dissipation-assisted prethermalization is orders of magnitude longer than prethermalization due to the coherent dynamics. We show that it is associated with the creation of momentum-position correlations, which remain nonzero for even longer times than mean-field predicts. This implies that cavity cooling of an atomic ensemble into the self-organized phase can require longer time scales than the typical experimental duration. In general, these results demonstrate that noise and dissipation can substantially slow down the onset of thermalization in long-range interacting many-body systems.

DOI: 10.1103/PhysRevLett.117.083001

The quest for a systematic understanding of nonequilibrium phenomena is an open problem in theoretical physics for its importance in the description of dynamics from the microscopic up to astrophysical scales [1–3]. Aspects of these dynamics are studied in the relaxation of systems undergoing temporal changes (quenches) of the control field across a critical point [4–6]. Quenches across a nonequilibrium phase transition provide further insight into the interplay between noise and external drives on criticality and thermalization [7,8]. In this context, photonic systems play a prominent role, thanks to their versatility [9–15].

Polarizable particles in a high-finesse cavity, like in the setup illustrated in Fig. 1(a), offer a unique system to study relaxation in long-range interacting systems. Here, multiple photon scattering mediates particle-particle interactions whose range scales with the system size in a single-mode cavity [15–18]. In this limit, atomic ensembles in cavities are expected to share several features with other long-range interacting systems such as gravitational clusters and nonneutral plasmas in two or more dimensions [3,16,19]. The equilibrium thermodynamics of these systems can exhibit ensemble inequivalence [3,20], while quasistationary states (QSSs) typically characterize the out-of-equilibrium dynamics [3,21–23]. QSSs are metastable states in which the system is expected to remain trapped in the thermodynamic limit; they are Vlasov-stable solutions and thus depend on the initial state. So far, however, evidence of QSSs has been elusive. It has been conjectured that noise and dissipation can set a time scale that limits the QSS lifetime [24–27] and possibly gives rise to dynamical phase transitions [25]. In Ref. [28], it was shown that, in the presence of dissipation due to viscous damping or local inelastic collisions, the relaxation dynamics of long-range interacting systems can be cast in terms of so-called scaling QSSs, which are solutions of the kinetic mean-field equation and asymptotically tend to a unique QSS [28]. Accordingly, one would expect to observe QSSs in cavity systems [19]. In Ref. [16], however, we found no evidence of the typical superlinear dependence on $N$ of the QSS time scale [3], which we attributed to the effect of noise and dissipative processes. Nonetheless, the dissipative dynamics is here due to retardation effects in the coupling between the atoms and a global variable, the cavity field, and can also establish long-range correlations [29,30] whose influence on the relaxation dynamics is still unexplored.

In this work, we characterize the interplay between dissipative and conservative long-range forces in the semiclassical dynamics of $N$ polarizable particles (atoms) confined within a high-finesse single-mode cavity and transversally driven by a laser [16,31–33] [see Fig. 1(a)]. The particles' motion is along the cavity axis ($x$ axis), and the dynamics results from their optomechanical coupling with the cavity mode at wave number $k$ and spatial mode function $\cos(kx)$. We focus on the regime where the laser frequency $\omega_L$ is smaller than the cavity frequency $\omega_c$, such that $\Delta_c = \omega_L - \omega_c < 0$. Here, the dynamics is characterized by a thermal stationary state, which can exhibit a second-order driven-dissipative phase transition (spatial self-organization) as a function of the laser intensity and of $\Delta_c$ [31]. This transition is due to the interplay between the dispersive and the dissipative forces: The dispersive forces tend to order the atoms in gratings for which the order parameter $\Theta = \sum_{j=1}^{N} \cos(kx_j)/N \to \pm 1$, with $x_j$ the particles' positions, and the intracavity photon number is maximum. The dissipative forces, instead, are due to

 

PRL 117, 083001 (2016) PHYSICAL REVIEW LETTERS week ending 19 AUGUST 2016

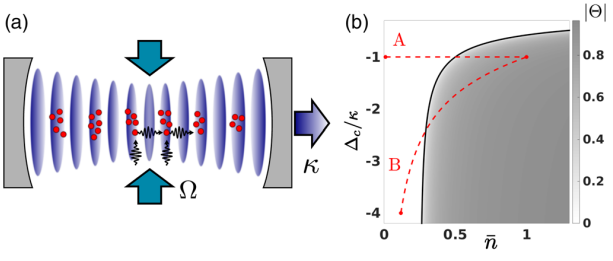


FIG. 1. (a) Atoms interact with the standing-wave mode of a cavity and are transversally driven by a laser. The laser amplitude ($\Omega$) and/or frequency ($\Delta_c$) are suddenly quenched across the threshold, above which the atoms organize in regular spatial patterns at the steady state. The coherent scattering amplitude per atom, $S$, is tuned by the laser, $S \propto \Omega$, and the resonator dissipates photons at rate $\kappa$. (b) Phase diagram of the second-order self-organization transition as a function of $\bar{n}$ (proportional to $S^2$) and $\Delta_c/\kappa$ (that determines the asymptotic temperature). The black line separates the homogeneous phase (with order parameter $\Theta = 0$) from the self-organized one (with $\Theta \to \pm 1$). The red dashed lines $A$ and $B$ illustrate the initial and final values, respectively, of the sudden quenches we analyze.

retardation effects in the dynamics of atoms and field: For $\Delta_c < 0$, they cool the atoms into a thermal state whose effective temperature $T_{\rm eff}$ is determined by $\Delta_c$ and by the cavity loss rate $\kappa$: $k_B T_{\rm eff} = \hbar(\Delta_c^2 + \kappa^2)/(-4\Delta_c)$, with $k_B$ the Boltzmann constant [30–32,34–37]. $T_{\rm eff}$ determines the threshold $S_c$ of the coherent laser scattering amplitude $S$ per atom at which spatial self-organization occurs, such that $\sqrt{N} S_c = 2k_B T_{\rm eff}/\hbar$ [31,34,38], and separates the regime where the spatial distribution is uniform and $\Theta \simeq 0$ from the symmetry broken phase in which the atoms form Bragg gratings, as shown in Fig. 1(b).

We analyze the semiclassical dynamics of the atoms after a quench across the transition using a Fokker-Planck equation (FPE) for the phase space distribution $f(x_1, \ldots, x_N; p_1, \ldots, p_N; t)$ at time $t$ and as a function of the atoms' positions $x_j$ and the momenta $p_j$. The FPE is valid when the cavity linewidth $\kappa$ exceeds the recoil frequency $\omega_r = \hbar k^2/(2m)$ and the width of the momentum distribution $\Delta p$ is larger than the photon linear momentum $\hbar k$ [30]. It reads [31,39]

$$\partial_t f = \{H, f\} + \bar{n}\mathcal{L}_\beta f + O(U_0), \tag{1}$$

where Hamiltonian $H = \sum_{j=1}^N p_j^2/(2m) + \hbar\Delta_c \bar{n} N \Theta^2$ determines the coherent dynamics and is a realization of the anisotropic Hamiltonian Mean Field model (HMF) [16,21,40]. The dimensionless parameter $\bar{n} = NS^2/(\kappa^2 + \Delta_c^2)$ scales the depth of the conservative potential. It also scales the dissipator $\mathcal{L}_\beta$, describing the effective long-ranged friction and diffusion [30,31]:

$$\mathcal{L}_\beta f = \sum_i^N \frac{\Gamma}{N} \sum_j^N \sin(kx_i)\partial_{p_i} \sin(kx_j)\left(p_j + \frac{m}{\beta}\partial_{p_j}\right) f, \tag{2}$$

with $\Gamma = 2\omega_r \hbar\kappa\beta$ and $\beta = (k_B T_{\rm eff})^{-1}$. For $\Delta_c < 0$, the incoherent dynamics drives the system into the stationary state $f_S(\beta, \bar{n}) = f_0 \exp(-\beta H)$, where $f_0$ warrants normalization. This state is well defined in the thermodynamic limit we choose, according to which, as $N$ is increased, the quantity $NS^2$ (and thus $\bar{n}$) is kept constant. This choice warrants that the Hamiltonian satisfies Kac's scaling [3].

The relaxation dynamics following a sudden quench at $t = 0$ is numerically evaluated by means of stochastic differential equations (SDE). Averages are taken over several trajectories, sampling the dynamics of $N$ atoms according to the given initial distribution [30,41]. Before the quench is performed ($t < 0$), we assume that the system has reached the equilibrium solution $f_S(\beta, \bar{n}_i)$ of the FPE at a given value of $\bar{n} = \bar{n}_i$ and $\Delta_c$. At $t = 0$, the value of $\bar{n}$ is quenched from $\bar{n}_i < \bar{n}_c$, deep in the disordered phase, to $\bar{n}_f > \bar{n}_c$, well inside the ordered phase. This corresponds to the horizontal path $A$ of Fig. 1(b), keeping $\Delta_c$, and hence the asymptotic temperature, constant. We evolve the initial state setting $\bar{n} = \bar{n}_f$ in Eq. (1). In what follows, we focus on quenches from the disordered to the ordered phase along path $A$; nevertheless, the essential features of the dynamics we will report on characterize also the quenches in the opposite direction as well as along paths of type $B$, which connects points with different asymptotic temperatures (see Supplemental Material [42]).

The time evolution of the modulus of the order parameter $\langle|\Theta|\rangle$ is displayed in Fig. 2(a) for different values of $\bar{n}_f$: $\langle|\Theta|\rangle$ tends towards an asymptotic value that is closer to unity the larger is $\bar{n}_f$. Before reaching the steady state, the dynamics go through different stages, which we classify as follows: (i) A fast relaxation towards an intermediate value of the magnetization with time scale $t \lesssim 10^2\kappa^{-1}$; this time scale decreases with $\bar{n}_f$. (ii) A transient regime where $\langle|\Theta|\rangle$ seems to grow logarithmically with time. (iii) Finally, the dissipation becomes dominant and brings the system to the asymptotic value, which is exponentially approached over time scales of the order of $10^6\kappa^{-1}$. These time scales are illustrated in Fig. 2(a) and here reported for $N = 50$ particles but generally depend on $N$, as we discuss later on.

We first observe that, being $\Delta_c$ negative, the growth of $\langle|\Theta|\rangle$ [Fig. 2(a)] corresponds to a monotonic decrease of the potential energy, $V = \hbar\Delta_c \bar{n} N \Theta^2$. In the fast relaxation stage (i), this decrease is well fitted by an exponential and is associated with a corresponding decrease of the relative fluctuations (see the inset), indicating that the cavity field exponentially grows and creates a mechanical potential, which increasingly localizes the atoms at its minima. The exponential potential depth growth is due to this

PRL 117, 083001 (2016) PHYSICAL REVIEW LETTERS week ending 19 AUGUST 2016

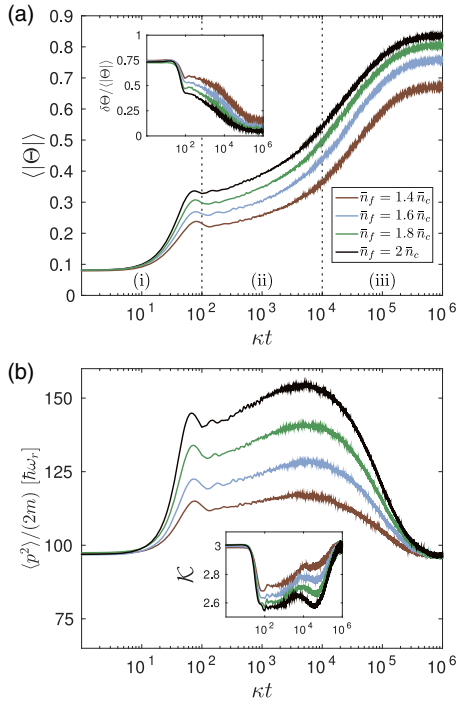


FIG. 2. Numerical simulation of the dynamics following a sudden quench along path $A$ using the SDE [31]. At $t = 0$, the atoms are in the stationary state of Eq. (1) for $\bar{n}_i = 0.01\bar{n}_c$ with $\Delta_c = -\kappa$, and $\bar{n}$ is quenched to the value $\bar{n}_f > \bar{n}_c$ [see the legend in (a)]. (a) The modulus of the order parameter $\langle|\Theta|\rangle$ and (b) the single-particle kinetic energy $\langle p^2/(2m)\rangle$ (in units of $\hbar\omega_r$) as a function of time (in units of $\kappa^{-1}$) for $N = 50$. The corresponding insets display the time evolution of the relative localization $\delta\Theta/\langle|\Theta|\rangle$, where $\delta\Theta = \sqrt{\langle\Theta^2\rangle - \langle|\Theta|\rangle^2}$, and of the kurtosis $\mathcal{K}$. The initial values $\langle|\Theta|\rangle_{t=0} \simeq 1/\sqrt{\pi N} \approx 0.08$ in (a) are due to finite $N$ [31]. Here, $\kappa \approx 390\omega_r$ and $N|U_0| = 0.05\kappa$. The three relaxation stages are indicated by the labels (i), (ii), and (iii).

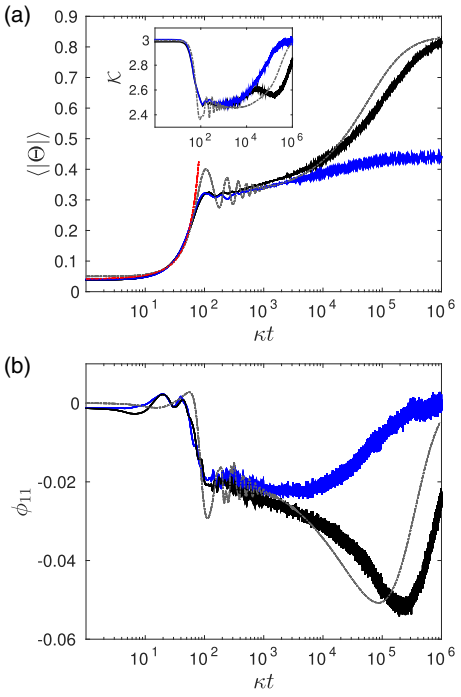


FIG. 3. Dynamics following a sudden quench along path $A$ with $\bar{n}_f = 2\bar{n}_c$ and $N = 200$. At $t = 0$, the atoms are in the stationary state of Eq. (1) for $\bar{n}_i = 0.01\bar{n}_c$ and $\Delta_c = -\kappa$. Subplot (a) compares the evolution of $\langle|\Theta|\rangle$ and $\mathcal{K}$ (inset) obtained by integrating Eq. (1) (black line) with the one found after setting $\Gamma = U_0 = 0$ (blue line). The red line is the fit obtained by a stability analysis of the homogeneous Vlasov solution, the dashed-dotted line by a mean-field model (see Supplemental Material [42]). (b) Time evolution of the QSS observable $\phi_{11}$ [Eq. (3)] corresponding to the curves in (a).

nonlinearity: The more the atoms become localized in the Bragg grating, the larger is the scattering amplitude and, thus, the potential depth. The increasing localization correspondingly augments the kinetic energy, as visible in Fig. 2(b). In this regime, thus, the total energy is conserved, and the dynamics is coherent and consists in a transfer of energy from spatial into momentum fluctuations. Correspondingly, the single-particle momentum distribution becomes increasingly nonthermal, as visible by inspecting the time evolution of the kurtosis, $\mathcal{K} = \langle p^4\rangle/\langle p^2\rangle^2$, shown in the inset in Fig. 2(b): $\mathcal{K}$ exponentially deviates from the value of the initial Gaussian ("thermal") state, for which $\mathcal{K}_{\text{gauss}} = 3$. We have verified that this dynamics is well described by a Vlasov equation for the single-particle distribution $f_1(x, p; t)$, which we derive assuming $f(x_1, \ldots, x_N; p_1, \ldots, p_N; t) = \prod_{j=1}^{N} f_1(x_j, p_j; t)$, integrating out the $N - 1$ variables from Eq. (1) for the initial uniform distribution and taking the thermodynamic limit (see Supplemental Material [42] and Ref. [43]). Figure 3(a) compares the result of the FPE with the predictions of the Vlasov equation (red curve), showing an excellent agreement in the fast relaxation regime. Numerical and analytical results show that the time scale of this dynamics depends on $N$ only through the parameter $\bar{n}$ (and is thus constant when Kac's scaling applies); see also Supplemental Material [42].

After this fast relaxation, the growth in the order parameter and in the kinetic energy seems logarithmic in time. This transient regime (ii) is of Hamiltonian origin: It exhibits damped oscillations, which can be understood as oscillations of the atoms at the minima. Energy is periodically transferred from the kinetic to the potential energy. Since the potential energy depends on a global variable, energy is exchanged between the particles by means of elastic collisions, hence damping the oscillations. Correspondingly, the kurtosis starts to increase towards the Gaussian value, showing that the sample starts to equilibrate. In order to verify this hypothesis, in Fig. 3(a), we compare the predictions of the full simulation (black

PRL 117, 083001 (2016) PHYSICAL REVIEW LETTERS week ending 19 AUGUST 2016

curves) for the order parameter and kurtosis with the ones obtained after setting $\Gamma = 0$ in Eq. (1) (blue curves): In the transient regime, the curves nearly overlap for $t \lesssim 10^4\kappa^{-1}$. Noise and dissipation, however, lead to a discrepancy between the predictions of the Hamiltonian and of the full FPE. This discrepancy becomes increasingly evident at longer time scales: When the dynamics is solely Hamiltonian, in fact, the kurtosis increases monotonically towards the Gaussian value. Because of the analogy with the Hamiltonian dynamics, some of the features of the transient regime are reminiscent of the HMF, where for a similar quench a violent relaxation is observed and then followed by prethermalization in a QSS [21,40]. In our case, for $\Gamma \neq 0$, as in Ref. [16], we do not find evidence of a superlinear scaling with $N$ of the QSS lifetime. The QSS lifetime, in fact, is limited by the dissipative effects, which have the same physical origin as the long-range conservative forces and whose characteristic time scale is linear in $N$ (see Supplemental Material [42] and Ref. [43]). Note that at the end of this stage the atoms are localized, but their temperature is hotter than $T_{\mathrm{eff}}$.

In stage (iii), when the effect of dissipation becomes relevant, the atoms are cooled and further localized at the minima. The kurtosis, however, further decreases till reaching a minimum, before increasing again towards the Gaussian value. We first compare this behavior with the predictions of a mean-field (MF) model, which we extract from Eq. (1) by means of the factorization ansatz; see Supplemental Material [42]. The gray lines in Fig. 3(a) and its inset show the MF predictions as a function of time and indicate that, even though MF reproduces qualitatively the dynamical features, it fails to give the correct time scale by at least one order of magnitude. Further insight is provided by the observable for QSSs [28], which we here define as

$$\phi_{11} = \frac{\langle |\sin(kx)p| \rangle}{\langle |\sin(kx)| \rangle \langle |p| \rangle} - 1. \tag{3}$$

When $\phi_{11} \neq 0$, the distribution is not factorizable into a kinetic and a potential term. Figure 3(b) displays the time evolution of $\phi_{11}$ for the Hamiltonian, mean-field, and full dynamics. In stages (i) and (ii), the three models predict approximately the same behavior. Instead, in stage (iii), $\phi_{11}$ evolves differently: For both MF and full FPE it exhibits a minimum, however reached at different times, which seems to possess the features of a scaling QSS, namely, a sequence of QSSs with identical correlations [28]. Its nature could be understood in terms of the onset of collective oscillations which are (almost) decoupled from noise and dissipation. Analogous behaviors have been reported for the case of atomic arrays in a cavity [29,44]. Since the trajectories of $\phi_{11}$ are different for the three types of simulations, the corresponding QSSs are expected to not be the same. In particular, the discrepancy between full FPE and MF in stage (iii) remains of the same order when scaling up the system, while instead Hamiltonian prethermalization tends towards the corresponding mean-field prediction. Figure 4 displays the relaxation time scales for the MF and the full FPE: The two curves suggest a linear increase with $N$ for both cases; nevertheless, they run parallel, thus showing that the discrepancy is a scalable effect. We deduce that this discrepancy is due to the momentum-position correlations due to noise, which are otherwise discarded in the MF treatment.

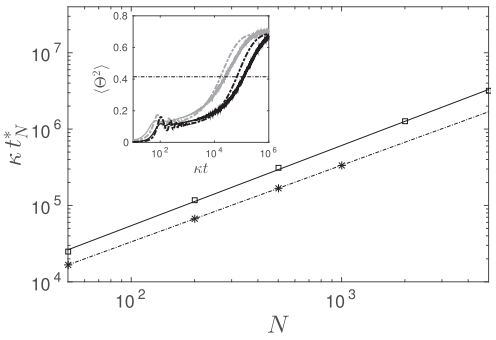


FIG. 4. Relaxation after a sudden quench along path $A$ for the parameters of Fig. 3 ($\bar{n}_f = 2\bar{n}_c$) and for different $N$. Inset: Time evolution of $\langle\Theta^2\rangle$ for $N = 50$ (gray) and $N = 200$ (black). The dashed lines are the prediction of the MF model (see Supplemental Material [42]). The horizontal dashed line indicates where $\langle\Theta^2\rangle$ has reached 60% of its stationary value and identifies the corresponding time $t^*_N$. Onset: Time $t^*_N$ (in units of $\kappa^{-1}$) as a function of $N$ for the full FPE (squares) and MF (stars). The lines are the corresponding linear fits in the log-log plot.

This prethermalization is not related to the critical slowing down observed in Ref. [45] but is due to the creation of correlations between momentum and position and is reminiscent of kinetic-stop dynamics [46]. It implies that cavity cooling of a large sample of atoms into the self-organized phase, corresponding to a sudden quench along path $B$, can be very slow and thus inefficient (see also Ref. [34]). Our analysis sets the stage for the development of a kinetic equation that is valid in the full quantum regime [47–51].

We acknowledge discussions with Ralf Betzholz, Cesare Nardini, and Stefano Ruffo and support by the German Research Foundation (DFG, DACH project "Quantum crystals of matter and light") and by the German Ministry of Education and Research (BMBF "Q.com").

[1] T. Chou, K. Mallick, and R. K. P. Zia, Rep. Prog. Phys. **74**, 116601 (2011).

[2] Y. Levin, R. Pakter, F. B. Rizzato, T. N. Teles, and F. P. C. Benetti, Phys. Rep. **535**, 1 (2014).

[3] A. Campa, T. Dauxois, and S. Ruffo, Phys. Rep. **480**, 57 (2009).
[4] P. Calabrese and J. Cardy, J. Stat. Mech. (2007) P06008.
[5] L. Foini, L. F. Cugliandolo, and A. Gambassi, Phys. Rev. B **84**, 212404 (2011); F. Iglói and H. Rieger, Phys. Rev. Lett. **106**, 035701 (2011).
[6] A. Polkovnikov, K. Sengupta, A. Silva, and M. Vengalattore, Rev. Mod. Phys. **83**, 863 (2011).
[7] P. C. Hohenberg and B. I. Halperin, Rev. Mod. Phys. **49**, 435 (1977); M. C. Cross and P. C. Hohenberg, Rev. Mod. Phys. **65**, 851 (1993).
[8] L. M. Sieberer, M. Buchhold, and S. Diehl, arXiv:1512.00637.
[9] A. Tomadin and R. Fazio, J. Opt. Soc. Am. B **27**, A130 (2010).
[10] A. Aspuru-Guzik and P. Walther, Nat. Phys. **8**, 285 (2012).
[11] P. Kirton and J. Keeling, Phys. Rev. Lett. **111**, 100404 (2013).
[12] L. J. Zou, D. Marcos, S. Diehl, S. Putz, J. Schmiedmayer, J. Majer, and P. Rabl, Phys. Rev. Lett. **113**, 023603 (2014).
[13] I. Carusotto and C. Ciuti, Rev. Mod. Phys. **85**, 299 (2013).
[14] V. Peano, C. Brendel, M. Schmidt, and F. Marquardt, Phys. Rev. X **5**, 031011 (2015).
[15] H. Ritsch, P. Domokos, F. Brennecke, and T. Esslinger, Rev. Mod. Phys. **85**, 553 (2013).
[16] S. Schütz and G. Morigi, Phys. Rev. Lett. **113**, 203002 (2014).
[17] F. Piazza and H. Ritsch, Phys. Rev. Lett. **115**, 163601 (2015).
[18] E. Tesio, G. R. M. Robb, G.-L. Oppo, P. M. Gomes, T. Ackemann, G. Labeyrie, R. Kaiser, and W. J. Firth, Phil. Trans. R. Soc. A **372**, 20140002 (2014).
[19] R. Bachelard, T. Manos, P. de Buyl, F. Staniscia, F. S. Cataliotti, G. De Ninno, D. Fanelli, and N. Piovella, J. Stat. Mech. (2010) P06009.
[20] I. Latella, A. Pérez-Madrid, A. Campa, L. Casetti, and S. Ruffo, Phys. Rev. Lett. **114**, 230601 (2015).
[21] M. Antoni and S. Ruffo, Phys. Rev. E **52**, 2361 (1995).
[22] A. Gabrielli, M. Joyce, and B. Marcos, Phys. Rev. Lett. **105**, 210602 (2010).
[23] T. M. Rocha Filho, A. E. Santana, M. A. Amato, and A. Figueiredo, Phys. Rev. E **90**, 032133 (2014).
[24] S. Gupta and D. Mukamel, Phys. Rev. Lett. **105**, 040602 (2010).
[25] P.-H. Chavanis, F. Baldovin, and E. Orlandini, Phys. Rev. E **83**, 040101 (2011).
[26] C. Nardini, S. Gupta, S. Ruffo, T. Dauxois, and F. Bouchet, J. Stat. Mech. (2012) P12010.
[27] P. H. Chavanis, Eur. Phys. J. B **87**, 120 (2014).
[28] M. Joyce and T. Worrakitpoonpon, Phys. Rev. E **84**, 011139 (2011); M. Joyce, J. Morand, F. Sicard, and P. Viot, Phys. Rev. Lett. **112**, 070602 (2014); M. Joyce, J. Morand, and P. Viot, Phys. Rev. E **93**, 052129 (2016).
[29] J. K. Asbóth, P. Domokos, and H. Ritsch, Phys. Rev. A **70**, 013414 (2004).
[30] S. Schütz, H. Habibian, and G. Morigi, Phys. Rev. A **88**, 033427 (2013).
[31] S. Schütz, S. B. Jäger, and G. Morigi, Phys. Rev. A **92**, 063808 (2015).
[32] P. Domokos and H. Ritsch, Phys. Rev. Lett. **89**, 253003 (2002).
[33] A. T. Black, H. W. Chan, and V. Vuletić, Phys. Rev. Lett. **91**, 203001 (2003).
[34] W. Niedenzu, T. Grießer, and H. Ritsch, Europhys. Lett. **96**, 43001 (2011).
[35] P. Horak, G. Hechenblaikner, K. M. Gheri, H. Stecher, and H. Ritsch, Phys. Rev. Lett. **79**, 4974 (1997).
[36] V. Vuletić and S. Chu, Phys. Rev. Lett. **84**, 3787 (2000).
[37] A. Vukics and P. Domokos, Phys. Rev. A **72**, 031401(R) (2005).
[38] J. K. Asbóth, P. Domokos, H. Ritsch, and A. Vukics, Phys. Rev. A **72**, 053417 (2005).
[39] Equation (1) contains also the processes scaling with the dynamical Stark shift $U_0 = g^2/\Delta_a$, where $g$ is the cavity vacuum Rabi frequency and $\Delta_a = \omega_L - \omega_a$ the detuning between the laser and atomic transition frequency. These processes are here small but accounted for in the numerical simulations [31].
[40] K. Jain, F. Bouchet, and D. Mukamel, J. Stat. Mech. (2007) P11008.
[41] P. Domokos, P. Horak, and H. Ritsch, J. Phys. B **34**, 187 (2001).
[42] See Supplemental Material at http://link.aps.org/supplemental/10.1103/PhysRevLett.117.083001 for the quenches along path $B$ in Fig. 1 and the derivation of the mean-field FPE and the Vlasov equation.
[43] S. B. Jäger, S. Schütz, and G. Morigi, Phys. Rev. A **94**, 023807 (2016).
[44] O. S. Mishina, New J. Phys. **16**, 033021 (2014).
[45] M. J. Bhaseen, J. Mayoh, B. D. Simons, and J. Keeling, Phys. Rev. A **85**, 013817 (2012).
[46] B. Olmos, I. Lesanovsky, and J. P. Garrahan, Phys. Rev. Lett. **109**, 020403 (2012).
[47] D. Nagy and P. Domokos, Phys. Rev. Lett. **115**, 043601 (2015).
[48] M. Kulkarni, B. Öztop, and H. E. Türeci, Phys. Rev. Lett. **111**, 220408 (2013).
[49] F. Piazza and P. Strack, Phys. Rev. A **90**, 043823 (2014).
[50] K. Baumann, C. Guerlin, F. Brennecke, and T. Esslinger, Nature (London) **464**, 1301 (2010); F. Brennecke, R. Mottl, K. Baumann, R. Landig, T. Donner, and T. Esslinger, Proc. Natl. Acad. Sci. U.S.A. **110**, 11763 (2013).
[51] M. Wolke, J. Klinner, H. Keßler, and A. Hemmerich, Science **337**, 75 (2012); J. Klinder, H. Keßler, M. Wolke, L. Mathey, and A. Hemmerich, Proc. Natl. Acad. Sci. U.S.A. **112**, 3290 (2015).

# Supplemental Material for Dissipation-Assisted Prethermalization in Long-Range Interacting Atomic Ensembles

### Mean-Field equation and Vlasov limit

The mean-field equation is derived from Eq. (1) in the main text by assuming $f(x_1,\dots,x_N;p_1,\dots,p_N;t)=\prod_{j=1}^{N} f_1(x_j,p_j;t)$, and integrating out the $N-1$ variables. It reads

$$\partial_t f_1 = \{H_{\mathrm{MF}}[f_1], f_1\} + \bar{n}\mathcal{L}_{\beta,\mathrm{MF}} f_1 \tag{S1}$$

where the mean-field Hamiltonian $H_{\mathrm{MF}}[f_1]$ is given by

$$H_{\mathrm{MF}}[f_1] = \frac{p^2}{2m} + \frac{2\hbar\Delta_c\bar{n}}{N}\left(\frac{1}{2}\cos(kx) + (N-1)\langle\cos(kx')\rangle_{f_1} - \frac{\hbar k\beta\kappa}{2m\Delta_c}(N-1)\langle p'\sin(kx')\rangle_{f_1}\right)\cos(kx)\,,$$

with $\langle\mathcal{A}(x',p')\rangle_{f_1} = \int_0^{\lambda}\mathrm{d}x'\int_{-\infty}^{\infty}\mathrm{d}p'\mathcal{A}(x',p')f_1(x',p')$ and $\mathcal{A}$ a phase space function. Furthermore the mean-field dissipator $\mathcal{L}_{\beta,\mathrm{MF}}$ is defined as

$$\mathcal{L}_{\beta,\mathrm{MF}} f_1 = \frac{\Gamma}{N}\sin^2(kx)\partial_p\left(p + \frac{m}{\beta}\partial_p\right) f_1\,.$$

The dissipator $\mathcal{L}_{\beta,\mathrm{MF}}$ is responsible for the relaxation of the system to the thermal stationary state with temperature $\beta^{-1} = k_B T_{\mathrm{eff}} = \hbar(\Delta_c^2+\kappa^2)/(-4\Delta_c)$ [S1–S3]. Since the dissipator decreases with $N^{-1}$ (for increasing $N$), the mean-field predicts a relaxation timescale that extends linearly with $N$. Although the relaxation for the full FPE, Eq. (1) in the main text, is orders of magnitudes slower (see Fig. 4 in the paper), the corresponding growth of the timescale with $N$ is almost indistinguishable from a linear one.

In order to make some statements for the short time dynamics we derive the Vlasov equation. This equation is derived from Eq. (S1) after performing the limit $N\to\infty$ with $NS^2$ =const. and reads

$$\partial_t f_1 + \frac{p}{m}\partial_x f_1 - \partial_x V[f_1]\partial_p f_1 = 0\,, \tag{S2}$$

where the Vlasov potential $V[f_1]$ is

$$V[f_1] = 2\hbar\Delta_c\bar{n}\left(\langle\cos(kx')\rangle_{f_1} - \frac{\hbar k\beta\kappa}{2m\Delta_c}\langle p'\sin(kx')\rangle_{f_1}\right)\cos(kx)\,.$$

The stability analysis of Eq. (S2) shows that a spatially homogeneous distribution is unstable against small fluctuations $\delta f$ when $\bar{n}_f > \bar{n}_c$. The fluctuations exhibit exponential growth at rate $\gamma$, which monotonously increases with $\bar{n}_f$ and is a solution of the equation

$$[1 - 2\kappa\gamma/(\Delta_c^2+\kappa^2)]F(\gamma)\bar{n}_f/\bar{n}_c = 1\,, \tag{S3}$$

with $F(\gamma) = 1 - \sqrt{\pi}b\exp(b^2)\mathrm{erfc}(b)$, $b^2 = \hbar\gamma^2\beta/(4\omega_r)$ and erfc is the complementary error function. The solution (red line in Fig. 3(a) in the main text for a fixed value of $\bar{n}_f$) well fits the numerical result in the fast relaxation regime. Thus, this initial behaviour is analogous to the violent relaxation observed in the HMF and has mainly Hamiltonian origin.

### Quenches along path B

Figure S1 displays a sudden quench in the detuning $\Delta_c$ while keeping $\Omega$, hence the laser amplitude, constant. This quench corresponds to path B of Fig. 1(b) in the paper and alters both $\bar{n}$ and $\beta$ in Eq. (1), namely both the asymptotic order and temperature. We consider quenches from the disordered (with $\Delta_c=-4\kappa$) to the ordered phase (with $\Delta_c=-\kappa$), and vice versa, assuming that the initial state is the asymptotic state of the parameter choice before the quench. Also in this case the three regimes can be identified. Remarkably, for the quench from the ordered to the disordered phase, the system remains for long times trapped in an ordered pattern. The pattern stays stable due to the long-range forces. This transient is further accompanied by a momentum distribution that is narrower than the initial and the asymptotic value, as visible in the inset of subplot (b). On

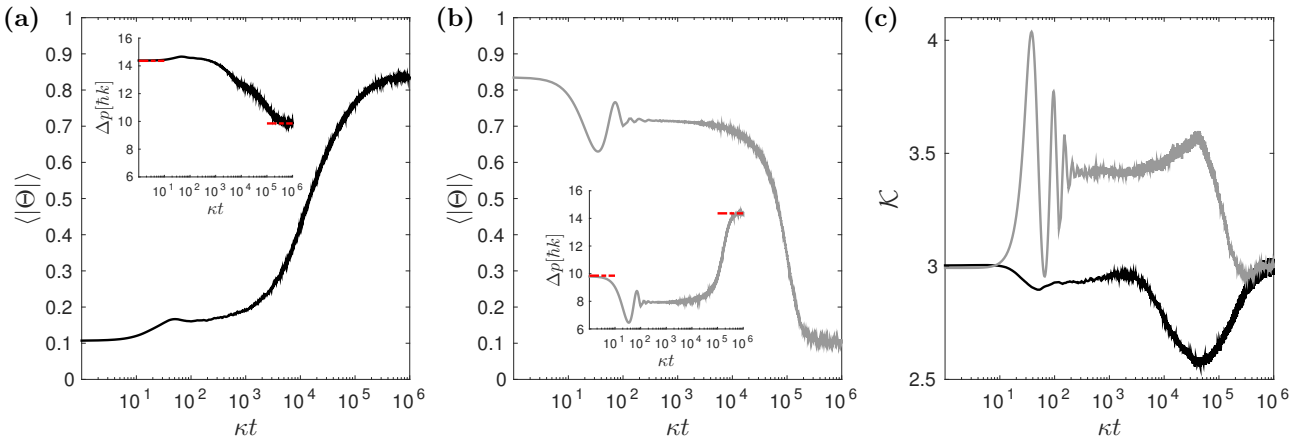


FIG. S1: Numerical simulation of the dynamics for $N = 50$ atoms following a sudden quench along path B, where $\Delta_c$ is varied but the laser intensity is kept fixed. The black line corresponds to the results for the evolution when the value of the detuning is suddenly quenched from $\Delta_c = -4\kappa$ with $\bar{n}_i \approx 0.44\,\bar{n}_c$ to $\Delta_c = -\kappa$ with $\bar{n}_f = 2\,\bar{n}_c$. The grey line displays the case where initial and final points are swapped. (a) and (b): Time evolution of $\langle|\Theta|\rangle$ and $\Delta p$ (inset) as a function of time (in units of $\kappa^{-1}$). Subplot (c) displays the behaviour of the kurtosis $\mathcal{K}$.

the other hand, the momentum distribution is markedly non-Gaussian, as visible in (c). This behaviour shows that, even if the final value of the parameter $\bar{n}$ is well below threshold and the asymptotic number of intracavity photons $\langle\hat{a}^\dagger\hat{a}\rangle \approx N\bar{n}\langle\Theta^2\rangle$ is small, yet there is a metastable regime in which the number of intracavity photons is significantly larger, due to the metastable atomic patterns which support superradiant scattering of photons into the resonator until they decay.

[S1] S. Schütz and G. Morigi, Phys. Rev. Lett. **113**, 203002 (2014).
[S2] S. Schütz, S. B. Jäger, and G. Morigi, Phys. Rev. A **92**, 063808 (2015).
[S3] S. B. Jäger, S. Schütz, and G. Morigi, Phys. Rev. A **94**, 023807 (2016).

## 2.3.3 Quenches across the self-organization transition in multi-mode cavities

New Journal of Physics **20**, 025004 (2018)

DOI: https://doi.org/10.1088/1367-2630/aaa161

Authors: Tim Keller [1,4], Valentin Torggler[2,4] , Simon B. Jäger[1] , Stefan Schütz[1,3] , Helmut Ritsch[2], and Giovanna Morigi[1]

[1] *Theoretische Physik, Universität des Saarlandes, D-66123 Saarbrücken, Germany*
[2] *Institut für Theoretische Physik, Universität Innsbruck, A-6020 Innsbruck, Austria*
[3] *icFRC, IPCMS (UMR 7504) and ISIS (UMR 7006), University of Strasbourg and CNRS, F-67000 Strasbourg, France*
[4] First authors

**Author Contributions:**
T. Keller, S. B. Jäger, H. Ritsch, and G. Morigi developed the theoretical model. Analytical results were derived by T. Keller, V. Torggler, and S. B. Jäger. Numerical simulations were performed and developed by S. Schütz, T. Keller, and V. Torggler. The results and calculations were discussed and checked by all authors. The article was mainly written by V. Torggler, S. B. Jäger, H. Ritsch, and G. Morigi.

**Abstract:**
A cold dilute atomic gas in an optical resonator can be radiatively cooled by coherent scattering processes when the driving laser frequency is tuned close to but below the cavity resonance. When the atoms are sufficiently illuminated, their steady state undergoes a phase transition from a homogeneous distribution to a spatially organized Bragg grating. We characterize the dynamics of this self-ordering process in the semi- classical regime when distinct cavity modes with commensurate wavelengths are quasi-resonantly driven by laser fields via scattering by the atoms. The lasers are simultaneously applied and uniformly illuminate the atoms; their frequencies are chosen so that the atoms are cooled by the radiative processes, and their intensities are either suddenly switched or slowly ramped across the self-ordering transition. Numerical simulations for different ramp protocols predict that the system will exhibit long-lived metastable states, whose occurrence strongly depends on the initial temperature, ramp speed, and the number of atoms.

New Journal of Physics
The open access journal at the forefront of physics

Deutsche Physikalische Gesellschaft DPG IOP Institute of Physics

PAPER • OPEN ACCESS

# Quenches across the self-organization transition in multimode cavities

To cite this article: Tim Keller *et al* 2018 *New J. Phys.* **20** 025004

IOP Publishing New J. Phys. 20 (2018) 025004 https://doi.org/10.1088/1367-2630/aaa161

New Journal of Physics
The open access journal at the forefront of physics

Deutsche Physikalische Gesellschaft DPG
IOP Institute of Physics

Published in partnership with: Deutsche Physikalische Gesellschaft and the Institute of Physics

OPEN ACCESS

RECEIVED
22 September 2017

REVISED
30 November 2017

ACCEPTED FOR PUBLICATION
13 December 2017

PUBLISHED
7 February 2018



PAPER

# Quenches across the self-organization transition in multimode cavities

**Tim Keller**[1,4], **Valentin Torggler**[2,4], **Simon B Jäger**[1], **Stefan Schütz**[1,3], **Helmut Ritsch**[2] and **Giovanna Morigi**[1]

[1] Theoretische Physik, Universität des Saarlandes, D-66123 Saarbrücken, Germany
[2] Institut für Theoretische Physik, Universität Innsbruck, A-6020 Innsbruck, Austria
[3] icFRC, IPCMS (UMR 7504) and ISIS (UMR 7006), University of Strasbourg and CNRS, F-67000 Strasbourg, France
[4] First authors

**E-mail:** simonjaeger1@aol.com

**Keywords:** cavity QED, long-range interactions, out-of-equilibrium dynamics, cavity cooling, stochastic differential equations, metastability, self-organization

## Abstract

A cold dilute atomic gas in an optical resonator can be radiatively cooled by coherent scattering processes when the driving laser frequency is tuned close to but below the cavity resonance. When the atoms are sufficiently illuminated, their steady state undergoes a phase transition from a homogeneous distribution to a spatially organized Bragg grating. We characterize the dynamics of this self-ordering process in the semi-classical regime when distinct cavity modes with commensurate wavelengths are quasi-resonantly driven by laser fields via scattering by the atoms. The lasers are simultaneously applied and uniformly illuminate the atoms; their frequencies are chosen so that the atoms are cooled by the radiative processes, and their intensities are either suddenly switched or slowly ramped across the self-ordering transition. Numerical simulations for different ramp protocols predict that the system will exhibit long-lived metastable states, whose occurrence strongly depends on the initial temperature, ramp speed, and the number of atoms.

## 1. Introduction

Laser light creates an attractive optical potential for cold atoms when far detuned below an optical transition. Such potential can be significantly enhanced if the light is confined by an optical resonator [1–4]. In addition, if the laser illuminates the atoms, trapping is induced by a dynamical optical potential emerging from the interference between the scattered light and the laser, which tends to order the particles at the maxima of the intensity [4, 5]. The interference contrast and thus the trapping depends on the relative positions of the scattering atoms. Therefore, this phenomenon can be also understood in terms of an effective long-range force, which is mediated by the collectively scattered photons [5–9]. This force also has a dissipative component, which is due to the dissipative nature of the resonator and which cools the atoms when the pump is tuned below the cavity resonance [3, 10]. Theoretical studies with single-mode resonators have predicted that this dissipation can establish long-range correlations and support the onset of metastable ordered structures [11, 12].

In a multimode cavity and for several illumination frequencies, competing ordering processes are present and lead to richer phase dynamics. In a two-mode cavity, like the one depicted in figure 1(a), the transition to self-organization can be a phase transition of the first or second order depending on the laser intensities and on their relative strength [13]. The corresponding self-ordered phases can exhibit superradiant scattering either in one or in both cavity modes, as illustrated in figure 1(b), while the asymptotic distribution of the atoms can be thermal provided that the lasers' frequencies are suitably chosen [13]. In our example the particles can order in a lattice at a given length scale $\lambda$ and/or on a lattice with half the period $\lambda/2$. For these settings we numerically analyze the semi-classical dynamics following sudden quenches or slow ramps of the laser intensities across the thresholds separating the homogeneous from one of the self-organized phases. We describe the evolution by stochastic differential equations, which correspond to the Fokker–Planck equation derived in [14] for a similar system. We find that even at very long times the atoms' spatial distribution strongly depends on the initial

IOP Publishing New J. Phys. 20 (2018) 025004 T Keller et al

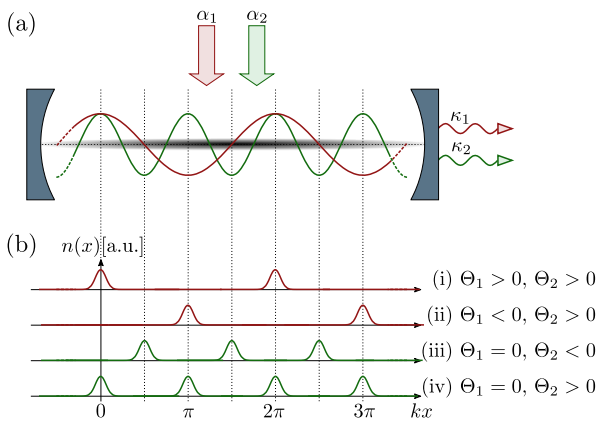


**Figure 1.** (**a**) Cold atoms are confined within an optical cavity and move along the cavity axis ($x$ axis). They coherently scatter photons from transverse lasers with rescaled amplitudes $\alpha_1$ and $\alpha_2$ into the (correspondingly) resonant cavity modes with spatial mode functions $\cos(kx)$ (red) and $\cos(2kx)$ (green) and loss rates $\kappa_1$ and $\kappa_2$, respectively. (**b**) Sketch of the atomic density distribution $n(x)$ along the cavity axis (in units of $1/k$) for the four possible stationary self-organized orders. On the right we report the corresponding values of the quantities $\Theta_1$ and $\Theta_2$, which signal the Bragg order in modes 1 and 2, respectively. See text and [13] for details.

temperature, ramp speed, and quench protocol, such that the system gets trapped in long-lived metastable states. In particular, for quenches starting with ensembles at low temperatures, the buildup of long-range order requires longer times than that for higher initial temperatures does.

Our work is organized as follows: in section 2 we introduce the system and the semi-classical equations describing the dynamics. The atoms' stationary properties are then summarized in a phase diagram, which is derived from [13]. In section 3 we numerically study the real-time dynamics when the parameters are varied within the phase diagram according to different quench protocols. In section 4 we analyze the dynamics of the distributions from the spatially homogeneous to the organized ones with different momentum widths. In section 5 we compare the predictions of the stochastic differential equations we employ with an extended approach including the dynamical evolution of the field modes introduced in [15, 16]. Conclusions are drawn and future perspectives are discussed in section 6.

## 2. Semi-classical dynamics

The system we consider consists of a gas of $N$ cold atoms with mass $m$, which are trapped inside a high-finesse optical resonator and coherently scatter laser light into the cavity modes. The atomic motion is confined along the cavity axis (here the $x$ axis) by a tight external dipole trap [17, 18] and is here described in the semi-classical limit.

The geometry of the setup is illustrated in figure 1. Lasers with (rescaled) intensity $\alpha_n$ propagate in a direction orthogonal to the cavity axis and are quasi-resonant with the standing wave cavity modes $\cos(nkx)$ with frequency $\omega_{c,n}$ and wave number $nk$ ($n = 1, 2$)[5]. The lasers have frequency $\omega_{p,n}$ and linear polarization, which is parallel to that of the corresponding cavity mode. Each pair of laser and cavity mode couples to an atomic dipolar transition at frequency $\omega_{a,n}$, where $\Omega_{p,n}$ and $g_n$ are the laser and vacuum Rabi frequency, respectively. Spontaneous scattering processes are suppressed when the absolute value of the detuning $\Delta_{a,n} = \omega_{p,n} - \omega_{a,n}$ exceeds the coupling strength and the detuning $\Delta_n = \omega_{p,n} - \omega_{c,n}$ between the laser and cavity mode by orders of magnitude: $|\Delta_{a,n}| \gg \Omega_{p,n}, g_n, |\Delta_n|$. The relevant dissipative process is given by cavity decay, and we denote by $\kappa_n$ the loss rate of cavity mode $n = 1, 2$.

In the so-called bad cavity limit, assuming that the cavity field loss rates are faster than the rate of the dynamics of the atomic motion, one can eliminate the cavity field variables from the equations of motion of the atoms by means of coarse graining in time. This gives rise to an effective model, where the atoms experience a long-range interaction mediated by the cavity photons, while retardation effects and fluctuations of the cavity field are responsible for friction forces and diffusion. In the semi-classical limit one can derive a Fokker–Planck equation for the atoms' position and momentum distribution, assuming that the single-atom momentum distribution has a width $\Delta p$ which, at all instants of time, is orders of magnitude greater than the photon recoil $\hbar k$: $\Delta p \gg \hbar k$ [13, 14, 20]. The corresponding stochastic differential equations read as

[5] This can be realised by assuming $\omega_{c,2} = 2\omega_{c,1} \equiv 2\omega_c$, which yields $k_2 = 2k_1 \equiv 2k$. Another possible realisation, where $\omega_{c,1} \approx \omega_{c,2}$, has been discussed in [13]; it uses two optical single-mode cavities crossing at an angle of 60°. For a similar experimental setup see also [19].

IOP Publishing New J. Phys. 20 (2018) 025004 T Keller et al

$$\mathrm{d}x_j = \frac{p_j}{m}\mathrm{d}t, \tag{1a}$$

$$\mathrm{d}p_j = (F_{j,\mathrm{ad}} + F_{j,\mathrm{ret}})\mathrm{d}t + \mathrm{d}W_j^{(1)} + \mathrm{d}W_j^{(2)}, \tag{1b}$$

where

$$F_{j,\mathrm{ad}} = -\sum_{n=1,2} 2\hbar nk\frac{\alpha_n}{\hbar\beta_n}\sin(nkx_j)\Theta_n, \tag{2}$$

$$F_{j,\mathrm{ret}} = -\sum_{n=1,2} \frac{\hbar(nk)^2}{m}\alpha_n\frac{\kappa_n}{-\Delta_n}\sin(nkx_j)\frac{1}{N}\sum_{l=1}^{N} p_l\sin(nkx_l), \tag{3}$$

and

$$\alpha_n = \frac{4NS_n^2\Delta_n^2}{(\Delta_n^2+\kappa_n^2)^2}, \tag{4}$$

$$\beta_n = \frac{-4\Delta_n}{\hbar(\Delta_n^2+\kappa_n^2)}. \tag{5}$$

Here, $S_n = g_n\Omega_n/\Delta_{\mathrm{a},n}$ is the amplitude of coherent scattering by a single atom and has the dimension of a frequency, while $\mathrm{d}W_j^{(1)}$ and $\mathrm{d}W_j^{(2)}$ in equation (1*b*) describe Wiener processes, which fulfill $\langle \mathrm{d}W_i^{(n)}\rangle = 0$ and $\langle \mathrm{d}W_i^{(n)}\mathrm{d}W_j^{(m)}\rangle = 2D_{ij}^n\delta_{nm}\mathrm{d}t$ ($n$, $m = 1$, 2 and $i$, $j = 1, \ldots, N$). Here,

$$D_{ij}^n = (\hbar nk)^2\frac{\alpha_n}{\hbar N\beta_n}\left(\frac{\kappa_n}{-\Delta_n}\right)\sin(nkx_i)\sin(nkx_j). \tag{6}$$

Finally, the parameter

$$\Theta_n = \frac{1}{N}\sum_{i=1}^{N}\cos(nkx_i) \tag{7}$$

quantifies the Bragg ordering of the atoms in the cavity mode with wave number $nk$. In particular, $|\Theta_n| = 1$ when the atoms are localized either at the maxima or at the minima of $\cos(nkx)$, which is the configuration which maximizes the intracavity field intensity. We identify $\Theta_n$ with the order parameter for self-organization in the corresponding cavity mode [13]. Below, we denote by 'long-wavelength order' any configuration with a non-vanishing value of $\Theta_1$, corresponding to a Bragg grating with period $\lambda = 2\pi/k$. Similarly, 'short-wavelength order' refers to a configuration with $\Theta_2 \neq 0$, corresponding to a Bragg grating with $\lambda/2$. Note that here and in the rest of the paper we discard the dynamical Stark shift of the cavity frequency assuming that this is much smaller than the cavity mode linewidth $Ng_n^2/|\Delta_{\mathrm{a},n}| \ll \kappa_n$. For details refer to [13].

### 2.1. Stationary states

Analysis of the Fokker–Planck equation on the basis of equation (1) allows one to identify the conditions for the existence of a stationary state. This state exists provided that $\Delta_n < 0$ and $\beta_1 = \beta_2 \equiv \beta$ (see equation (5)). In this case the atoms' distribution in the steady state reads as [13]

$$f_{\mathrm{st}}(x_1, p_1, \ldots, x_N, p_N) = \frac{\exp(-\beta H_{\mathrm{eff}})}{\mathcal{Z}(\beta)} \tag{8}$$

where $H_{\mathrm{eff}}$ is the effective Hamiltonian derived after eliminating the cavity field variables,

$$H_{\mathrm{eff}} = \sum_{j=1}^{N}\frac{p_j^2}{2m} - \sum_{n=1,2} N\frac{\alpha_n}{\beta_n}\Theta_n^2, \tag{9}$$

while $\mathcal{Z}(\beta)$ denotes the partition function:

$$\mathcal{Z}(\beta) = \frac{1}{\Delta^N}\int_{-\infty}^{\infty}\mathrm{d}p_1\ \ldots\ \int_{-\infty}^{\infty}\mathrm{d}p_N\int_0^{\lambda}\mathrm{d}x_1\ \ldots\ \int_0^{\lambda}\mathrm{d}x_N\ \mathrm{e}^{-\beta H_{\mathrm{eff}}}, \tag{10}$$

with $\lambda = 2\pi/k$ and $\Delta = 2\pi\hbar$ as the single particle unit phase space volume. In the following we assume that the cavity decay rates are equal,

$$\kappa_1 = \kappa_2 =: \kappa, \tag{11}$$

so that the condition for the existence of the stationary state in equation (8) becomes

$$\Delta_1 = \Delta_2 =: \Delta_c < 0. \tag{12}$$

The phase diagram of the system can be determined by using the steady state, equation (8), in the form of a thermal state. On the basis of this observation we introduce the temperature $T$ of the stationary state, which is defined as

IOP Publishing New J. Phys. 20 (2018) 025004 T Keller et al

$$k_B T = \beta^{-1} = \frac{\hbar(\Delta_c^2 + \kappa^2)}{-4\Delta_c}, \tag{13}$$

with $k_B$ as the Boltzmann constant. The steady-state temperature $T$ has the same functional dependence on $\Delta_c$ and $\kappa$ as for a single-mode cavity [7, 14]. We can further define the free energy per particle $\mathcal{F}$ using formal equivalence with the canonical ensemble of equilibrium statistical mechanics [7]:

$$\mathcal{F} = -\frac{1}{N\beta}\ln(\mathcal{Z}(\beta)). \tag{14}$$

Following the procedure detailed in [7, 12, 13] we can calculate $\mathcal{F}$ as

$$\mathcal{F} = \inf_{\theta_1,\theta_2} F(\theta_1, \theta_2) \tag{15}$$

with

$$\beta F(\theta_1, \theta_2) = \frac{\ln(\pi\hbar\omega_r\beta)}{2} + \alpha_1\theta_1^2 + \alpha_2\theta_2^2 - \ln(I(\theta_1, \theta_2)) \tag{16}$$

and

$$I(\theta_1, \theta_2) = \int_0^{2\pi} \mathrm{d}q\ \mathrm{e}^{2\alpha_1\theta_1\cos(q)+2\alpha_2\theta_2\cos(2q)}. \tag{17}$$

Here $\omega_r = \hbar k^2/(2m)$ is the recoil frequency. We determine the value of $\mathcal{F}$ in an appropriately defined thermodynamic limit, which consists in keeping $\alpha_n$ constant for $N \to \infty$. The global minima of $F$ are the resulting stationary phases. The corresponding points $(\theta_{1,\min}, \theta_{2,\min})$ where $F$ achieves its minimum are the stationary values for the order parameters $\Theta_1 = \theta_{1,\min}$ and $\Theta_2 = \theta_{2,\min}$; they are determined by $\alpha_1$ and $\alpha_2$. When the fields are sufficiently weak, then $\Theta_1 = \Theta_2 = 0$, the density is homogeneous and there is no structural order. We call this phase paramagnetic, borrowing the notation of the generalized Hamiltonian mean-field model (GHMF) [21–23] to which this model can be mapped. The possible ordered phases in the steady state are illustrated in figure 1(b) and take one of four sets of values. In particular, the ferromagnetic phase is characterized by (i) $\Theta_1 > 0$, $\Theta_2 > 0$, and (ii) $\Theta_1 < 0$, $\Theta_2 > 0$, exhibiting Bragg order in both cavity modes. In contrast, the nematic phases, (iii) and (iv), are characterized by no order in the long-wavelength mode, $\Theta_1 = 0$, while $\Theta_2$ can be either negative or positive.

We note that the spatial distributions depicted in figure 1(b) corresponding to phases (i), (ii), (iii), and (iv) are only possible configurations out of many. For example configuration (i) can also correspond to all atoms sitting at one site $kx = 0$. Order here refers to Bragg gratings corresponding to the long- and short-wavelength modes. No long-wavelength order is found in the case of $\Theta_1 = 0$, where photons scattered into the long-wavelength mode destructively interfere. However, $\Theta_1$ cannot give more detailed information about the positions of the atoms in the long-wavelength mode. The same is true for short-wavelength order and $\Theta_2$.

The resulting phase diagram in the $\alpha_1 - \alpha_2$ plane, shown in figure 2, reproduces that in [13]. The phases are separated by either first- or second-order transitions, which have been determined using Ehrenfest's criterion [23]. The shaded areas show stability regions in which the free energy has a local minimum that corresponds to the paramagnetic (dark gray region) and nematic (light gray region) phases. Examples of the free-energy landscape in the $\Theta_1 - \Theta_2$ plane are shown in subplots (b) and (c). Subplot (b) corresponds to the parameters of the red bullet labeled (b) in subplot (a): Here, the free energy exhibits two symmetric global minima which correspond to the ferromagnetic phase. In subplot (c), which corresponds to the parameters of the red bullet labeled (c), there is an additional local minimum corresponding to a nematic phase. In the latter there is only ordering in the short-wavelength lattice, while $\Theta_1 = 0$. We call this region *bistable*, which refers to the existence of a second, metastable state in which the system can be dynamically trapped.

## 3. Dynamics of self-organization

We now examine the dynamics of the system when the values of $\alpha_1$ and $\alpha_2$ are varied as a function of time. Experimentally, this corresponds to varying the pump laser intensities or their detuning with respect to the cavity mode frequencies. At time $t = 0$ we assume that the system is prepared in the stationary state of a paramagnetic phase, described by the distribution in equation (8), by setting $\alpha_n = \alpha_{ni} \ll 1$ in equation (9) ($n = 1, 2$). The values $\alpha_n$ appearing in the equations of motion (1) are then varied in time, by performing either (i) a sudden quench, i.e. a sudden switching of the values to $\alpha_{1f}$ and $\alpha_{2f}$, or (ii) a slow quench, which consists in varying $\alpha_n(t)$ monotonically and continuously in time towards the final values $\alpha_{1f}$ and $\alpha_{2f}$. We choose the final values $\alpha_{nf}$ in the ferromagnetic phase. The quench protocols we consider are illustrated by the green lines in figure 2(a): for sudden quenches, the initial and final values are two points connected by a green line. A slow quench sweeps across the intermediate points along the line. We are interested in determining the dynamics leading to the steady state.

IOP Publishing New J. Phys. 20 (2018) 025004 T Keller et al

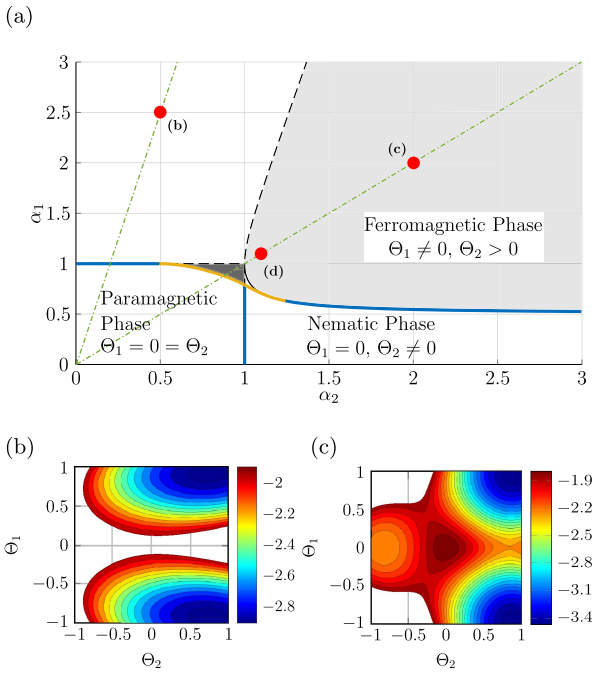


**Figure 2.** (a) Phase diagram of the stationary phases, corresponding to the global minima of equation (16), in plane $\alpha_1 - \alpha_2$. Blue (yellow) lines indicate second (first) order phase transitions. The light gray area (dark gray area) within the ferromagnetic phase indicates the parameter region where the nematic (paramagnetic) phase is the local minimum of the free energy. The red circles labeled (b) and (c) indicate the parameters for which the contour plots of free energy in subplots (b) and (c) are shown in the $\Theta_1 - \Theta_2$ landscape. The free energy in subplot (b) exhibits two global minima at $\Theta_1 = \pm 0.92$ and $\Theta_2 = 0.73$; in (c) the two global minima of the ferromagnetic phase are at $\Theta_1 = \pm 0.97$ and $\Theta_2 = 0.88$, and the local minimum in the nematic phase is at $\Theta_1 = 0$ and $\Theta_2 = -0.83$ (the contour of $\mathcal{F}$ is below a convenient threshold). The green dash–dot lines in subplot (a) illustrate the paths of the quench protocols discussed in section 3. Circle (d) indicates the parameters of the quench discussed in section 3.3.

In what follows we perform numerical simulations of equation (1) using the parameters of a gas of $^{85}$Rb atoms. In particular, we take $k = 2\pi/\lambda$ with $\lambda = 780$ nm as the wavelength of the $D_2$ line. The corresponding recoil frequency is $\omega_r = 2\pi \times 3.86$ kHz. The cavity linewidth is taken to be $\kappa = 2\pi \times 1.5$ MHz, so that $\kappa \approx 388.6\omega_r$. A possible realization of the two-mode setup here considered has been discussed in [13, 19].

### 3.1. Sudden quench into the ferromagnetic phase

We first consider sudden quenches from $\alpha_{1i}$, $\alpha_{2i}$ in the paramagnetic phase to $\alpha_{1f}$, $\alpha_{2f}$ in the ferromagnetic phase, keeping $\alpha_{1i}/\alpha_{2i} = \alpha_{1f}/\alpha_{2f} = 5$. The initial values are vanishingly small and the atoms are at the corresponding stationary distribution, which is a thermal distribution at the temperature determined by the corresponding detuning, equation (13), with homogeneous density. The detuning before and after the quench is taken to be equal; thus it is expected that the atoms reach a thermal distribution with the same temperature as the initial state.

Figure 3 shows the distribution $\mathcal{P}_t(\Theta)$ for order parameters $\Theta_1$ and $\Theta_2$ as a function of time for $(\alpha_{1f}, \alpha_{2f}) = (2.5, 0.5)$. It is defined as a time sequence of normalized histograms:

$$\mathcal{P}_t(\Theta) = \frac{\#\text{ trajectories with } \Theta(t) \in [\Theta - \Delta_\Theta/2,\ \Theta + \Delta_\Theta/2]}{\#\text{ trajectories } \times \Delta_\Theta}, \tag{18}$$

where $\Theta$ is calculated on each trajectory of the simulations with the stochastic differential equations and its value is determined according to the precision $\Delta_\Theta$ of the grid in $\Theta$. We observe that at a given time scale of the order of $10^2/\kappa$, $\mathcal{P}_t(\Theta_1)$ splits into two branches corresponding to two possible orders in the long-wavelength lattice. This symmetry breaking is well known from the single-mode case [5]. The order parameter of the short-wavelength mode $\Theta_2$, which is weakly pumped, substantially grows to a positive value long after the symmetry breaking. The fact that $\mathcal{P}_t(\Theta_2)$ vanishes for negative $\Theta_2$ values comes from the ordering of the atoms close to the anti-nodes of the dominant long-wavelength mode field $\cos(kx)$ (see figure 1).

The distributions $\mathcal{P}(\Theta_n)$ at the asymptotics are reported in the right panels of figure 3. They are obtained by averaging $\mathcal{P}_t(\Theta_n)$ over times $t \geqslant 10^6/\kappa$, where a stable configuration is reached. Formally

IOP Publishing New J. Phys. 20 (2018) 025004 T Keller et al

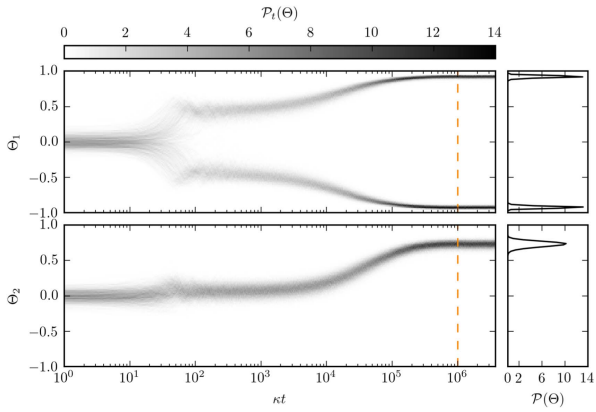


**Figure 3.** Dynamics following a sudden quench from $\alpha_{1i}$, $\alpha_{2i} \ll 1$ to $\alpha_{1f} = 2.5$, $\alpha_{2f} = 0.5$ with the detuning kept constant $\Delta_c = -\kappa$. The left panels display the contour plots of distribution $\mathcal{P}_t(\Theta)$ (equation (18)) for $\Theta = \Theta_1$ and $\Theta = \Theta_2$ as a function of time (in units of $1/\kappa$). The distribution is extracted from numerical simulations using equation (1) for $N = 100$ atoms and 1000 trajectories. The grid in $\Theta$ for the left panels has a minimum step $\Delta_\Theta = 2/111$; the grayscale gives the relative weight. The right panels display the distributions $\mathcal{P}(\Theta_1)$ and $\mathcal{P}(\Theta_2)$ as a function of $\Theta_1$ and $\Theta_2$, respectively (see equation (19)). Here, the time average is obtained for $N_t = 113$ instants of time chosen between $t_1 = 10^6/\kappa$ and $t_f = 3.77 \times 10^6/\kappa$. The vertical dashed lines in the left panels mark the instant of time $t_1 = 10^6/\kappa$.

$$\mathcal{P}(\Theta) = \sum_{i=1}^{N_t} \mathcal{P}_{t_i}(\Theta)/N_t, \tag{19}$$

where $N_t$ is the number of instants of times at which the distribution is sampled in the interval $[t_1,\ t_f]$, with $t_1 = 10^6/\kappa$ and $t_f = t_{N_t} > t_1$. Comparing the widths of the distributions in the right panels of figure 3 one observes that after sufficiently long times the long-wavelength order parameter fluctuates less than the short-wavelength order parameter.

Figures 4(a)–(b) display the dynamics of the mean absolute value of the order parameters for different values of $N$. Figure 4(c) shows the time evolution of the fluctuations of the order parameters $\delta\Theta_n = \sqrt{\langle\Theta_n^2\rangle - \langle|\Theta_n|\rangle^2}$ for $N = 100$ particles. The order parameters asymptotically tend to the values predicted by the free energy, indicated by the horizontal dashed lines, for a time scale of the order of $10^6/\kappa$. Meanwhile the fluctuation $\delta\Theta_1$ relaxes to a much smaller value than the asymptotic value of $\delta\Theta_2$ reproducing the widths of the distributions in the right panels in figure 3. The time evolution of $\langle|\Theta_1|\rangle$, in particular, is reminiscent of the one observed for quenches into the ferromagnetic phase in a single-mode resonator [11]. It can be separated into three stages which we call (in order of their temporal appearance) (i) violent relaxation, which corresponds to an exponential increase of the absolute value of the order parameter $\langle|\Theta_1|\rangle$; (ii) transient dynamics, which corresponds to power-law scaling with time; and (iii) the relaxation phase, where the mean values tend exponentially towards the asymptotic value. Violent relaxation can be described by a mean-field model [12]; in the transient stage coherent dynamics prevails, while the relaxation stage is dominated by dissipation [11]. The transient and relaxation stages are characterized by time scales which increase with $N$ but have different functional dependence [12]. The time scale $10^6/\kappa$ can here be identified as the one at which the asymptotic state is reached for $N \lesssim 200$, while for larger numbers of particles longer time scales shall be considered.

Interestingly, in the transient phase there is ordering only in the long-wavelength mode of the cavity, while ferromagnetic order is finally established by dissipation on a longer time scale. The metastable phase of the transient dynamics can therefore be denoted by 'nematic': its lifetime increases with $N$ and for $N \sim 200$ it is of the order of $t \sim 10^4/\kappa$. However, this metastable nematic state cannot be understood in terms of the landscape of the free energy, but rather seems to exhibit the features of a quasi-stationary state due to long-range coherent dynamics analogous to that reported in [22]. This conjecture is also supported by the behavior of the single-particle kinetic energy and of the kurtosis $\mathcal{K} = \langle p^4\rangle/\langle p^2\rangle^2$, which are shown in figure 5. The latter quantifies the deviation of the momentum distribution from a Gaussian one, for which it takes a value of $\mathcal{K}_{\text{Gauss}} = 3$. For these quantities we observe that in the metastable nematic phase the kinetic energy grows, while the distribution is non-thermal. Ordering in the second, short-wavelength lattice is accompanied by cooling into a thermal distribution.

We now compare the numerical results with the analytic theory for different quenches with the same initial values of $\alpha_{1i}$, $\alpha_{2i} \ll 1$ but with different endpoints $\alpha_{1f}$, $\alpha_{2f}$. We take different endpoints from the paramagnetic to the ferromagnetic phase, under the constraint $\alpha_{1f}/\alpha_{2f} = 5$. The circles in figure 6 correspond to the numerical results for 100 particles at time $t_f > 10^6/\kappa$, where we expect the system to reach the steady state.

IOP Publishing New J. Phys. 20 (2018) 025004 T Keller et al

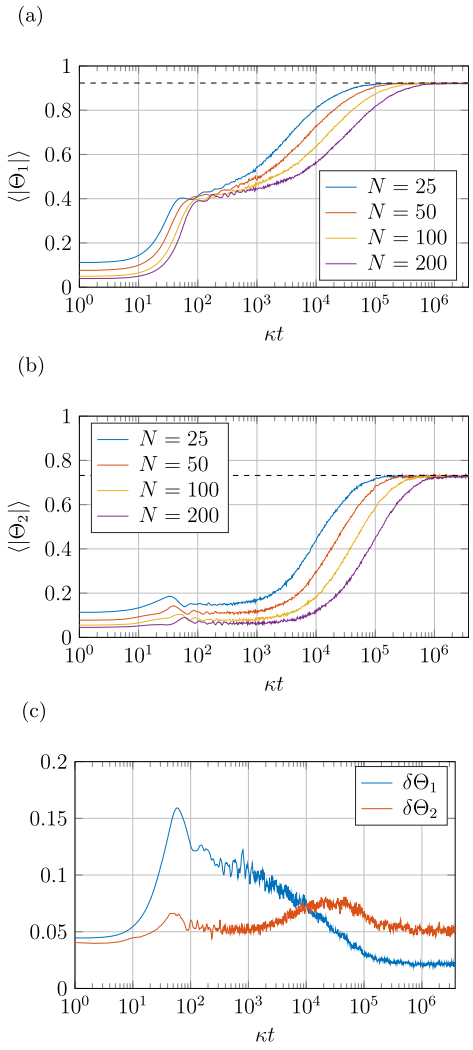


**Figure 4.** Dynamics of (a) $\langle|\Theta_1|\rangle$, (b) $\langle|\Theta_2|\rangle$, and (c) their fluctuations $\delta\Theta_n = \sqrt{\langle\Theta_n^2\rangle - \langle|\Theta_n|\rangle^2}$ as a function of time (in units of $1/\kappa$). The parameters and quench protocol are the same as in figure 3; the curves are however evaluated for different numbers of atoms and of trajectories. In (a) and (b) the data correspond to $N = 25,\ 50,\ 100,\ 200$ particles (see legends for color code) and respectively 1000, 500, 250, 125 trajectories. The horizontal dashed lines indicate the values predicted by the global minimum of the free energy in equation (16). The finite values of the order parameters at $t = 0$ are due to finite size effects, $\langle|\Theta_n(0)|\rangle = 1/\sqrt{\pi N}$. The curves in (c) are calculated for $N = 100$ and 250 trajectories.

These are in good agreement with the analytical results (dashed lines) based on an evaluation of the corresponding observables at the global minimum of the free energy. The interval where $\langle|\Theta_n|\rangle$ grows monotonically from $\sim 1/\sqrt{N}$ to the value of the ferromagnetic phase is expected to shrink as $N$ is increased, in agreement with a second-order phase transition at the thermodynamic limit. Further information on the onset of this ferromagnetic order can be gained by the probability $P_t(\Theta_2 < 0)$ that $\Theta_2$ is negative at $t$:

$$P_t(\Theta_2 < 0) = \int_{-1}^{0} \mathrm{d}\Theta_2 \mathcal{P}_t(\Theta_2). \tag{20}$$

We note that in the paramagnetic phase (homogeneous spatial distribution) we expect $P_t(\Theta_2 < 0) \simeq 0.5$. In contrast, due to the given mode structure we expect that $P_t(\Theta_2 < 0) \simeq 0$ for long-wavelength ordering in the ferromagnetic phase. Indeed, as $\alpha_{1\mathrm{f}}$ increases across the critical value, $P_t(\Theta_2 < 0)$ quickly drops down to zero.

### 3.2. Sudden quenches into the bistable phase

We now turn to the dynamics following sudden quenches from the paramagnetic to the ferromagnetic phase but following the right path of figure 2(a), which consists in equal effective pumping $\alpha_{1\mathrm{i}}/\alpha_{2\mathrm{i}} = \alpha_{1\mathrm{f}}/\alpha_{2\mathrm{f}} = 1$. In this parameter region (the bistable phase) the free energy exhibits a local minimum, which is nematic. As in the

IOP Publishing New J. Phys. 20 (2018) 025004 T Keller et al

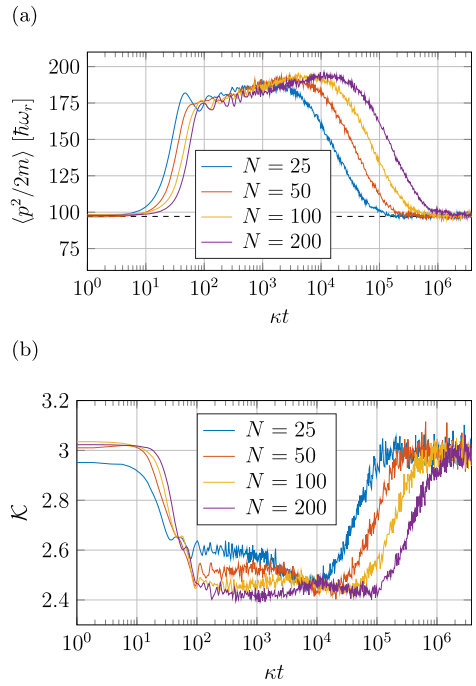


**Figure 5.** Dynamics of (a) the single-particle kinetic energy $\langle p^2/2m\rangle$ (in units of $\hbar\omega_r$) and (b) kurtosis $\mathcal{K} = \langle p^4\rangle/\langle p^2\rangle^2$ for $N = 25,\ 50,\ 100,\ 200$ particles (see legends) and respectively 1000, 500, 250, 125 trajectories. The other parameters and quench protocol are the same as in figure 4. The horizontal dashed line in (a) indicates the asymptotic value predicted by equation (13).

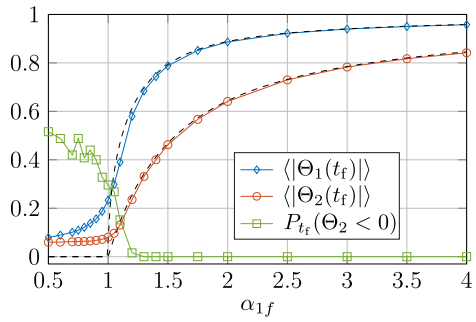


**Figure 6.** Asymptotic values of $\langle|\Theta_1(t_f)|\rangle$, $\langle|\Theta_2(t_f)|\rangle$, and $P_{t_f}(\Theta_2 < 0)$, equation (20), as a function of $\alpha_{1f}$. The quenches start from the same initial values in the paramagnetic phase ($\alpha_{1i},\ \alpha_{2i} \ll 1$ and $\Delta_c = -\kappa$) and end up with different values $\alpha_{1f},\ \alpha_{2f}$ with $\alpha_{1f} = 5\alpha_{2f}$ (lying along the left green line in figure 2(a)) and $\Delta_c = -\kappa$. The circles correspond to the results of the numerical simulations at $t_f = 3.77 \times 10^6/\kappa$ with $N = 100$ particles and 250 trajectories. The dashed lines indicate the predictions of the global minima of equation (16).

previous case, the initial values $\alpha_{1i},\ \alpha_{2i}$ are vanishingly small and the atoms are at the corresponding stationary distribution, whose temperature is determined by the detuning $\Delta_c$ and whose spatial density is homogeneous. The quench is performed by switching the laser power while keeping the detuning constant; thus the atoms should reach a thermal distribution with the same temperature as the initial state.

Figure 7 shows the time evolution of the trajectories' $\Theta$-distribution for $\alpha_{1f} = \alpha_{2f} = 2$ and $\Delta_c = -\kappa$. In contrast to the previous section, here a finite fraction of trajectories gets trapped in the nematic phase with a vanishing value of $\Theta_1$ and a finite probability that $\Theta_2$ takes negative values. This is visible in the small extra peaks in $\mathcal{P}(\Theta_1)$ and $\mathcal{P}(\Theta_2)$ (right panels). The trapping occurs at the time scale of the violent relaxation, and it seems stable over times of the order of $10^6/\kappa$. We conjecture that it also persists at asymptotic times. In figure 8 the time evolution of the mean absolute value of the order parameters is shown for different numbers of particles. While $\langle|\Theta_2|\rangle$ reaches the same stationary value (in reality its value decreases slightly with $N$), the asymptotic value

IOP Publishing New J. Phys. 20 (2018) 025004 T Keller et al

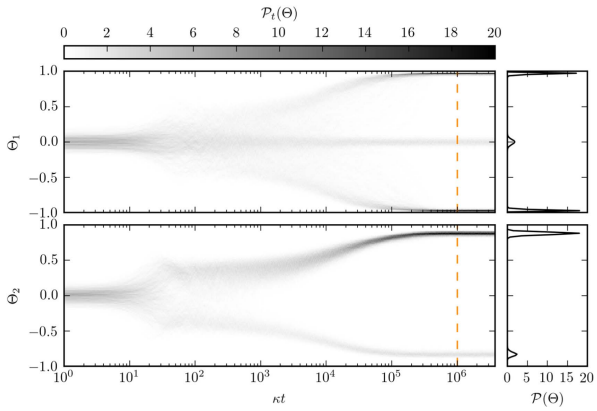


**Figure 7.** Dynamics following a sudden quench from $\alpha_{1i}$, $\alpha_{2i} \ll 1$ to $\alpha_{1f} = \alpha_{2f} = 2$ with the detuning kept constant $\Delta_c = -\kappa$ (red circle (c) in figure 2(a)). The left panels display the contour plot of the distribution $\mathcal{P}_t(\Theta)$ (equation (18)) for $\Theta = \Theta_1$ and $\Theta = \Theta_2$ as a function of time (in units of $1/\kappa$). The distribution is extracted from the numerical simulations using equation (1) for $N = 100$ atoms and 1000 trajectories. The right panels display distributions $\mathcal{P}(\Theta_1)$ and $\mathcal{P}(\Theta_2)$ as a function of $\Theta_1$ and $\Theta_2$, respectively (see equation (19)). See figure 3 for further details.

of $\langle|\Theta_1|\rangle$ decreases as $N$ grows. This suggests that the probability that the dynamics gets trapped in the local minimum increases with the number of particles. The asymptotic value of $\delta\Theta_1 = \sqrt{\langle\Theta_1^2\rangle - \langle|\Theta_1|\rangle^2}$ in subplot (c) reflects the contribution of these trajectories.

The mean single-particle kinetic energy and kurtosis are shown in figure 9. From their behavior we infer that the metastable nematic state does not significantly deviate from a thermal distribution with the expected asymptotic temperature (equation (13)).

Peculiar features of these dynamics become visible when inspecting the probability $P_t(\Theta_2 < 0)$ at the asymptotics and as a function of $\alpha_{1f}$ in figure 10. As in figure 6, it vanishes upon leaving the paramagnetic phase, but increases again as the $\alpha_{1f}$, $\alpha_{2f}$ chosen are deeper into the bistable phase of figure 2(a). Correspondingly, $\langle|\Theta_1|\rangle$ starts to decrease as $\alpha_{1f}$ increases, which suggests that from this point on the depth of the local minimum grows. The value of the order parameter $\langle|\Theta_2|\rangle$ at which $P_t(\Theta_2 < 0)$ starts to grow again signifies a threshold, above which the local minimum is sufficiently deep to stably trap particles.

### 3.3. Slow ramp into the bistable phase

We now consider linear ramps of $\alpha_n(t)$ across the transition region separating the paramagnetic from the bistable region. The ramp protocols have duration $\tau$ and sweep between the values $[\varepsilon, \alpha_{nf}]$, with $\varepsilon \ll 1$. In particular, $\alpha_n(t) = \varepsilon + \alpha_{nf}\frac{t}{\tau}$ if $t \in [0, \tau]$, while for $t > \tau$, $\alpha_n(t)$ is constant and equal to $\alpha_{nf}$. Note that a sudden quench is the limit $\tau \to 0$ of a linear quench. We choose to vary the values of $\alpha_n(t)$ along the rightmost green line in figure 2(a), so that $\alpha_1(t) = \alpha_2(t)$ at all instants of time, with $\alpha_{nf}$ in the bistable phase. We further keep $\Delta_c$ constant, and vary only the pump intensity. This means that the asymptotic temperatures at each value of $\alpha_n$ are equal.

Figure 11 shows the dynamics of the mean absolute value of the order parameters for $\alpha_{1f} = \alpha_{2f} = 2$ for linear ramps with different durations $\tau$. The dynamics following the sudden quench (figures 8(a) and (b)) is shown for comparison (blue curve). We observe that the dynamics of the order parameters exhibits an exponential increase which occurs almost simultaneously for both $\langle|\Theta_1|\rangle$ and $\langle|\Theta_2|\rangle$. This behavior seems to be initiated at the instant of time when the parameters $\alpha_n(t)$ cross the critical point of the phase diagram. Moreover, for sufficiently slow ramps $\langle|\Theta_1|\rangle$ approaches the asymptotic value of the free energy's global minimum, signaling stationary long-wavelength order.

We further note that for $\tau \lesssim 10^3/\kappa$ the order parameters undergo a three-stage dynamics, as for the sudden quench (we attribute the fluctuations to the statistics of the trajectories). For slower ramps, the mean value of the order parameters tends exponentially towards the steady state, which approaches the free energy's global minimum in equation (16) for $\tau > 10^4/\kappa$. We believe that this behavior is determined by the ramp duration $\tau$ with respect to the time scale of the transient dynamics, and thus by the time the parameters $\alpha_n(t)$ spend close to the transition point. This conjecture is supported by the analysis of the time evolution of the single-particle kinetic energy shown in figure 12, which corresponds to the curves in figure 11. For faster ramps it is similar to the sudden quench, exhibiting first a violent relaxation followed by a time interval when the dynamics is predominantly coherent, and then an exponential decay to the steady-state value due to cavity cooling. In

IOP Publishing New J. Phys. 20 (2018) 025004 T Keller et al

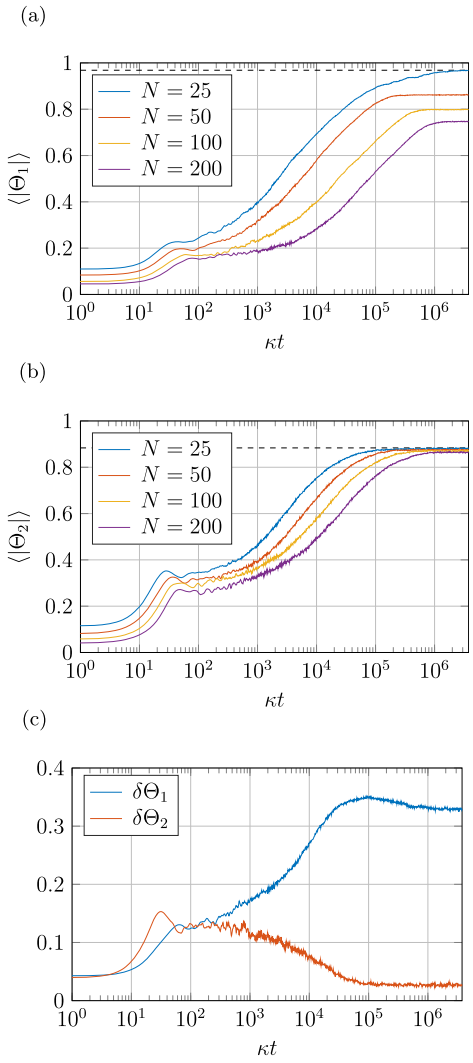


**Figure 8.** Dynamics of (a) $\langle|\Theta_1|\rangle$, (b) $\langle|\Theta_2|\rangle$, and (c) their fluctuations $\delta\Theta_n = \sqrt{\langle\Theta_n^2\rangle - \langle|\Theta_n|\rangle^2}$ as a function of time (in units of $1/\kappa$). The parameters and quench protocol are the same as in figure 7; the curves are evaluated for different numbers of atoms and of trajectories. In (a) and (b) the data correspond to $N = 25,\ 50,\ 100,\ 200$ particles (see legends for color code) and respectively 1000, 500, 250, 125 trajectories. The horizontal dashed lines indicate the values predicted by the global minimum of the free energy in equation (16). The finite values of the order parameters at $t = 0$ are due to finite size effects, $\langle|\Theta_n(0)|\rangle = 1/\sqrt{\pi N}$. The curves in (c) are calculated for $N = 100$ and 250 trajectories.

contrast, upon increasing the ramp duration towards slower ramps this transient regime disappears. In particular, for the slowest ramp considered here, dissipation leads to quasi-adiabatic dynamics. Figure 13 shows order parameters $\langle|\Theta_1(t)|\rangle$ and $\langle|\Theta_2(t)|\rangle$ at $t = 3.77 \times 10^6/\kappa$, where the curves of figure 11 reach an asymptotic behavior. Self-organization in the long-wavelength grating depends on the ramp duration $\tau$ and is found for $\tau > 10^4/\kappa$. Note that short-wavelength order quantified by $\langle|\Theta_2(t)|\rangle$ only slightly depends on the ramp duration.

On a microscopic scale, it seems that the reason for better long-wavelength ordering after slower ramps is that more time is spent close to the transition line ($\alpha_1 = \alpha_2 \sim 1$), where the local minimum of the free energy is not deep enough to stably trap the system. In order to test this conjecture, we consider a two-step quench protocol which splits the sudden quench of section 3.2 into two subsequent quenches. One occurs at $t = 0$ from a paramagnetic to a ferromagnetic bistable phase, but close to the transition line: $\alpha_{1\mathrm{int}} = \alpha_{2\mathrm{int}} = 1.1$. This quench shows a vanishing value of $P_t(\Theta_2 < 0)$ for sufficiently long times as in figure 10. The second sudden quench occurs after an elapsed time $\tau$ and goes from this intermediate point to $\alpha_{1\mathrm{f}} = \alpha_{2\mathrm{f}} = 2$. The detuning $\Delta_c$ is kept constant during the evolution.

IOP Publishing New J. Phys. 20 (2018) 025004 T Keller et al

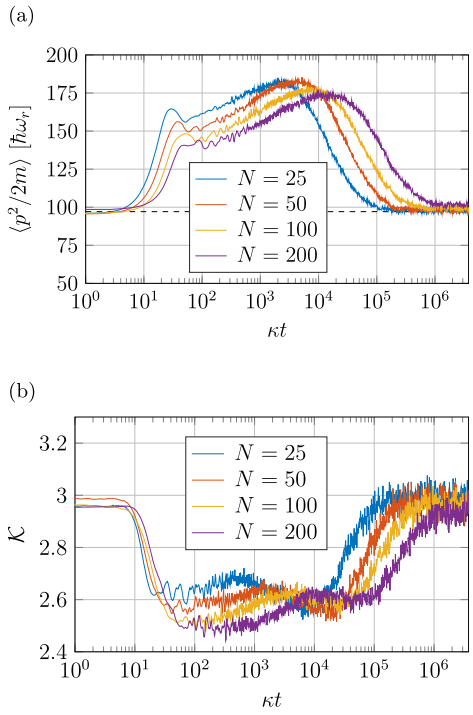


**Figure 9.** Dynamics of (a) the single-particle kinetic energy $\langle p^2/2m\rangle$ (in units of $\hbar\omega_r$) and (b) the kurtosis $\mathcal{K} = \langle p^4\rangle/\langle p^2\rangle^2$ for $N = 25,\ 50,\ 100,\ 200$ particles (see legends) and respectively 1000, 500, 250, 125 trajectories. The other parameters and initial conditions are the same as in figure 8. The horizontal dashed line in (a) indicates the asymptotic value predicted by equation (13).

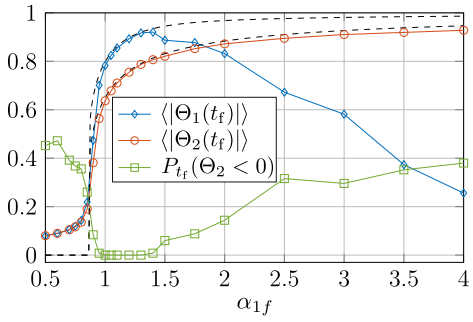


**Figure 10.** Asymptotic values of $\langle|\Theta_1(t_f)|\rangle$, $\langle|\Theta_2(t_f)|\rangle$, and $P_{t_f}(\Theta_2 < 0)$, equation (20), as a function of $\alpha_{1f}$. The quenches start from the same initial values in the paramagnetic phase ($\alpha_{1i}$, $\alpha_{2i} \ll 1$ and $\Delta_c = -\kappa$) and end up with different values $\alpha_{1f}$, $\alpha_{2f}$ with $\alpha_{1f} = \alpha_{2f}$ (lying along the right green line in figure 2(a)) and $\Delta_c = -\kappa$. The circles correspond to the results of the numerical simulations at $t_f = 3.77 \times 10^6/\kappa$ with $N = 100$ particles and 250 trajectories. The dashed lines indicate the predictions of the global minima of equation (16).

Figure 14 shows the time evolution of the mean absolute values of the order parameters for different time intervals $\tau$ between the two quenches. The order parameters undergo an initial violent relaxation at $t = 0$, when the first sudden quench occurs, and a second one immediately after the second quench (which looks like a jump in logarithmic scale). As expected, the longer the time between the two quenches, the closer the asymptotic value to that of the global minimum. Inspecting the dynamics of the kinetic energy in figure 15 we observe that for large $\tau$ the atoms are cooled into the stationary state at $\alpha_n \sim 1$. At this point of the phase diagram the free energy has two ferromagnetic global minima, while the nematic local minimum is very shallow. The system thus gets cooled close to the global minima of the free energy at $\alpha_n = 2$, and remains trapped there after the second quench.

Figure 16 shows the mean absolute values of the order parameters, as extracted from the numerical data at $t = 3.77 \times 10^6/\kappa$, as a function of the time between the two quenches. These values are compared to the

IOP Publishing New J. Phys. 20 (2018) 025004 T Keller et al

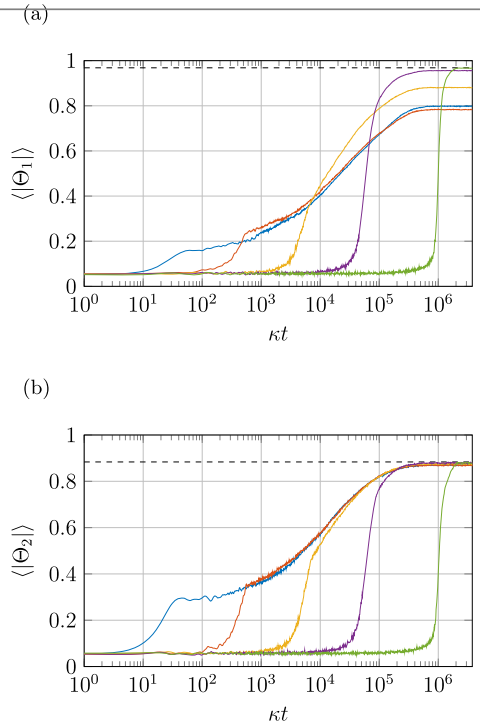


**Figure 11.** Mean value of order parameters (a) $\langle|\Theta_1|\rangle$ and (b) $\langle|\Theta_2|\rangle$ as a function of time (in units of $1/\kappa$) for $N = 100$ and $\Delta_c = -\kappa$, evaluated numerically with 250 trajectories. The curves are the time evolution during and after linear ramps of duration $\tau = 0$ (blue), $\tau = 5.5 \times 10^2/\kappa$ (red), $\tau = 6.8 \times 10^3/\kappa$ (yellow), $\tau = 8.5 \times 10^4/\kappa$ (purple), and $\tau = 2 \times 10^6/\kappa$ (green). The ramps occur from the paramagnetic to the bistable phase, specifically from $\alpha_{1i} = \alpha_{2i} = \varepsilon \ll 1$ to $\alpha_{1f} = \alpha_{2f} = 2$. As before, at $t = 0$ the initial state of the atoms is the steady state, equation (8), for $\alpha_n = \alpha_{ni}$ and $\Delta_c = -\kappa$. The dashed horizontal lines show the steady-state values of the global minima of the free energy, equation (16).

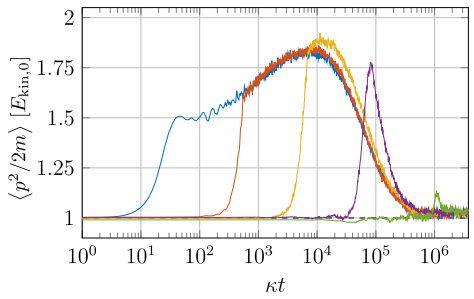


**Figure 12.** Mean value of the single-particle kinetic energy $\langle p^2/(2m)\rangle$ (in units of $E_{\mathrm{kin},0} = \hbar\kappa/4$) as a function of time (in units of $1/\kappa$) for the same parameters and color codes as in figure 11.

predictions of the global minimum of the free energy at $\alpha_1 = \alpha_2 = 2$ and $\Delta_c = -\kappa$. The behavior is quite similar to that observed when performing a linear ramp of corresponding duration (figure 13). Dynamical ordering in the long-wavelength mode thus seems to require that the atoms are initially cooled close to the global minima. This is realized by means of sufficiently long time $\tau$ spent close to the transition point.

## 4. Cooling into organized structures

We now analyze sudden quenches of the parameter $\alpha_n$ starting with different initial single-particle momentum widths. A possible realization is a quench in the detuning since $\Delta_c$ controls the steady-state temperature (see equation (13)). Using these we consider quenches which could lead to either heating or cooling of the system to the stationary temperature $T_0$,

IOP Publishing New J. Phys. 20 (2018) 025004 T Keller et al

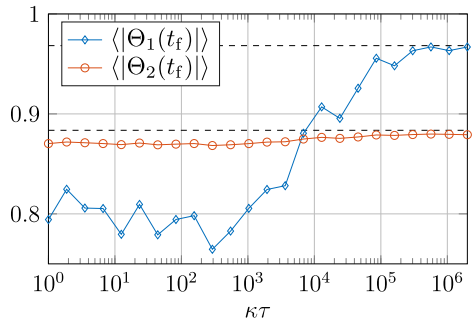


**Figure 13.** Values of $\langle|\Theta_1(t_f)|\rangle$ (blue) and $\langle|\Theta_2(t_f)|\rangle$ (red) at $t_f = 3.77 \times 10^6/\kappa$ and as a function of the ramp duration $\tau$ (in units of $1/\kappa$) for the same parameters as in figure 11. The dashed horizontal lines show the steady-state value predicted by the free energy, equation (16).

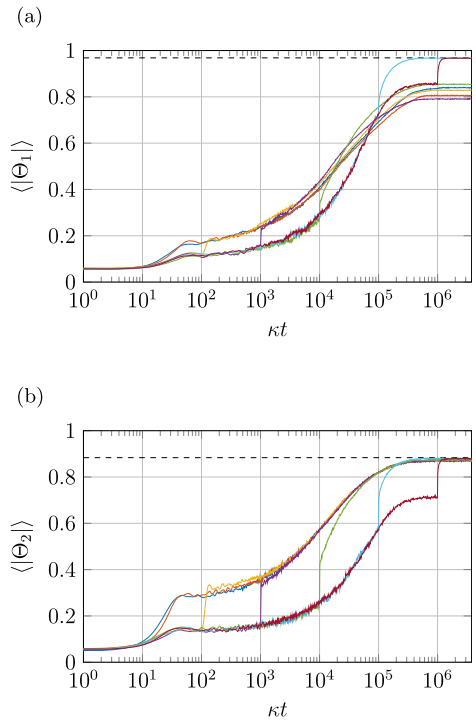


**Figure 14.** Dynamics of $\langle|\Theta_1|\rangle$ and $\langle|\Theta_2|\rangle$ as a function of time (in units of $1/\kappa$) for the two-step quench protocol. Here, the parameters $\alpha_n$ suddenly ramp at $t = 0$ from the initial values $\alpha_{1i}$, $\alpha_{2i} \ll 1$ to $\alpha_{1int} = \alpha_{2int} = 1.1$; after a time interval $\tau$, there is a second quench from $\alpha_{1int} = \alpha_{2int} = 1.1$ to $\alpha_{1f} = \alpha_{2f} = 2$. The parameters are $\Delta_c = -\kappa$, $N = 100$ with 250 trajectories, and $\tau = 1/\kappa$ (blue), $10/\kappa$ (red), $10^2/\kappa$ (yellow), $10^3/\kappa$ (purple), $10^4/\kappa$ (green), $10^5/\kappa$ (light blue) and $10^6/\kappa$ (dark red). The dashed horizontal lines show the values predicted by the global minimum of the free energy, equation (16), at $\alpha_1 = \alpha_2 = 2$ and $\Delta_c = -\kappa$.

$$k_B T_0 = \frac{\hbar\kappa}{2}, \tag{21}$$

namely, the minimal temperature achieved by cavity cooling, which is equivalent to setting $\Delta_c = -\kappa$. Therefore, we also consider initial thermal distributions which are spatially uniform and have a temperature $T_{ini} < T_0$. The initial momentum distributions we consider are Gaussian and their width is $\Delta p^2 = m k_B T_{ini}$.

Figure 17 shows the time evolution of the mean absolute values of the order parameters for different values of $T_{ini}$ ranging from $0.1T_0$ up to $5T_0$. The asymptotic value of $\langle|\Theta_1|\rangle$ increases with the initial temperature: The hotter the system is initially, the smaller the fraction of trajectories which remain trapped in the metastable, nematic state is. The corresponding time evolution of the mean kinetic energy per particle is displayed in figure 18 and it shows that for $T_{ini} = 2T_0$ (and even more for $T_{ini} = 5T_0$) the system stays relatively hot over time

IOP Publishing New J. Phys. 20 (2018) 025004 T Keller et al

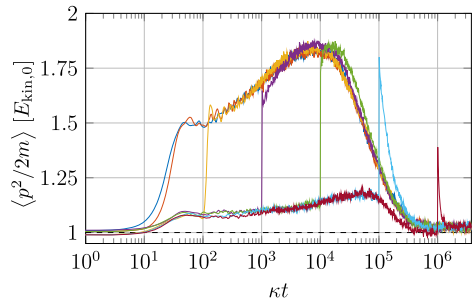


**Figure 15.** Mean kinetic energy per particle $\langle p^2/2m\rangle$ (in units of the asymptotic value $E_{\mathrm{kin},0} = \hbar\kappa/4$) as a function of time (in units of $1/\kappa$) for the same parameters and color codes as in figure 14.

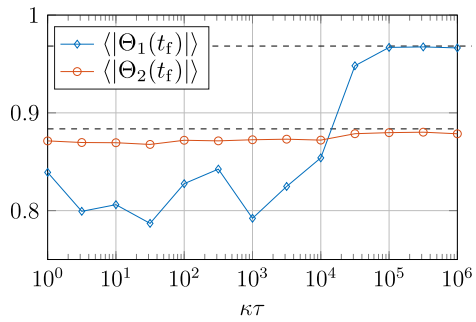


**Figure 16.** The symbols correspond to $\langle|\Theta_1(t_f)|\rangle$ (blue) and $\langle|\Theta_2(t_f)|\rangle$ (red) at $t_f = 3.77 \times 10^6/\kappa$ as a function of the time between the two quenches, $\tau$ (in units of $1/\kappa$), for the same parameters as in figure 14. The dashed horizontal lines show the steady-state values predicted by the global minimum of the free energy, equation (16), at $\alpha_1 = \alpha_2 = 2$ and $\Delta_c = -\kappa$.

scales of the order of $10^4/\kappa$. For lower initial temperatures, the system is instead heated by the energy released by the sudden quench before relaxation cools the atoms.

As shown in figure 17, for initially cold samples a long-wavelength Bragg grating is formed faster than for hotter samples. In this case we recognize a three-stage dynamics like the one observed for sudden quenches of the laser intensity, when a transient long-range order is established for times $t > 10/\kappa$ and $t < 10^3/\kappa$. For $t > 10^3/\kappa$ dissipation becomes significant and $\langle|\Theta_1|\rangle$ increases to a stationary value. This relaxation stage is also present for samples with initial temperatures higher than $T_0$; however, in this hotter case it is significantly faster. Taking a threshold value $\langle|\Theta_1|\rangle|_{\mathrm{thres}} = 0.5$, we observe that buildup of long-wavelength order can be up to a hundred times shorter than for a cold initial state. This is reminiscent of the Mpemba effect in supercooled water [24–28]. Its origin could be traced to a suppression of long-wavelength order if short-wavelength order is already established on a much shorter time scale, as shown in figure 17(b).

In figure 17(a) we observe that the final value of $\langle|\Theta_1|\rangle$ does not coincide with its predicted stationary value even after very long cooling times. This can also be seen in figure 19, which shows the mean absolute value of the order parameters at $t = 3.77 \times 10^6/\kappa$ as a function of the initial temperature for $N = 100, 200$. One would expect that $\langle|\Theta_1|\rangle$ should have reached a constant value corresponding to the stationary state. Apparently this is not the case and even for finite $N$ a significant fraction of trajectories converge to and remain in the local minimum. This behavior gets much less pronounced when the initial temperature lies above a certain threshold set by the energy released by the quench itself.

## 5. Comparison of numerical approaches

The discussion in this paper is based on results obtained by numerical integration of stochastic differential equations (1) and on their comparison with the corresponding analytical model. Both rely on the validity of the so-called bad cavity limit, where cavity damping is the shortest time scale, and particularly on treating retardation as a small parameter in the dynamics. This regime allows one to systematically describe quantum fluctuations of the cavity degrees of freedom by eliminating the cavity variables from the equations of motion of

IOP Publishing New J. Phys. 20 (2018) 025004 T Keller et al

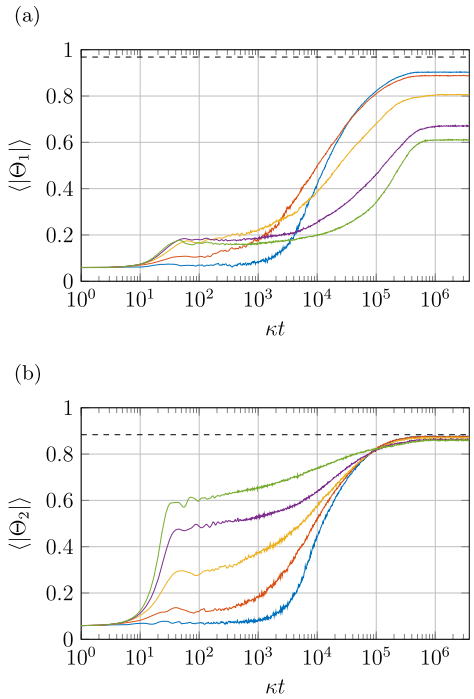


**Figure 17.** Dynamics of (a) $\langle|\Theta_1|\rangle$ and (b) $\langle|\Theta_2|\rangle$ as a function of time (in units of $1/\kappa$) after a sudden quench at $t = 0$ from $\alpha_{1i} = \alpha_{2i} = 0$ and $T_{ini}$ to $\alpha_{1f} = \alpha_{2f} = 2$ and $\Delta_c = -\kappa$ (corresponding to the asymptotic temperature $T_0$) for $N = 100$ and 250 trajectories. The different curves correspond to $T_{ini} = 5T_0$ (blue), $2T_0$ (red), $T_0$ (yellow), $0.5T_0$ (purple) and $0.1T_0$ (green). The dashed horizontal lines show the steady-state values predicted by the global minimum of the free energy, equation (16).

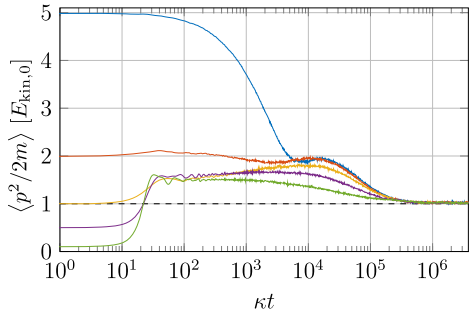


**Figure 18.** Mean kinetic energy per particle $\langle p^2/2m\rangle$ (in units of $E_{\mathrm{kin},0} = \hbar\kappa/4$) as a function of time (in units of $1/\kappa$) for the same parameters and color codes as in figure 17. The horizontal dashed line corresponds to the asymptotic value $\langle p^2/2m\rangle = E_{\mathrm{kin},0}$.

the external degrees of freedom. We now compare these predictions with those of the stochastic differential equations derived in [15], where the cavity degrees of freedom are treated in the semi-classical limit but included at all orders of retardation expansion. These stochastic differential equations are here extended to our setup composed of two cavity modes [16]:

$$\mathrm{d}x_j = \frac{p_j}{m}\mathrm{d}t, \tag{22a}$$

$$\mathrm{d}p_j = \sum_{n=1,2} 2\hbar nkS_n\mathcal{E}_{n,\mathrm{r}}\sin(nkx_j)\mathrm{d}t, \tag{22b}$$

$$\mathrm{d}\mathcal{E}_{n,\mathrm{r}} = (-\Delta_n\mathcal{E}_{n,\mathrm{i}} - \kappa_n\mathcal{E}_{n,\mathrm{r}})\mathrm{d}t + \mathrm{d}\xi_{n,\mathrm{r}}, \tag{22c}$$

$$\mathrm{d}\mathcal{E}_{n,\mathrm{i}} = (\Delta_n\mathcal{E}_{n,\mathrm{r}} - \kappa_n\mathcal{E}_{n,\mathrm{i}} - NS_n\Theta_n)\mathrm{d}t + \mathrm{d}\xi_{n,\mathrm{i}}, \tag{22d}$$

where $\mathcal{E}_{n,\mathrm{r}} = \mathrm{Re}\{\mathcal{E}_n\}$ and $\mathcal{E}_{n,\mathrm{i}} = \mathrm{Im}\{\mathcal{E}_n\}$ are the real and imaginary parts of the positive-frequency component of the cavity field mode $n = 1, 2$. The Wiener processes $\mathrm{d}\xi_{n,\mathrm{i}}$, $\mathrm{d}\xi_{n,\mathrm{r}}$ have a vanishing first moment,

IOP Publishing New J. Phys. 20 (2018) 025004 T Keller et al

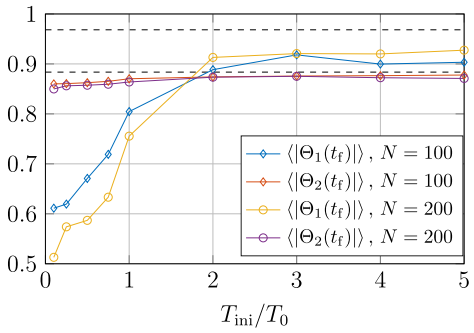


**Figure 19.** The symbols correspond to the values of $\langle|\Theta_1(t_\mathrm{f})|\rangle$ (blue, yellow) and $\langle|\Theta_2(t_\mathrm{f})|\rangle$ (red, purple) at $t_\mathrm{f} = 3.77 \times 10^6/\kappa$ as a function of $T_{\mathrm{ini}}$ (in units of $T_0$) for the same parameters as in figure 14 but for $N = 200$ particles (125 trajectories). See inset for the color code. The dashed horizontal lines show the steady-state values predicted by the global minimum of the free energy, equation (16).

$\langle \mathrm{d}\xi_{n,\mathrm{i}}\rangle = 0 = \langle \mathrm{d}\xi_{n,\mathrm{r}}\rangle$, while the second moments fulfill $\langle \mathrm{d}\xi_{n,\mathrm{i}}\mathrm{d}\xi_{m,\mathrm{i}}\rangle = \delta_{nm}\kappa/2\mathrm{d}t$, $\langle \mathrm{d}\xi_{n,\mathrm{r}}\mathrm{d}\xi_{m,\mathrm{r}}\rangle = \delta_{nm}\kappa/2\mathrm{d}t$, and $\langle \mathrm{d}\xi_{n,\mathrm{r}}\mathrm{d}\xi_{m,\mathrm{i}}\rangle = 0$.

The results of the simulations based on the two approaches for a single-mode cavity show good agreement. For the two-mode cavity we generally find qualitative agreement. Quantitative discrepancies are found in general for the momentum distribution: The simulations based on equation (22) predict for certain parameters samples whose temperatures are 10% hotter than the ones obtained with equation (1). Small differences are also found for the order parameters after the quenches into the bistable phase.

Figure 20 shows a representative result of the discrepancies found after the quench protocol discussed in section 3.2. The two simulations predict different stationary values for both the kinetic energy and the order parameters. We believe that this discrepancy is due to retardation effects, which are neglected in the approach of equation (1) and become relevant when the atoms are trapped at tight minima.

In order to test our conjecture we use the prediction of the kinetic theory of [29, 30], where the temperature of the stationary thermal distribution was corrected by the contribution from the atoms' localization at the minima of the self-organized lattice,

$$k_\mathrm{B}\tilde{T} = \hbar\frac{\Delta_\mathrm{c}^2 + \kappa^2}{4|\Delta_\mathrm{c}|} + \hbar\frac{\omega_0^2}{|\Delta_\mathrm{c}|}. \tag{23}$$

Here, $\omega_0$ is the frequency of oscillation about the lattice minima in the harmonic approximation. It can be estimated by using equation (22*b*) and imposing the equality

$$\mathrm{d}p_j \approx \sum_{n=1,2} 2\hbar(nk)^2 S_n \mathcal{E}_{n,\mathrm{r}} x_j \mathrm{d}t \equiv -m\omega_0^2 x_j \mathrm{d}t.$$

This delivers an analytic estimate of the frequency

$$\omega_0^2 = \omega_\mathrm{r}\frac{\Delta_\mathrm{c}^2 + \kappa^2}{-\Delta_\mathrm{c}}(\alpha_1\Theta_1 + 4\alpha_2\Theta_2),$$

where we use equation (4). For the parameters of the quench in figure 20, with $\Delta_\mathrm{c} = -\kappa$ and $\alpha_1 = \alpha_2 = 2$, we obtain $k_\mathrm{B}\tilde{T} \approx 1.1 k_\mathrm{B} T_0$, where $T_0$ is the temperature given in equation (21). Indeed, this corrected value of the final temperature is in good agreement with the discrepancy observed in figure 20(a).

This hypothesis is also consistent with the discrepancy observed in the asymptotic values of the order parameters. In fact, the stationary temperature and the final values of the order parameters are related: the stationary values of the order parameters are determined by the parameters $\alpha_1$, $\alpha_2$ [13] and thus depend on both field intensities and detunings (see equation (4)). According to this hypothesis, the asymptotic values of the order parameters for the simulation using equation (22) should be the ones corresponding to the system's parameters with the corrected temperature $\tilde{T}$; hence we shall minimize the free energy of equation (16) using $\tilde{\beta} = 1/(k_\mathrm{B}\tilde{T})$, equation (23), instead of $1/(k_\mathrm{B}T_0)$. This is equivalent to rescaling the phase diagram in figure 2(a) using the prescription $\tilde{\alpha}_n = \alpha_n T_0/\tilde{T} < \alpha_n$, and results in a smaller stationary value of the order parameter, which is consistent with the discrepancies visible in figures 20(b) and (c).

IOP Publishing New J. Phys. 20 (2018) 025004 T Keller et al

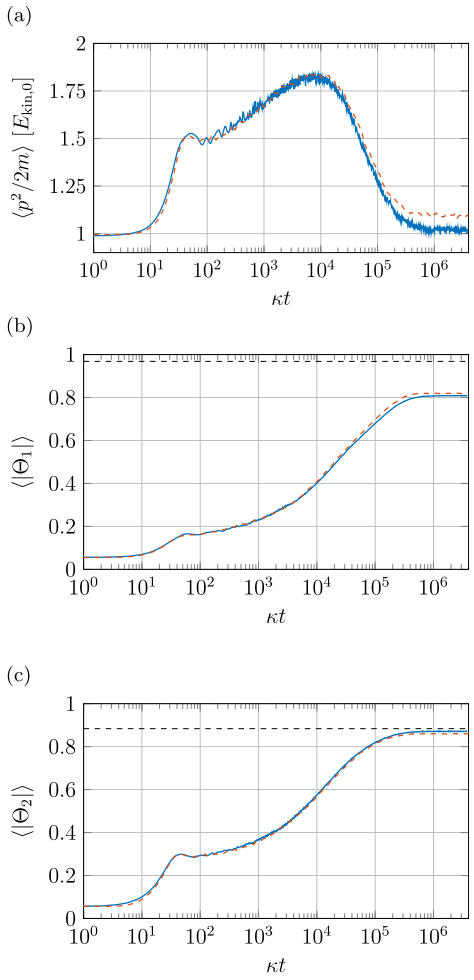


**Figure 20.** Dynamics of (a) single-particle kinetic energy (in units of $E_{\mathrm{kin},0}$), (b) $\langle|\Theta_1|\rangle$, and (c) $\langle|\Theta_2|\rangle$ as a function of time (in units of $1/\kappa$) following a quench at $t = 0$ from $\alpha_{1\mathrm{i}} = \alpha_{2\mathrm{i}} \ll 1$ to $\alpha_1 = \alpha_2 = 2$ for $\Delta_c = -\kappa$ and $N = 100$. The blue (red) lines correspond to simulations using equation (1) (equation (22)). The black dashed lines denote the values of the order parameters obtained by the free energy, equation (16). In (a) the blue (red) line corresponds to 250 (500) trajectories. In (b) and (c) the blue and red lines correspond to 1000 (500) trajectories. Note that a quench from $\alpha_1$, $\alpha_2$ as performed in section 3.2 for fixed $\Delta_c = -\kappa$ corresponds for the simulation of equation (22) to a quench in the pumping strength $S_n$ such that $NS_n^2 = \alpha_n\kappa^2$. At $t_f = 3.77 \times 10^6/\kappa$ we observe that 16.9% (15.4%) of the trajectories are in the nematic phase using equation (1) (equation (22)).

## 6. Conclusions

In this work we have studied the semi-classical dynamics of atoms interacting with two cavity modes after quenches of the intensity and/or frequency of the pumping lasers. In the quench protocols the laser parameters were varied across transition lines separating a disordered phase from an ordered self-organized phase. We could verify numerically that the states reached at the asymptotics of the dynamics correspond to the minima of the free energy of a corresponding thermodynamic description developed in [13]. This picture is further confirmed by the comparison with numerical simulations based on different initial assumptions. This analysis shows, in particular, that trapping of the system in the local minima of the free energy crucially depends on the initial temperature and on the cooling rate.

We observe, in addition, that the system can be trapped in metastable configurations for transient times which cannot be understood in terms of the effective thermodynamic description. For hundreds of particles the lifetime of these states is about four orders of magnitude longer than the cavity lifetime, and is expected to increase with $N$. They share analogies with metastable configurations found in the GHMF when performing quenches in the microcanonical ensemble [22]. Since the phase diagrams of the GHMF and the model here considered can be formally mapped onto each other [13], we conjecture that these metastable configurations

could be due to the coherent dynamics. This conjecture can be tested by means of a mean-field analysis such as the one performed in [12] for a single-mode cavity.

Interestingly, when the initial temperature of the atomic ensemble is different from the stationary temperature of cavity cooling, we observe that the final magnitude of asymptotic order changes. In particular when the initial temperature is even lower than the predicted cavity cooling temperature, the probability that the system remains trapped in metastable configurations is further increased. This is similar to the behavior of supercooled water [24–28].

Here we consider the very special case of two commensurate modes. While this already highlights many generic properties of the dynamics, future considerations certainly should include the case in which the wavelengths of the cavity modes are incommensurate [31], so that the ordering mechanisms are much more intensely competing and a multitude of metastable states can form. A further interesting direction is operation with much colder temperatures or in the side-band resolved cooling regime [32]. Here it is intriguing to consider in which form metastable states survive deep in the quantum regime. Besides diffusion they could be depleted via tunneling and atom–field entanglement plays an important role in this dynamics [33], a process which should also be relevant in closely related schemes of simulated quantum annealing [34].

## Acknowledgments

The authors thank Tobias Donner, Sebastian Krämer, and Francesco Rosati for stimulating and helpful discussions. This work was supported by the German Research Foundation (DFG, DACH project 'Quantum crystals of matter and light') and by the European Commission (ITN 'ColOpt'). V T and H R are supported by Austrian Science Fund Project No. I1697-N27. T K and V T contributed equally to this work.

## ORCID iDs

Helmut Ritsch https://orcid.org/0000-0001-7013-5208

## References

[1] Horak P, Hechenblaikner G, Gheri K M, Stecher H and Ritsch H 1997 *Phys. Rev. Lett.* **79** 4974
[2] Domokos P and Ritsch H 2003 *J. Opt. Soc. Am.* B **20** 1098
[3] Black A T, Chan H W and Vuletić V 2003 *Phys. Rev. Lett.* **91** 203001
[4] Baumann K, Guerlin C, Brennecke F and Esslinger T 2010 *Nature* **464** 1301
[5] Asbóth J K, Domokos P, Ritsch H and Vukics A 2005 *Phys. Rev.* A **72** 053417
[6] Schütz S and Morigi G 2014 *Phys. Rev. Lett.* **113** 203002
[7] Schütz S, Jäger S B and Morigi G 2015 *Phys. Rev.* A **92** 063808
[8] O'Dell D H J, Giovanazzi S and Kurizki G 2003 *Phys. Rev. Lett.* **90** 110402
[9] Münstermann P, Fischer T, Maunz P, Pinkse P W H and Rempe G 2000 *Phys. Rev. Lett.* **84** 4068
[10] Vuletić V and Chu S 2000 *Phys. Rev. Lett.* **84** 3787
[11] Schütz S, Jäger S B and Morigi G 2016 *Phys. Rev. Lett.* **117** 083001
[12] Jäger S B, Schütz S and Morigi G 2016 *Phys. Rev.* A **94** 023807
[13] Keller T, Jäger S B and Morigi G 2017 *J. Stat. Mech.* **6** 064002
[14] Schütz S, Habibian H and Morigi G 2013 *Phys. Rev.* A **88** 033427
[15] Domokos P, Horak P and Ritsch H 2001 *J. Phys.* B **34** 187
[16] Torggler V and Ritsch H 2014 *Optica* **1** 336
[17] Brennecke F, Donner T, Ritter S, Bourdel T, Köhl M and Esslinger T 2007 *Nature* **450** 268
[18] Landig R, Hruby L, Dogra N, Landini M, Mottl R, Donner T and Esslinger T 2016 *Nature* **532** 476
[19] Léonard J, Morales A, Zupancic P, Esslinger T and Donner T 2017 *Nature* **543** 87
[20] Dalibard J and Cohen-Tannoudji C 1985 *J. Phys.* B **18** 1661
[21] Campa A, Dauxois T and Ruffo S 2009 *Phys. Rep.* **480** 57
[22] Teles T N, Benetti F P d C, Pakter R and Levin Y 2012 *Phys. Rev. Lett.* **109** 230601
[23] Pikovsky A, Gupta S, Teles T N, Benetti F P d C, Pakter R, Levin Y and Ruffo S 2014 *Phys. Rev.* E **90** 062141
[24] Auerbach D 1995 *Am. J. Phys.* **63** 882
[25] Brownridge J D 2011 *Am. J. Phys.* **79** 78
[26] Tao Y, Zou W, Jia J, Li W and Cremer D 2017 *J. Chem. Theory Comput.* **13** 55
[27] Jin J and Goddard W A III 2015 *J. Phys. Chem.* C **119** 2622
[28] Zhang X *et al* 2014 *Phys. Chem. Chem. Phys.* **16** 22995–3002
[29] Niedenzu W, Grießer T and Ritsch H 2011 *Europhys. Lett.* **96** 43001
[30] Grießer T, Niedenzu W and Ritsch H 2012 *New J. Phys.* **14** 053031
[31] Habibian H, Winter A, Paganelli S, Rieger H and Morigi G 2013 *Phys. Rev. Lett.* **110** 075304
[32] Krämer S and Ritsch H 2014 *Phys. Rev.* A **90** 033833
[33] Maschler C, Ritsch H, Vukics A and Domokos P 2007 *Opt. Commun.* **273** 446
[34] Torggler V, Krämer S and Ritsch H 2017 *Phys. Rev.* A **95** 032310

Section 2.4

## Summary

In this chapter we derived and studied the spatial self-organization of atoms coupling dispersively to an optical resonator.

In the first section 2.1 we derived a Fokker-Planck equation describing the semiclassical dynamics of the particles where the cavity degrees of freedom can be eliminated. We showed that the multiple-scattered cavity photons mediate long-range coherent and dissipative forces between the atoms.

By these means we analyzed steady-state properties of self-organization in section 2.2. Here, we showed that the stationary state can be mapped to the canonical ensemble of models from physics of long-range interactions [23, 31]. These models can exhibit phase diagrams with various phases and features such as ensemble inequivalence, that are usually not realizable by short-range interactions [23, 26, 108, 109].

In section 2.3 we studied out-of-equilibrium properties of spatial self-organization. We investigated the dynamics after quenches across phase transitions and the relaxation towards the stationary state. We determined mean-field properties and show in particular that mean field can describe the dynamics on short timescales while it fails to predict the correct relaxation timescales [22, 25]. Furthermore, we discussed the role of dissipation that stabilizes metastable states of the system [25] and we investigated the nature of metastable states after quenches into different phases in multimode cavities [27].

# Chapter 3

# Optomechanical effects in steady-state superradiance

The main focus of this chapter is the study of optomechanical effects in steady-state superradiance. In section 3.1 we present the model and provide a short overview of steady-state superradiance without optomechanical effects. We then analyze optomechanical effects in steady-state superradiance in section 3.2 using a mean-field theory to describe the motion of the particles in the ultra-cold as well as in the thermal realm. In section 3.3 we focus on the semiclassical dynamics of the atoms and study the cooling of the external degrees of freedom in the superradiant regime. The last section 3.4 summarizes this chapter.

Section 3.1

# Introduction to steady-state superradiance

In this section we introduce the model of incoherently-driven quasispins coupling to a resonator. We present a mean-field description of this model and discuss the analogies with the Kuramoto model that describes the effect of synchronization in an ensemble of coupled oscillators. In the end of this section we give a short overview of past and current work that is connected to the studies that we present in this chapter.

## 3.1.1 The model of steady-state superradiance

We consider $N$ particles with mass $m$ that can be effectively described by dipoles consisting of an excited state $|e\rangle_j$ and ground state $|g\rangle_j$ with $j = 1, ..., N$. Every particle can emit photons into a common mode of the resonator. In this setting, an ensemble of particles can superradiantly emit photons into the resonator mode (see section 1.3). This is an interference effect that gives rise to a macroscopic build up of coherence in the collective dipole. In the regime where the cavity decay rate determines the fastest timescale, typically, excitations are lost on a timescale that is proportional to the inverse of the collective linewidth of the dipole.

In this section we include an incoherent pump of the particles that balances the losses of excitations. We will show that the rate of the incoherent pump can be tuned such that superradiance persists even at steady state. This effect of steady-state superradiance appears in the regime where the incoherent pump is larger than the single particle linewidth, in order to obtain population inversion, but smaller than the collective linewidth such that coherences are not immediately destroyed by the incoherent driving.

In what follows we will present the theoretical model and derive its prediction.

### Master equation

We describe the evolution in terms of a master equation for the density matrix $\hat{\rho}$ including the internal and external degrees of freedom of the $N$ particles and the cavity degrees of freedom. This master equation is given by

$$\frac{\partial \hat{\rho}}{\partial t} = \frac{1}{i\hbar}[\hat{H}, \hat{\rho}] + w \sum_{j=1}^{N} \mathcal{L}[\hat{\sigma}_j^\dagger]\hat{\rho} + \kappa \mathcal{L}[\hat{a}]\hat{\rho}, \tag{3.1.1}$$

where the coherent dynamics is governed by the Hamiltonian

$$\hat{H} = \sum_{j=1}^{N} \frac{\hat{p}_j^2}{2m} + \hbar\Delta \hat{a}^\dagger \hat{a} + \sum_{j=1}^{N} \hbar \frac{g}{2} \cos(k\hat{x}_j)(\hat{a}^\dagger \hat{\sigma}_j + \hat{\sigma}_j^\dagger \hat{a}). \tag{3.1.2}$$

The first term in Eq. (3.1.2) is the kinetic energy of the particles with momentum operator $\hat{p}_j$. The second term is the energy of the cavity field in the frame rotating with the atomic transition frequency $\omega_a$ such that $\Delta = \omega_c - \omega_a$ is the detuning between the cavity frequency

$\omega_c$ and the atomic transition frequency $\omega_a$. For the description of the cavity mode we use the photon annihilation and creation operators, $\hat{a}$ and $\hat{a}^\dagger$ with $[\hat{a}, \hat{a}^\dagger] = 1$. The coupling between every atom and the cavity mode is governed by the vacuum Rabi frequency $g$ and the mode function $\cos(k\hat{x})$. Here, $\hat{x}_j$ is the position operator fulfilling the commutation relation $[\hat{x}_j, \hat{p}_l] = i\hbar\delta_{j,l}$ with the momentum operators. The interaction between the mode and the dipole is described by the Jaynes-Cummings term where $\hat{\sigma}_j = |g\rangle_j\langle e|$ is the lowering operator for the internal state of the $j$th particle. The incoherent part of the dynamics in Eq. (3.1.1) is governed by $w\mathcal{L}[\hat{\sigma}_j^\dagger]$ and $\kappa\mathcal{L}[\hat{a}]$ using the definition of Eq. (1.1.11). Here, we introduced the cavity decay rate $\kappa$ and the rate of incoherent pumping $w$. The spontaneous decay of the excited state is neglected here since we assume the excited state $|e\rangle$ to be metastable.

**Effective Master equation**

If we assume that the cavity decay rate $\kappa$ and the detuning $\Delta$ are much larger than the repump rate $w$, the collective coupling $\sqrt{N}g$, the recoil frequency $\omega_R = \hbar k^2/(2m)$ and the Doppler shift $k\Delta p/m$, where $\Delta p$ denotes the single-particle momentum width, we can eliminate the cavity degrees of freedom as we present in App. A.1. The elimination of the cavity degrees of freedom allows us to derive an effective Born-Markov master equation for the reduced density matrix $\hat{\rho}_N$ describing the atomic degrees of freedom. This master equation reads

$$\frac{\partial\hat{\rho}_N}{\partial t} = \frac{1}{i\hbar}\left[\hat{H}_{\text{eff}}, \hat{\rho}_N\right] + w\sum_{j=1}^{N}\mathcal{L}[\hat{\sigma}_j^\dagger]\hat{\rho}_N + \Lambda\mathcal{L}[\hat{X}]\hat{\rho}_N, \tag{3.1.3}$$

with the effective Hamiltonian

$$\hat{H}_{\text{eff}} = \sum_{j=1}^{N}\frac{\hat{p}_j^2}{2m} - \hbar N\Lambda\frac{\Delta}{\kappa}\hat{X}^\dagger\hat{X}, \tag{3.1.4}$$

and the collective coupling $\Lambda = N\Gamma_c$. The single particle linewidth $\Gamma_c$ is defined as

$$\Gamma_c = \frac{g^2\kappa}{\kappa^2 + 4\Delta^2}$$

and the collective dipole $\hat{X}$ takes the form

$$\hat{X} = \frac{1}{N}\sum_{j=1}^{N}\hat{\sigma}_j\cos(k\hat{x}_j). \tag{3.1.5}$$

Due to the elimination of the cavity degrees of freedom there are now two terms in the master equation that describe effects mediated by the long-range dipole-dipole interactions. The operator $\hbar N\Lambda(\Delta/\kappa)\hat{X}^\dagger\hat{X}$, in the effective Hamiltonian (Eq. (3.1.4)), describes a coherent interaction while $\Lambda\mathcal{L}[\hat{X}]$, in the master equation (3.1.3), describes a decay of the collective dipole $\hat{X}$.[1]

[1]Notice that retardation effects between atomic and cavity degrees of freedom give rise to other couplings that we do not report here since we assume that they are negligibly small in the limit where

$$w, \Lambda, k\Delta p/m \ll \kappa, \Delta.$$

We call a state $\hat{\rho}_N$ superradiant if the expectation value $\langle \hat{X}^\dagger \hat{X} \rangle$, with $\langle \hat{O} \rangle = \mathrm{Tr}(\hat{O}\hat{\rho}_N)$ for an operator $\hat{O}$, does not vanish in the limit $N \to \infty$. Therefore, in order for $\hat{\rho}_N$ to be superradiant, it describes a macroscopic, coherent superposition of excited and ground states. Steady-state superradiance describes the effect that superradiance is observed at steady state, namely for a state that fulfills $\partial\hat{\rho}_N/(\partial t) \approx 0$ using Eq. (3.1.3).[2] It appears in the regime where the incoherent pump $w$ is larger than the single-particle linewidth $\Gamma_c$ but smaller than the collective linewidth $\Lambda = N\Gamma_c$. In the following we review steady-state superradiance neglecting the motion of the particles.

### 3.1.2 Dynamics of the spins

In this subsection we discard the optomechanical coupling to the external degrees of freedom assuming the spins are pinned. We review basic results from Refs. [32, 110, 111] using a mean-field theory, as they provide an important basis for the studies presented in section 3.2.

#### Threshold of superradiant emission

The equations of motion for $\langle \hat{\sigma}_j \rangle$ and $\langle \hat{\sigma}_j^z \rangle$ can be derived from Eq. (3.1.3). They read

$$\frac{d\langle \hat{\sigma}_j \rangle}{dt} = -\frac{w}{2}\langle \hat{\sigma}_j \rangle - i\frac{\Lambda}{2}\alpha^* \langle \hat{\sigma}_j^z \hat{X} \rangle, \tag{3.1.6}$$

$$\frac{d\langle \hat{\sigma}_j^z \rangle}{dt} = w(1 - \langle \hat{\sigma}_j^z \rangle) - [i\alpha\Lambda \langle \hat{X}^\dagger \hat{\sigma}_j \rangle + \mathrm{H.c.}], \tag{3.1.7}$$

where $\alpha = 2\Delta/\kappa - i$. We will use a mean-field description of Eqs. (3.1.6), (3.1.7) that relies on factorizing expectation values of products of operators for the case $N \gg 1$ [3]. Using mean-field and assuming that the state of the spins is symmetric in particle exchange we derive two coupled non-linear differential equations for $X = \langle \hat{\sigma}_j \rangle$ and $Z = \langle \hat{\sigma}_j^z \rangle$ that read

$$\frac{dX}{dt} = -\left(\frac{w}{2} - i\alpha^*\frac{\Gamma_c}{2}\right) X - i\frac{(N-1)\Gamma_c}{2}\alpha^* XZ, \tag{3.1.8}$$

$$\frac{dZ}{dt} = (w + \Gamma_c)\left(\frac{w - \Gamma_c}{w + \Gamma_c} - Z\right) - 2(N-1)\Gamma_c |X|^2. \tag{3.1.9}$$

Stationary solutions of Eq. (3.1.8) and Eq. (3.1.9) that fulfill $d|X_0|^2/dt = 0$ and $dZ_0/dt = 0$ are

$$X_0 = 0, \tag{3.1.10}$$

$$Z_0 = \frac{w - \Gamma_c}{w + \Gamma_c}. \tag{3.1.11}$$

Since $\langle \hat{X}^\dagger \hat{X} \rangle = |X_0|^2 = 0$, this steady state describes a non-superradiant state. However, this solution is not necessarily stable. A small perturbation $\delta X$ can give rise to the

[2] For us it is sufficient that the collective dipole remains coherent for a sufficiently long time scale that might also be described by a metastable state of the system. In this case we will still use the term "steady-state superradiance".

[3] The approaches that are used in Refs. [32, 110, 111] are beyond mean-field and take into account at least two-particle correlations. We will motivate the mean-field approach in subsection 3.2.3.

onset of a superradiant emission. This small perturbation follows on short timescales the differential equation

$$\begin{aligned}\frac{d\delta X}{dt} =& -\left(\frac{w}{2} - i\alpha^*\frac{\Gamma_c}{2}\right)\delta X - i\frac{(N-1)\Gamma_c}{2}\alpha^* Z_0 \delta X \\ =& \left[\frac{-(w+\Gamma_c)+(N-1)\Gamma_c Z_0}{2} + i\frac{\Delta}{\kappa}\left(\Gamma_c - (N-1)\Gamma_c Z_0\right)\right]\delta X,\end{aligned}$$

that is derived by linearizing Eq. (3.1.8). The perturbation will exponentially increase if

$$(N-1)\Gamma_c Z_0 > w + \Gamma_c, \tag{3.1.12}$$

and therefore a small perturbation $\delta X$ will give rise to an initial superradiant emission. The inequality (3.1.12) can only be fulfilled if $Z_0 > 0$ that implies, using Eq. (3.1.11),

$$\Gamma_c < w. \tag{3.1.13}$$

This is the lower threshold for superradiant emission.

On the other hand assuming a strong incoherent pump $w \gg \Gamma_c$, we get $Z_0 \approx 1$ using Eq. (3.1.11), that is the case of a saturated ensemble of dipoles. In this case the inequality (3.1.12) leads to a second threshold for the repump rate

$$w < N\Gamma_c, \tag{3.1.14}$$

in order to observe superradiance.

Collecting the two results in Eqs. (3.1.13) and (3.1.14) we conclude that superradiance is expected in the regime

$$\Gamma_c < w < N\Gamma_c. \tag{3.1.15}$$

For this choice of $w$ we can calculate the stable steady states of Eq. (3.1.8) and Eq. 3.1.9 that read

$$|X|^2 = \frac{w+\Gamma_c}{2(N-1)\Gamma_c}, \tag{3.1.16}$$

$$Z = \frac{w+\Gamma_c}{2(N-1)\Gamma_c}\left(\frac{w-\Gamma_c}{w+\Gamma_c} - \frac{w+\Gamma_c}{(N-1)\Gamma_c}\right), \tag{3.1.17}$$

providing that $d|X|^2/dt = 0$ and $dZ/dt = 0$. For the choice of $w \propto N$ this state describes superradiance at steady state since $\langle \hat{X}^\dagger \hat{X}\rangle = |X|^2 \neq 0$ in the limit $N \to \infty$.

In Fig. 3.1 we plot the steady state of $|X|^2$ in subplot (a) and the steady state of $Z$ in subplot (b) for $N = 10^4$, respectively. The superradiant phase is visible in Fig. 3.1(a) where $|X|^2$ is different from zero. We see that $|X|^2$ increases with $w$ until it reaches a maximum at $w \approx N\Gamma_c/2$ and then decreases again. In Fig. 3.1(b) the two thresholds given by Eq. (3.1.15) are visible as discontinuities of $Z$. Here, we observe that $Z < 0$ for values $w < \Gamma_c$ while for $w > \Gamma_c$ we observe population inversion, $Z > 0$. The value of $Z$ increases monotonically until $w \approx N\Gamma_c$ where the ensemble of dipoles is saturated, $Z = 1$.

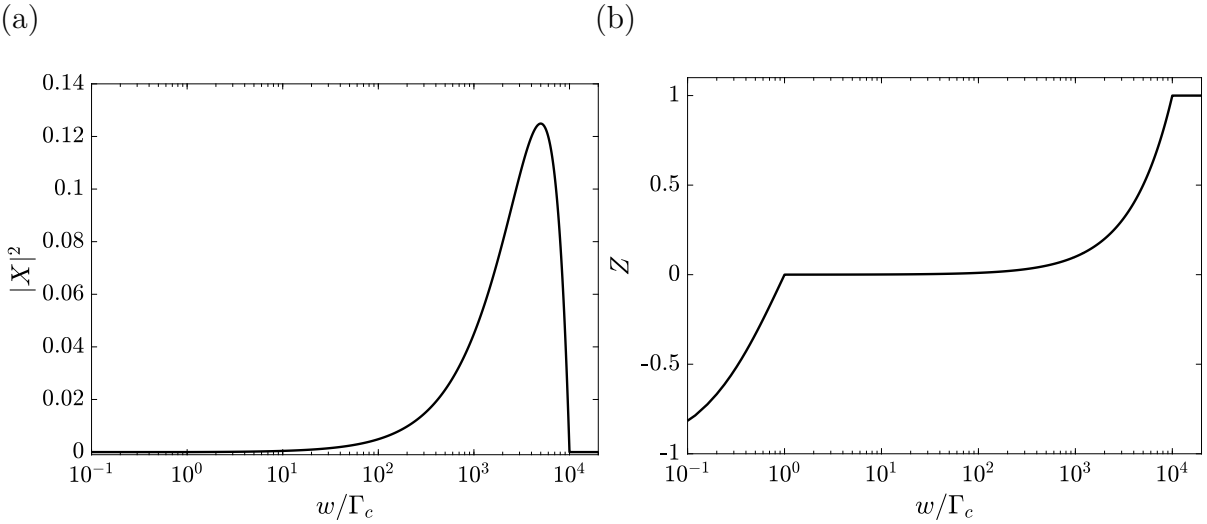


Figure 3.1: The stable steady state of $|X|^2$ (a) and $Z$ (b) for $N = 10^4$ as a function of $w$ in units of $\Gamma_c$ derived from Eqs. (3.1.8) and (3.1.9).

### Synchronization of the spins

In the following we want to review analogies between steady-state superradiance and the Kuramoto model. The latter is probably the most studied model exhibiting synchronization in a network of coupled oscillators [18, 19, 112–114]. The Kuramoto model for $N$ oscillators is described by the equations

$$\frac{d\theta_i}{dt} = \omega_i + \frac{K}{N}\sum_{j=1}^{N}\sin(\theta_j - \theta_i), \tag{3.1.18}$$

where $\theta_i$ is an angle, $\omega_i$ is the frequency, $K$ is the coupling, and $i = 1, 2, ..., N$. In this case if the dynamics of the $N$ oscillators is decoupled, $K = 0$, every oscillator oscillates with its own frequency $\omega_i$. Introducing the collective variable

$$re^{i\psi} = \frac{1}{N}\sum_{j=1}^{N} e^{i\theta_j},$$

where $r \in [0, 1]$ measures the coherence and $\psi$ is the collective phase of the oscillators, we may rewrite Eq. (3.1.18) as

$$\frac{d\theta_i}{dt} = \omega_i + Kr\sin(\psi - \theta_i). \tag{3.1.19}$$

This shows that the coupling of the single oscillators with each other can be understood as a coupling of the single oscillator to a collective oscillator. In the differential equation (3.1.19) of $\theta_i$ there are now two terms that compete: the first term, $\omega_i$, forces the oscillator to rotate with frequency $\omega_i$, the second term, $Kr\sin(\psi-\theta_i)$, tries to synchronize the phase to the phase of the collective oscillator $\psi$ by minimizing the difference $\psi - \theta_i$. The Kuramoto model predicts a synchronized phase with the signature of a non-vanishing coherence $r$ and a collective phase $\psi$ for $K > K_c > 0$, where $K_c$ is a threshold value and depends on the distribution of the frequencies $\omega_i$.[4]

[4]This is a very simplified statement, in fact, there can be very different synchronization phenomena depending on the coupling and the frequency distribution [19, 115–117]. The presented statement is true for a homogeneous coupling and an unimodal frequency distribution [19]

To show the analogies of the Kuramoto model and the model of steady-state superradiance we use a mean-field description. We assume $\langle \hat{X}\hat{\sigma}_i^z\rangle \approx \langle \hat{X}\rangle\langle\hat{\sigma}_i^z\rangle$ and $\Delta = 0$. In this case we derive the dynamics of the single-particle effective spin using Eq. (3.1.3) that reads

$$\frac{d\langle\hat{\sigma}_i\rangle}{dt} = -\frac{w}{2}\langle\hat{\sigma}\rangle_i - \frac{\Lambda}{2}\langle\hat{X}\rangle\langle\hat{\sigma}_i^z\rangle. \tag{3.1.20}$$

Defining now phase and coherence of the $i$th dipole using $\langle\hat{\sigma}\rangle_i = r_i e^{i\theta_i}$ and phase and coherence of the collective dipole with $\langle\hat{X}\rangle = re^{i\psi}$, we may rewrite Eq. (3.1.20) as

$$\frac{dr_i}{dt}e^{i\theta_i} + ir_i e^{i\theta_i}\frac{d\theta_i}{dt} = -\frac{w}{2}r_i e^{i\theta_i} + \frac{\Lambda}{2}re^{i\psi}\langle\hat{\sigma}_i^z\rangle. \tag{3.1.21}$$

The corresponding equations for real and imaginary part can be cast in the forms

$$\frac{dr_i}{dt} = -\frac{w}{2}r_i + \frac{\Lambda}{2}r\cos(\psi-\theta_i)\langle\hat{\sigma}_i^z\rangle, \tag{3.1.22}$$

$$\frac{d\theta_i}{dt} = \frac{\Lambda}{2}\frac{r}{r_i}\sin(\psi-\theta_i)\langle\hat{\sigma}_i^z\rangle. \tag{3.1.23}$$

Equation (3.1.23) is very similar to Eq. (3.1.19) and shows the same coupling of the single particle phase to the collective phase. In order to reach synchronization one needs a sufficiently large positive coupling and therefore $\langle\hat{\sigma}_i^z\rangle > 0$. Population inversion is reached when the incoherent repump rate $w$ exceeds the dipole relaxation $\Gamma_c$, $w > \Gamma_c$.

### 3.1.3 Overview and state of the art

Steady-state superradiance was first theoretically analyzed in Ref. [32]. For a realization with ensemble of earth-alkali metal atoms in a bad resonator, it was predicted that the light field can have a linewidth that can be as narrow as a few mHz [32]. Theoretical studies applied cumulant and Monte Carlo methods for characterizing steady-state superradiance [32, 110, 111, 118]. The first experimental realization of a superradiant laser is presented in Ref. [33] with Rubidium atoms. Realizations with strontium atoms are presented in Refs. [119, 120]. Ongoing work also investigates the crossover from lasing to steady-state superradiance [119, 121, 122] and related setups have lately also been proposed to study dissipative time crystals [114, 123, 124].

In the following we analyze the effect of the optomechanical coupling on the dynamics towards steady-state superradiance.

Section 3.2

# Mean-field theory for superradiance

In this section we discuss the mean-field description of steady-state superradiance including optomechanical effects.

## 3.2.1 Dynamical phase transitions to optomechanical superradiance

This subsection reports text and results that are published in Ref. [125]. We discuss the interplay between superradiant emission and quantum fluctuations due to the recoiling atoms, when the atoms' dipolar transitions couple to the mode of a lossy standing-wave resonator. In contrast to Refs. [12, 80, 126–128], here the atoms are incoherently pumped, as shown in Fig. 3.2, and therefore no coherence is established by the process pumping energy into the system. The system parameters are in the regime where stationary super-

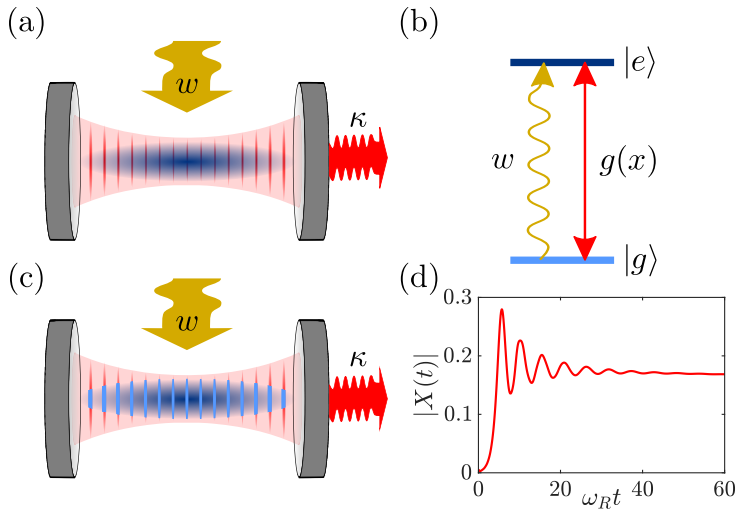


Figure 3.2: (a) An atomic gas initially forms a Bose-Einstein condensate and is confined within a standing-wave resonator, which emits photons at rate $\kappa$. (b) The metastable atomic transition $|g\rangle \rightarrow |e\rangle$ couples to the cavity mode and is incoherently pumped at rate $w$. After the first superradiant decay (c) the atoms form density gratings. (d) The emitted field $X(t)$ (here in the reference frame of the atomic frequency) becomes coherent for sufficiently large values of $w$, such that one grating is mechanically stable.

radiant emission (SSR) is predicted [32, 33, 110, 111, 121, 122]: In a homogeneous medium, SSR consists in the buildup of a stable macroscopic dipole, that acts as a stationary source of coherent light. The dynamical properties can be understood in terms of a peculiar time crystal [114], which locks at a frequency determined by the incoherent pump rate $w$. In a homogeneous medium the transition from normal to SSR fluorescence is controlled by $w$ when the superradiant decay rate is larger than the rates characterizing other incoherent

processes. Here, we show that in the presence of the optomechanical coupling with the external degrees of freedom SSR corresponds to spatio-temporal long-range order and is reached when the characteristic rates exceed the recoil frequency, scaling the mechanical energy exchanged with radiation. When instead the recoil frequency becomes comparable with the pump or the superradiant decay rate, then the superradiant emitted light can become either chaotic or incoherent. The chaotic phase, in particular, characterizes the asymptotic phase of an incoherent dynamics, it emerges from the interplay between quantum fluctuations, noise, and global interactions mediated by the cavity field, and is thus qualitatively different from chaos reported in quantum dynamics of Hamiltonian global-range interacting systems [129, 130].

When $\kappa$ and $\Delta$ are the largest rates the dynamics of the $N$ incoherently-driven bosonic atoms with mass $m$ can be cast in terms of long-range dipolar and optomechanical interactions in the atoms' Hilbert space. Then, the cavity field follows adiabatically the atomic motion, $\hat{a} \propto \hat{X}$ [131, 132] and the dynamics is governed by Eq. (3.1.3). For $N \gg 1$ the quantum dynamics is numerically intractable due to the adverse Liouville space scaling. We neglect single-atom radiative decay at rate $\Gamma_c$, assuming time scales $t < 1/\Gamma_c$ and $N \gg 1$. Since $1/\Gamma_c = N/\Lambda$, this time scale can be stretched to $t \to \infty$ in a thermodynamic limit $N \to \infty$ where $\Lambda$ is kept constant [129, 132]. Under these assumptions we finally obtain the mean-field master equation for the single-particle density matrix $\hat{\rho}_1$ (assuming that $\hat{\rho}_N$ is a product state at $t = 0$):

$$\frac{\partial \hat{\rho}_1}{\partial t} = \mathcal{L}_{\rm mf}[\hat{\rho}_1]\hat{\rho}_1 = \frac{1}{i\hbar}[\hat{H}_{\rm mf}(\hat{\rho}_1), \hat{\rho}_1] + w\mathcal{L}[\hat{\sigma}^\dagger]\hat{\rho}_1, \tag{3.2.1}$$

where $\hat{\rho}_1 = \mathrm{Tr}_{N-1}\{\hat{\rho}_N\}$ is obtained by tracing out $N-1$ atoms. The details of the calculation are shown in subsection 3.2.3. Now the incoherent evolution is due entirely to the incoherent pump and the interactions with the resonator are given by the mean-field Hamiltonian:

$$\hat{H}_{\rm mf} = \frac{\hat{p}^2}{2m} - \frac{\hbar\Lambda}{2}\left(\alpha X\{\hat{\rho}_1\}^*\hat{\sigma} + \alpha^* X\{\hat{\rho}_1\}\hat{\sigma}^\dagger\right)\cos(k\hat{x}), \tag{3.2.2}$$

with $\alpha = 2\Delta/\kappa - i$. Here, the Rabi frequency is proportional to the mean-field order parameter

$$X\{\hat{\rho}_1\} = \mathrm{Tr}\{\hat{\sigma}\cos(k\hat{x})\hat{\rho}_1\}, \tag{3.2.3}$$

and thus depends on the global macroscopic dipole. Note that $X$ generates the intracavity field and within the mean-field treatment determines the field's coherence properties. By neglecting the diffusion due to the incoherent pump, Eq. (3.2.1) can be reduced to a Vlasov equation with a potential that depends on the macroscopic dipole of the initial state, and whose stable solutions are metastable states of the out-of-equilibrium dynamics [23, 133].

### Stability of an arbitrary stationary state

The short timescale is governed by the stability of a stationary state of the mean-field master equation (3.2.1). The stability of a stationary state $\hat{\rho}_0$, with $\partial_t\hat{\rho}_0 = 0$, is determined by the initial dynamics of a density matrix $\hat{\rho} = \hat{\rho}_0 + \delta\hat{\rho}$ where $\delta\hat{\rho}$ is a small perturbation [23]. If this perturbation is amplified over time we can state that $\hat{\rho}_0$ is unstable, otherwise $\hat{\rho}_0$ is stable.

Using the mean-field master equation (3.2.1) we derive an equation of motion for $\delta\hat{\rho}$ that takes the form

$$\frac{\partial\delta\hat{\rho}}{\partial t} = i\frac{\Lambda}{2}\left(\alpha\delta X^*[\hat{J}_1,\hat{\rho}_0] - \text{H.c.}\right) + \mathcal{L}_{\text{mf}}[\hat{\rho}_0]\delta\hat{\rho}. \tag{3.2.4}$$

Here we have defined $\alpha = 2\Delta/\kappa - i$ and used the definition

$$\mathcal{L}_{\text{mf}}[\hat{\rho}_0]\delta\hat{\rho} = \frac{1}{i\hbar}[\hat{H}_{\text{mf}}[\hat{\rho}_0],\delta\hat{\rho}_1] + w\mathcal{L}[\hat{\sigma}^\dagger]\delta\hat{\rho}, \tag{3.2.5}$$

with $\hat{J}_1 = \hat{\sigma}\cos(k\hat{x})$ and $\delta X = X\{\delta\hat{\rho}\}$. In Eq. (3.2.4), we have included only first order perturbations in $\delta\hat{\rho}$ and we have discarded the second order. Applying the Laplace transform $\text{L}[f](s) = \int_0^\infty dt\, e^{-st} f(t)$ we derive the following equation

$$\mathbf{D}(s)\begin{pmatrix}\text{L}[\delta X](s)\\ \text{L}[\delta X^*](s)\end{pmatrix} = \begin{pmatrix}\text{Tr}\left(\hat{J}_1[s-\mathcal{L}_{\text{mf}}[\hat{\rho}_0]]^{-1}\delta\hat{\rho}(0)\right)\\ \text{Tr}\left(\hat{J}_1^\dagger[s-\mathcal{L}_{\text{mf}}[\hat{\rho}_0]]^{-1}\delta\hat{\rho}(0)\right)\end{pmatrix}$$

with

$$\mathbf{D}(s) = \begin{pmatrix}1+C_{11}(s) & C_{12}(s)\\ C_{21}(s) & 1+C_{22}(s)\end{pmatrix}. \tag{3.2.6}$$

The entries of the matrix take the forms

$$C_{11} = -i\frac{\Lambda}{2}\alpha^*\text{Tr}\left(\hat{J}_1\left(s-\mathcal{L}_{\text{mf}}[\hat{\rho}_0]\right)^{-1}[\hat{J}_1^\dagger,\hat{\rho}_0]\right), \tag{3.2.7}$$

$$C_{12} = -i\frac{\Lambda}{2}\alpha\text{Tr}\left(\hat{J}_1\left(s-\mathcal{L}_{\text{mf}}[\hat{\rho}_0]\right)^{-1}[\hat{J}_1,\hat{\rho}_0]\right), \tag{3.2.8}$$

$$C_{21} = -i\frac{\Lambda}{2}\alpha^*\text{Tr}\left(\hat{J}_1^\dagger\left(s-\mathcal{L}_{\text{mf}}[\hat{\rho}_0]\right)^{-1}[\hat{J}_1^\dagger,\hat{\rho}_0]\right), \tag{3.2.9}$$

$$C_{22} = -i\frac{\Lambda}{2}\alpha\text{Tr}\left(\hat{J}_1^\dagger\left(s-\mathcal{L}_{\text{mf}}[\hat{\rho}_0]\right)^{-1}[\hat{J}_1,\hat{\rho}_0]\right). \tag{3.2.10}$$

Inverting $\mathbf{D}(s)$ and applying the inverse Laplace transformation, we obtain the dynamics of $\delta X$. In order to derive the dynamics we need to know the poles of the matrix $\mathbf{D}(s)^{-1}$. These are roots of the dispersion relation

$$D(s) = \det(\mathbf{D}(s)) = 0. \tag{3.2.11}$$

The complex solution $\gamma$ of Eq. (3.2.11) with the largest real part $\text{Re}(\gamma)$ gives the dominant contribution to the dynamics of $\delta X$. Therefore this determines whether the stationary solution $\hat{\rho}_0$ is stable or not. If $\text{Re}(\gamma) > 0$ the perturbation $\delta\hat{\rho}$ will exponentially grow and thus $\hat{\rho}_0$ is an unstable stationary solution. Otherwise, if $\text{Re}(\gamma) \leq 0$, $\hat{\rho}_0$ is stable.

We will now use this result in order to derive the stability of an incoherent stationary state $\hat{\rho}_0$ with $X\{\hat{\rho}_0\} = 0$. Such a state is of the form

$$\hat{\rho}_0 = |e\rangle\langle e| \otimes \hat{\rho}_{\text{mom}}, \tag{3.2.12}$$

where $\hat{\rho}_{\text{mom}}$ is a state describing the external degrees of freedom and fulfills $[\hat{p}^2,\hat{\rho}_{\text{mom}}] = 0$.

**Stability of the incoherent state**

Since $X\{\hat{\rho}_0\} = 0$ we observe that the matrix in Eq. (3.2.6) becomes diagonal. Therefore, if we want to find the zeros of the dispersion relation in Eq. (3.2.11) it is sufficient to solve the equation

$$1 + C_{11}(s) = 0. \tag{3.2.13}$$

Using the duality of the Schrödinger and Heisenberg pictures we obtain

$$\begin{aligned} C_{11} =& -i\frac{\Lambda}{2}\alpha^* \mathrm{Tr}\left(\hat{J}_1 \left(s - \mathcal{L}_{\mathrm{mf}}\right)^{-1} [\hat{J}_1^\dagger, \hat{\rho}_0]\right) \\ =& -i\frac{\Lambda}{2}\alpha^* \int_0^\infty dt e^{-st} \mathrm{Tr}\left(\hat{J}_1 e^{\mathcal{L}_{\mathrm{mf}} t}[\hat{J}_1^\dagger, \hat{\rho}_0]\right) \\ =& -i\frac{\Lambda}{2}\alpha^* \int_0^\infty dt e^{-st} \langle [\hat{J}_1(t), \hat{J}_1^\dagger(0)]\rangle_{\hat{\rho}_0}. \end{aligned} \tag{3.2.14}$$

Here we use the definition that for an operator $\hat{A}$ the expectation value is defined as $\langle \hat{A}\rangle_{\hat{\rho}} = \mathrm{Tr}(\hat{A}\hat{\rho})$.

In the homogeneous case, we calculate $\hat{J}_1(t)$, and it takes the form

$$\hat{J}_1(t) = \hat{\sigma}(0) e^{-\frac{w}{2}t} \cos\left(k\hat{x}(t)\right), \tag{3.2.15}$$

with $\hat{x}(t) = \hat{x}(0) + k\hat{p}(0)t/m$. Using Eq. (3.2.15) in Eq. (3.2.14) we obtain

$$C_{11} = i\frac{\Lambda}{2}\alpha^* \int_0^\infty dt e^{-\left(s+\frac{w}{2}\right)t} \left\langle \cos(k\hat{x}) \cos\left(k\hat{x}(t)\right)\right\rangle_{\hat{\rho}_{\mathrm{mom}}}, \tag{3.2.16}$$

where we explicitly used the fact that all particles are in the excited state and therefore $\langle \hat{\sigma}\hat{\sigma}^\dagger\rangle = 0$ holds. From the identity

$$e^{ik\hat{x} + ik\hat{p}/mt} = e^{ik\hat{x}} e^{ik\hat{p}/mt} e^{i\omega_R t}$$

and $e^{ik\hat{x}}|p\rangle = |p + \hbar k\rangle$ we can show that

$$\begin{aligned} I =& \int dp \left\langle p \middle| \cos(k\hat{x}) \frac{e^{ik\hat{x}} e^{ik\hat{p}/mt} + e^{-ik\hat{x}} e^{-ik\hat{p}/mt}}{2} \hat{\rho}_{\mathrm{mom}} \middle| p \right\rangle \\ =& \frac{1}{4}\int dp \langle p|\hat{\rho}_{\mathrm{mom}}|p\rangle (e^{ikp/mt} + e^{-ikp/mt}) \\ &+ \frac{1}{4}\left(\langle \hbar k \middle| \hat{\rho}_{\mathrm{mom}}| - \hbar k\rangle + \langle -\hbar k \middle| \hat{\rho}_{\mathrm{mom}}|\hbar k\rangle\right) e^{-i2\omega_R t}, \end{aligned} \tag{3.2.17}$$

with $\omega_R = \hbar k^2/(2m)$ the recoil frequency. In Eq. (3.2.17) we used $\langle p|\hat{\rho}_{\mathrm{mom}}|p'\rangle = 0$ for $p' \neq \pm p$. This is true since $\hat{\rho}_{\mathrm{mom}}$ commutes with $\hat{p}^2$. Using

$$C_{11} = i\frac{\Lambda}{2}\alpha^* \int_0^\infty dt e^{-\left(s+\frac{w}{2}-i\omega_R\right)t} I \tag{3.2.18}$$

and Eq. (3.2.17) we get

$$\begin{aligned} C_{11} =& i\frac{\Lambda y}{4}\alpha^* \int_{-\infty}^\infty dp \frac{\langle p|\hat{\rho}_{\mathrm{mom}}|p\rangle}{y^2 + \left(\frac{kp}{m}\right)^2} \\ &+ i\frac{\Lambda}{8}\alpha^* \frac{\langle \hbar k \middle| \hat{\rho}_{\mathrm{mom}}| - \hbar k\rangle + \langle -\hbar k \middle| \hat{\rho}_{\mathrm{mom}}|\hbar k\rangle}{y + i2\omega_R}, \end{aligned} \tag{3.2.19}$$

with $y = s + w/2 - i\omega_R$.

**Stability of a thermal state**

In the following we analyze the stability of a thermal state $\hat{\rho}_1^{(0)} = |e\rangle\langle e| \otimes \exp(-\beta\hat{p}^2/2m)/Z$, with inverse temperature $\beta$ and partition function $Z$. This is an incoherent state with $X\{\hat{\rho}_1^{(0)}\} = 0$. Using $\hat{\rho}_0 = |e\rangle\langle e| \otimes \hat{\rho}_{\rm mom}$ with

$$\hat{\rho}_{\rm mom} = \frac{1}{\sqrt{2\pi p_0^2}} \exp\left(-\beta \frac{\hat{p}^2}{2m}\right), \tag{3.2.20}$$

the dispersion relation in Eq. (3.2.13), can be simplified to

$$1 + i\frac{\Lambda y}{4}\alpha^* \int_{-\infty}^{\infty} dp \sqrt{\frac{\beta}{2m\pi}} \frac{\exp\left(-\beta\frac{p^2}{2m}\right)}{y^2 + \left(\frac{kp}{m}\right)^2} = 0, \tag{3.2.21}$$

where we used $y = s + w/2 - i\omega_R$. Using the substitution $p = \sqrt{m/\tilde{\beta}}u$, with $\tilde{\beta}^{-1} = \hbar\Lambda^2/(2\omega_R)$, we can rewrite Eq. (3.2.21) as

$$1 + i\alpha^* \frac{y}{4\Lambda} \int_{-\infty}^{\infty} du \sqrt{\frac{\beta}{2\pi\tilde{\beta}}} \frac{\exp\left(-\frac{\beta}{\tilde{\beta}}\frac{u^2}{2}\right)}{\left(\frac{y}{\Lambda}\right)^2 + u^2} = 0. \tag{3.2.22}$$

From Eq. (3.2.22) we calculate the value $\gamma$ that corresponds to the solution $s = y - w/2 + i\omega_R$ with the largest real part. This exponent will be dominant for the time evolution of the thermal state. The short-time dynamics is determined by this exponent

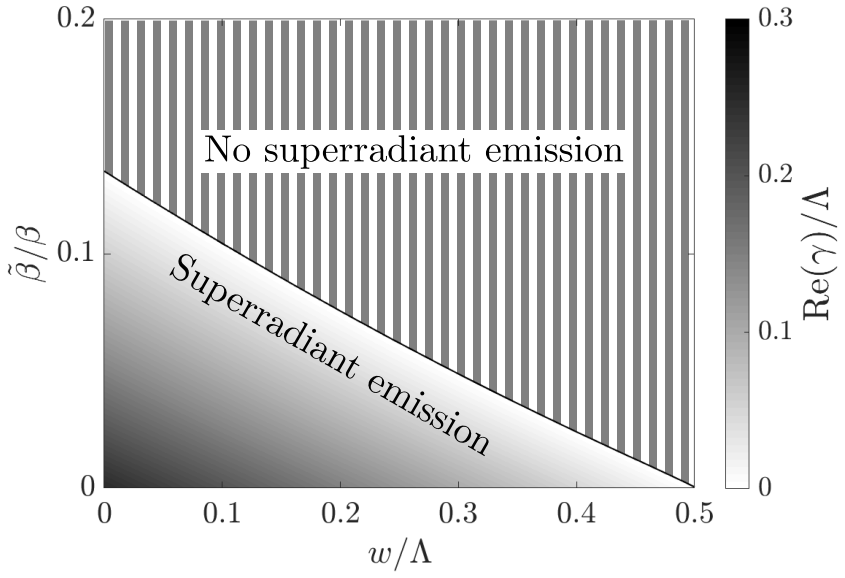


Figure 3.3: Contour plot of the rate $\gamma$ of the first superradiant emission as a function of the incoherent pump rate $w$ (in units of $\Lambda$) and of the atomic gas temperature $1/\beta$ (in units of $\tilde{\beta}^{-1} = \hbar\Lambda^2/(2\omega_R)$). The solid line separates the regime in which the atoms undergo superradiant decay from the one where thermal fluctuations suppress superradiance (stripes).

as a function of $w$ and $\beta$. No superradiant emission is found when $X\{\hat{\rho}_1^{(0)}\} = 0$ is

stable to small fluctuations. If instead it exponentially increases as $X \sim \exp(\gamma t)$ with $\mathrm{Re}(\gamma) > 0$, then the system undergoes superradiant decay with rate $\mathrm{Re}(\gamma)$. Figure 3.3 shows the contour plot of the exponent $\mathrm{Re}(\gamma)$ as a function of both $w$ and $\beta$. We find a threshold temperature $k_B T_c \approx 0.1\hbar\Lambda^2/(2\omega_R)$. For $T > T_c$ thermal fluctuations suppress superradiance. For $T < T_c$ superradiance is found for a finite interval of the pump rate $0 < w \leq w_{\max}(\beta)$, which increases with the ratio $\eta = \beta/\bar{\beta} = T_c/T$. For $\eta \to \infty$ the upper bound is $w_{\max} = \Lambda/2$, it coincides with the value found for a homogeneous medium [132].

**Dynamics of an ultracold atomic ensemble**

We now study the dynamics of an ensemble of atoms in the zero-temperature limit, when the atoms initially form a Bose-Einstein condensate (BEC). We neglect onsite interactions and analyze the dynamics of the external degrees of freedom on the closed family of momentum states $|\Psi_0\rangle = |0\rangle$ (the BEC) and $|\Psi_n\rangle = (|n\hbar k\rangle + |-n\hbar k\rangle)/\sqrt{2}$ $(n = 1, 2, \ldots)$. These states are coupled by absorption and emission of cavity photons; their energy $E_{\mathrm{kin},n} = n^2\hbar\omega_R$ is an integer multiple of $\omega_R$. The asymptotic behavior of Eq. (3.2.1) is strictly defined in the thermodynamic limit and is determined by means of a recursive procedure that we explain in the following.

Using Eq. (3.2.1) one can show that

$$\begin{aligned}\frac{d}{dt}\langle\hat{H}_{\mathrm{mf}}\rangle =& \frac{d}{dt}\left(\frac{\langle\hat{p}^2\rangle}{2m} - \frac{\hbar\Lambda\Delta}{\kappa/2}|X|^2\right)\\ =& \mathrm{Tr}\left(\hat{H}_{\mathrm{mf}}\frac{\partial\hat{\rho}_1}{\partial t}\right) + \mathrm{Tr}\left(\frac{\partial\hat{H}_{\mathrm{mf}}}{\partial t}\hat{\rho}_1\right)\\ =& \frac{\hbar\Lambda\Delta}{\kappa}w|X|^2 - \frac{\hbar\Lambda}{2}\left(\alpha^*\frac{dX}{dt}X^* + \mathrm{c.c}\right).\end{aligned} \tag{3.2.23}$$

Explicitly denoting the amplitude and phase $X = |X|e^{i\phi}$ we obtain

$$\frac{d}{dt}\langle\hat{H}_{\mathrm{mf}}\rangle = \frac{\hbar\Lambda\Delta}{\kappa}w|X|^2 + \hbar\Lambda|X|^2\frac{d\phi}{dt} - \frac{\hbar\Lambda\Delta}{\kappa}\frac{d|X|^2}{dt}. \tag{3.2.24}$$

Now, assuming that there exists a stationary state with $d\langle\hat{p}^2\rangle/dt = 0$ and $d|X|^2/dt = 0$, we arrive at

$$\frac{d\phi}{dt} = -\frac{w\Delta}{\kappa}. \tag{3.2.25}$$

Therefore to find a stationary solution for the system we need to solve

$$\mathcal{L}_{\mathrm{mf}}\left[\hat{\rho}_1\right]\hat{\rho}_1 = \frac{1}{i\hbar}\left[\frac{\hbar w\Delta}{\kappa}\hat{\sigma}^\dagger\hat{\sigma}, \hat{\rho}_1\right]. \tag{3.2.26}$$

This is equivalent to calculating the stationary state in the frame rotating with the frequency shown in Eq. (3.2.25). To characterize and numerically determine this solution we use the order parameter $X$. For the numerical calculation of the stationary state we start from an order parameter $X > 0$ and find $\hat{\rho}_0$ to recalculate the new value of $X = \mathrm{Tr}(\hat{\sigma}\cos(k\hat{x})\hat{\rho}_0)$. We iterate this step until $\hat{\rho}_0$ and $X$ converge. In the case when there is a solution of Eq. (3.2.26) with $X \neq 0$ we know that there is a coherent stationary state. However, this state does not need to be stable. To calculate the stability we use the dispersion relation in Eq. (3.2.11).

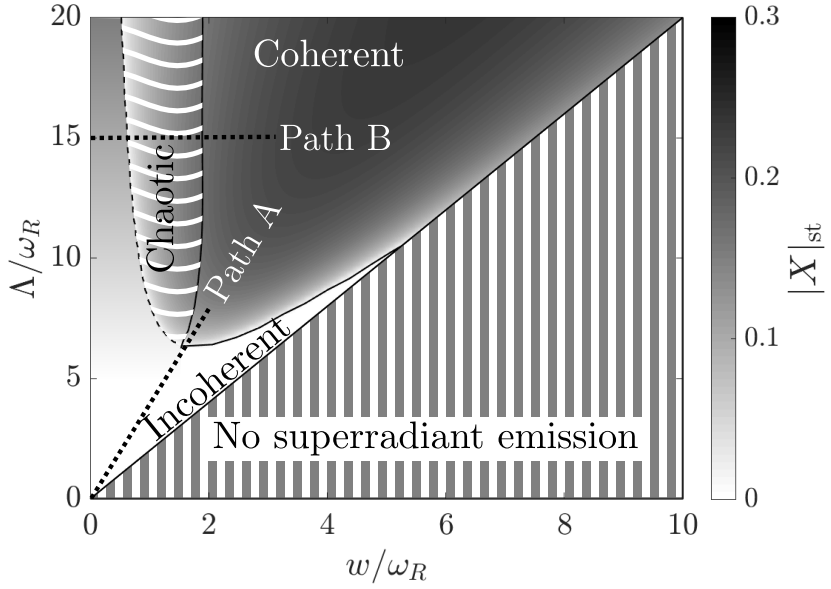


Figure 3.4: Phase diagram in the $w/\omega_R$–$\Lambda/\omega_R$ plane when the atoms initially form a Bose-Einstein condensate at $T = 0$. The phases are labeled by the coherence properties of the emitted light. The emitted field is given by $X(t)$ and is obtained by solving Eq. (3.2.1) at the asymptotic dynamics. Path A (Path B) shows the parameters of Fig. 3.5 (Fig. 3.6). In the striped region superradiant decay is suppressed (it corresponds to the region at $T = 0$ and $w > \Lambda/2$ in Fig. 3.3).

In Fig. 3.4 we report the converged values of $X$ and therefore the coherence properties of the emitted light in a $w - \Lambda$ phase diagram. We first note the normal (striped) phase with $w > \Lambda/2$, where there is no superradiant emission. The transition from normal to superradiant phase (without optomechanical coupling) has been discussed in the literature [32, 110, 111, 114, 134]. Within the regime where SSR is expected, we now find that the optomechanical coupling gives rise to three phases which we denote by incoherent, coherent, and chaotic, corresponding to the coherence properties of the emitted light. In the incoherent phase only the solution with $X = 0$ is stable and collective effects are suppressed. In the coherent phase there is one stable solution with $X \neq 0$. As visible in the phase diagram, the condition for the appearance of this phase is that the superradiant linewidth exceeds a minimum value determined by the recoil frequency, $\Lambda > \Lambda_c$ with $\Lambda_c \sim 6\omega_R$. Finally, the chaotic phase is found for $\Lambda > \Lambda_c$, when the pump rate is below a threshold $w_c(\Lambda)$. Here, both solutions with $X \neq 0$ and $X = 0$ are unstable.

We verified these predictions by numerically integrating Eq. (3.2.1) with the initial state $\rho_1(0)$ at $T = 0$ on the grid of momentum states $p = 0, \pm\hbar k, \ldots, \pm 15\hbar k$. Figure 3.5(a) displays three evolutions of $|X(t)|$ for different values of $\Lambda$ along Path A of Fig. 3.4, where a direct transition occurs from an incoherent to a coherent (SSR) phase. For all values the intracavity field $|X(t)|$ first grows exponentially, and subsequently reaches a maximum at a time scale $\tau_c \sim 1/\Lambda$. After this time scale: (i) For $\Lambda < \Lambda_c$ the intracavity field $|X(t)|$ decays to zero. This dynamics is accompanied by the formation of a statistical mixture of states $|e, \Psi_{2n}\rangle$ and $|e, \Psi_{2n+1}\rangle$, which dephases the macroscopic dipole and leads to suppression of superradiant emission. (ii) For $\Lambda \sim \Lambda_c$ the field undergoes fast oscillations and then slowly decays to zero. (iii) For $\Lambda > \Lambda_c$ the field oscillates about

a finite asymptotic value and the atoms form a stable spatial pattern. This dynamics exhibits the general features of a dynamical phase transition, which occurs after the first superradiant emission at $t \sim \tau_c$. After $\tau_c$ the macroscopic dipole $X$ decays to zero or oscillates about a finite metastable value. We denote the asymptotic value of the order parameter by $X_{\rm st}(\Lambda)$, which we determine by numerical evolution of $|X(t)|$, taking $|X_{\rm st}(\Lambda)| = |X(t_{\rm f})|$, where at $t_{\rm f}$ the dipole $|X(t)|$ has reached a constant value. We compare this result with the asymptotic solution $\hat{\rho}_{\rm st}$ of Eq. (3.2.1), calculated using the iterative procedure. Along Path A this iterative procedure always converges to either $X_{\rm st} = 0$ for $\Lambda < \Lambda_c$ and $X_{\rm st} > 0$ for $\Lambda > \Lambda_c$. As visible in Fig. 3.5(b), the predictions obtained by numerical integration (circles) and by the iterative procedure (dashed line) qualitatively agree and exhibit the features of a second-order phase transition. We also present a measure for the entanglement between the internal and external degrees of freedom. Since the system relaxes to an incoherent state for $\Lambda < \Lambda_c$, all particles are in the excited state and therefore the system has no entanglement between internal and external degrees of freedom. However, if the system is in the coherent phase, for $\Lambda > \Lambda_c$, we observe entanglement between internal and external degrees. This claim can be verified by an analysis of the partial transpose $\hat{\rho}_{\rm st}^{\rm PPT}$ of the stationary state $\hat{\rho}_{\rm st}$ [135]. The matrix $\hat{\rho}_{\rm st}^{\rm PPT}$ is calculated from $\hat{\rho}_{\rm st}$ by applying the transpose on the internal degrees of freedom only. In the case where internal and external degrees of freedom are not entangled $\hat{\rho}_{\rm st}^{\rm PPT}$ is a positive matrix. On the other hand if $\hat{\rho}_{\rm st}^{\rm PPT}$ is not positive we know that there is entanglement. To check whether the internal and external degrees of freedom are entangled in the coherent phase we calculate the minimum eigenvalue

$$\lambda_{\rm min} = \min\{\lambda | \lambda \text{ is eigenvalue of } \hat{\rho}_{\rm st}^{\rm PPT}\}. \tag{3.2.27}$$

If this eigenvalue is negative we know that the system is entangled. The numerical calculated values for $\lambda_{\rm min}$ are shown in Fig. 3.5(c). Its behavior shows that at the buildup of SSR internal and external degrees of freedom become entangled.

The transition separating the coherent from the chaotic phase occurs for $\Lambda > \Lambda_c$ as a function of $w$: The properties of the emitted light dramatically depend on whether $w$ is smaller or larger than a critical value $w_c(\Lambda)$. Figure 3.6(a) displays the numerical results for the real and the imaginary part of $X(t)$ for a fixed time interval for (i) $w < w_c$, where the dynamics is chaotic, (ii) $w \simeq w_c$ where the dynamics is mainly characterized by the appearance of two subharmonics, and (iii) for $w > w_c$, where the dynamics is evidently coherent. The spectrum of the emitted light is displayed in Fig. 3.6(b) as a function of $w$ and for the parameters of Path B of Fig. 3.4. The transition from regular oscillations to chaos occurs at a value $w_c$ where two sidebands appear. We analytically determine $w_c$ by means of a stability analysis. This analysis also delivers the frequencies of the sideband at $w = w_c$ and the Lyapunov exponent $\gamma_L = {\rm Re}(\gamma)$. As is visible in Fig. 3.6(c), $\gamma_L$ changes sign at $w = w_c$ and is positive for $w < w_c$. The trajectory of subplot (a)-(i) corresponds to the value of $w$ where the spectrum is dense: In this parameter regime the stability analysis predicts the transition from chaotic to incoherent dynamics. Numerical simulations show that for $w < w_c$ the density grating becomes unstable and the system jumps back and forth between a prevailing occupation of the set of states corresponding to an even grating, $\{|e, \Psi_{2n}\rangle, |g, \Psi_{2n+1}\rangle, n = 0, 1, 2, ...\}$, and of the ones corresponding to an odd grating, $\{|e, \Psi_{2n+1}\rangle, |g, \Psi_{2n}\rangle, n = 0, 1, 2, ...\}$. While the states within each set are coupled by coherent processes, the two sets are only coupled to each other by the incoherent pump: For $w < w_c$ the long-range optomechanical interactions tend to form a grating, which locks the phase of the field, while the incoherent pump induces quantum

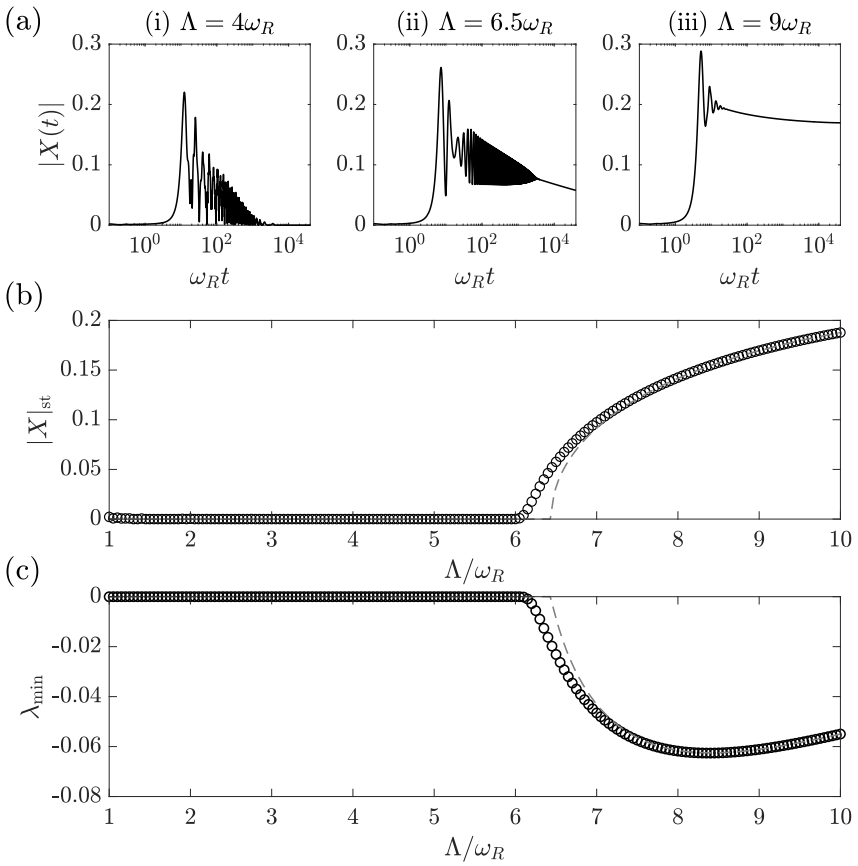


Figure 3.5: The incoherent-coherent transition for the parameters of Path A of Fig. 3.4 ($w = \Lambda/4$ and $\Delta = \kappa/2$). Subplot (a), from left to right: Dynamics of $X$ for $\Lambda = 4, 6.5, 9\omega_R$. (b) The asymptotic value for the mean-field order parameter $|X(t_{\rm f})|$ and (c) the minimum eigenvalue $\lambda_{\rm min}$ of the partial transpose of the asymptotic density matrix, signalling entanglement between external and internal degrees of freedom, as a function of $\Lambda$ (in units of $\omega_R$). Black circles: Numerical results at time $t_{\rm f} = 4\times10^4\omega_R^{-1}$; Dashed lines: Steady-state values from the iterative solution of $\partial_t\rho_1 = 0$, Eq. (3.2.1).

jumps between different gratings. An analysis of the entanglement is possible only from the coherent side, where the non-linear master equation has one stationary solution, and shows that internal and external degrees of freedom are entangled for $w > w_c$. For the transition from chaotic to coherent the analysis needs to be adjusted. Therefore we introduce a time-averaged minimum eigenvalue

$$\bar{\lambda}_{\rm min} = \frac{1}{t_{\rm end}} \int_0^{t_{\rm end}} \lambda_{\rm min}(t) dt, \tag{3.2.28}$$

with simulation time $t_{\rm end}$. To find $\bar{\lambda}_{\rm min}$ we need to calculate $\lambda_{\rm min}(t)$ as a function of time

$$\lambda_{\rm min}(t) = \min\{\lambda | \lambda \text{ is eigenvalue of } \hat{\rho}(t)^{\rm PPT}\}. \tag{3.2.29}$$

We plot $\bar{\lambda}_{\rm min}$ in Fig. 3.7(a) where we observe that $\bar{\lambda}_{\rm min} < 0$ for the shown interval of $w$. The minimal eigenvalue calculated with the iterative method is shown as the gray, dashed line. While the results of both methods agree in the coherent phase $w > w_c$ we

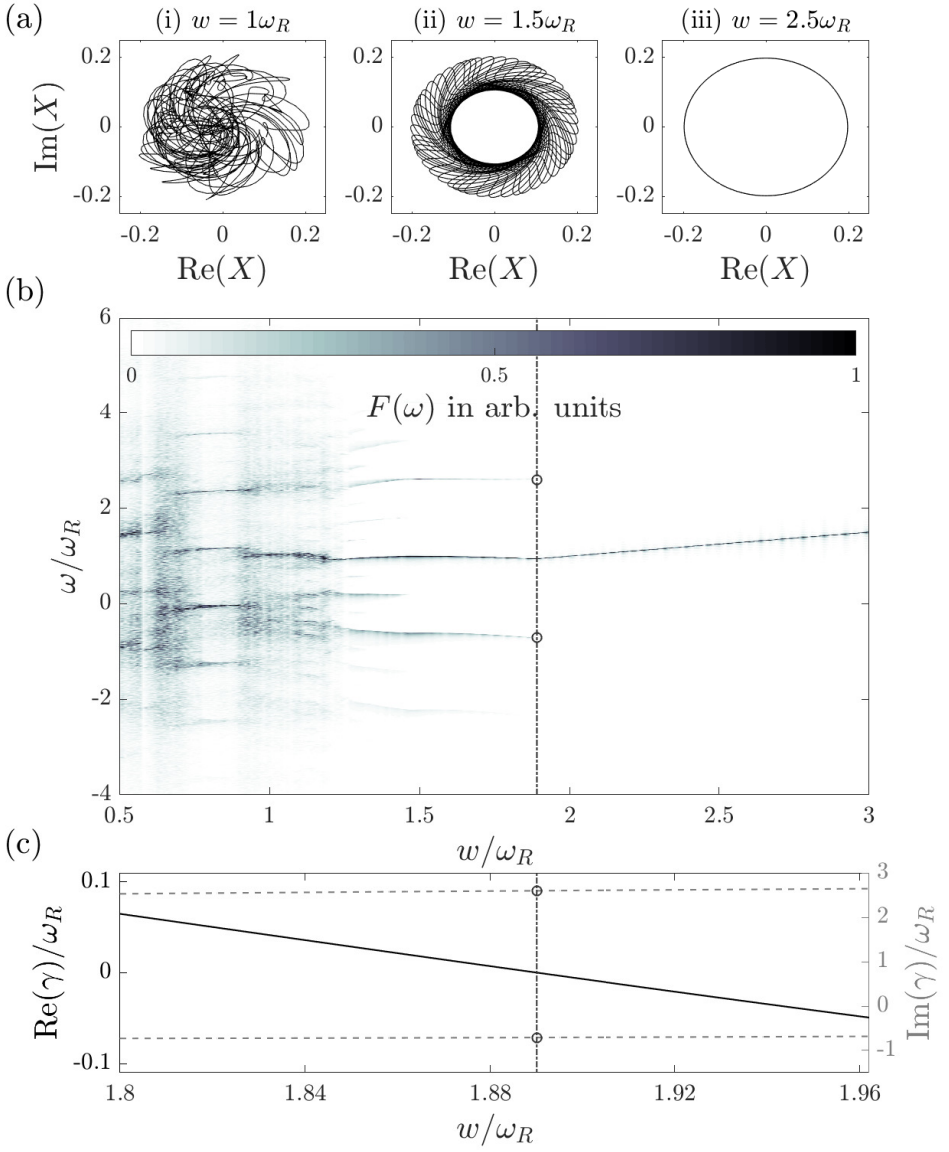


Figure 3.6: The chaotic-coherent transition for the parameters of Path B of Fig. 3.4 ($\Lambda = 15\omega_R$ and $\Delta = \kappa/2$). (a) From left to right: Real and imaginary part of $X$ for $w = 1, 1.5, 2.5\omega_R$ (here for the time interval $t \in [9.8 \times 10^3, 10^4]/\omega_R$). (b) Contour plot of the spectrum of the emitted light $F(\omega)$ (arbitrary units) as a function of $w$ and of the frequency $\omega$ (in units of $\omega_R$). Here, $F(\omega) \propto \left|\int_0^{t_{\rm end}} e^{i\omega t} X(t) dt\right|$ is found by integrating Eq. (3.2.1) until $t_{\rm end} = 10^4 \omega_R^{-1}$. (c) The real (solid) and imaginary part (dashed) of the exponent $\gamma$ (in units of $\omega_R$) giving the stability of the stationary solutions. The vertical dashed lines indicate the critical pumping strength $w_c(\Lambda)$, where Re($\gamma$) changes sign and the sidebands appear, the circles mark the corresponding frequencies.

observe large discrepancies in the chaotic phase. For completeness we also report the

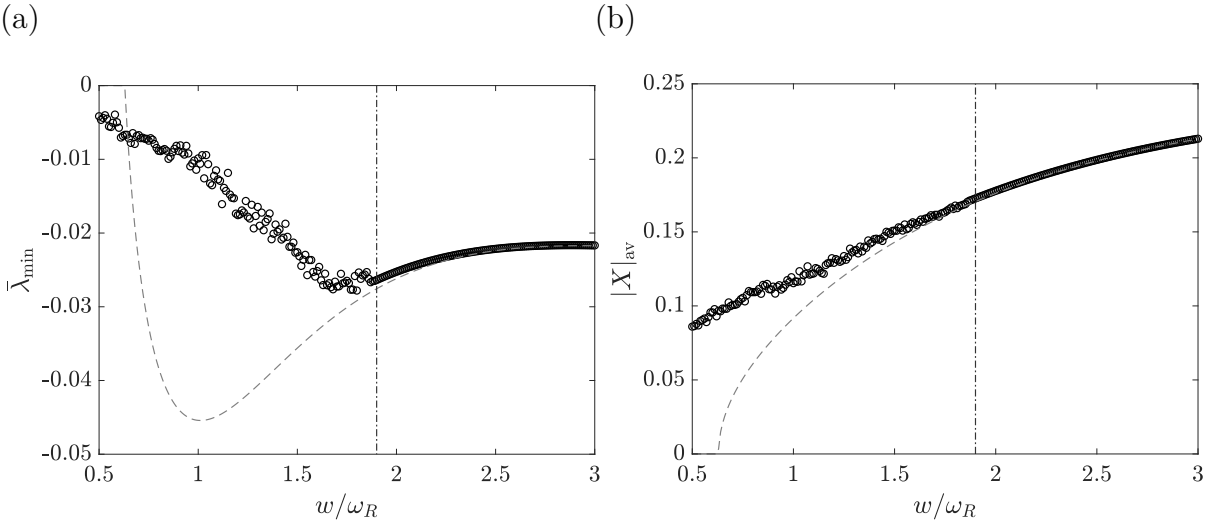


Figure 3.7: (a) The time-averaged minimum eigenvalue $\bar{\lambda}_{\min}$ calculated using Eq. (3.2.28) (black circles) with $t_{\text{end}} = 10^4\omega_R^{-1}$ as a function of $w$ in units of $\omega_R$. The gray, dashed line corresponds to the value of $\lambda_{\min}$ calculated using the coherent stationary state. (b) The time-averaged mean-field order parameter $|X|_{\text{av}}$ (black circles) with $t_{\text{end}} = 10^4\omega_R^{-1}$ and the asymptotic result (gray, dashed line) as a function of $w$ in units of $\omega_R$. The vertical dashed lines in subplot (a) and (b) show the critical pumping strength $w_c(\Lambda)$. The equations are integrated in the momentum interval $[-15\hbar k, 15\hbar k]$ for $\Lambda = 15\omega_R$ and $\Delta = \kappa/2$.

time-averaged mean-field order parameter

$$|X|_{\text{av}} = \frac{1}{t_{\text{end}}}\int_0^{t_{\text{end}}} |X(t)|dt \tag{3.2.30}$$

in Fig. 3.7(b). The time-averaged mean-field order parameter $|X|_{\text{av}}$ and the asymptotic result agree in the coherent phase while $|X|_{\text{av}}$ is larger in the chaotic phase. Notice that the discrepancies in the chaotic phase are expected since here the asymptotic state is not a stable state and the description in terms of a single stationary state fails. We remark that in the coherent phase the frequency of the oscillator depends on the incoherent pump rate, $\omega_a + \Delta w/\kappa$, showing that this spatio-temporal self-organization exhibits the features of time crystals [114].

Finally, we conclude that the phase diagram can be observed by tuning the superradiant linewidth and the pump rate across values of the order of the recoil frequency $\omega_R$, the phases are signaled by the first-order correlation function of the emitted light. These dynamics can be realized when the resonator linewidth $\kappa$ exceeds by several orders of magnitude $\omega_R$ and when other incoherent processes can be discarded over the time scales where the dynamical phase transition occurs. Specifically, the spontaneous decay of the dipolar transition shall be orders of magnitude smaller than the recoil frequency, which can be realized using a Raman transition between metastable hyperfine states, as for instance in Refs. [33, 103, 105].

### 3.2.2 Superradiance and thermal noise

In the following we will use the mean-field approach to describe the time evolution of a thermal gas. In particular we are interested to study the effects of thermal noise on steady-state superradiance. We simulate the mean-field master equation (3.2.1) decomposing the Hilbert space of the external degrees of freedom into different momentum families as we report in App. A.2.

#### Onset of superradiance

We want to show that the value of $\gamma$ found using Eq. (3.2.22) is compatible with the numerical integration of the mean-field master equation (3.2.5). We choose the parameters $\Lambda = 40\omega_R$, $\Delta = \kappa/2$, and $\beta^{-1} = 20\hbar\omega_R$ such that $\tilde{\beta}^{-1} = 800\hbar\omega_R$ and $\tilde{\beta}/\beta = 1/40$. For these parameters the ensemble will undergo superradiant emission whenever $w < w_c$ with $w_c \lesssim 0.4\Lambda$. Figure 3.8(a) shows the dynamics of the order parameter $|X(t)|$ for four different values of $w$ as a function of time. The black line corresponds to $w = 10\omega_R$, the green (dark gray) line to $w = 6\omega_R$, the blue (gray) line to $w = 3\omega_R$ and the violet (light gray) line to $w = \omega_R$. The time axes are rescaled with the exponents $\mathrm{Re}(\gamma)$ that are calculated using Eq. (3.2.22).

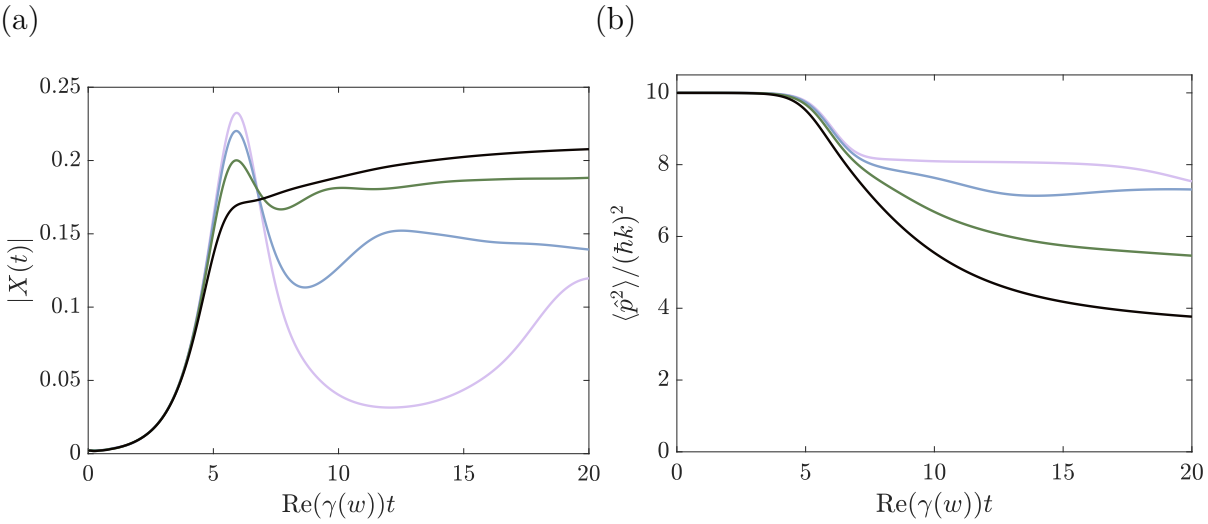


Figure 3.8: (a) The absolute value of the mean-field order parameter $|X(t)|$ and (b) the second moment of momentum $\langle\hat{p}^2\rangle$ as function of time in units of $\mathrm{Re}(\gamma(w))^{-1}$. The black lines corresponds to $w = 10\omega_R$, the green (dark gray) lines to $w = 6\omega_R$, the blue (gray) lines to $w = 3\omega_R$ and the violet (light gray) lines to $w = \omega_R$. For every value of $w$ we calculated $\gamma(w)$ using Eq. (3.2.22) and rescaled the time axis by $\mathrm{Re}(\gamma(w))$. The remaining parameters are $\Delta = \kappa/2$, $\beta^{-1} = 20\hbar\omega_R$, and $\Lambda = 40\omega_R$. For the simulations we used a momentum cut off at $p_{\max} = 16\hbar k$.

All four lines agree on a timescale of the order $\mathrm{Re}(\gamma)^{-1}$, thus showing that the linearized master equation (3.2.4) is valid and the exponential increase of $|X(t)|$ with exponent $\mathrm{Re}(\gamma)$ can explain the dynamics. However, on a longer timescale we observe that the curves show different behavior.

The onset of synchronization is not only visible in the coherences of the system but also in the motional degrees of freedom. One example is the kinetic energy that is shown

in Fig. 3.8(b) with the same color scheme as the ones in subplot (a). After a transient, we observe a decrease of the kinetic energy whose gradient increases with $w$. This decrease of the kinetic energy can be understood deriving the time evolution of the kinetic energy using Eq. (3.2.5). We get

$$\begin{aligned}\frac{d}{dt}\frac{\langle\hat{p}^2\rangle}{2m} =& \frac{\hbar\Lambda}{2}\left[w\frac{\Delta}{\kappa/2}|X(t)|^2 + 2\mathrm{Im}\left(\frac{dX(t)}{dt}X(t)^*\right)\right] \\ =& \hbar\Lambda\left[\frac{w}{2}\frac{\Delta}{\kappa/2} + \frac{d\phi}{dt}\right]|X(t)|^2, \end{aligned} \tag{3.2.31}$$

where we used $X(t) = |X(t)|e^{i\phi(t)}$. From this equation we see that $d\phi/dt$ determines the growth of the kinetic energy. For our parameters choice, at short time scales (when $\delta X(t) \approx |\delta X(t)|e^{i\mathrm{Im}(\gamma)t}$ holds), the system loses kinetic energy since

$$\frac{w}{2}\frac{\Delta}{\kappa/2} < \frac{d\phi}{dt} \approx \mathrm{Im}(\gamma).$$

This fits to the initial behavior visible in Fig. 3.8(b).

We want to discuss now the dynamics of the system towards a metastable state.

### Dynamics towards a metastable state

On a longer timescale the dynamics of the order parameter $|X(t)|$ can change for different values of $w$. In Fig. 3.9 we plot the dynamics of $|X|$ and $\langle\hat{p}^2\rangle$ up to $t = 400\omega_R^{-1}$. We

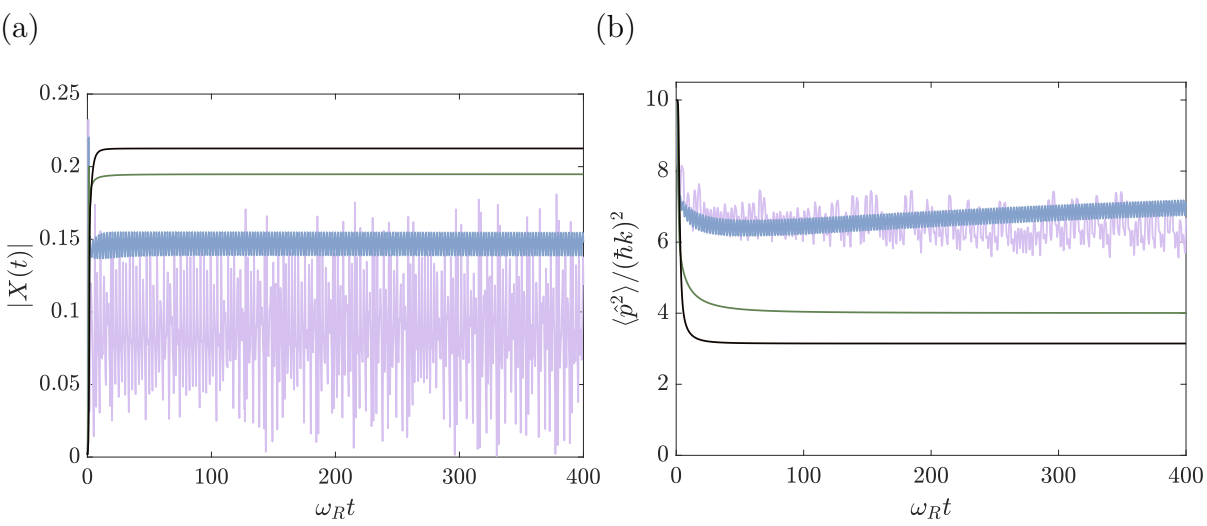


Figure 3.9: (a) The absolute value of the mean-field order parameter $|X(t)|$ and (b) the second moment of momentum $\langle\hat{p}^2\rangle$ as function of time in units of $\omega_R^{-1}$. The black lines corresponds to $w = 10\omega_R$, the green (dark gray) lines to $w = 6\omega_R$, the blue (gray) lines to $w = 3\omega_R$ and the violet (light gray) lines to $w = \omega_R$. We used a cut-off at $p_{\max} = 16\hbar k$. The remaining parameters are the same as in Fig. 3.8 and the simulation time is $t = 400\omega_R^{-1}$

observe that for $w = 10\omega_R$ (black curve) and $w = 6\omega_R$ (green, dark gray curve) $|X|$ and $\langle\hat{p}^2\rangle$ reach a constant value. The asymptotic values depend on $w$. The dynamical behavior of $|X|$ and $\langle\hat{p}^2\rangle$ changes significantly for the values $w = 3\omega_R$ (blue, gray curve)

and $w = 1\omega_R$ (violet, light gray curve). For $w = 3\omega_R$ we observe an oscillation of the order parameter as well as of the mean kinetic energy. These oscillations seem to have an almost well-defined frequency. In the case of $w = \omega_R$, instead, we observe oscillations that appear chaotic.

To analyze this dynamics we calculate the absolute value of the Laplace transform on the imaginary axis

$$F(\omega) \propto \left| \int_0^{t_{\text{end}}} dt e^{i\omega t} X(t) \right|, \tag{3.2.32}$$

where $t_{\text{end}}$ denotes the time over which we integrate the dynamics. For every value of $w$ we normalize $F(\omega)$ with its maximum value such that $F(\omega) \leq 1$ and $F(\omega) = 1$ at the maximum. The results are plotted in Fig. 3.10. For large enough values for $w$

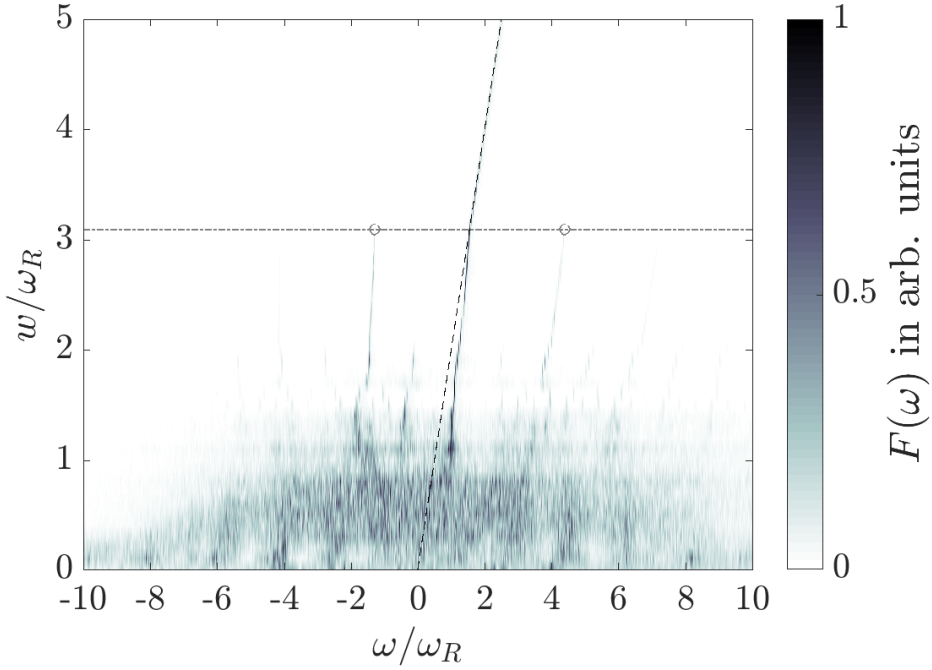


Figure 3.10: The function $F(\omega)$ as defined in Eq. (3.2.32). Here we used $t_{\text{end}} = 1200\omega_R^{-1}$, $\Lambda = 40\omega_R$, and $\Delta = \kappa/2$. The dashed black line corresponds to the frequency of the steady-state superradiance $\omega_0 = -w/2$ (see Eq. (3.2.25)). The dashed-dotted gray horizontal line corresponds to a stability line of the stationary state. The circles correspond to the imaginary part of $\gamma$ found by the stability analysis. For the simulations we used a cut-off at $p_{\max} = 16\hbar k$.

we observe a single peak of $F(\omega)$. This peak appears at the frequency $\omega_0 = -w/2$, corresponding to the case of steady-state superradiance. It is the frequency for that $d\langle\hat{p}^2\rangle/dt = 0$ in Eq. (3.2.31). If $w$ becomes smaller than $w \sim 3\omega_R$, we observe the appearance of sidebands in $F$. When $w$ is further decreased, more sidebands appear, until the spectrum becomes almost continuous. This is also reflected in the dynamics of $|X|$ where the oscillations become chaotic. The onset of the oscillation can also be understood by calculating the stability of the stationary state using the methods of the previous subsection 3.2.1 (Eq. (3.2.11)). The dashed-dotted gray horizontal line at $w_t \approx 3.1\omega_R$ corresponds to a transition where $\text{Re}(\gamma)$ changes its sign. This agrees with the threshold

for the oscillations. The value of $\gamma_L = \mathrm{Re}(\gamma)$ can be seen as a Lyapunov exponent that describes the transition from a steady-state superradiant to a chaotic phase. Moreover, we found two solutions $\gamma_\pm$ of the dispersion relation at $w = w_t = 3.1\omega_R$ that changed there sign. The corresponding imaginary parts of $\gamma_\pm$ are depicted by circles on the dashed-dotted line. They are compatible with the frequencies that occur at the threshold.

We want to study now the asymptotic state of the system. In Fig. 3.11 we plotted in subplot (a) the values of $|X|$ and in (b) the values of $\langle\hat{p}^2\rangle$ at $t = 400\omega_R^{-1}$. The dashed line corresponds to the coherent stationary state. For $w > 3.1\omega_R$ we see that numerical

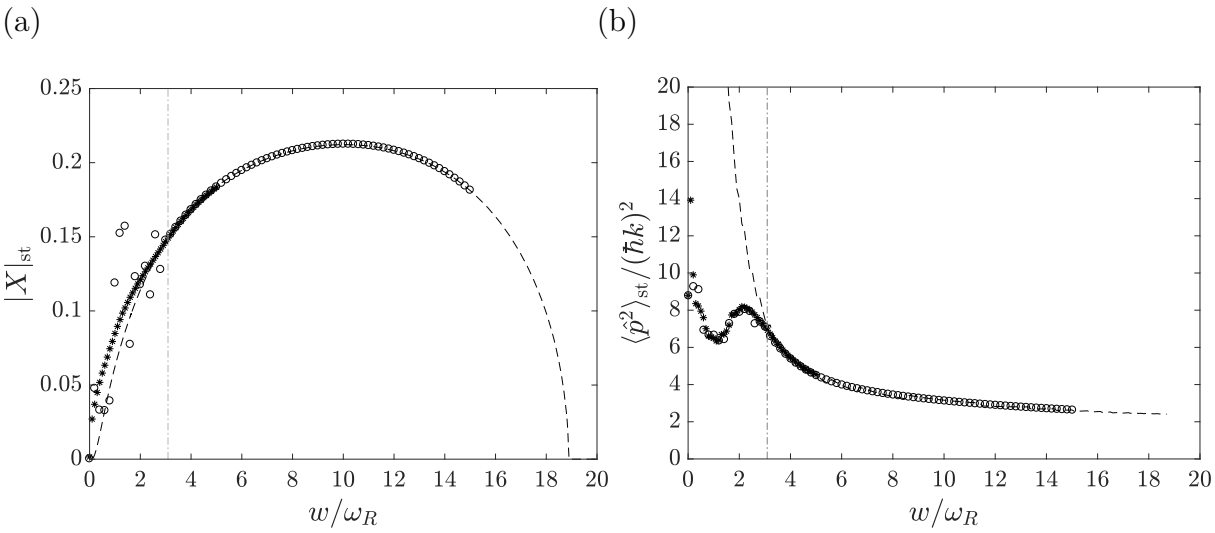


Figure 3.11: (a) The mean-field order parameter $|X(t)|$ at $t = 400\omega_R^{-1}$ (circles) and the average $|X|_{\mathrm{av}}$ using Eq. (3.2.30) for $t_{\mathrm{end}} = 1200\omega_R^{-1}$ (stars). (b) the second moment of momentum $\langle\hat{p}^2\rangle(t)$ at $t = 400\omega_R^{-1}$ (circles) and the average $\langle\hat{p}^2\rangle_{\mathrm{av}}$ calculated using Eq. (3.2.33) for $t_{\mathrm{end}} = 1200\omega_R^{-1}$ (stars). The dashed lines are the stationary values. The gray vertical lines at $w = w_t = 3.1\omega_R$ are the stability threshold for the stationary state. For all calculated values we used a cut-off at $p_{\max} = 16\hbar k$ and $\Delta = \kappa/2$.

and analytical results are in very good agreement. Below this threshold, the values of $|X|$ and $\langle\hat{p}^2\rangle$ oscillate. To provide some insight into the asymptotic dynamics of the system we calculate the time-averaged variables $|X|_{\mathrm{av}}$, defined in Eq. (3.2.30), and

$$\langle\hat{p}^2\rangle_{\mathrm{av}} = \frac{1}{t_{\mathrm{end}}}\int_0^{t_{\mathrm{end}}} dt\langle\hat{p}^2\rangle(t). \tag{3.2.33}$$

The corresponding results are shown in Fig. 3.11 for $t_{\mathrm{end}} = 1200\omega_R^{-1}$. For values $w > w_t = 3.1\omega_R$ we observe the final values of $|X(t)|$ and the averaged values $|X|_{\mathrm{av}}$ agree. Furthermore both are in agreement with the calculated stationary state. We may thus assume that the simulation time was long enough such that the time averaged variable in Eq. (3.2.30) and Eq. (3.2.33) coincide with the stationary values. For values $w < w_t$ we observe discrepancies between all three quantities. The oscillations in $X$ and $\langle\hat{p}^2\rangle$ lead to the deviations between the averaged values and the ones calculated at a fixed time. Moreover, we observe that even the time-averaged quantities differ from the calculated stationary values. The time-averaged value $|X|_{\mathrm{av}}$ is slightly larger than the stationary value while the time-averaged kinetic energy $\langle\hat{p}^2\rangle_{\mathrm{av}}$ is smaller than the corresponding

stationary value. With these results we conclude that chaotic light emission of the atomic ensemble is stable and can also be observed in the thermal regime.

The next subsection is dedicated to a discussion of the validity of the mean-field approach.

### 3.2.3 Correlations in steady-state superradiance

In the following we will derive a hierarchy of coupled master equation[5] for the $l$-particle density matrix with $l = 1, 2, ..., N$. From this we will show how one can derive a consistent mean-field theory that relies on discarding two- and higher-number particle correlations in determining the dynamics of steady-state superradiance.

#### Evolution of the $l$-particle density matrix

We start with the full dynamics of $N$ particles. Their Hilbert space is the tensor product $\mathcal{H}^{\otimes N}$ of the single-particle Hilbert space $\mathcal{H}$. We denote the $N$-particle density matrix by $\hat{\rho}_N$ and define the $l$-particle density matrix $\hat{\rho}_l$ by tracing out $N - l$ particles degrees of freedom, such that $\mathrm{Tr}_{N-l}(\hat{\rho}_N) = \hat{\rho}_l$. Using this definition we can now derive a dynamical equation for $\hat{\rho}_l$ that can be calculated by applying $\mathrm{Tr}_{N-l}$ on Eq. (3.1.3). The time evolution for $\hat{\rho}_l$ for $1 \leq l \leq N-1$ may then be written as

$$\frac{\partial \hat{\rho}_l}{\partial t} = \frac{1}{i\hbar}[\hat{H}_l, \hat{\rho}_l] + \mathcal{D}_l\hat{\rho}_l + \mathcal{L}_l[\hat{\rho}_{l+1}], \tag{3.2.34}$$

with

$$\hat{H}_l = \sum_{j=1}^{l} \frac{\hat{p}_j^2}{2m} - \frac{\hbar\Delta}{\kappa}\frac{\Lambda}{N}\hat{J}_l^\dagger \hat{J}_l, \tag{3.2.35}$$

$$\begin{aligned}\mathcal{D}_l\hat{\rho}_l = &-\frac{\Lambda}{2N}\left(\hat{J}_l^\dagger \hat{J}_l\hat{\rho}_l + \hat{\rho}_l\hat{J}_l^\dagger \hat{J}_l - 2\hat{J}_l\hat{\rho}_l\hat{J}_l^\dagger\right) \\ &- \sum_{j=1}^{l}\frac{w}{2}\left(\hat{\sigma}_j\hat{\sigma}_j^\dagger\hat{\rho}_l + \hat{\rho}_l\hat{\sigma}_j\hat{\sigma}_j^\dagger - 2\hat{\sigma}_j^\dagger\hat{\rho}_l\hat{\sigma}_j\right),\end{aligned} \tag{3.2.36}$$

and

$$\mathcal{L}_l[\hat{\rho}_{l+1}] = i\left(1 - \frac{l}{N}\right)\frac{\Lambda}{2}\alpha[\hat{J}_l, \hat{\mathcal{X}}_l^*[\hat{\rho}_{l+1}]] + \mathrm{H.c.}\,, \tag{3.2.37}$$

and where $\alpha = 2\Delta/\kappa - i$. Furthermore we assumed that the density matrix $\hat{\rho}_N$ does not change under particle permutation and introduced

$$\hat{\mathcal{X}}_l[\hat{\rho}_{l+1}] = \mathrm{Tr}^{(l+1)}\left(\hat{\sigma}_{l+1}\cos(k\hat{x}_{l+1})\hat{\rho}_{l+1}\right), \tag{3.2.38}$$

for $1 \leq l \leq N-1$ and

$$\hat{J}_l = \sum_{j=1}^{l}\hat{\sigma}_j\cos(k\hat{x}_j), \tag{3.2.39}$$

[5]This approach is similar to the BBGKY (Bogoliubov-Born-Green-Kirkwood-Yvon)-Hierarchy that has been applied to long-range interacting systems [23, 136].

for $1 \leq l \leq N$. Here $\mathrm{Tr}^{(k)}$ denotes the trace over the $k$th Hilbert space $\mathcal{H}$ in the tensor product. For a trace class operator $\hat{O}$ over the Hilbert space $\mathcal{H}^{\otimes m}$, $m > k$, with basis states $|i_1, p_1\rangle \otimes |i_2, p_2\rangle \otimes ... \otimes |i_m, p_m\rangle$, internal states $i_l \in \{g, e\}$, external states $p_l \in \mathbb{R}$, $l = 1, ..., m$, the partial trace $\mathrm{Tr}^{(k)}$ is defined as

$$\mathrm{Tr}^{(k)}(\hat{O}) = \int_{-\infty}^{\infty} dp_k \left[\langle e_k, p_k|\hat{O}|e_k, p_k\rangle + \langle g_k, p_k|\hat{O}|g_k, p_k\rangle\right].$$

The terms in Eqs. (3.2.35) and (3.2.36) describe the dynamics of the system inside the space of $l$ particles. The term in Eq. (3.2.37), instead, couples the $l$-particle density matrix and the $l + 1$-particle density matrix.

We will now use Eq. (3.2.34) to describe the coupled dynamics of the mean-field density matrix $\hat{\rho}_1$ to higher-number particle correlations and discuss when they can be discarded.

### Coupled dynamics of mean-field and two-particle correlations

To derive the mean-field master equation we use Eq. (3.2.34) for $l = 1$ and decompose the two-particle density matrix into a factorizable density matrix $\hat{\rho}_1 \otimes \hat{\rho}_1$ and two-particle correlations $\hat{g}_2$ such that [23]

$$\hat{\rho}_2 = \hat{\rho}_1 \otimes \hat{\rho}_1 + \hat{g}_2. \tag{3.2.40}$$

The equation of motion for the two-particle correlations $\hat{g}_2$ can be written

$$\frac{\partial \hat{g}_2}{\partial t} = \frac{\partial \hat{\rho}_2}{\partial t} - \frac{\partial \hat{\rho}_1}{\partial t} \otimes \hat{\rho}_1 - \hat{\rho}_1 \otimes \frac{\partial \hat{\rho}_1}{\partial t}. \tag{3.2.41}$$

Now explicitly using Eq. (3.2.34) for $l = 1$ and $l = 2$ and Eq. (3.2.40) we can derive[6]

$$\frac{\partial \hat{\rho}_1}{\partial t} = \mathcal{L}_{\mathrm{mf}}[\hat{\rho}_1]\hat{\rho}_1 + \mathcal{L}_1[\hat{g}_2], \tag{3.2.42}$$

$$\frac{\partial \hat{g}_2}{\partial t} = \hat{A}_1 + \hat{A}_2, \tag{3.2.43}$$

where we used the definitions

$$\begin{aligned}\hat{A}_1 =& \frac{1}{i\hbar}[\hat{H}_2, \hat{\rho}_2] - \frac{1}{i\hbar}[\hat{H}_1, \hat{\rho}_1] \otimes \hat{\rho}_1 - \frac{1}{i\hbar}\hat{\rho}_1 \otimes [\hat{H}_1, \hat{\rho}_1] \\ &+ D_2\hat{\rho}_2 - (D_1\hat{\rho}_1) \otimes \hat{\rho}_1 - \hat{\rho}_1 \otimes (D_1\hat{\rho}_1)\end{aligned} \tag{3.2.44}$$

and

$$\hat{A}_2 = \mathcal{L}_2[\hat{\rho}_3] - \mathcal{L}_1[\hat{\rho}_2] \otimes \hat{\rho}_1 - \hat{\rho}_1 \otimes \mathcal{L}_1[\hat{\rho}_2]. \tag{3.2.45}$$

The term $\mathcal{L}_{\mathrm{mf}}$ is the mean-field master equation

$$\mathcal{L}_{\mathrm{mf}}[\hat{\rho}_1]\hat{\rho}_1 = \frac{1}{i\hbar}[\hat{H}_{\mathrm{mf}}, \hat{\rho}_1] + \mathcal{L}_{\Lambda/N}[\hat{\sigma}\cos(k\hat{x})]\hat{\rho}_1 + \mathcal{L}_w[\hat{\sigma}^\dagger]\hat{\rho}_1, \tag{3.2.46}$$

with the mean-field Hamiltonian

$$\hat{H}_{\mathrm{mf}} = \frac{\hat{p}^2}{2m} - \frac{\hbar\Lambda}{N}\frac{\Delta}{\kappa}\hat{\sigma}^\dagger\hat{\sigma}\cos^2(k\hat{x}) - \frac{\hbar\Lambda}{2}\left(\alpha X(\hat{\rho}_1)^*\hat{\sigma} + \alpha^* X(\hat{\rho}_1)\hat{\sigma}^\dagger\right)\cos(k\hat{x}). \tag{3.2.47}$$

[6] This is similar to the Lenard-Balescu equation while the mean-field equation without the coupling to $\hat{g}_2$ can be seen as a Vlasov equation [23].

Here we defined

$$X(\hat{\rho}_1) = \mathrm{Tr}(\hat{\sigma}\cos(k\hat{x})\hat{\rho}_1). \tag{3.2.48}$$

We can simplify $\hat{A}_1$ in Eq. (3.2.44) to obtain the following form

$$\hat{A}_1 = \frac{1}{i\hbar}[\hat{H}_2, \hat{g}_2] + \mathcal{D}_2\hat{g}_2 + i\frac{\Lambda}{2N}\left(\alpha[\hat{J}_1, \hat{\rho}_1]\otimes\hat{\rho}_1\hat{J}_1^\dagger + \alpha\hat{\rho}_1\hat{J}_1^\dagger\otimes[\hat{J}_1,\hat{\rho}_1] - \mathrm{H.c.}\right). \tag{3.2.49}$$

For the calculation of $\hat{A}_2$ we need an expression for the three-particle density matrix and this will include three-particle correlations. We write

$$\hat{\rho}_3 = \hat{\rho}_1\otimes\hat{\rho}_1\otimes\hat{\rho}_1 + \sum_{i,j,k=1}^{3}|\epsilon_{ijk}|\hat{h}_{ij,k} + \hat{g}_3,$$

where $\hat{h}_{ij,k}$ describes two-particle correlations between $i$ and $j$ but no correlations between $i$ and $k$ and between $j$ and $k$ with $i,j,k\in\{1,2,3\}$. The three particle correlations are characterized by $\hat{g}_3$ and $\epsilon_{ijk}$ is the Levi-Cevita tensor. The final form of $\hat{A}_2$ reads

$$\begin{aligned}\hat{A}_2 =& -i\frac{\Lambda}{2N}[\alpha X_0^*\hat{J}_2 + \alpha^*\hat{J}_2^\dagger X_0, \hat{\rho}_1\otimes\hat{\rho}_1] + i\frac{(1-2/N)\Lambda}{2}[\alpha X_0^*\hat{J}_2 + \alpha^*\hat{J}_2^\dagger X_0, \hat{g}_2]\\ &+ i\frac{(1-2/N)\Lambda}{2}\left(\alpha\hat{\mathcal{X}}_1^*[\hat{g}_2]\otimes[\hat{J}_1,\hat{\rho}_1] + \alpha[\hat{J}_1,\hat{\rho}_1]\otimes\hat{\mathcal{X}}_1^*[\hat{g}_2] - \mathrm{H.c.}\right)\\ &- i\frac{\Lambda}{2N}\left(\alpha[\hat{J}_1,\hat{\mathcal{X}}_1^*[\hat{g}_2]]\otimes\hat{\rho}_1 + \alpha\hat{\rho}_1\otimes[\hat{J}_1,\hat{\mathcal{X}}_1^*[\hat{g}_2]] - \mathrm{H.c.}\right) + \mathcal{L}_2[\hat{g}_3].\end{aligned} \tag{3.2.50}$$

From Eq. (3.2.49) and (3.2.50) we see that when we assume that $\hat{g}_2 = 0$ and $\hat{g}_3 = 0$ at $t = 0$ then $\hat{g}_2$ will remain small on a timescale $T$ that is sufficiently small compared to $N\Lambda^{-1}$. Therefore on a timescale

$$T \ll N\Lambda^{-1} \tag{3.2.51}$$

we may assume that mean-field is valid and we can neglect the contribution of $\hat{g}_2$ to the mean-field master equation (3.2.46).

Section 3.3

# Synchronization-assisted cooling

In this section we discuss cooling effects in presence of steady-state superradiance using a semiclassical approach. In both subsections we show published and peer-reviewed articles and provide a contribution list of the authors.

## 3.3.1 Supercooling of Atoms in an Optical Resonator

Physical Review Letters **116**, 153002 (2016)

DOI: 10.1103/PhysRevLett.116.153002

Authors: Minghui Xu[1,2], Simon B. Jäger[3], S. Schütz[3], J. Cooper[1], Giovanna Morigi[3], and M. J. Holland[1,2]

[1] *JILA, National Institute of Standards and Technology and Department of Physics, University of Colorado, Boulder, Colorado 80309-0440, USA*
[2] *Center for Theory of Quantum Matter, University of Colorado, Boulder, Colorado 80309, USA*
[3] *Theoretische Physik, Universität des Saarlandes, D-66123 Saarbrücken, Germany*



**Author Contributions:**
The theoretical model was developed by M. Xu, S. Schütz, G. Morigi, and M. J. Holland. Numerical simulations were performed by M. Xu, S. Schütz, and S. B. Jäger. Analytical calculations were performed by M. Xu, S. B. Jäger, and J. Cooper. The results were checked and discussed by all authors. The article was mainly written by M. Xu and M. J. Holland.

**Abstract:**
We investigate laser cooling of an ensemble of atoms in an optical cavity. We demonstrate that when atomic dipoles are synchronized in the regime of steady-state superradiance, the motion of the atoms may be subject to a giant frictional force leading to potentially very low temperatures. The ultimate temperature limits are determined by a modified atomic linewidth, which can be orders of magnitude smaller than the cavity linewidth. The cooling rate is enhanced by the superradiant emission into the cavity mode allowing reasonable cooling rates even for dipolar transitions with ultranarrow linewidth.

PRL 116, 153002 (2016) PHYSICAL REVIEW LETTERS week ending 15 APRIL 2016

# Supercooling of Atoms in an Optical Resonator

Minghui Xu,[1,2] Simon B. Jäger,[3] S. Schütz,[3] J. Cooper,[1] Giovanna Morigi,[3] and M. J. Holland[1,2]
[1]JILA, National Institute of Standards and Technology and Department of Physics, University of Colorado, Boulder, Colorado 80309-0440, USA
[2]Center for Theory of Quantum Matter, University of Colorado, Boulder, Colorado 80309, USA
[3]Theoretische Physik, Universität des Saarlandes, D-66123 Saarbrücken, Germany
(Received 11 December 2015; published 15 April 2016)

We investigate laser cooling of an ensemble of atoms in an optical cavity. We demonstrate that when atomic dipoles are synchronized in the regime of steady-state superradiance, the motion of the atoms may be subject to a giant frictional force leading to potentially very low temperatures. The ultimate temperature limits are determined by a modified atomic linewidth, which can be orders of magnitude smaller than the cavity linewidth. The cooling rate is enhanced by the superradiant emission into the cavity mode allowing reasonable cooling rates even for dipolar transitions with ultranarrow linewidth.

DOI: 10.1103/PhysRevLett.116.153002

The discovery of laser cooling [1] has enabled new areas of quantum gas physics and quantum state engineering [2]. Laser cooling is an essential technology in many fields, including precision measurements, quantum optics, and quantum information processing [3–5]. Doppler laser cooling [6,7] relies on repeated cycles of electronic excitation by lasers followed by spontaneous relaxation, reaching temperature limits determined by the atomic linewidth. Only specific atomic species can be Doppler cooled because they should possess an internal level structure that allows for closed cycling transitions.

Cavity-assisted laser cooling [8,9] utilizes the decay of an optical resonator instead of atomic spontaneous emission for energy dissipation. It is based on the preferential coherent scattering of laser photons into an optical cavity [10,11]. Temperatures that can be achieved in this way are limited by the cavity linewidth. Since the particle properties enter only through the coherent scattering amplitude, cavity-assisted cooling promises to be applicable to any polarizable object [12–20], including molecules [17,18] and even mesoscopic systems such as nanoparticles [19,20].

The many-atom effects of cavity-assisted cooling were theoretically discussed by Ritsch and collaborators [21] and experimentally reported [22,23]. The cavity-mediated atom-atom coupling typically leads to a cooling rate that is faster for an atomic ensemble than for a single atom. Self-organization may occur and is observed as patterns in the atomic distribution that maximize the cooperative scattering. Recently, it has been shown that the long-range nature of the cavity-mediated interaction between atoms gives rise to interesting prethermalization behavior [24]. In spite of the intrinsic many-body nature, the underlying cooling mechanism shares much with the single-atom case, and indeed the final temperature observed in these systems is limited by the cavity linewidth.

In this Letter, we demonstrate that the mechanical action of the atom-cavity coupling takes on a dramatically new character for atoms in the regime of steady-state superradiance [25–30]. Specifically, the frictional force on a single atom is significantly enhanced, and the final temperature is much lower than the temperature that can be achieved in cavity-assisted cooling [10,11]. Furthermore, as the atom number increases, the cooling may become faster due to the increasing rate of superradiant collective emission. We show that ability to achieve much lower temperatures than for single-atom cavity-assisted cooling derives from the emergence of atom-atom dipole correlations in the many-body atomic ensemble.

Steady-state superradiant lasers were proposed in Ref. [25] as possible systems for generating milliHertz linewidth light, and demonstrated in a recent experiment using a two-photon Raman transition [27]. In steady-state superradiance, the cavity decay is much faster than all other processes and plays the role of a dissipative collective coupling for the atoms that leads to the synchronization of atomic dipoles [29,30]. The emergence of a macroscopic collective dipole induces an extremely narrow linewidth for the generated light [25,30]. The optimal parameters are in the weak-coupling regime of cavity QED [31], which is opposite to the strong-coupling situation usually considered in cavity-assisted cooling [8,9]. Superradiant lasers require weak-dipole atoms (e.g., using intercombination lines or other forbidden transitions) confined in a high-finesse optical cavity.

We consider an ensemble of $N$ pointlike two-level atoms with transition frequency $\omega_a$ and natural linewidth $\gamma$, interacting with a single-mode cavity with resonance frequency $\omega_c$ and linewidth $\kappa$, as shown in Fig. 1. The atoms are restricted to move freely along the direction of the cavity axis ($x$ axis) and are tightly confined in the other two directions. The atom-cavity coupling is given by $g\cos(kx)$, where $g$ is the vacuum Rabi frequency at the

 

PRL 116, 153002 (2016) PHYSICAL REVIEW LETTERS week ending 15 APRIL 2016

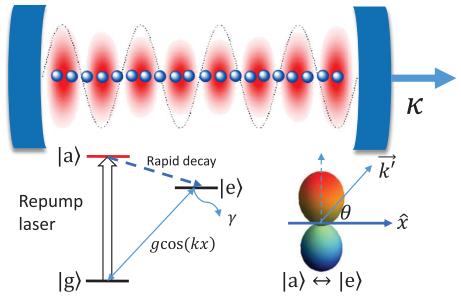


FIG. 1. Atoms with ultranarrow transition $|g\rangle \leftrightarrow |e\rangle$ are confined to the axis of a standing-wave mode of an optical cavity. Different implementations of pumping may be considered [25,27]. In the simplest scenario shown, a transition is driven from the ground state $|g\rangle$ to an auxiliary state $|a\rangle$ that rapidly decays to the excited state $|e\rangle$. In this way $|a\rangle$ can be adiabatically eliminated and a two-state pseudospin description in the $\{|g\rangle, |e\rangle\}$ subspace used, with repumping corresponding to an effective rate $w$ from $|g\rangle$ to $|e\rangle$. If the repumping laser is directed normal to the cavity axis, the absorption does not modify the momentum. Momentum recoil is induced by the on-axis component of the wave vector $\vec{k}'$ of the dipole radiation pattern for the $|a\rangle \leftrightarrow |e\rangle$ transition.

field maximum, and $\cos(kx)$ describes the one-dimensional cavity mode function [32]. The atoms are incoherently repumped at rate $w$, providing the photon source.

The Hamiltonian in the rotating frame of the atomic transition frequency is given by

$$\hat{H} = \hbar\Delta\hat{a}^\dagger\hat{a} + \sum_{j=1}^{N}\frac{\hat{p}_j^2}{2m} + \hbar\frac{g}{2}\sum_{j=1}^{N}(\hat{a}^\dagger\hat{\sigma}_j^- + \hat{\sigma}_j^+\hat{a})\cos(k\hat{x}_j), \tag{1}$$

where $\Delta = \omega_c - \omega_a$. We have introduced the bosonic annihilation and creation operators, $\hat{a}$ and $\hat{a}^\dagger$, for cavity photons. The $j$th atom is represented by Pauli pseudospin operators, $\hat{\sigma}_j^z$ and $\hat{\sigma}_j^- = (\hat{\sigma}_j^+)^\dagger$, and position and momentum $\hat{x}_j$ and $\hat{p}_j$, respectively.

In the presence of dissipation, the evolution of the system is described by the Born-Markov quantum master equation for the density matrix $\hat{\rho}$ for the cavity and atoms,

$$\frac{d}{dt}\hat{\rho} = \frac{1}{i\hbar}[\hat{H},\hat{\rho}] + \kappa\mathcal{L}[\hat{a}]\rho + w\sum_{j=1}^{N}\int_{-1}^{1}duN(u)\mathcal{L}[\hat{\sigma}_j^+ e^{iuk'\hat{x}_j}]\rho, \tag{2}$$

where $\mathcal{L}[\hat{\mathcal{O}}]\hat{\rho} = (2\hat{\mathcal{O}}\hat{\rho}\hat{\mathcal{O}}^\dagger - \hat{\mathcal{O}}^\dagger\hat{\mathcal{O}}\hat{\rho} - \hat{\rho}\hat{\mathcal{O}}^\dagger\hat{\mathcal{O}})/2$ is the Linbladian superoperator describing the incoherent processes. The term proportional to $\kappa$ describes the cavity decay. The repumping is the term proportional to $w$ and is modeled by spontaneous absorption with recoil [33]. The recoil is parametrized by the normalized emission pattern $N(u)$ and wave vector $k'$. We neglect free-space spontaneous emission, since the natural linewidth $\gamma$ is assumed to be extremely small for atoms with an ultraweak-dipole transition.

In the regime of interest, the cavity linewidth is much larger than other system frequencies, and the cavity field can be adiabatically eliminated, resulting in phase locking of the cavity field to the collective atomic dipole [26,29,30]. In order to correctly encapsulate the cavity cooling mechanism, the adiabatic elimination of the cavity field must be expanded beyond leading order. This includes retardation effects between the cavity field and atomic variables. As shown in the Supplemental Material [34], in the large $\kappa$ limit [35],

$$\hat{a}(t) \approx \frac{-i\frac{g}{2}\hat{J}^-}{\kappa/2 + i\Delta} + \frac{\frac{d}{dt}(i\frac{g}{2}\hat{J}^-)}{(\kappa/2 + i\Delta)^2} - \frac{2i\sqrt{\Gamma_C}}{g}\hat{\xi}(t) + \mathcal{O}[\kappa^{-3}], \tag{3}$$

where $\hat{J}^- = \sum_{j=1}^{N}\hat{\sigma}_j^-\cos(k\hat{x}_j)$ is the collective dipole operator, $\Gamma_C = g^2\kappa/4(\kappa^2/4 + \Delta^2)$ is the spontaneous emission rate through the cavity, and $\hat{\xi}(t)$ is the quantum noise originating from the vacuum field entering through the cavity output.

The dipole force on the $j$th atom is given by the gradient of the potential energy, which takes the form

$$F_j = \frac{d}{dt}\hat{p}_j = -\nabla_j\hat{H} = \frac{1}{2}\hbar kg\sin(k\hat{x}_j)(\hat{\sigma}_j^+\hat{a} + \hat{a}^\dagger\hat{\sigma}_j^-). \tag{4}$$

We maximize the single-atom dissipative force by working at the detuning $\Delta = \kappa/2$ [34], and in that case by substituting Eq. (3) into Eq. (4), we find

$$\begin{aligned}\frac{d}{dt}\hat{p}_j \approx & -\frac{1}{2}\hbar k\Gamma_C\sin(k\hat{x}_j)((1+i)\hat{\sigma}_j^+\hat{J}^- + (1-i)\hat{J}^+\hat{\sigma}_j^-) \\ & -\frac{1}{2}\eta\Gamma_C\sin(k\hat{x}_j)\sum_{l=1}^{N}(\hat{\sigma}_j^+\hat{\sigma}_l^- + \hat{\sigma}_l^+\hat{\sigma}_j^-)\frac{1}{2}[\sin(k\hat{x}_l), \hat{p}_l]_+ \\ & + \hat{\mathcal{N}}_j.\end{aligned} \tag{5}$$

Here the anticommutator is $[\hat{A},\hat{B}]_+ = \hat{A}\hat{B} + \hat{B}\hat{A}$. We have defined $\eta = 4\omega_r/\kappa$, which characterizes the likelihood that a photon emission into the cavity mode will be in the same direction as the motion, in terms of the recoil frequency $\omega_r = \hbar k^2/2m$. The three terms on the right-hand side of Eq. (5) can be interpreted as the conservative force, the friction, and the noise-induced momentum fluctuations, respectively.

For temperatures above the recoil temperature, the motion is well described by a semiclassical treatment. A systematic semiclassical approximation, to make the mapping $\langle\hat{x}_j\rangle \to x_j$ and $\langle\hat{p}_j\rangle \to p_j$, where $x_j$ and $p_j$ are classical variables, is based on the symmetric ordering of operator expectation values. In order to accurately incorporate the effects of quantum noise, we match the equations of motion for the second-order moments of momenta between the quantum and semiclassical theories so that

PRL 116, 153002 (2016) PHYSICAL REVIEW LETTERS week ending 15 APRIL 2016

we obtain the correct momentum diffusion [34]. This procedure yields Ito stochastic equations,

$$\frac{d}{dt}p_j \approx \hbar k\Gamma_C \sin(kx_j)(\mathrm{Im}[\langle\hat{\sigma}_j^+\hat{J}^-\rangle] - \mathrm{Re}[\langle\hat{\sigma}_j^+\hat{J}^-\rangle]) - \eta\Gamma_C \sin(kx_j)\sum_{l=1}^{N}\mathrm{Re}[\langle\hat{\sigma}_j^+\hat{\sigma}_l^-\rangle]\sin(kx_l)p_l + \xi_j^p, \tag{6}$$

where $\xi_j^p$ is the classical noise and $\langle\xi_j^p(t)\xi_l^p(t')\rangle = D^{jl}\delta(t-t')$ with diffusion matrix

$$D^{jl} = \hbar^2k^2\Gamma_C \sin(kx_j)\sin(kx_l)\mathrm{Re}[\langle\hat{\sigma}_l^+\hat{\sigma}_j^-\rangle] + \hbar^2k'^2w\bar{u^2}\langle\hat{\sigma}_j^-\hat{\sigma}_l^+\rangle\delta_{jl}, \tag{7}$$

involving the geometrical average $\bar{u^2} \equiv \int_{-1}^{1} u^2N(u)du$ and Kronecker delta $\delta_{jl}$. The momentum evolution is paired with the usual equation for $x_j$,

$$\frac{d}{dt}x_j = \frac{p_j}{m}. \tag{8}$$

We first consider the case in which the effect of recoil associated with the repumping is neglected; i.e., we set $k' = 0$. This determines the ultimate temperature limit imposed by the vacuum noise due to the cavity output. For the one-atom case, we can then find the friction ($\alpha$) and diffusion ($D$) coefficient from Eq. (6) and Eq. (7). The steady-state temperature $T$ for the single atom (labeled by 1) is

$$k_BT = \frac{\langle p_1^2\rangle}{m} = \frac{D}{2m\alpha} = \frac{\hbar\kappa}{4}, \tag{9}$$

since

$$D = \hbar^2k^2\Gamma_C\sin^2(kx_1)\langle\hat{\sigma}_1^+\hat{\sigma}_1^-\rangle, \quad \alpha = \eta\Gamma_C\sin^2(kx_1)\langle\hat{\sigma}_1^+\hat{\sigma}_1^-\rangle. \tag{10}$$

Note that this is precisely the same temperature limit previously found in the cavity-assisted cooling case where the system is operating in the strong coupling cavity-QED region. Here the rate of the decay into the cavity mode is proportional to $\Gamma_C\langle\hat{\sigma}_1^+\hat{\sigma}_1^-\rangle$, which is applicable to the weak coupling regime of cavity QED [31]. In Fig. 2(a), we show a numerical simulation of the cooling trajectory of a single atom as a function of time. As expected, the final temperature $k_BT$ asymptotes to $\hbar\kappa/4$ and the cooling rate is well approximated by $R_S = \eta\Gamma_C\langle\hat{\sigma}_1^+\hat{\sigma}_1^-\rangle$.

The cooling in the many-atom case exhibits a distinctly different character. A feature of this model is the pseudospin-to-motion coupling of the atoms. In order to close the evolution equations of the atomic motion as described by Eq. (6) and Eq. (8), it is necessary to solve the pseudospin dynamics. For this purpose, we derive in the Supplemental Material [34] the quantum master equation for the pseudospins,

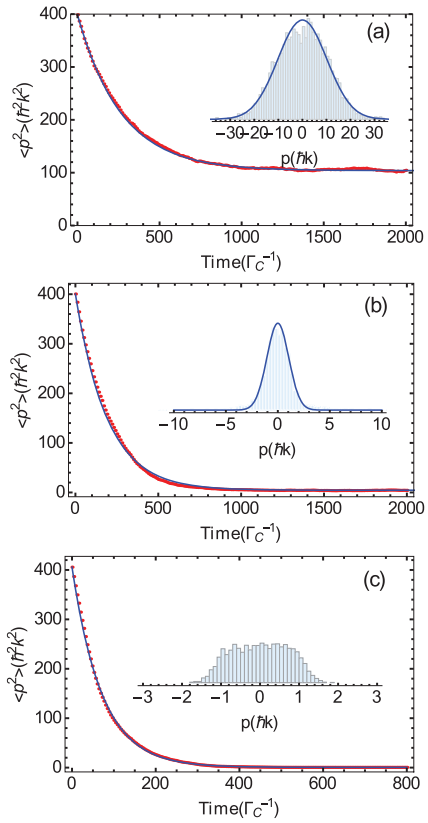


FIG. 2. Time evolution of the average momentum square (red dots) evaluated from 4000 trajectories simulated by integrating Eqs. (6) and (8) for 1 (a), 20 (b), and 60 atoms (c). The blue solid line is a fit to an exponential decay. The parameters are $\Delta = \kappa/2 = 100$, $\Gamma_C = 0.1$, and $\omega_r = 0.25$. The repumping rates are chosen such that the average atomic population inversion in all cases is the same [$w = 0.15$ (a), 0.28 (b), 1.3 (c)]. Insets show the momentum statistics. The blue solid line is a fit to a Gaussian distribution.

$$\frac{d}{dt}\hat{\rho} = \frac{1}{i\hbar}[\hat{H}_{\mathrm{eff}},\hat{\rho}] + \Gamma_C\mathcal{L}[\hat{J}^-]\hat{\rho} + w\sum_{j=1}^{N}\int_{-1}^{1}duN(u)\mathcal{L}[\hat{\sigma}_j^+e^{iuk'\hat{x}_j}]\rho, \tag{11}$$

where the effective Hamiltonian $\hat{H}_{\mathrm{eff}} = -\hbar\Gamma_C\hat{J}^+\hat{J}^-/2$ describes the coherent coupling between atoms, and the collective decay [term proportional to $\Gamma_C$ in Eq. (11)] leads to dissipative coupling. It is the dissipative coupling that gives rise to dipole synchronization and steady-state superradiance [25–30]. The full pseudospin Hilbert space dimension scales exponentially with the atom number. To solve Eq. (11), we employ a cumulant approximation that is applicable to many atoms [26,29,30]. All nonzero observables are expanded in terms of $\langle\hat{\sigma}_j^+\hat{\sigma}_j^-\rangle$ and $\langle\hat{\sigma}_j^+\hat{\sigma}_l^-\rangle$ ($j \neq l$), describing the population inversion and spin-spin

PRL 116, 153002 (2016) PHYSICAL REVIEW LETTERS week ending 15 APRIL 2016

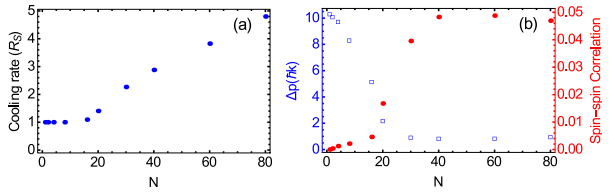


FIG. 3. (a) Cooling rate (in units of the single atom cooling rate $R_S$) as a function of atom number. (b) Final momentum width ($\Delta p = \sqrt{\langle p^2 \rangle}$, blue squares) and spin-spin correlation (red dots) as a function of atom number. The parameters are the same as those in Fig. 2.

correlations, respectively. Their equations of motion are derived in the Supplemental Material [34].

Simulations of the cooling dynamics for many atoms are shown in Figs. 2(b) and 2(c). Remarkably, we find the collective atomic effects lead to a more rapid cooling rate, and, simultaneously, to a lower final temperature. Figure 3 shows the cooling rate (a) and the final momentum width (b) as a function of the atom number. We note that the cooling rate exhibits two kinds of behavior, hinting towards the existence of an $N$-dependent threshold; see Fig. 3(a). For $N \lesssim 20$, the cooling rate is independent of $N$, while for $N \gtrsim 20$, it increases monotonically. Correspondingly, in this regime, the momentum width reaches a minimum independent of $N$; see Fig. 3(b). When the final temperature gets closer to the recoil temperature, the momentum distribution is no longer Gaussian, rendering the notion of temperature invalid. The semiclassical treatment predicts a uniform distribution in the momentum interval $[-\hbar k, \hbar k]$ corresponding to the recoil limit, as shown in the inset of Fig. 2(c). We note that sub-Doppler temperatures for a similar setup have been reported in Refs. [36–38], where spontaneous decay was assumed to be the fastest incoherent process. Differing from that regime, the recoil limit is here reached thanks to the small spontaneous decay rate. When the temperature approaches the recoil temperature, however, the validity of the semiclassical treatment of atomic motion is questionable and a full quantum model is necessary in order to determine the asymptotic energy. These results demonstrate that not only is the cooling more efficient due to the rapid rate of superradiant light emission, but also the final temperature is determined by the relaxation rate $\Gamma_C$ of the atomic dipole, and not by the cavity linewidth.

The principal new feature is that spin-spin correlations between atoms develop due to the cavity-mediated coupling. In order to measure the extent of this effect, we introduce $\langle \hat{\sigma}^+ \hat{\sigma}^- \rangle_E$ defined as averaged spin-spin correlations,

$$\langle \hat{\sigma}^+ \hat{\sigma}^- \rangle_E = \left( \langle \hat{J}^+ \hat{J}^- \rangle - \sum_{j=1}^{N} \langle \hat{\sigma}_j^+ \hat{\sigma}_j^- \rangle \cos^2(k x_j) \right) / [N(N-1)]. \tag{12}$$

Figure 3(b) shows $\langle \hat{\sigma}^+ \hat{\sigma}^- \rangle_E$ as a function of the atom number. The equilibrium temperature decreases as the collective spin-spin correlation emerges. This is reminiscent of the linewidth of the superradiant laser, where the synchronization of spins leads to a significant reduction of the linewidth to the order of $\Gamma_C$ [25,30]. The establishment of spin-spin correlations is a competition between dephasing due to both cavity output noise and repumping, and the dissipative coupling between atoms which tends to synchronize the dipoles [30]. Since the coupling strength scales with $N$, a sufficient atom number is required to establish strong spin-spin correlations [30].

Further characterizing the ultimate temperature limits, Fig. 4(a) shows the final momentum width as a function of $\Gamma_C$. We see that as $\Gamma_C$ is decreased, the final temperature reduces in proportion to $\Gamma_C$ until it hits the recoil limit. This effect is consistent with a significantly increased friction coefficient providing a reduction of the order of the final temperature from the one to many atom case from $\kappa$ to $\Gamma_C$.

So far our discussion has neglected the recoil associated with repumping. We have done that because its effect on the final temperature will depend crucially on specifics of its implementation, including factors such as the polarizations and directions of repump lasers, the atomic system, and the transitions used. However, in the specific repumping model shown in Fig. 1, the magnitude of $k'$ controls the recoil effect of the repumping on the momentum diffusion. Figure 4(b) shows the final momentum width as a function of repumping for $k' = 0$ and $k' = k$. Again, in the region of small and large repumping, where spin-spin correlations are very small, the final temperature is high. When the recoil due to repumping is included, the final temperature becomes higher and is eventually determined by $w\bar{u^2}$. However, for weak repumping, with $w$ not significantly larger then $\Gamma_C$ it is still possible to achieve temperatures not much higher than that predicted when pump recoil was neglected. This is especially promising for the implementation of supercooling in realistic experimental systems. Note that $k = k'$ is more or less a worst case scenario, since by using a dipole allowed transition for the relaxation from the auxiliary state to the excited state, one could, in

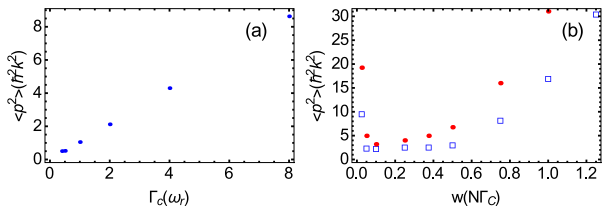


FIG. 4. (a) Final momentum width as a function of $\Gamma_C$ for 40 atoms. The parameters are $\Delta = \kappa/2 = 200$, $w = N\Gamma_C/4$, and $\omega_r = 0.25$. (b) Final momentum width as a function of repumping strength for 40 atoms without ($k' = 0$, blue squares) and with recoil associated with repumping ($k' = k$, red dots). The parameters are $\Delta = \kappa/2 = 200$, $\Gamma_C = 0.5$, and $\omega_r = 0.25$.

principle, use a much reduced frequency with correspondingly small recoil.

In conclusion, we have proposed supercooling of the atomic motion along the axis of an optical cavity. The superradiant emission was observed to lead to an enhanced cooling rate and extremely low final temperature. The ultimate temperatures were constrained by the relaxation of the atomic dipole, and may be orders of magnitude lower than for single atom cooling where temperatures are limited by the cavity linewidth. From a broader viewpoint, we have demonstrated an example of many-body laser cooling in which all motional degrees of freedom of a collective system are simultaneously cooled, and in which macroscopic spin-spin correlations are essential and must develop for the cooling mechanism to work.

We acknowledge helpful discussions with A. M. Rey, J. Ye, and J. K. Thompson. This work has been supported by the DARPA QuASAR program, the NSF (Grants No. AMO-1404263, No. PFC-1125844, and No. QIS-1521080), NIST, the German Research Foundation (DACH project "Quantum crystals of matter and light"), and the German Ministry of Education and Research BMBF (Q.Com).

[1] C. E. Wieman, D. E. Pritchard, and D. J. Wineland, Rev. Mod. Phys. **71**, S253 (1999).
[2] I. Bloch, J. Dalibard, and W. Zwerger, Rev. Mod. Phys. **80**, 885 (2008).
[3] A. D. Ludlow, M. M. Boyd, J. Ye, E. Peik, and P. O. Schmidt, Rev. Mod. Phys. **87**, 637 (2015).
[4] I. A. Walmsley, Science **348**, 525 (2015).
[5] D. J. Wineland, Rev. Mod. Phys. **85**, 1103 (2013).
[6] T. W. Hänsch and A. L. Schawlow, Opt. Commun. **13**, 68 (1975).
[7] D. J. Wineland and W. M. Itano, Phys. Rev. A **20**, 1521 (1979).
[8] P. Domokos and H. Ritsch, J. Opt. Soc. Am. B **20**, 1098 (2003).
[9] H. Ritsch, P. Domokos, F. Brennecke, and T. Esslinger, Rev. Mod. Phys. **85**, 553 (2013).
[10] P. Horak, G. Hechenblaikner, K. M. Gheri, H. Stecher, and H. Ritsch, Phys. Rev. Lett. **79**, 4974 (1997).
[11] V. Vuletić and S. Chu, Phys. Rev. Lett. **84**, 3787 (2000).
[12] J. McKeever, J. R. Buck, A. D. Boozer, A. Kuzmich, H.-C. Nägerl, D. M. Stamper-Kurn, and H. J. Kimble, Phys. Rev. Lett. **90**, 133602 (2003).
[13] P. Maunz, T. Puppe, I. Schuster, N. Syassen, P. W. H. Pinkse, and G. Rempe, Nature (London) **428**, 50 (2004).
[14] D. R. Leibrandt, J. Labaziewicz, V. Vuletić, and I. L. Chuang, Phys. Rev. Lett. **103**, 103001 (2009).
[15] M. H. Schleier-Smith, I. D. Leroux, H. Zhang, M. A. Van Camp, and V. Vuletić, Phys. Rev. Lett. **107**, 143005 (2011).
[16] M. Wolke, J. Klinner, H. Kessler, and A. Hemmerich, Science **337**, 75 (2012).
[17] G. Morigi, P. W. H. Pinkse, M. Kowalewski, and R. deVivie-Riedle, Phys. Rev. Lett. **99**, 073001 (2007).
[18] B. L. Lev, A. Vukics, E. R. Hudson, B. C. Sawyer, P. Domokos, H. Ritsch, and J. Ye, Phys. Rev. A **77**, 023402 (2008).
[19] N. Kiesel, F. Blaser, U. Delic, D. Grass, R. Kaltenbaek, and M. Aspelmeyer, Proc. Natl. Acad. Sci. U.S.A. **110**, 14180 (2013).
[20] J. Millen, P. Z. G. Fonseca, T. Mavrogordatos, T. S. Monteiro, and P. F. Barker, Phys. Rev. Lett. **114**, 123602 (2015).
[21] P. Domokos and H. Ritsch, Phys. Rev. Lett. **89**, 253003 (2002).
[22] H. W. Chan, A. T. Black, and V. Vuletić, Phys. Rev. Lett. **90**, 063003 (2003).
[23] K. J. Arnold, M. P. Baden, and M. D. Barrett, Phys. Rev. Lett. **109**, 153002 (2012).
[24] S. Schütz and G. Morigi, Phys. Rev. Lett. **113**, 203002 (2014).
[25] D. Meiser, J. Ye, D. R. Carlson, and M. J. Holland, Phys. Rev. Lett. **102**, 163601 (2009).
[26] D. Meiser and M. J. Holland, Phys. Rev. A **81**, 033847 (2010); **81**, 063827 (2010).
[27] J. G. Bohnet, Z. Chen, J. M. Weiner, D. Meiser, M. J. Holland, and J. K. Thompson, Nature (London) **484**, 78 (2012).
[28] J. G. Bohnet, Z. Chen, J. M. Weiner, K. C. Cox, and J. K. Thompson, Phys. Rev. Lett. **109**, 253602 (2012).
[29] Minghui Xu, D. A. Tieri, E. C. Fine, J. K. Thompson, and M. J. Holland, Phys. Rev. Lett. **113**, 154101 (2014).
[30] Minghui Xu and M. J. Holland, Phys. Rev. Lett. **114**, 103601 (2015).
[31] P. Meystre and M. Sargent III, *Elements of Quantum Optics* (Springer, New York, 1998).
[32] The finite spatial mode of the cavity causes a spread in $g$. This leads to a reduced effective atom number, which has no significant impact on the cooling mechanisms discussed in this Letter.
[33] H. Haken, *Laser Theory* (Springer, Berlin, 1984).
[34] See Supplemental Material at http://link.aps.org/supplemental/10.1103/PhysRevLett.116.153002, which includes Refs. [26,29], for the derivation of the equations for the adiabatic elimination of the cavity mode, for the external motion of atoms, and for the internal dynamics of atoms.
[35] This requires $\kappa \gg \sqrt{N\bar{n}}g, w$, and $k\sqrt{\langle p^2 \rangle}/m$, where $\bar{n}$ is the mean photon number in the cavity.
[36] T. Salzburger and H. Ritsch, Phys. Rev. Lett. **93**, 063002 (2004).
[37] T. Salzburger, P. Domokos, and H. Ritsch, Phys. Rev. A **72**, 033805 (2005).
[38] T. Salzburger and H. Ritsch, Phys. Rev. A **74**, 033806 (2006).

# Supplemental Material for Supercooling of Atoms in an Optical Resonator

## I. ADIABATIC ELIMINATION OF THE CAVITY MODE

The regime of steady-state superradiance is defined by a timescale separation between the single cavity mode and the atomic degrees of freedom. The typical relaxation time of the cavity mode is of the order of $T_C \sim |\kappa + i\Delta|^{-1}$, while the one of the atoms is given by $T_A \sim \left(\max\left\{\sqrt{N\bar{n}}g, w, k\sqrt{\langle p^2\rangle}/m\right\}\right)^{-1}$, where $\bar{n}$ is the mean photon number in the cavity. In order to eliminate the cavity field quasiadiabatically we need the relaxation time of the cavity to be much shorter than the timescale on which the atoms are evolving, namely $T_A \gg T_C$. To this end, we start with the quantum Langevin equation for the cavity field according to the quantum master equation [Eq. (2) in the paper],

$$\frac{d}{dt}\hat{a} = -\frac{\kappa}{2}\hat{a} - i\Delta\hat{a} - i\frac{g}{2}\hat{J}^- + \sqrt{\kappa}\hat{\xi}(t)\,, \tag{S1}$$

where $\hat{\xi}(t)$ is the quantum white noise and $\langle\hat{\xi}(t)\hat{\xi}^\dagger(t')\rangle = \delta(t-t')$. The formal solution to Eq. (S1) is

$$\hat{a}(t) = e^{-(\kappa/2+i\Delta)\Delta t}\hat{a}(t_0) - i\frac{g}{2}\int_0^{\Delta t} ds e^{-(\kappa/2+i\Delta)s}\hat{J}^-(t-s) + \hat{\mathcal{F}}(t)\,, \tag{S2}$$

where $\hat{\mathcal{F}}(t) = \sqrt{\kappa}\int_0^{\Delta t} ds e^{-(\kappa/2+i\Delta)s}\hat{\xi}(t-s)$ is the noise term and $\Delta t = t - t_0$. Under the approximation of coarse graining ($T_A \gg \Delta t \gg T_C$), the first term on the right-hand side (RHS) of Eq. (S2) vanishes, and it can be shown that

$$\langle\hat{\mathcal{F}}(t)\hat{\mathcal{F}}^\dagger(t')\rangle \approx e^{-\kappa|t'-t|/2 - i\Delta(t-t')} \approx \frac{\kappa}{\kappa^2/4+\Delta^2}\delta(t-t')\,. \tag{S3}$$

It would be convenient to choose $\hat{\mathcal{F}}(t) = -i\frac{\sqrt{\Gamma_C}}{g/2}\hat{\xi}(t)$, with

$$\Gamma_C = \frac{g^2\kappa/4}{\kappa^2/4+\Delta^2}. \tag{S4}$$

Furthermore, the integral in Eq. (S2) can be expanded in powers of $1/(\kappa/2+i\Delta)$. As a result we obtain

$$\hat{a}(t) \approx \frac{-i\frac{g}{2}\hat{J}^-}{\kappa/2+i\Delta} - \frac{\frac{d}{dt}(-i\frac{g}{2}\hat{J}^-)}{(\kappa/2+i\Delta)^2} + \hat{\mathcal{F}}(t) + O[(\kappa/2+i\Delta)^{-3}]\,. \tag{S5}$$

As can be seen from Eq. (S5), the retardation effects between the cavity field and atomic variables are included.

## II. EXTERNAL MOTION OF ATOMS

In this section we derive the force for the external degrees of freedom, including friction and noise. We will end up with a classical description of the particles' external degrees of freedom and derive a Langevin equation for the momenta of the particles.

The force on the $j$-th atom $\hat{F}_j$ is given by

$$\hat{F}_j = \frac{d}{dt}\hat{p}_j = \hbar k\sin(k\hat{x}_j)\frac{g}{2}(\hat{\sigma}_j^+\hat{a} + \hat{a}^\dagger\hat{\sigma}_j^-) + \hat{\mathcal{N}}_j^{\text{pump}}\,, \tag{S6}$$

where $\hat{\mathcal{N}}_j^{\text{pump}}$ represents the random force due to recoil of the incoherent pumping process.
Substituting Eq. (S5) into the above equation , we have

$$\begin{aligned}\frac{d}{dt}\hat{p}_j \approx{}& \hbar k\sin(k\hat{x}_j)\frac{\Gamma_C}{2}\left(-i\hat{\sigma}_j^+\hat{J}^- + i\hat{J}^+\hat{\sigma}_j^-\right) - \hbar k\sin(k\hat{x}_j)\frac{\Gamma_\Delta}{2}\sum_{l=1}^{N}\cos(kx_l)\left(\hat{\sigma}_j^+\hat{\sigma}_l^- + \hat{\sigma}_l^+\hat{\sigma}_j^- - \beta_1\hat{\sigma}_j^+\frac{d}{dt}\hat{\sigma}_l^- - \beta_1^*\frac{d}{dt}\hat{\sigma}_l^+\hat{\sigma}_j^-\right)\\ &- \sin(k\hat{x}_j)\frac{\Gamma_C}{2}\sum_{l=1}^{N}\frac{\eta}{2}\left[\sin(k\hat{x}_l),\hat{p}_l\right]_+\left(\hat{\sigma}_j^+\hat{\sigma}_l^- + \hat{\sigma}_l^+\hat{\sigma}_j^- + \beta_2\hat{\sigma}_j^+\hat{\sigma}_l^- + \beta_2^*\hat{\sigma}_l^+\hat{\sigma}_j^-\right) + \hat{\mathcal{N}}_j\,,\end{aligned} \tag{S7}$$

where $\left[\hat{A},\hat{B}\right]_+ = \hat{A}\hat{B}+\hat{B}\hat{A}$ is the anticommutator and the coefficients are

$$\Gamma_\Delta = \frac{g^2\Delta/2}{\kappa^2/4+\Delta^2}, \quad \beta_1 = \frac{\kappa}{\kappa^2/4+\Delta^2} + i\frac{\kappa^2/4-\Delta^2}{\Delta(\kappa^2/4+\Delta^2)}, \quad \beta_2 = i\frac{\kappa^2/4-\Delta^2}{\kappa\Delta}, \quad \eta = \frac{4\omega_r\Delta}{\kappa^2/4+\Delta^2}\,. \tag{S8}$$

Here $\hat{\mathcal{N}}_j = \hat{\mathcal{N}}_j^{\rm cav} + \hat{\mathcal{N}}_j^{\rm pump}$ is the sum of the noise processes originating from the cavity output $\hat{\mathcal{N}}_j^{\rm cav}$ and repumping $\hat{\mathcal{N}}_j^{\rm pump}$. In the first line of equation (S7) we neglect $\beta_1$ because in the steady state superradiance regime it holds that $|\beta_1|\langle\hat{\sigma}_j^+\frac{d}{dt}\hat{\sigma}_l^-\rangle \sim \frac{w}{\kappa}\langle\hat{\sigma}_j^+\hat{\sigma}_l^-\rangle \ll \langle\hat{\sigma}_j^+\hat{\sigma}_l^-\rangle$. This has also been checked numerically. Therefore we get

$$\frac{d}{dt}\hat{p}_j = \frac{d}{dt}\hat{p}_j^0 + \hat{\mathcal{N}}_j\,, \tag{S9}$$

where we define the force without noise as

$$\begin{aligned}\frac{d}{dt}\hat{p}_j^0 \approx{}& \hbar k\sin(k\hat{x}_j)\frac{\Gamma_C}{2}\left(-i\hat{\sigma}_j^+\hat{J}^- + i\hat{J}^+\hat{\sigma}_j^-\right) - \hbar k\sin(k\hat{x}_j)\frac{\Gamma_\Delta}{2}\sum_{l=1}^{N}\cos(kx_l)\left(\hat{\sigma}_j^+\hat{\sigma}_l^- + \hat{\sigma}_l^+\hat{\sigma}_j^-\right)\\ &- \sin(k\hat{x}_j)\frac{\Gamma_C}{2}\sum_{l=1}^{N}\frac{\eta}{2}\left[\sin(k\hat{x}_l),\hat{p}_l\right]_+\left(\hat{\sigma}_j^+\hat{\sigma}_l^- + \hat{\sigma}_l^+\hat{\sigma}_j^- + \beta_2\hat{\sigma}_j^+\hat{\sigma}_l^- + \beta_2^*\hat{\sigma}_l^+\hat{\sigma}_j^-\right).\end{aligned} \tag{S10}$$

We work at the detuning $\Delta = \kappa/2$ so that $\eta$ is maximized and $\beta_2$ vanishes. As a result we obtain

$$\frac{d}{dt}\hat{p}_j^0 \approx \hbar k\sin(k\hat{x}_j)\frac{\Gamma_C}{2}\left(-i\hat{\sigma}_j^+\hat{J}^- + i\hat{J}^+\hat{\sigma}_j^- - \hat{\sigma}_j^+\hat{J}^- - \hat{J}^+\hat{\sigma}_j^-\right) - \sin(k\hat{x}_j)\frac{\Gamma_C}{2}\sum_{l=1}^{N}\frac{\eta}{2}\left[\sin(k\hat{x}_l),\hat{p}_l\right]_+\left(\hat{\sigma}_j^+\hat{\sigma}_l^- + \hat{\sigma}_l^+\hat{\sigma}_j^-\right). \tag{S11}$$

The first term on the RHS of Eq. (S11) represents forces originating from the adiabatic component of the cavity field, while the second term represents the frictional force arising from retardation effects. The noise term $\hat{\mathcal{N}}_j$ in equation (S9) gives rise to momentum diffusion due to quantum noises associated with incoherent processes. So we derive the equations of motion for the second moments of momenta,

$$\frac{d}{dt}\left\langle\hat{p}_j\hat{p}_l\right\rangle = \left\langle\hat{p}_j^0\frac{d\hat{p}_l^0}{dt}\right\rangle + \left\langle\frac{d\hat{p}_j^0}{dt}\hat{p}_l^0\right\rangle + \Gamma_C\hbar^2k^2\langle\sin(k\hat{x}_j)\sin(k\hat{x}_l)\hat{\sigma}_j^+\hat{\sigma}_l^-\rangle + w\delta_{jl}\hbar^2k'^2\overline{u^2}\langle\hat{\sigma}_j^-\hat{\sigma}_l^+\rangle\,, \tag{S12}$$

where $\delta_{jl}$ is the Kronecker delta, and $\overline{u^2}$ is the second moment of the dipole radiation pattern, *i.e.*,

$$\overline{u^2} = \int_{-1}^{1} du N(u)u^2 = \frac{2}{5}\,, \tag{S13}$$

where we have taken the dipole pattern $N(u) = \frac{3}{2}|u|\sqrt{1-u^2}$.

We treat the external atomic motion classically under the assumption that the momentum width of the particles $\sqrt{\langle p^2\rangle}$ is larger than the single photon recoil $\hbar k$. So we make the mapping $\langle\hat{p}_j\rangle \to p_j$ and $\langle\hat{x}_j\rangle \to x_j$. As a result this leads to

$$\frac{d}{dt}p_j = \frac{d}{dt}p_j^0 + \xi_j^p\,, \tag{S14}$$

with

$$\frac{d}{dt}p_j^0 = \hbar k\sin(kx_j)\Gamma_C\left(\mathrm{Im}[\langle\hat{\sigma}_j^+\hat{J}^-\rangle] - \mathrm{Re}[\langle\hat{\sigma}_j^+\hat{J}^-\rangle]\right) - \sin(kx_j)\Gamma_C\sum_{l=1}^{N}\eta\mathrm{Re}[\langle\hat{\sigma}_j^+\hat{\sigma}_l^-\rangle]\sin(kx_l)p_l\,, \tag{S15}$$

where $\xi_j^p$ is the classical noise acting on the momentum of $j$-th atom and $\langle\xi_j^p(t)\xi_l^p(t')\rangle = D^{jl}\delta(t-t')$. The diffusion matrix $D^{jl}$ can be computed by making quantum-classical correspondence for the second moments. According to Eq. (S14),

$$\frac{d}{dt}\langle p_jp_l\rangle = \left\langle p_j^0\frac{dp_l^0}{dt}\right\rangle + \left\langle\frac{dp_j^0}{dt}p_l^0\right\rangle + D^{jl}\,. \tag{S16}$$

We use symmetric ordering of quantum operators for the quantum-classical correspondence, *i.e.*, $\frac{1}{2}\left\langle\left[\hat{p}_j,\frac{d\hat{p}_l}{dt}\right]_+\right\rangle \to \left\langle p_j\frac{dp_l}{dt}\right\rangle$. Matching Eq. (S12) and Eq. (S16), we get

$$D^{jl} = \Gamma_C\hbar^2k^2\sin(kx_j)\sin(kx_l)\mathrm{Re}[\langle\hat{\sigma}_l^+\hat{\sigma}_j^-\rangle] + w\delta_{jl}\hbar^2k'^2\overline{u^2}\langle\hat{\sigma}_j^-\hat{\sigma}_l^+\rangle\,. \tag{S17}$$

Therefore, we could simulate the external motion of atoms with Eq. (S14) and the equation of motion for $x_j$

$$\frac{d}{dt}x_j = \frac{p_j}{m}\,. \tag{S18}$$

The classical noises $\xi_j^p$ with diffusion matrix $D^{jl}$ make sure that we have the right second order moments for momenta.

### III. INTERNAL DYNAMICS OF ATOMS

For the complete simulation of the atomic variables we also need to derive an equation for the internal degrees of freedom. In this section we will derive the equations of motions for the spins in which we drop third-order cumulants. For the internal dynamics of atoms in a superradiant laser, it is sufficient to keep the first order term in Eq. (S5),

$$\hat{a}(t) \approx -i\frac{\Gamma_C}{g}\hat{J}^- - \frac{\Gamma_\Delta}{g}\hat{J}^- + \hat{\mathcal{F}}(t)\,. \tag{S19}$$

Here, retardation effects are not included because they give rise to corrections that are of higher order and their contribution is negligible. This was also checked numerically. The adiabatic elimination of the cavity field leads to an effective quantum master equation for the atomic spins only

$$\frac{d}{dt}\rho = \frac{1}{i\hbar}[\hat{H}_{\rm eff},\rho] + \Gamma_C\mathcal{L}[\hat{J}^-]\rho + w\sum_{j=1}^{N}\int_{-1}^{1} duN(u)\mathcal{L}[\hat{\sigma}_j^+ e^{i\vec{k}'\cdot\vec{x}_j}]\rho\,, \tag{S20}$$

where the Hamiltonian $\hat{H}_{\rm eff} = -\frac{\hbar\Gamma_\Delta}{2}\hat{J}^+\hat{J}^-$ describes the coherent coupling between each pair of atoms, and the collective decay [term $\Gamma_C\mathcal{L}[\hat{J}^-]$ in Eq. (S20)] leads to dissipative coupling. We want to emphasize that this atomic master equation is not sufficient for the external degrees of freedom, which are treated in section II separately, and for which retardation effects are not negligible.

The spin degrees of freedom of atoms scale exponentially with the number of atoms. To solve Eq. (S20), we thus use a semiclassical approximation that is applicable to large atom numbers in the steady-state superradiance [S1, S2]. Cumulants for the expectation values of spin operators are expanded to second order. Because of the U(1) symmetry, $\langle\hat{\sigma}_j^+\rangle = 0$. Therefore, all nonzero observables are expanded in terms of $\langle\hat{\sigma}_j^+\hat{\sigma}_j^-\rangle$ and $\langle\hat{\sigma}_j^+\hat{\sigma}_l^-\rangle$ ($j \neq l$). Their equations of motion can then be found from the effective master equation,

$$\begin{aligned}
\frac{d}{dt}\langle\hat{\sigma}_j^+\hat{\sigma}_j^-\rangle &= w(1-\langle\hat{\sigma}_j^+\hat{\sigma}_j^-\rangle) - \frac{1}{2}(\Gamma_C + i\Gamma_\Delta)\cos(k\hat{x}_j)\langle\hat{J}^+\hat{\sigma}_j^-\rangle - \frac{1}{2}(\Gamma_C - i\Gamma_\Delta)\cos(k\hat{x}_j)\langle\hat{\sigma}_j^+\hat{J}^-\rangle,\\
\frac{d}{dt}\langle\hat{\sigma}_j^+\hat{\sigma}_l^-\rangle &= -w\langle\hat{\sigma}_j^+\hat{\sigma}_l^-\rangle + \frac{1}{2}(\Gamma_C + i\Gamma_\Delta)\cos(k\hat{x}_j)\langle\hat{J}^+\hat{\sigma}_l^-\hat{\sigma}_j^z\rangle + \frac{1}{2}(\Gamma_C - i\Gamma_\Delta)\cos(k\hat{x}_l)\langle\hat{\sigma}_l^z\hat{\sigma}_j^+\hat{J}^-\rangle\\
&\approx -\Big(w + (\Gamma_C + i\Gamma_\Delta)\cos^2(k\hat{x}_j)\langle\hat{\sigma}_j^+\hat{\sigma}_j^-\rangle + (\Gamma_C - i\Gamma_\Delta)\cos^2(k\hat{x}_l)\langle\hat{\sigma}_l^+\hat{\sigma}_l^-\rangle\Big)\langle\hat{\sigma}_j^+\hat{\sigma}_l^-\rangle\\
&\quad + \frac{1}{2}(\Gamma_C + i\Gamma_\Delta)\cos(k\hat{x}_j)(2\langle\hat{\sigma}_j^+\hat{\sigma}_j^-\rangle - 1)\langle\hat{J}^+\hat{\sigma}_l^-\rangle + \frac{1}{2}(\Gamma_C - i\Gamma_\Delta)\cos(k\hat{x}_l)(2\langle\hat{\sigma}_l^+\hat{\sigma}_l^-\rangle - 1)\langle\hat{\sigma}_j^+\hat{J}^-\rangle,
\end{aligned} \tag{S21}$$

describing the population inversion and spin-spin correlation respectively. In deriving Eq. (S21), we have dropped the third-order cumulants. In the simulations we integrate (S14), (S18) and (S21) simultaneously.

[S1] D. Meiser and M. J. Holland, Phys. Rev. A **81**, 033847 (2010); *ibid.* **81**, 063827 (2010).
[S2] Minghui Xu, D. A. Tieri, E. C. Fine, J. K. Thompson, and M. J. Holland, Phys. Rev. Lett. **113**, 154101 (2014).

### 3.3.2 Semiclassical theory of synchronization-assisted cooling

Physical Review A **95**, 063852 (2017)

DOI: 10.1103/PhysRevA.95.063852

Authors: Simon B. Jäger[1], Minghui Xu[2,3,4], Stefan Schütz[1], M. J. Holland[2,3], and Giovanna Morigi[1]

[1] *Theoretische Physik, Universität des Saarlandes, D-66123 Saarbrücken, Germany*
[2] *JILA, National Institute of Standards and Technology and Department of Physics, University of Colorado, Boulder, Colorado 80309-0440, USA*
[3] *Center for Theory of Quantum Matter, University of Colorado, Boulder, Colorado 80309, USA*
[4] *Department of Physics and Astronomy, Shanghai Jiao Tong University, Shanghai 200240, China*



**Author Contributions:**
The theoretical model was developed by all authors. Numerical simulations were performed by S. B. Jäger with the assistance of S. Schütz. Analytical calculations were performed by S. B. Jäger and G. Morigi. The results were checked and discussed by all authors. The article was mainly written by S. B. Jäger, M. J. Holland, and G. Morigi.

**Abstract:**
We analyze the dynamics leading to radiative cooling of an atomic ensemble confined inside an optical cavity when the atomic dipolar transitions are incoherently pumped and can synchronize. Our study is performed in the semiclassical regime and assumes that cavity decay is the largest rate in the system dynamics. We identify three regimes characterizing the cooling. At first hot atoms are individually cooled by the cavity friction forces. After this stage, the atoms' center-of-mass motion is further cooled by the coupling to the internal degrees of freedom while the dipoles synchronize. In the latest stage dipole-dipole correlations are stationary and the center-of-mass motion is determined by the interplay between friction and dispersive forces due to the coupling with the collective dipole. We analyze this asymptotic regime by means of a mean-field model and show that the width of the momentum distribution can be of the order of the photon recoil. Furthermore, the internal excitations oscillate spatially with the cavity standing wave forming an antiferromagnetic-like order.

PHYSICAL REVIEW A **95**, 063852 (2017)

# Semiclassical theory of synchronization-assisted cooling

Simon B. Jäger,[1] Minghui Xu,[2,3,4] Stefan Schütz,[1,*] M. J. Holland,[2,3] and Giovanna Morigi[1]

[1]*Theoretische Physik, Universität des Saarlandes, D-66123 Saarbrücken, Germany*

[2]*JILA, National Institute of Standards and Technology and Department of Physics, University of Colorado, Boulder, Colorado 80309-0440, USA*

[3]*Center for Theory of Quantum Matter, University of Colorado, Boulder, Colorado 80309, USA*

[4]*Department of Physics and Astronomy, Shanghai Jiao Tong University, Shanghai 200240, China*

(Received 6 February 2017; published 30 June 2017)

We analyze the dynamics leading to radiative cooling of an atomic ensemble confined inside an optical cavity when the atomic dipolar transitions are incoherently pumped and can synchronize. Our study is performed in the semiclassical regime and assumes that cavity decay is the largest rate in the system dynamics. We identify three regimes characterizing the cooling. At first hot atoms are individually cooled by the cavity friction forces. After this stage, the atoms' center-of-mass motion is further cooled by the coupling to the internal degrees of freedom while the dipoles synchronize. In the latest stage dipole-dipole correlations are stationary and the center-of-mass motion is determined by the interplay between friction and dispersive forces due to the coupling with the collective dipole. We analyze this asymptotic regime by means of a mean-field model and show that the width of the momentum distribution can be of the order of the photon recoil. Furthermore, the internal excitations oscillate spatially with the cavity standing wave forming an antiferromagnetic-like order.

DOI: 10.1103/PhysRevA.95.063852

## I. INTRODUCTION

Radiative cooling is based on tailoring the scattering cross section of photons from atoms, molecules, and optomechanical structures. It achieves a net and irreversible transfer of mechanical energy into the modes of the electromagnetic field by means of a coherent process followed by dissipation, which in atomic and molecular media is usually spontaneous emission [1,2]. By these means ultralow temperatures have been realized, paving the way to unprecedented levels of quantum control of the dynamics from the microscopic [3,4] up to the mesoscopic realm [5–7].

Despite this remarkable progress, radiative cooling of optically dense atomic or molecular ensembles to quantum degeneracy remains a challenge. Here cooperative effects of light scattering usually hinder the laser cooling dynamics, because of the enhanced probability of reabsorbing the spontaneously emitted photons [8–10]. Among possible strategies [11] and implementations [12], one promising scheme uses elastic scattering into the mode of a high-finesse resonator for avoiding spontaneous emission, while the irreversible mechanism leading to dissipation is provided by cavity decay [13–16]. In this regime the width of the asymptotic momentum distribution is typically limited by the resonator line width [15]. In single-mode standing-wave cavities, moreover, the dispersive mechanical forces of the cavity induce a stationary density modulation, which appear when the intensity of the transverse laser driving the atoms exceeds a threshold value [17–20].

Self-trapping and cooling of atoms in cavities are also expected when the atoms are incoherently pumped [21–23]. In setups where the dipoles can synchronize [24], a cavity-assisted cooling mechanism was recently identified whose dynamics exhibit giant friction forces [25]. Figure 1 schematically illustrates the setup: the atomic dipolar transitions are transversally driven by an external incoherent pump and strongly couple with the high-finesse mode of a standing-wave resonator, whose decay rate exceeds by orders of magnitude the incoherent pump rate. The numerical analysis performed in Ref. [25] showed that the medium could reach ultralow asymptotic temperatures that were orders of magnitude smaller than the cavity line width.

The purpose of this paper is to perform a detailed analysis of the semiclassical dynamics of the synchronization-assisted cooling mechanism of Ref. [25]. Our study extends the work in Ref. [25] and builds a consistent theoretical framework from which we can extract analytical predictions on the dynamics. We show that the cooling dynamics is essentially determined by the three stages we illustrate in Fig. 2(a): initially hot atoms are cooled by the resonator until the time scale of the external degrees of freedom becomes of the order of the time scale of the internal degrees of freedom. In the second stage the dipoles synchronize and establish correlations with the atoms' spatial distribution. In the final stage dipole-dipole correlations are stationary and the motion is cooled down to temperatures that are determined by the pump rate, providing this is chosen within the interval of values allowing synchronization. Even though the steady state exhibits no density modulations, synchronization leads to correlations between the internal and the external degrees of freedom and in the asymptotic limit the atomic excitations oscillate in space with the intensity of the intracavity field, as shown in Fig. 2(b).

The dynamics we discuss complements the studies performed in Refs. [21–23], where the incoherent pump rate was instead the fastest rate of the dynamics. We argue that the resulting regimes are essentially different: for example, in our case at steady state the atoms are not spatially localized and the mean-field character of dipole-dipole correlations is dominant.

*Present address: icFRC, IPCMS (UMR 7504) and ISIS (UMR 7006), University of Strasbourg and CNRS, 67000 Strasbourg, France.

 

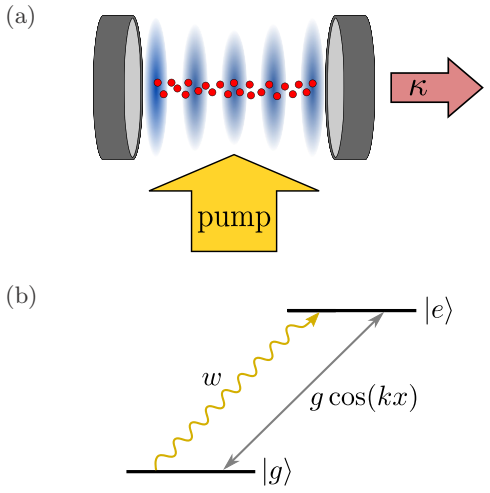


FIG. 1. (a) Atoms are transversally driven by an incoherent pump at rate $w$ and strongly couple with the mode of a standing-wave cavity. (b) The relevant internal states are the two metastable states $|g\rangle$ and $|e\rangle$, which can be the ground and excited states of the intercombination line of an alkali-earth metal atom or two sublevels of a hyperfine multiplet. The dipolar transitions strongly couple to the cavity mode with position-dependent strength $g\cos(kx)$, with $g$ the vacuum Rabi frequency and $k$ the cavity wave number. The cavity decay rate is the largest parameter of the dynamics, i.e., $\kappa \gg g, w$.

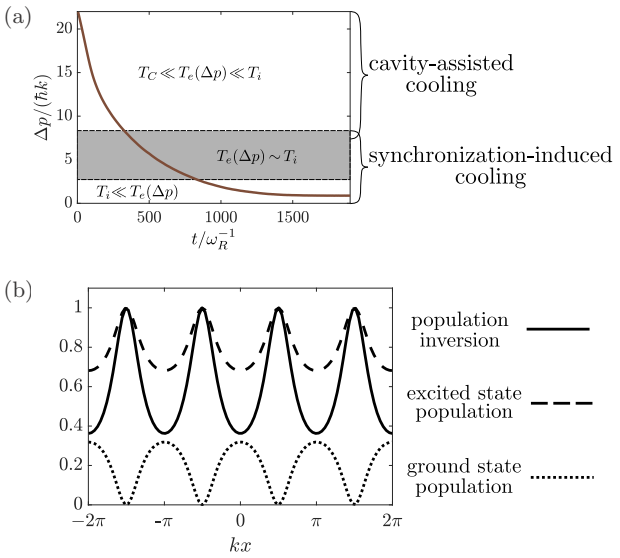


FIG. 2. (a) Example of the time evolution of the one-particle momentum width $\Delta p$ and schematic overview of the regimes characterizing the dynamics of synchronization-assisted cooling. The width $\Delta p$ determines the characteristic time scale $T_e$ of the atoms' external motion, which is inversely proportional to the mean Doppler shift $k\Delta p/m$. The time scales of reference are determined by cavity decay, $T_C \sim \kappa^{-1}$, and by the spins pump rate, $T_i \sim 1/w$. Initially, $T_e \ll T_i$ and the atoms' center-of-mass motion is cooled by the cavity forces. When the atoms are sufficiently cold that $T_e$ becomes comparable to $T_i$, the cooling dynamics is determined by the nonadiabatic coupling of the external motion with the spin dynamics. The final stages are characterized by the regime $T_e \gg T_i$ and exhibit temperatures that are orders of magnitude smaller than $\kappa$. (b) The correlations between internal and external degrees of freedom give rise to a position-dependent expectation value of population inversion (solid line) that oscillates with the cavity intensity $\cos^2(kx)$ and is maximum at the nodes.

This article is organized as follows. In Sec. II we start from the Heisenberg-Langevin equations of atoms and cavity and derive a semiclassical model for the external degrees of freedom. In Sec. III we determine a mean-field model and test the validity of its predictions. We then use the mean-field model to analyze the steady state and estimate the final temperature. The conclusions are drawn in Sec. IV, while the appendices provide details of the calculations of Secs. II and III.

## II. SEMICLASSICAL MODEL OF SYNCHRONIZATION-INDUCED COOLING

The system we consider consists of $N$ atoms of mass $m$ that are confined within a high-finesse optical resonator and are constrained to move only along the cavity axis, which we denote by the $x$ axis. The setup is illustrated in Fig. 1. The atomic dipolar transition is incoherently driven by a transverse pump (directed orthogonal to the cavity axis) at rate $w$. Each atom is composed of two metastable states, $|g\rangle$ and $|e\rangle$, and strongly couples to a mode of the cavity with position-dependent strength $g\cos(kx)$, with $g$ the vacuum Rabi frequency and $k$ the cavity wave number. We discard the instability of the excited state, so that atomic emission only occurs into the cavity mode. This can be realized when $|g\rangle$ and $|e\rangle$ form the intercombination line of alkali-earth metals [26] or when they are two substates of the hyperfine multiplet coupled by a two-photon transition, of which one dipole transition is coupled with the resonator [24]. In either case the atomic transition frequency $\omega_a$ is determined by the energy splitting between the two levels, while the mechanical effects of light scale with the recoil frequency $\omega_R = \hbar k^2/(2m)$. To good approximation, this is determined by the wave number $k$ of the cavity mode.

In this section we start from the Heisenberg-Langevin equations of motion for the cavity, electronic, and center-of-mass degrees of freedom, and derive the equations in the limit in which the atoms' center-of-mass motion can be treated semiclassically. The parameter regime we consider is the one of synchronization: The cavity decay rate $\kappa$ is the fastest rate of the dynamics and the value of the incoherent pump rate $w$ is chosen within the lower and the upper synchronization thresholds [27], as we specify below. The recoil frequency $\omega_R$ is typically the smallest parameter of the dynamics, so that $\omega_R < w \ll \kappa$, which is consistent with the validity of the semiclassical treatment we apply in this work.

### A. Heisenberg-Langevin equations

We denote by $\hat{a}$ and $\hat{a}^\dagger$ the annihilation and creation operators of a cavity photon at frequency $\omega_c$ and wave number $k$. The atoms are assumed to be distinguishable and are labeled by $j$ $(j = 1, \ldots, N)$. Their canonically conjugated position

and momentum are denoted by $\hat{x}_j$ and $\hat{p}_j$ and the lowering, raising, and population-inversion operators by $\hat{\sigma}_j = |g\rangle_j\langle e|$, $\hat{\sigma}_j^\dagger = |e\rangle_j\langle g|$, and $\hat{\sigma}_j^z = |e\rangle_j\langle e| - |g\rangle_j\langle g|$, respectively.

The Hamiltonian governing the coherent dynamics in the frame rotating at the frequency $\omega_a$ reads

$$\hat{H} = \hbar\Delta\hat{a}^\dagger\hat{a} + \sum_{j=1}^{N}\frac{\hat{p}_j^2}{2m} + \hbar\frac{g}{2}\sum_{j=1}^{N}[\hat{a}^\dagger\hat{\sigma}_j\cos(k\hat{x}_j) + \text{H.c.}], \tag{1}$$

with $\Delta = \omega_c - \omega_a$ the detuning between cavity and atomic transition frequency.

The Heisenberg-Langevin equations for the relevant operators include the cavity damping at rate $\kappa$, the incoherent pump at rate $w$, and the corresponding Gaussian input noise operators $\hat{a}_{\text{in}}$ and $\hat{\sigma}_{\text{in},j}$, respectively, and read

$$\frac{d}{dt}\hat{x}_j = \frac{\hat{p}_j}{m}, \tag{2}$$

$$\frac{d}{dt}\hat{p}_j = \hbar k\frac{g}{2}[\hat{a}^\dagger\hat{\sigma}_j\sin(k\hat{x}_j) + \text{H.c.}], \tag{3}$$

$$\frac{d}{dt}\hat{\sigma}_j = -\frac{w}{2}\hat{\sigma}_j + i\frac{g}{2}\cos(k\hat{x}_j)\hat{\sigma}_j^z\hat{a} - \sqrt{w}\hat{\sigma}_j^z\hat{\sigma}_{\text{in},j}^\dagger, \tag{4}$$

$$\frac{d}{dt}\hat{\sigma}_j^z = w(1-\hat{\sigma}_j^z) + [ig\hat{a}^\dagger\hat{\sigma}_j\cos(k\hat{x}_j) + \text{H.c.}] + 2\sqrt{w}(\hat{\sigma}_{\text{in},j}\hat{\sigma}_j + \hat{\sigma}_j^\dagger\hat{\sigma}_{\text{in},j}^\dagger), \tag{5}$$

$$\frac{d}{dt}\hat{a} = \left(-i\Delta - \frac{\kappa}{2}\right)\hat{a} - \sum_{j=1}^{N} i\frac{g}{2}\hat{\sigma}_j\cos(k\hat{x}_j) + \sqrt{\kappa}\hat{a}_{\text{in}}. \tag{6}$$

Here, $\langle\hat{\sigma}_{\text{in},j}(t)\rangle = 0 = \langle\hat{a}_{\text{in}}(t)\rangle$, $\langle\hat{\sigma}_{\text{in},j}^\dagger(t)\hat{\sigma}_{\text{in},j'}(t')\rangle = 0 = \langle\hat{a}_{\text{in}}^\dagger(t)\,\hat{a}_{\text{in}}(t')\rangle$, $\langle\hat{a}_{\text{in}}(t)\hat{a}_{\text{in}}^\dagger(t')\rangle = \delta(t-t')$, and $\langle\hat{\sigma}_{\text{in},j}(t)\hat{\sigma}_{\text{in},j'}^\dagger(t')\rangle = \delta_{jj'}\delta(t-t')$. The expectation values $\langle\cdot\rangle$ are taken over the tensor product between the initial density matrix of system and external Markovian environment with vanishing mean number of photons [28].

### B. Coarse-grained dynamics

We derive an effective model by assuming that the decay rate of the resonator $\kappa$ is the largest rate of the dynamics. This allows us to identify a coarse-grained time scale $\Delta t$ that is infinitesimal for the internal degrees of freedom but over which the cavity degrees of freedom can be eliminated from the equations of the atomic dynamics.

The coarse-grained cavity field operator is given by the time average $\bar{\hat{a}}(t) = \langle\hat{a}(t)\rangle_{\Delta t}$, where $\langle\hat{\zeta}(t)\rangle_{\Delta t} \equiv \int_t^{t+\Delta t} dt'\hat{\zeta}(t')/\Delta t$. It takes the form

$$\bar{\hat{a}}(t) \approx \frac{-i\frac{Ng}{2}}{i\Delta + \kappa/2}\left(\langle\hat{X}\rangle_{\Delta t} - \frac{1}{i\Delta + \kappa/2}\left\langle\frac{d}{dt}\hat{X}\right\rangle_{\Delta t}\right) + \hat{\mathcal{F}}(t) \tag{7}$$

and is here expressed in terms of the synchronization order parameter $\hat{X}$ of Ref. [25]:

$$\hat{X}(t) = \frac{1}{N}\sum_{l=1}^{N}\hat{\sigma}_l\cos(k\hat{x}_l). \tag{8}$$

It is possible to provide a physical interpretation of the various terms on the right-hand side (RHS) of Eq. (7). The first term is the adiabatic component, where the cavity field follows instantaneously the atomic state given by $\hat{X}(t)$. The second term depends on the time derivative of $\hat{X}$, and thus on memory effects of the internal and external degrees of freedom in lowest order. It is hence a nonadiabatic correction. Finally, the third term on the RHS gives the contribution of the quantum noise, whose explicit form is reported in Appendix A.

Before we proceed, we observe that the characteristic time scales of the atomic motion, and thus of $\hat{X}$, are determined by the incoherent pump rate $w$ for the internal degrees of freedom, $T_i \sim 1/w$, and by the mean kinetic energy $E_{\text{kin}} = \langle p^2\rangle/(2m)$ for the external degrees of freedom, as illustrated in Fig. 2(a). More specifically, the characteristic time of the external motion scales with $T_e \sim 1/R_{\text{Doppler}}$, where $R_{\text{Doppler}} \approx 2\sqrt{\omega_R E_{\text{kin}}/\hbar}$ is the mean Doppler shift. When the atoms are sufficiently hot, it is necessary to include nonadiabatic corrections when eliminating the cavity field. However, since $T_i$ is typically orders of magnitude larger than $T_C$ for the parameters of interest, only the retardation effects of the external degrees of freedom can be relevant over the time scale $\Delta t$, hence in Eq. (7) we shall use

$$\left\langle\frac{d}{dt}\hat{X}\right\rangle_{\Delta t} \approx \frac{1}{N}\sum_{j=1}^{N}\left\langle\hat{\sigma}_j\frac{d}{dt}[\cos(k\hat{x}_j)]\right\rangle_{\Delta t}. \tag{9}$$

On the basis of these considerations, in the coarse-grained time scale the dynamics of the internal degrees of freedom is solely determined by the adiabatic component of the cavity field. The corresponding equations read (from now on the operators are assumed to be in the coarse-grained time scale and we omit to write $\langle\cdot\rangle_{\Delta t}$):

$$\frac{d}{dt}\hat{\sigma}_j = -\frac{w}{2}\hat{\sigma}_j + \frac{N\Gamma_C}{2}(-i\alpha^*)\cos(k\hat{x}_j)\hat{\sigma}_j^z\hat{X} - \sqrt{w}\hat{\sigma}_j^z\hat{\sigma}_{\text{in},j}^\dagger, \tag{10}$$

$$\frac{d}{dt}\hat{\sigma}_j^z = w(1-\hat{\sigma}_j^z) - [N\Gamma_C(i\alpha)\hat{X}^\dagger\hat{\sigma}_j\cos(k\hat{x}_j) + \text{H.c.}] + 2\sqrt{w}(\hat{\sigma}_{\text{in},j}\hat{\sigma}_j + \hat{\sigma}_j^\dagger\hat{\sigma}_{\text{in},j}^\dagger), \tag{11}$$

where

$$\Gamma_C = \frac{g^2/4}{\Delta^2 + \kappa^2/4}\kappa \tag{12}$$

is the effective atomic line width while

$$\alpha = \frac{\Delta}{\kappa/2} - i$$

is a dimensionless parameter, which is purely imaginary when $\Delta = 0$.

Retardation effects are instead important for the dynamics of the external degrees of freedom in the initial stage of the dynamics. By keeping the nonadiabatic corrections to the cavity field, according to the prescription of Eq. (9), their dynamics read

$$\frac{d}{dt}\hat{p}_j = \hat{F}_j^{(0)} + \hat{F}_j^{(1)} + \hat{\mathcal{N}}_j. \tag{13}$$

Here $\hat{F}_j^{(0)}$ and $\hat{F}_j^{(1)}$ are force operators that describe the adiabatic and nonadiabatic contribution of the cavity field, respectively, while $\hat{\mathcal{N}}_j$ describes a position-dependent Gaussian noise:

$$\hat{F}_j^{(0)} = -\hbar k \frac{N\Gamma_C}{2}\alpha \hat{X}^\dagger \hat{\sigma}_j \sin(k\hat{x}_j) + \text{H.c.} \tag{14}$$

$$\hat{F}_j^{(1)} = -\frac{N\Gamma_C}{2}\frac{\omega_R \kappa}{\Delta^2+\kappa^2/4} i\alpha^2 \times \frac{1}{2N}\sum_{l=1}^{N}[\sin(k\hat{x}_l),\hat{p}_l]_+ \hat{\sigma}_l^\dagger \hat{\sigma}_j \sin(k\hat{x}_j) + \text{H.c.}, \tag{15}$$

$$\hat{\mathcal{N}}_j = \hbar k \frac{g}{2}\hat{\mathcal{F}}(t)^\dagger \hat{\sigma}_j \sin(k\hat{x}_j) + \text{H.c.}, \tag{16}$$

where $[A,B]_+ = AB + BA$. The nonadiabatic component $\hat{F}_j^{(1)}$ scales with the ratio $R_{\text{Doppler}}/\sqrt{\kappa^2/4+\Delta^2}$ with respect to the adiabatic component. It can be discarded in the later stages of the dynamics, that is when the atoms are sufficiently cold so that $R_{\text{Doppler}} \sim w$ corresponding to $T_e \sim T_i$.

It is important to emphasize the motivation for the definition of the synchronization order parameter $\hat{X}$ in Eq. (8). This definition generalizes the collective spin $\hat{j}_- = (\sum_{i=1}^N \hat{\sigma}_i)/N$, which has a nonvanishing expectation value in the synchronized phase [27]. Operators $\hat{X}$ and $\hat{j}_-$ in fact coincide when the atoms are localized at the positions where $\langle\cos(k\hat{x}_j)\rangle = 1$ for all atoms. In the generalized form, the synchronization order parameter $\hat{X}$ depends explicitly on the correlations between the internal degrees of freedom and the atomic positions within the cavity optical lattice. We will see that this property can lead to cooling when the dipoles synchronize.

### C. Semiclassical dynamics of the external degrees of freedom

We now assume that the width $\Delta p$ of the single atom momentum distribution is $\Delta p \gg \hbar k$ at all stages of the dynamics, where $\hbar k$ is the linear momentum carried by a cavity photon. In this limit the recoil frequency $\omega_R$ is assumed to be the smallest frequency scale and a semiclassical description of the atomic center-of-mass motion is justified [29]. By means of this description the equation of motion for the atomic momentum reads

$$\frac{d}{dt}p_j = F + \xi_j^p, \tag{17}$$

where $F = F_j^{(0),\text{sc}} + F_j^{(1),\text{sc}}$ and

$$F_j^{(0),\text{sc}} = -\hbar k \sin(kx_j)\frac{N\Gamma_C}{2}\alpha\langle\hat{X}^\dagger\hat{\sigma}_j\rangle + \text{H.c.}\,, \tag{18}$$

$$F_j^{(1),\text{sc}} = -\frac{N\Gamma_C}{2}\frac{\omega_R\kappa}{\Delta^2+\kappa^2/4} i\alpha^2 \sin(kx_j) \times \frac{1}{N}\sum_{l=1}^{N}\sin(kx_l)p_l\langle\hat{\sigma}_l^\dagger\hat{\sigma}_j\rangle + \text{H.c.} \tag{19}$$

In Eq. (18) we use $\langle\hat{X}\hat{\sigma}_j\rangle = \sum_{l=1}^N \cos(kx_l)\langle\hat{\sigma}_l^\dagger\hat{\sigma}_j\rangle/N$. The stochastic variable $\xi_j^p$ describes the properties of the Gaussian noise, $\langle\xi_j^p(t)\xi_l^p(t')\rangle = D^{jl}\delta(t-t')$ with

$$D^{jl} = \Gamma_C\hbar^2k^2\sin(kx_j)\sin(kx_l)\text{Re}[\langle\hat{\sigma}_l^\dagger\hat{\sigma}_j\rangle]. \tag{20}$$

According to this semiclassical model, the dynamics is determined by these equations together with the equations $\dot{x}_j = p_j/m$ and the quantum mechanical equations for the internal degrees of freedom (10) and (11). The latter, in particular, now depend on the semiclassical variables $x_j$.

Figures 3 and 4 display $\langle p^2\rangle$ and the corresponding correlations $\langle X^\dagger X\rangle$ as a function of time, assuming that there are initially no correlations between the dipoles and that at $t=0$ the atoms' motion is in a thermal state at a given temperature $T$ (the subplots from top to bottom correspond to decreasing values of $T$). The solid curves have been numerically evaluated by integrating Eqs. (10) and (11), after performing a second order cumulant expansion for the spins as shown in Appendix B, together with the stochastic differential equation (17) [30]. For the parameter choice we considered the semiclassical dynamics predict the exponential decrease of the kinetic energy towards an asymptotic value which is of the order of the recoil energy. Comparison with the time evolution of the correlations $\langle X^\dagger X\rangle$ shows that these reach the asymptotic value at a rate comparable with the initial cooling rate. These correlations can be measured by detecting the intracavity photon number, since $\langle\hat{a}^\dagger\hat{a}\rangle \propto N^2\langle\hat{X}^\dagger\hat{X}\rangle$, and signify the build-up of spin-spin correlations and of correlations between the spins and their external positions within the cavity lattice. We denote by synchronization-induced cooling the cooling dynamics that is intrinsically connected with the buildup of these correlations and thus of the intracavity field.

### D. Unravelling the semiclassical dynamics

In order to gain insight into the mechanisms which lead to the observed behavior, we compare these curves with the corresponding predictions obtained by either only considering the cavity friction component of the force given in Eq. (19), thus setting $F = F_j^{(1),\text{sc}}$ in Eq. (17) (dotted line), or by only considering the component of the force given in Eq. (18), thus setting $F = F_j^{(0),\text{sc}}$ in Eq. (17) (dashed line). The resulting curves in Figs. 3(b)–3(c) and of Figs. 4(b)–4(c) show that $F_j^{(0),\text{sc}}$ is primarily responsible for the build-up of spin-spin correlations and for the cooling dynamics when the atomic initial temperature is sufficiently low [the friction force tends instead to heat the distribution in (c)].

A different behavior is observed in Figs. 3(a) and 4(a): Although the friction force contributes to the buildup of the cavity field, none of the individual components reproduce the full semiclassical dynamics. In particular, the adiabatic component leads to a larger asymptotic value of the mean kinetic energy, while the cavity friction force cools the motion at a significantly slower rate. Figure 5 displays the momentum distribution that each of these dynamics predict at $t \approx 2\times10^3\omega_R^{-1}$. Remarkably, they qualitatively agree for small momenta, as visible in subplot (a). In (b), however, we observe discrepancies at large momenta. The distribution due to the adiabatic component of the force exhibits atoms at large momenta. These atoms, instead, are cooled by the cavity friction force. We further note that the momentum distribution

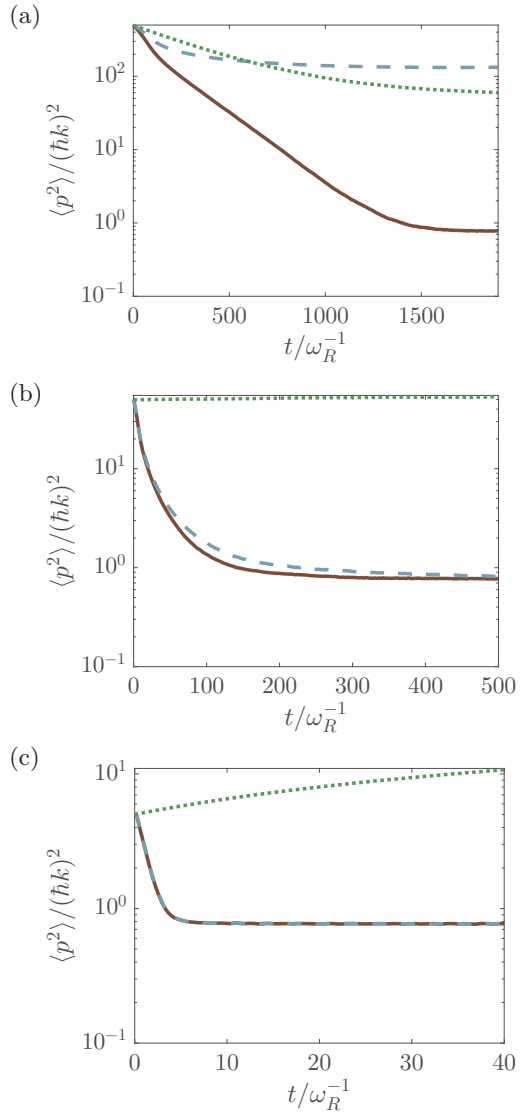


FIG. 3. Dynamics of the width $\langle p^2\rangle$ of the single-atom momentum distribution [in units of $(\hbar k)^2$] as a function of time (in units of $1/\omega_R$). The solid curves are determined by integrating Eqs. (10), (11) (using the cumulant expansion, see Appendix B) and (17) assuming that initially all atoms are in the excited state and are uniformly spatially distributed, while their momentum distribution is thermal with width (a) $\langle p^2(0)\rangle = 500(\hbar k)^2$; (b) $\langle p^2(0)\rangle = 50(\hbar k)^2$; (c) $\langle p^2(0)\rangle = 5(\hbar k)^2$. The dashed and dotted lines are the corresponding simulations obtained by integrating the equations after setting in Eq. (17) $F = F_j^{(1),\mathrm{sc}}$(dotted line) and $F = F_j^{(0),\mathrm{sc}}$ (dashed line). The parameters are $N = 100$, $\kappa = 780\omega_R$, $N\Gamma_C = 40\omega_R$, $\Delta = \kappa/2$, $w = N\Gamma_C/4$.

is approximately flat in the momentum interval $[-\hbar k,\hbar k]$, suggesting that the stationary state is nonthermal.

We further characterize the dynamics by inspecting the time evolution of the kurtosis $\mathcal{K}(t)$, which is defined as

$$\mathcal{K}(t) = \langle p(t)^4\rangle/\langle p(t)^2\rangle^2,$$

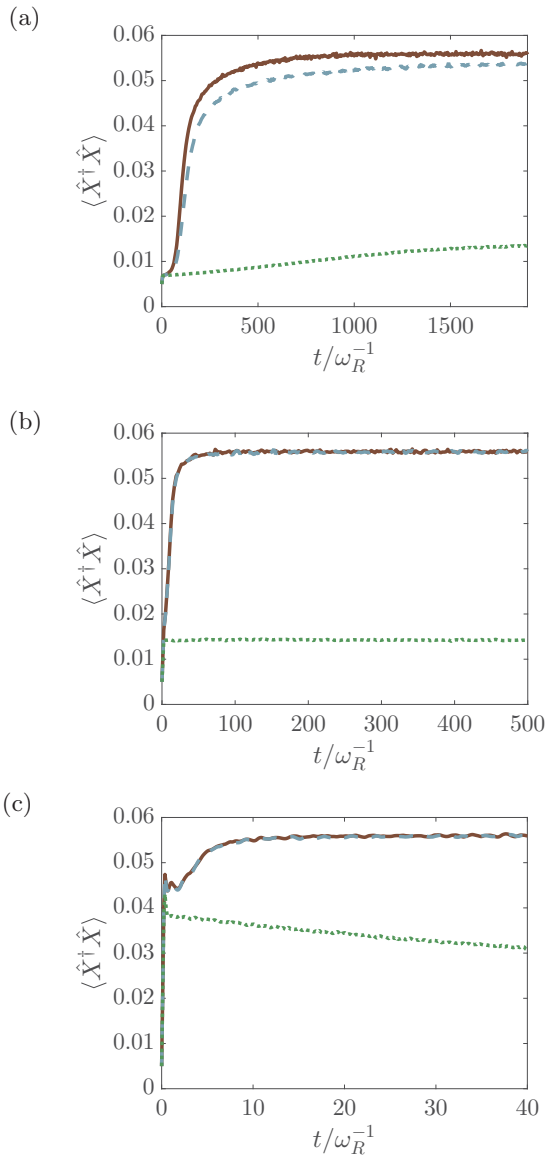


FIG. 4. Correlation $\langle \hat{X}^\dagger \hat{X}\rangle$ as a function of time (in units of $1/\omega_R$). This quantity signifies the occurrence of synchronization. Subplots (a)–(c) respectively correspond to the dynamics of subplots (a)–(c) of Fig. 3.

with $\langle p(t)^n\rangle$ the $n$th moment of the single particle distribution at time $t$. The kurtosis for a Gaussian distribution is 3, so that deviations from this value signal that the distribution is nonthermal. Figure 6 shows the kurtosis $\mathcal{K}(t)$ for the dynamics reported in Fig. 3(a). The distribution is nonthermal at all times, including the asymptotic limit, where it tends towards the value 2. The large value it reaches during the evolution is attributed to the existence of tails of the momentum distribution at large $p$. These components are cooled by the cavity friction force at a later stage of the dynamics, as visible by comparing these dynamics with the one in which the cavity friction force is set to zero (dashed line). When instead the initial temperature is very low, the kurtosis is well described by the sole effect of

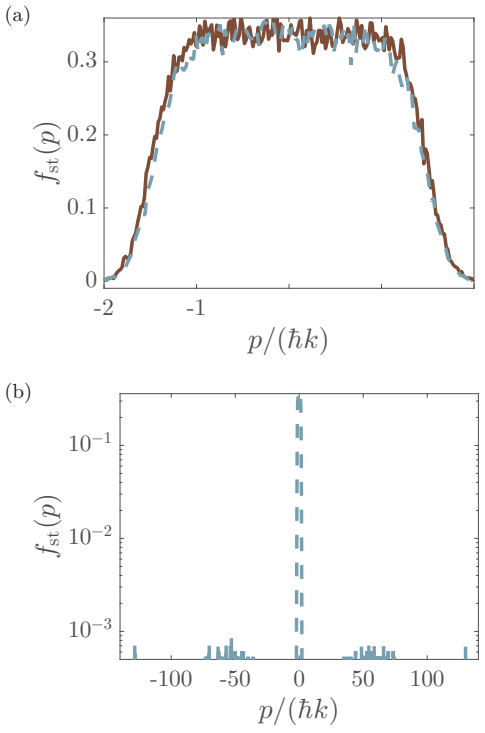


FIG. 5. (a) Momentum distribution $f_{st}(p)$ as a function of $p$ (in units of $\hbar k$) and resulting from the dynamics of Fig. 3 (a) at time $t \simeq 2000\omega_R^{-1}$. The solid and dashed lines illustrate the momentum distributions obtained by considering the full force and only the adiabatic component, respectively, in Eq. (17). Subplot (b) shows the momentum distribution (in logarithmic scale) over the full initial range of values, demonstrating the existence of long tails. These are responsible for the discrepancy observed in the asymptotic limit of the corresponding curves in Fig. 3(a).

the adiabatic component of the force, as visible in the inset of Fig. 6.

This analysis suggests that the friction and the adiabatic forces have very different velocity capture ranges, and in particular the cavity friction forces precool the atoms until a regime in which retardation effects become very small.

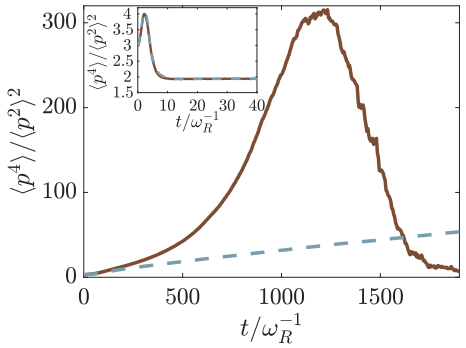


FIG. 6. Kurtosis $\mathcal{K} = \langle p^4\rangle/\langle p^2\rangle^2$ as a function of time for the dynamics of Fig. 3(a). The inset shows the kurtosis for the parameters as in Fig. 3(c): Both curves relax to approximately the same value $\mathcal{K} \approx 2$.

In this regime, we will show that synchronization-induced cooling efficiently concentrates the atoms in a narrow velocity distribution that can be of the order of the recoil frequency. The time scales associated with these dynamics are illustrated in Fig. 2 and are at the basis of the theoretical treatment presented in what follows.

## III. LOCAL MEAN-FIELD MODEL

We now analyze the dynamics in the regime where the dipoles have synchronized, corresponding to the stage where the correlations $\langle X^\dagger X\rangle$ have built up. We perform our study by means of a mean-field approximation, namely, by assuming

$$\langle\hat\sigma_j\rangle = s_j, \tag{21}$$

$$\langle\hat\sigma_j^z\rangle = z_j, \tag{22}$$

where $s_j, z_j$ are scalars. This consists of approximating $\langle\hat\sigma_j^\dagger\hat\sigma_i\rangle \approx s_j^* s_i$ for $i \neq j$. Within this treatment, the synchronization order parameter reads

$$X = \langle\hat X\rangle = \sum_{j=1}^{N} s_j \cos(kx_j)/N. \tag{23}$$

It is worth emphasizing that we keep the correlations between the internal and the external degrees of freedom, but assume that particle-particle correlations are of mean-field type.

In the mean-field approximation Eqs. (10) and (11) take the form

$$\frac{ds_j}{dt} = -\frac{w}{2}s_j - \frac{N\Gamma_C}{2}i\alpha^* X\cos(kx_j)z_j, \tag{24}$$

$$\frac{dz_j}{dt} = w(1-z_j) + 2N\Gamma_C \mathrm{Im}\{\alpha X^* s_j\}\cos(kx_j), \tag{25}$$

where the noise due the incoherent pump is neglected. Furthermore we also neglect the nonadiabatic force given in Eq. (19). This is reasonable assuming that the atomic ensemble has a small single particle momentum width as visible in Figs. 3 and 4. The corresponding mean-field equations for the external degrees of freedom read

$$\frac{dx_j}{dt} = \frac{p_j}{m}, \tag{26}$$

$$\frac{dp_j}{dt} = -\hbar k\sin(kx_j)N\Gamma_C \mathrm{Re}\{\alpha X^* s_j\}, \tag{27}$$

where the force is the adiabatic component, Eq. (18), and consistent with the mean-field treatment we have discarded cavity shot noise.

### A. Comparison between mean-field and semiclassical model

We now test the predictions of the mean-field equations by comparing the mean-field dynamics with ones obtained integrating the semiclassical equations (10), (11), and (17). Since the mean-field treatment should more faithfully reproduce the full dynamics for increasing number of particles, we perform simulations for $N = 100$ and $N = 1000$ particles. In doing so we rescale the coupling strength $g$ so to keep $Ng^2$ and thus $N\Gamma_C$ constant [compare with Eq. (12)]. This

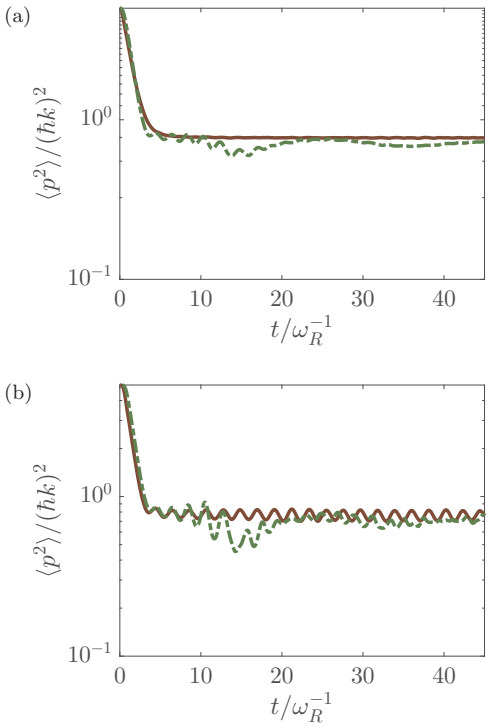


FIG. 7. Dynamics of $\langle p^2(t)\rangle$ (in units of $\hbar^2k^2$) as a function of time (in units of $\omega_R^{-1}$) for (a) $N = 100$ and (b) $N = 1000$ atoms. The solid lines are obtained by numerically integrating Eqs. (10) and (11) (using the cumulant expansion), and (17), whereas the dashed lines are the predictions of the mean field model in Eqs. (24), (25), and (27). The other parameters are the same as in Fig. 3(a). Note that $N\Gamma_C = 40\omega_R$. Accordingly, we rescale the value of $\Gamma_C$ when increasing $N$.

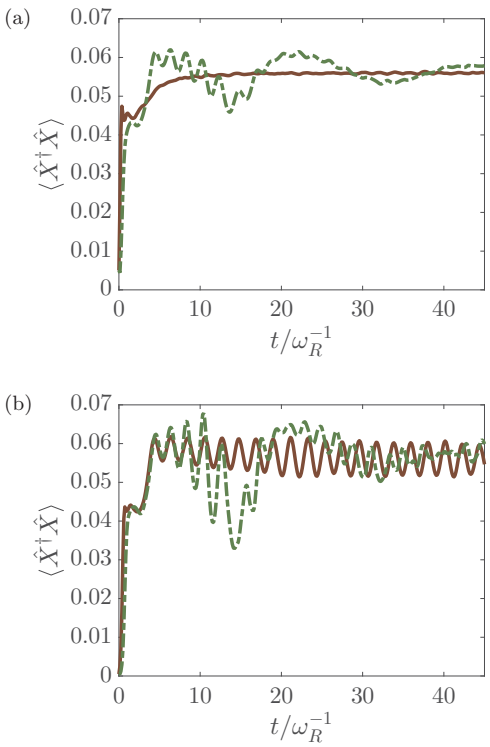


FIG. 8. Dynamics of $\langle \hat{X}^\dagger \hat{X}\rangle$ as a function of time (in units of $\omega_R^{-1}$ for (a) $N = 100$ and (b) $N = 1000$, corresponding to the subplots of Fig. 7.

implies that the upper synchronization threshold, $w = N\Gamma_C$ [27], is a constant for this thermodynamics limit, while the lower threshold $w = \Gamma_C$ [27] in this case scales with $1/N$ and thus vanishes for $N \to \infty$.

Figure 7 displays the dynamics of $\langle p^2(t)\rangle$ predicted by the semiclassical model (solid line) and by the mean-field model (dashed lines) for $\langle p^2(0)\rangle = 5\,(\hbar k)^2$. The two curves qualitatively agree. Moreover, their behavior at short times almost coincides and the time interval over which this occurs increases with $N$. A striking difference is the small frequency oscillation, which seems to solely characterize the mean-field dynamics. However, this oscillation becomes visible at time scales at which the mean-field and the semiclassical dynamics start to be quantitatively distinct. The fast oscillations, instead, are also reproduced by the semiclassical equations at $N = 1000$. They are also visible in the dynamics of the expectation value of $\langle \hat{X}^\dagger \hat{X}\rangle$, as shown in Fig. 8. We note that the mean-field and full semiclassical dynamics predict approximately the same stationary values of the correlations.

Figure 9 displays the spectral analysis of the two curves in Fig. 8(b). In detail, it illustrates the Laplace transform $S(i\omega)$, defined as

$$S(i\omega) = \int_0^\infty e^{i\omega t}[\langle \hat{X}^\dagger \hat{X}\rangle(t) - \langle \hat{X}^\dagger \hat{X}\rangle_{\rm st}]dt, \qquad (28)$$

where $\langle \hat{X}^\dagger \hat{X}\rangle_{\rm st} = \lim_{t\to\infty}\langle \hat{X}^\dagger \hat{X}\rangle(t)$. The spectrum of the mean-field data (dashed-dotted curve) and of the data predicted by the semiclassical model (solid curve) exhibits two sidebands at $\omega \simeq \pm 3\omega_R$, which we attribute to the oscillations in the potential confining the atoms (see next section). The mean-field simulations predict also two low-frequency sidebands at a frequency of the order of a fraction of the recoil frequency, which correspond to the slow oscillations observed in Fig. 8(b).

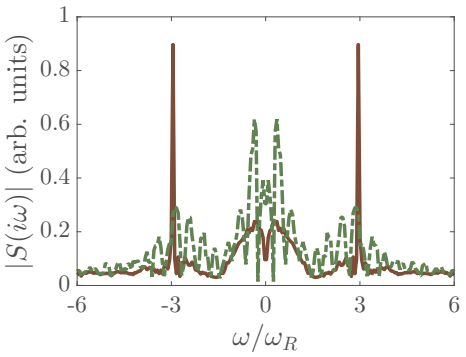


FIG. 9. Absolute value of the Laplace transform $S(i\omega)$, Eq. (28), in arbitrary units and as a function of $\omega$ (in units of $\omega_R$) for the curves in Fig. 8(b). The Laplace transform is evaluated over the same time interval as in Fig. 8(b).

### B. Dynamics at the asymptotic limit

Using the mean-field model we now investigate the dynamics at the asymptotic limit. In particular, we assume that the atoms are sufficiently cold so that at this stage $T_i \ll T_e$. It is therefore justified to adiabatically eliminate the internal degrees of freedom from the equations of motion of the atoms' external variables. The procedure is detailed in Appendix C and leads to the stationary values $s_j^{(0)}$ and $z_j^{(0)}$, which read

$$s_j^{(0)} = \frac{\xi(x_j)}{1+2|\xi(x_j)|^2}, \tag{29}$$

$$z_j^{(0)} = \frac{1}{1+2|\xi(x_j)|^2}, \tag{30}$$

and thus depend on the atomic position $x_j$ through the quantity

$$\xi(x_j) = \frac{N\Gamma_C}{w} X \cos(kx_j). \tag{31}$$

This quantity is proportional to the ratio $N\Gamma_C \cos(kx_j)/w$. It plays an analogous role to the saturation parameter in the dynamics of a driven dipole [31], but its source is of a completely different nature: it depends on the synchronization order parameter $X$, which is found by solving self-consistently the equation

$$\frac{1}{N}\sum_{j=1}^{N} \frac{|\xi(x_j)|^2}{1+2|\xi(x_j)|^2} = \frac{N\Gamma_C}{w}|X|^2. \tag{32}$$

Concise solutions, which are limiting cases, can be found by assuming that the atoms are tightly confined in a lattice, thereby fixing $\cos(kx_j) = \pm\delta$. For $\delta = 0$, for instance, the only solution is $X = 0$. For $\delta \neq 0$, instead, one finds

$$|X|^2 = \frac{w}{2N\Gamma_C}\left(1 - \frac{w}{\delta^2 N\Gamma_C}\right). \tag{33}$$

From this equation it follows that $|X|^2 = 0$ both when $w = 0$ and also when $w \geqslant N\Gamma_C\delta^2$, namely, when $w$ takes the value of the upper synchronization threshold for the corresponding configuration. In particular, the upper synchronization threshold is maximum when $\delta = 1$, which corresponds to the value reported in Ref. [27].

When instead the atoms are uniformly distributed over the cavity wavelength, Eq. (32) can be recast in the form

$$\frac{N\Gamma_C}{w}\frac{1}{2\pi}\int_0^{2\pi} d\theta \frac{\cos^2\theta}{1+2(N\Gamma_C/w)^2|X|^2\cos^2\theta} = 1. \tag{34}$$

By using

$$\frac{1}{2\pi}\int_0^{2\pi} d\theta \frac{\cos^2\theta}{1+2(N\Gamma_C/w)^2|X|^2\cos^2\theta} = \frac{1}{1+2(N\Gamma_C/w)^2|X|^2+\sqrt{1+2(N\Gamma_C/w)^2|X|^2}},$$

we get

$$|X|^2 = \frac{w}{2N\Gamma_C}\left[1 - \frac{w}{N\Gamma_C}\left(\frac{1}{2}+\sqrt{\frac{N\Gamma_C}{w}+\frac{1}{4}}\right)\right]. \tag{35}$$

From Eq. (35) one obtains that the upper synchronization threshold for particles that are homogeneously distributed over the cavity wavelength is given by $w = N\Gamma_C/2$.

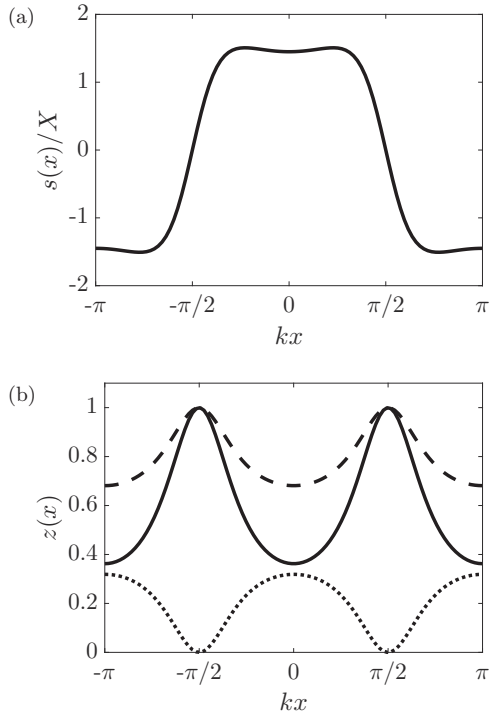


FIG. 10. Spatial dependence of (a) the dipole moment $s(x)$ [Eq. (29)] and (b) the population inversion $z(x)$ [Eq. (30)] for $w = N\Gamma_C/4$ and $|X|^2 \approx 0.055$. The dashed and dotted lines correspond to the excited state $e(x) = [1+z(x)]/2$ and ground state $g(x) = [1-z(x)]/2$ population, respectively. The $x$ axis is in units of $1/k$. We verified that this behavior is also predicted by the semiclassical model.

We now use this result to determine the spatial dependence of the dipole moment $s_j^{(0)}$ and of the population inversion $z_j^{(0)}$. These two quantities are plotted in Figs. 10(a) and 10(b), respectively, where we have used the definition $s_j^{(0)} \to s(x)$ $[z_j^{(0)} \to z(x)]$ in the continuum limit. We observe that at the nodes of $\cos(kx)$ the polarization $s(x)$ changes its sign where the population inversion is maximum. In turn, the population inversion is minimal close to the antinode where the polarization reaches its maximum absolute value. If one associates a well-defined magnetic moment to the two electronic states, then the resulting behavior corresponds to an effective antiferromagnetic order.

### C. Effective Hamiltonian

In the adiabatic limit, where one neglects retardation effects in the coupled dynamics between spin and center-of-mass motion, it is possible to derive an effective Hamiltonian for the atomic external variables. For this purpose we use Eqs. (29) and (30) in Eq. (27) to obtain

$$\dot{p}_j = -\hbar k w \frac{\Delta}{\kappa/2}\tan(kx_j)\frac{|\xi(x_j)|^2}{1+2|\xi(x_j)|^2}.$$

For $N \gg 1$ we can write this equations as $\dot{p}_j = -\partial V_{\rm eff}/\partial x_j$ where $V_{\rm eff}$ is an effective potential of the form

$$V_{\rm eff} = -\sum_{j=1}^{N} \frac{\hbar w}{4} \frac{\Delta}{\kappa/2} \ln[1 + 2|\xi(x_j)|^2]. \tag{36}$$

The corresponding mean-field Hamiltonian, $H_{\rm mean}$, reads

$$H_{\rm mean} = \frac{p^2}{2m} - \frac{\hbar w}{4} \frac{\Delta}{\kappa/2} \ln[1 + 2|\xi(x)|^2]. \tag{37}$$

The potential minima are at the positions $x$ where $\cos(kx) = \pm 1$. At these points the atoms would be trapped should their asymptotic temperature be smaller than the potential depth $-\hbar\Delta w/(2\kappa)\ln(1 + 2N\Gamma_C|X|_1^2/w)$ (here $|X|_1$ is the synchronization order parameter when the atoms are confined at $\cos(kx) = \pm 1$). Correspondingly, the atoms would form an antiferromagnetic spin chain, where the spins swap their orientation so to keep $s_j \cos(kx_j) = 1$. In order to verify whether this is the stationary state of the synchronization dynamics, one needs first to determine the asymptotic temperature. Part of this analysis is performed in the next section, where we determine the friction force due to the nonadiabatic coupling with the internal degrees of freedom.

### D. Dissipative mean-field dynamics

Retardation effects in the dynamics of the spins following the motion give rise to friction. The steady state results from the interplay between the friction and the dispersive force due to the effective potential. We now determine the friction forces in the last cooling stage. For this purpose we perform an expansion of the spin variables including terms to first order in the small parameter $\mathcal{R}_{\rm Doppler}/w$:

$$s = s^{(0)} + \frac{kp}{mw} s^{(1)}, \quad z = z^{(0)} + \frac{kp}{mw} z^{(1)}.$$

We then use the prescription $d/dt \to \partial/\partial t + p/m\partial/\partial x$ in Eqs. (24) and (25) and determine the corresponding stationary state (see Appendix D for details).

The friction force is the component of the force in Eq. (27) that depends on the retarded component,

$$F_{\rm ret} = -(\hbar k^2/m) p \sin(kx)(N\Gamma_C/w){\rm Re}\{\alpha X^* s^{(1)}\},$$

and takes the form

$$F_{\rm ret} = -8\omega_R p \frac{|\xi(x)|^2 \tan^2(kx)}{[1 + 2|\xi(x)|^2]^3} \frac{\Delta}{\kappa/2} \mathcal{F}_\Delta(|\xi(x)|^2) \tag{38}$$

with

$$\mathcal{F}_\Delta(|\xi(x)|^2) = \frac{1 - 2|\xi(x)|^2}{1 + \left(\frac{\Delta}{\kappa/2}\right)^2} - 2|\xi(x)|^4.$$

This equation shows that the friction force depends on the atomic position. It vanishes at the minima of the mean-field potential, where $\sin(kx) = 0$, but tends to pull out the atoms from these points, being positive about $x = n\pi/k$ for $\Delta > 0$. The friction coefficient is instead negative for values of $\xi(x)$ such that

$$|\xi(x)|^2 \leqslant \frac{1}{2|\alpha|^2}(\sqrt{2|\alpha|^2 + 1} - 1). \tag{39}$$

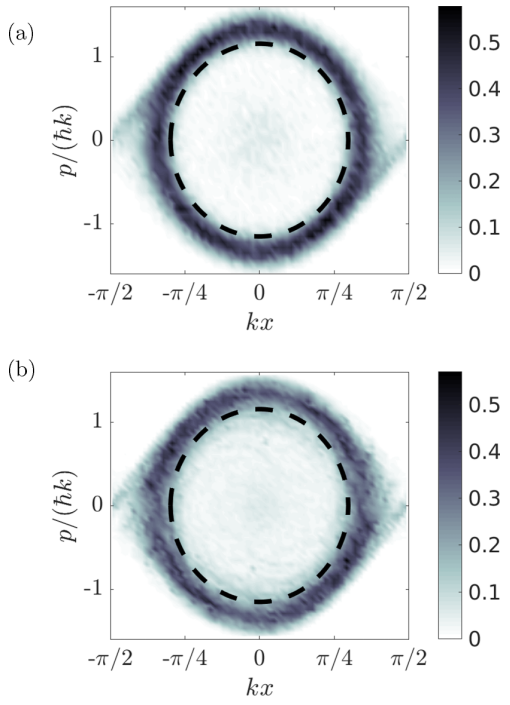


FIG. 11. Phase space histogram of the asymptotic dynamics of $N = 1000$ particles, the $x$ axis is in unit of $1/k$ and the trajectories are reported modulus the wavelength; the $p$ axis is in units of $\hbar k$. The parameters are the same as in Fig. 7(b), the time is of the order of $t \approx 50\omega_R^{-1}$. Subplot (a) reports 100 trajectories calculated using stochastic differential equations [30] simulating the dynamics of Eqs. (10), (11), and (17). Subplot (b) reports the corresponding mean-field simulations of Eqs. (24), (25), and (27). The black dashed line indicates the trajectory at energy $E_0$, Eq. (40).

The equality holds at the positions $x_0$, where the force changes sign. Hence, at the positions $x$ where $\cos^2(kx) < \cos^2(kx_0)$ the friction force is negative. Remarkably, these positions are close to the maxima of the mean-field potential.

Figure 11(a) displays the trajectories in phase space at steady state obtained by integrating the semiclassical equations, while subplot (b) shows the corresponding prediction of the mean-field model. Comparison between subplots (a) and (b) shows that the resulting trajectories form rings centered at $p = 0$ and at the points $x = n\pi$ with $n$ denoting any integer number. The rings are connected and the trajectories are indeed close to the separatrix. The separatrix represents the separation of the trajectories where the atoms are bound at the mean-field potential minima from the trajectories where the atoms are unbound. The dashed line indicates in particular the trajectory where the kinetic energy vanishes at the roots $x_0$ (namely, where the nonconservative force changes sign). Its energy is given by

$$E_0 = -\frac{\hbar w}{4} \ln[1 + 2|\xi(x_0)|^2]. \tag{40}$$

A careful comparison between subplots (a) and (b) shows that cavity shot noise [included in the simulation of (a)] tends to suppress the trajectories with energy below $E_0$. Figures 12(a) and 12(b) report the corresponding momentum and position

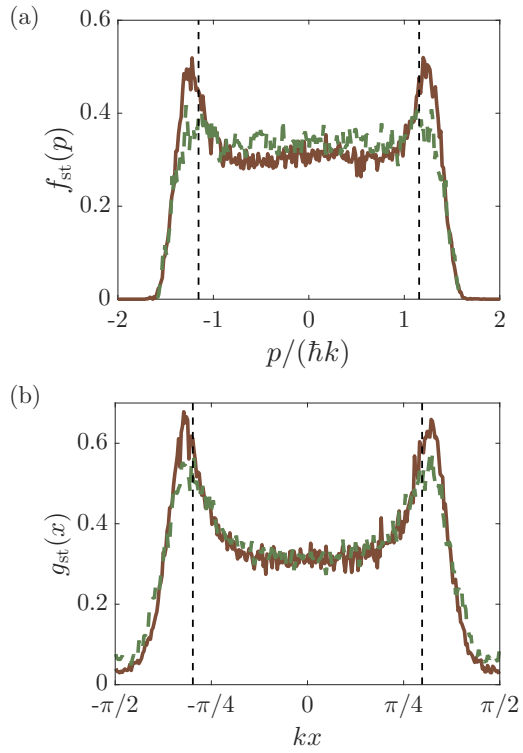


FIG. 12. (a) Momentum distribution $f_{st}(p)$ as a function of $p$ (in units of $\hbar k$) and (b) position distribution $g_{st}(x)$ as a function of $x$ (in units of $1/k$ and modulus the wavelength) corresponding to the distribution in Fig. 11. The brown solid line shows the prediction of the semiclassical simulation [corresponding to Fig. 11(a)]; the green dashed line shows the prediction of the mean-field model [Fig. 11(b)].

distributions, respectively. The momentum distribution, Fig. 12(a), is almost flat over the interval $[-p_0, p_0]$, such that $p_0^2 \sim 2mE_0$ (these points are indicated by the vertical dashed lines). The semiclassical simulations predict at these specific points two peaks, which are otherwise absent in the mean-field prediction. Instead, mean field and semiclassical simulations deliver very similar position distributions, as shown in Fig. 12(b). Here the two peaks of the distribution are located about the positions $x_0$ where the nonconservative force vanishes.

### E. Asymptotic temperature

We now estimate the asymptotic temperature by means of the fluctuation-dissipation theorem. The validity of the theorem is limited, since the stationary momentum distribution is not thermal, but allows us to gain insight into the dependence of the momentum distribution on the physical parameters. In what follows we extract the friction coefficient $\gamma$ from the force in Eq. (38):

$$\gamma(x) = 8\omega_R \frac{|\xi(x)|^2 \tan^2(kx)}{[1+2|\xi(x)|^2]^3} \frac{\Delta}{\kappa/2} \mathcal{F}_\Delta[|\xi(x)|^2]. \tag{41}$$

The calculations for the diffusion coefficients include spin noise due to the incoherent pump; their derivation is involved and reported in Appendix E. The resulting diffusion coefficient $D(x)$ is given in Eq. (E5). The final width of the momentum distribution is found after integrating $D(x)$ and $\gamma(x)$ over the asymptotic atomic spatial density distribution, which for convenience we assume to be uniform. This is a strong assumption since the spatial distribution that we observe in the actual simulations is not uniform and a more general treatment is required [32]. Denoting by $\bar{D}$ and $\bar{\gamma}$ the corresponding average values, we obtain

$$\langle p^2 \rangle_\infty = \frac{\bar{D}}{\bar{\gamma}}, \tag{42}$$

where $\langle p^2 \rangle_\infty = \lim_{t\to\infty} \langle p^2(t) \rangle$. Figure 13(a) displays the ratio of Eq. (42) as a function of the pump rate $w$ and for $\Delta = \kappa/2$. The minimal width is reached at a value between $w = N\Gamma_C/10$ and $w = N\Gamma_C/2$. For $w = N\Gamma_C/2$, in particular,

$$\frac{\langle p^2 \rangle_\infty}{2m} = \frac{\hbar w}{8} = \frac{\hbar N \Gamma_C}{16}.$$

Figure 13(b) shows the value of the pump rate which minimizes the momentum width as a function of $\Delta$. The corresponding temperature is shown as a function of $\Delta$ in subplot (c) and is minimized at $\Delta \approx \kappa/2$. The results suggest that lower temperatures can be reached by decreasing $N\Gamma_C$ (as long as this value is larger than the recoil frequency, consistently with the semiclassical treatment here applied).

### F. Discussion

The setup we analyze in this work is the same as the one discussed in Ref. [23]; nevertheless the studies in those papers focus on different parameter regimes, which lead to substantially different dynamics. These works predict lasing as well as spatial localization of the atoms in steady state when the atoms are incoherently pumped from the side. The model of Ref. [23], in particular, focuses on the dynamics of an atomic ensemble. It includes spontaneous emission and assumes that the rate of the incoherent pump is the largest parameter of the dynamics. With this choice population inversion is achieved.

A key point is that the faster time scale of the dynamics in Refs. [21–23] is determined by the pump rate and spontaneous decay. For this reason the regime is reached where the atomic internal degrees of freedom follow adiabatically the coupled dynamics of the external and of the resonator degrees of freedom. This is warranted when the atoms are localized in the antinodes of the cavity standing wave.

In Ref. [23] it is assumed that $N^2\langle \hat{X}^\dagger \hat{X} \rangle = \langle \sum_{i,j} \hat{\sigma}_i^\dagger \hat{\sigma}_j \cos(kx_i)\cos(kx_j) \rangle$ can be approximated by $\langle \sum_i \hat{\sigma}_i^\dagger \hat{\sigma}_i \cos^2(kx_i) \rangle$ discarding terms such as $\langle \hat{\sigma}_j^\dagger \cos(kx_j) \hat{\sigma}_i \cos(kx_i) \rangle$ for $i \neq j$. This is reasonable in the large repumping rate regime where synchronization between the dipoles of different atoms does not develop. This assumption leads to the scaling of the intracavity photon number with the number of atoms in the excited state and thus essentially with $N$ (see Appendix F for further details).

In contrast, here we consider the regime in which the cavity decay $\kappa$ sets the fastest time scale. Moreover, we choose the values of the pump rate for which synchronization is expected. As a result, the dynamics we predict is intrinsically due to collective effects, since it is dominated by mean-field correlations $\langle \hat{X}^\dagger \hat{X} \rangle \approx \langle \hat{X}^\dagger \rangle \langle \hat{X} \rangle$, thus they are prevailingly

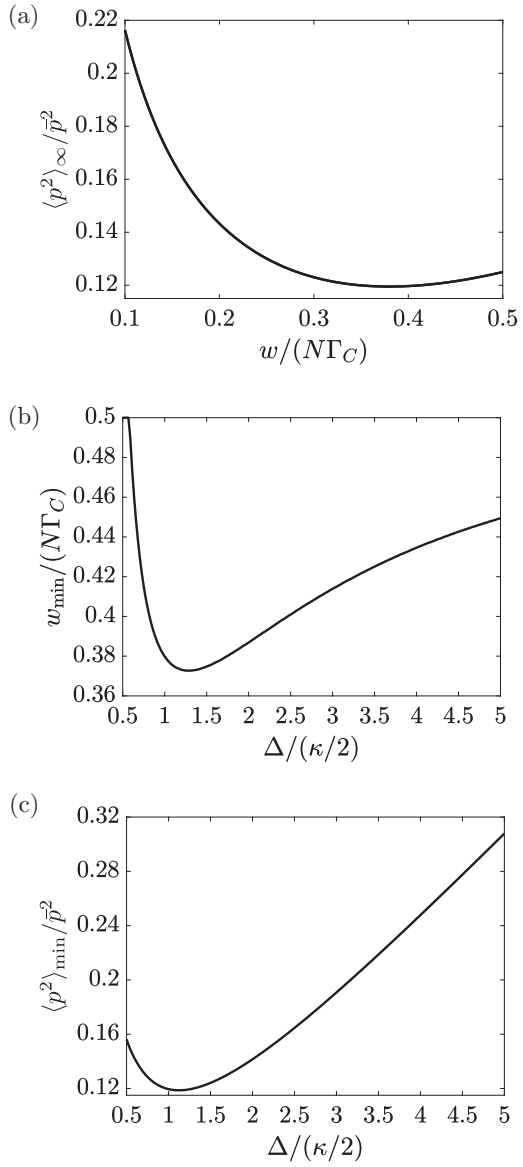


FIG. 13. (a) Stationary momentum width $\langle p^2\rangle_\infty$ [in units of $\bar{p}^2 = (\hbar k)^2 N\Gamma_C/(2\omega_R)$] as a function of $w$ (in units of $N\Gamma_C$) and for $\Delta = \kappa/2$. Subplot (b) shows the value of the pumping strength $w_{\min}$ (in units of $N\Gamma_C$) that minimizes the temperature for each value of the detuning $\Delta$ (in units of $\kappa/2$). Subplot (c) reports the corresponding value of the minimum width $\langle p^2\rangle_{\min}$ (in units of $\bar{p}^2$) as a function of $\Delta$ (in units of $\kappa/2$).

described by correlations of each dipole with all others [the corresponding terms are $N(N-1)$]. The field, in turn, scales with the synchronization order parameter $\hat{X}$, and thus the maximal intracavity photon number scales with $N^2$. In the setup of Refs. [21–23] a lasing phase is described which can be identified with a large intracavity photon occupation. In contrast, our parameter choice lies in the superradiance regime where the cavity state is near vacuum. Explicitly, the ratio between the photon number $\langle \hat{a}^\dagger \hat{a}\rangle$ and the atom number $N$, i.e., $N\Gamma_C\langle \hat{X}^\dagger \hat{X}\rangle/\kappa$, is much smaller than unity. For a more detailed study of the similarities and differences between superradiance and lasing we refer to Ref. [33]. In this sense the regime studied in Refs. [21–23] is complementary to the regime analyzed in this paper.

Finally, both models, the one of Ref. [23] and our model, predict stationary momentum distributions whose width is not determined by the width of the resonator. In our model, in particular, the lower bound is determined by the collective line width $N\Gamma_C$ and is ultimately bound by the recoil energy in order to keep the treatment consistent with the semiclassical approximation.

## IV. CONCLUSIONS

In this manuscript we have analyzed the semiclassical dynamics of the atomic external degrees of freedom in the parameter regime where the dipoles synchronize. We have shown that the large friction forces predicted in Ref. [25] are accompanied by the onset of an antiferromagnetic-like order, where internal and external degrees of freedom become correlated.

Minimal temperatures are found when the parameters are chosen so that the pump rate is in the synchronization regime, $w = N\Gamma_C/4$. In this regime the incoherent pump rate indeed determines the asymptotic width of the momentum distribution. Our results suggest the possibility that subrecoil temperature could be achieved by reducing $N\Gamma_C$, as long as this value is larger than the rate of spontaneous decay. Testing this conjecture requires a full quantum mechanical treatment of the dynamics in order to explore the ultimate limits. This is not straightforward due to the many-body character of the laser-cooling system presented here.

## ACKNOWLEDGMENTS

The authors acknowledge discussions with Helmut Ritsch and John Cooper. This work was supported by the German Research Foundation (DACH "Quantum crystals of matter and light" and the Priority Programme 1929), by the German Ministry of Research and Education (BMBF, "Qu.com"), and by the DARPA ATN program through Grant No. W911NF-16-1-0576 through ARO. The views and conclusions contained in this document are those of the authors and should not be interpreted as representing the official policies, either expressed or implied, of the U.S. Government. The U.S. Government is authorized to reproduce and distribute reprints for Government purposes notwithstanding any copyright notation herein.

## APPENDIX A: ELIMINATION OF THE CAVITY FIELD

The formal solution of the Heisenberg-Langevin equation (6) reads

$$\hat{a}(t) = e^{-(i\Delta+\kappa/2)t}\hat{a}(0) - i\frac{g}{2}\int_0^t d\tau e^{-(i\Delta+\kappa/2)(t-\tau)} \times \sum_{j=1}^{N}\cos[k\hat{x}_j(\tau)]\hat{\sigma}_j(\tau) + \sqrt{\kappa}\int_0^t d\tau e^{-(i\Delta+\kappa/2)(t-\tau)}\hat{a}_{\rm in}(\tau), \quad \text{(A1)}$$

with $\hat{a}(0)$ the operator at time $t = 0$. To eliminate the cavity field we have to substitute the operator $\hat{a}(t)$ and $\hat{a}^\dagger(t)$ in the Heisenberg-Langevin equations for the atomic degrees of freedom [Eqs. (3), (4), and (5)] with an averaged field

$$\bar{\hat{a}}(t) = \frac{1}{\Delta t}\int_t^{t+\Delta t} d\tau \hat{a}(\tau),$$

where we average over the time interval $\Delta t$. If we now assume that $T_C \ll \Delta t \ll T_e, T_i$ we may assume that $\bar{\hat{a}}(t)$ is stationary and thus

$$0 \approx \frac{d}{dt}\bar{\hat{a}}(t) = \frac{\hat{a}(t+\Delta t) - \hat{a}(t)}{\Delta t}. \tag{A2}$$

Equation (A2) together with Eq. (A1) can be cast into the form

$$\hat{a}(t) \approx \hat{A}(t) + \sqrt{\kappa}\int_t^{t+\Delta t} d\tau e^{-(i\Delta+\kappa/2)(t+\Delta t-\tau)}\hat{a}_{\rm in}(\tau)$$

with

$$\hat{A}(t) = -i\frac{Ng}{2}\int_t^{t+\Delta t} d\tau e^{-(i\Delta+\kappa/2)(t+\Delta t-\tau)}\hat{X}(\tau).$$

Here we used the definition of the synchronization order parameter $\hat{X}$ in Eq. (8) and that the time step $\Delta t$ fulfills $T_C \ll \Delta t$. With the substitution $u = t + \Delta t - \tau$ and renaming $u$ with $\tau$ again we get

$$\hat{A}(t) \approx -i\frac{Ng}{2}\int_0^{\infty} d\tau e^{-(i\Delta+\kappa/2)\tau}\hat{X}(t+\Delta t-\tau),$$

where the upper integration limit can be set to infinity because of $e^{-(i\Delta+\kappa/2)\Delta t} \approx 0$. By using a Taylor expansion we can rewrite $\hat{A}$ as

$$\hat{A}(t) = -i\frac{Ng}{2}\sum_{k=0}^{\infty}\left.\frac{d^k\hat{X}(u)}{du^k}\right|_{(u=t+\Delta t)}\frac{(-1)^k}{(i\Delta+\kappa/2)^{k+1}}.$$

If we now use that $\Delta t \ll T_e, T_i$ and $T_C \ll T_e$ we can neglect all summands corresponding to $k \geqslant 2$. The $k = 0$ term is the adiabatic cavity component whereby the $k = 1$ term is a retardation effect.

Under the discussed assumption the equation for the averaged cavity field annihilation operator reads

$$\bar{\hat{a}}(t) \approx \frac{-i\frac{Ng}{2}\langle\hat{X}\rangle_{\Delta t}}{i\Delta+\kappa/2} - \frac{-i\frac{Ng}{2}\left\langle\frac{d}{dt}\hat{X}\right\rangle_{\Delta t}}{(i\Delta+\kappa/2)^2} + \hat{\mathcal{F}}(t). \tag{A3}$$

We have introduced an effective Gaussian noise defined on the time scale of the atomic dynamics, which reads

$$\hat{\mathcal{F}}(t) = \sqrt{\kappa\Big/\left[\left(\frac{\kappa}{2}\right)^2 + \Delta^2\right]}\bar{\hat{a}}_{\rm in}(t), \tag{A4}$$

with

$$\bar{\hat{a}}_{\rm in}(t) = \frac{1}{\Delta t}\int_t^{t+\Delta t} d\tau\, \hat{a}_{\rm in}(\tau).$$

The time derivative of $\hat{X}$ in Eq. (A3) contains the nonadiabatic corrections to the cavity field, one can explicitly evaluate its form:

$$\frac{d}{dt}\hat{X} = \frac{1}{N}\sum_{j=1}^{N}\cos(k\hat{x}_j)\frac{d}{dt}\hat{\sigma}_j + \frac{1}{N}\sum_{j=1}^{N}\frac{d}{dt}[\cos(k\hat{x}_j)]\hat{\sigma}_j.$$

## APPENDIX B: NUMERICAL SIMULATIONS OF THE SEMICLASSICAL EQUATIONS

In order to perform the integration of Eqs. (10) and (11) we perform a second-order cumulant expansion and simulate the matrix $(\langle\hat{\sigma}_j^\dagger\hat{\sigma}_l\rangle)_{1\leqslant j,l\leqslant N}$ with

$$\frac{d}{dt}\langle\hat{\sigma}_j^\dagger\hat{\sigma}_j\rangle = w(1-\langle\hat{\sigma}_j^\dagger\hat{\sigma}_j\rangle) + N\Gamma_C{\rm Im}(\alpha\langle\hat{X}^\dagger\hat{\sigma}_j\rangle)\cos(kx_j), \tag{B1}$$

and for $l \neq j$

$$\begin{aligned}\frac{d}{dt}\langle\hat{\sigma}_j^\dagger\hat{\sigma}_l\rangle \approx &-\{w + \Gamma_C(i\alpha)\cos^2(kx_j)\langle\hat{\sigma}_j^\dagger\hat{\sigma}_j\rangle \\ &+ \Gamma_C(i\alpha)^*\cos^2(kx_l)\langle\hat{\sigma}_l^\dagger\hat{\sigma}_l\rangle\}\langle\hat{\sigma}_j^\dagger\hat{\sigma}_l\rangle \\ &+ N\frac{\Gamma_C}{2}(i\alpha)\cos(kx_j)(2\langle\hat{\sigma}_j^\dagger\hat{\sigma}_j\rangle - 1)\langle\hat{X}^\dagger\hat{\sigma}_l\rangle \\ &+ N\frac{\Gamma_C}{2}(i\alpha)^*\cos(kx_l)(2\langle\hat{\sigma}_l^\dagger\hat{\sigma}_l\rangle - 1)\langle\hat{\sigma}_j^\dagger\hat{X}\rangle.\end{aligned} \tag{B2}$$

The simulations are performed with $N = 100$ particles, the data correspond to the average taken over 1000 trajectories. The initial state is a thermal distribution at a fixed temperature $T$ that is spatially homogeneous, with all atoms are prepared in the excited state:

$$\hat{\rho}_0 = C\Pi_{j=1}^N \exp\left(-\beta\frac{p_j^2}{2m}\right)\otimes_{j=1}^N |e\rangle_j\langle e|. \tag{B3}$$

Here $C$ is a normalization constant and $\beta = (k_{\rm B}T)^{-1}$ with the Boltzmann constant denoted by $k_{\rm B}$.

## APPENDIX C: ADIABATIC ELIMINATION OF THE INTERNAL DEGREES OF FREEDOM IN THE MEAN-FIELD MODEL

In order to eliminate the internal degrees of freedom we observe that for both Eqs. (24) and (25), the second summands are invariant under the transformation $s_j \to \tilde{s}_j = s_j e^{-i\omega_0 t}$. Performing this transformation Eqs. (24) and (25) take the form

$$\frac{ds_j}{dt} = \left(i\omega_0 - \frac{w}{2}\right)s_j - i\frac{N\Gamma_C}{2}\alpha^* X\cos(kx_j)z_j, \tag{C1}$$

$$\frac{dz_j}{dt} = w(1-z_j) + 2N\Gamma_C{\rm Im}\{\alpha X^* s_j\}\cos(kx_j). \tag{C2}$$

We determine the stationary state by finding $\omega_0$ self-consistently. For the stationary values $s_j^{(0)}$ and $z_j^{(0)}$ of Eqs. (C1) and (C2), we find

$$s_j^{(0)} = \frac{N\Gamma_C\alpha^*}{2\omega_0 + iw}X\cos(kx_j)z_j^{(0)}.$$

We apply this result to determine the synchronization order parameter by using the expression

$$X = \sum_{j=1}^N s_j^{(0)}\cos(kx_j) = \frac{N\Gamma_C\alpha^*}{2\omega_0+iw}X\sum_{j=1}^N\cos^2(kx_j)z_j^{(0)}.$$

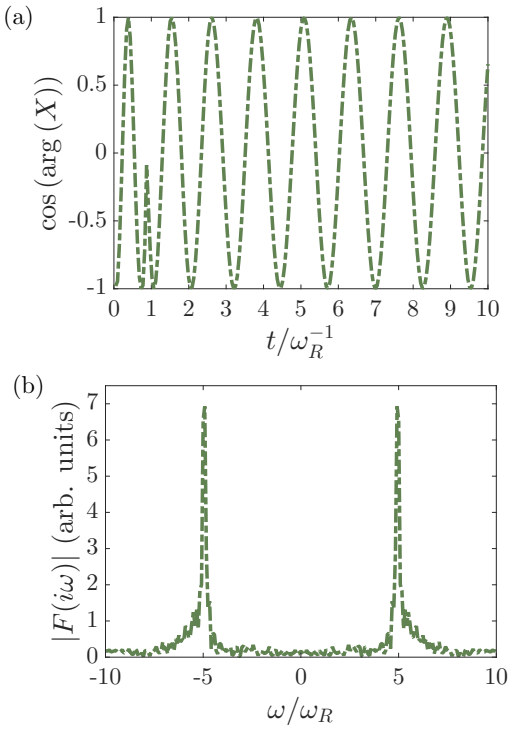


FIG. 14. (a) Dynamics of cos(arg(X)) as a function of time (in units of $\omega_R^{-1}$).The time evolution of the order parameter $X$ has been determined using the mean-field model for the same parameters as in Fig. 8(b). Subplot (b) shows the Laplace transform $F(i\omega) = \int_0^\infty dt e^{i\omega t} \cos\{\arg[X(t)]\}$ as a function of the frequency (in units of $\omega_R$). Two well-defined sidebands are visible at frequency $\omega \approx \pm 5\omega_R = \pm w/2$.

The latter can be recast in the form

$$\frac{N\Gamma_C \alpha^*}{2\omega_0 + iw} \sum_{j=1}^{N} \cos^2(kx_j) z_j^{(0)} = 1. \tag{C3}$$

This expression leads to the condition $N\Gamma_C\alpha^*/(2\omega_0 + iw) \in \mathbb{R}$, which is valid providing that

$$\omega_0 = \frac{w\Delta}{\kappa}. \tag{C4}$$

We numerically checked this result by calculating cos(arg(X)) using mean-field simulations, see Fig. 14(a). It was observed that $X$ oscillates with a well defined frequency, as visible in the Laplace transform of the signal; see Fig. 14(b). For the considered parameters $w/2 \approx 5\omega_R$. With this result for $\omega_0$ it is possible to obtain the stationary states $s_j^{(0)}$ and $z_j^{(0)}$ in Eqs. (29) and (30), respectively.

## APPENDIX D: CALCULATION OF THE FRICTION FORCE DUE TO THE COUPLING WITH THE SPINS

To calculate retardation effects in the elimination of the spins we replace $d/dt \to \partial/\partial t + p/m\partial/\partial x$ and identify the stationary state with

$$s = s^{(0)} + \frac{kp}{mw} s^{(1)}, \quad z = z^{(0)} + \frac{kp}{mw} z^{(1)}.$$

We do not use the index $j$, instead we employ $x$ and $p$ since the whole approach is valid for all particles when we work in the limit $N \to \infty$. If we now use the equations for $s^{(0)}$ and $z^{(0)}$ in Eqs. (29) and (30), this leads to the following equations for $s^{(1)}$ and $z^{(1)}$:

$$\frac{\partial s^{(0)}}{\partial x} = ik\frac{1}{2}\alpha^* s^{(1)} - ik\frac{1}{2}\frac{N\Gamma_C}{w}\alpha^* X \cos(kx) z^{(1)},$$
$$\frac{\partial z^{(0)}}{\partial x} = -kz^{(1)} + 2k\mathrm{Im}\left(\frac{N\Gamma_C}{w}\alpha X^* s^{(1)}\right)\cos(kx).$$

The solutions are

$$s^{(1)} = \xi(x) z^{(1)} + 2\frac{1}{i\alpha^*}\tan(kx)\xi(x)\frac{2|\xi(x)|^2 - 1}{[1 + 2|\xi(x)|^2]^2},$$
$$z^{(1)} = -\tan(kx)\frac{4|\xi(x)|^2}{[1 + 2|\xi(x)|^2]^3} + 4\frac{1 - \left(\frac{\Delta}{\kappa/2}\right)^2}{1 + \left(\frac{\Delta}{\kappa/2}\right)^2}\tan(kx)|\xi(x)|^2\frac{2|\xi(x)|^2 - 1}{[1 + 2|\xi(x)|^2]^3}.$$

## APPENDIX E: CALCULATION OF THE DIFFUSION COEFFICIENT

To calculate the diffusion coefficient we use [34]

$$2D = \int_0^\infty d\tau \left[\frac{1}{2}\langle F(0)F(\tau) + F(\tau)F(0)\rangle_{\hat{\rho}_{st}} - \langle F(0)\rangle_{\hat{\rho}_{st}}\langle F(\tau)\rangle_{\hat{\rho}_{st}}\right], \tag{E1}$$

where the force

$$F(\tau) = \frac{\hbar k}{2}\sin(kx) w\xi^* \hat{\sigma}(\tau) + \mathrm{H.c.}$$

is obtained after adiabatic elimination of the cavity [see Eq. (18)]. The expectation values are calculated with the stationary density matrix $\hat{\rho}_{\mathrm{st}}$ and $\langle . \rangle_{\hat{\rho}_{st}} = \mathrm{Tr}_i(. \hat{\rho}_{\mathrm{st}})$ where $\mathrm{Tr}_i$ is the trace over the internal degrees of freedom. As we can see in Eqs. (10) and (11) the motion of $\hat{\sigma}$, $\hat{\sigma}^\dagger$, and $\hat{\sigma}^z$ is coupled. We define the vector

$$v = \begin{pmatrix} \hat{\sigma} \\ \hat{\sigma}^\dagger \\ \hat{\sigma}^z \end{pmatrix}$$

and write the equations of motion for the spins as

$$\frac{dv}{dt} = \Omega v + b + \mathcal{S}, \tag{E2}$$

where the matrix $\Omega$ is defined as

$$\Omega = \begin{pmatrix} i\frac{w}{2}\alpha^* & 0 & -i\frac{w}{2}\alpha^*\xi \\ 0 & -i\frac{w}{2}\alpha & i\frac{w}{2}\alpha\xi^* \\ -iw\alpha\xi^* & iw\alpha^*\xi & -w \end{pmatrix},$$

and the vector $b$ reads

$$b = \begin{pmatrix} 0 \\ 0 \\ w \end{pmatrix}.$$

The noise $\mathcal{S}(\tau) = (S^-(\tau)\ S^+(\tau)\ S^z(\tau))^T$ is defined by

$$\langle \mathcal{S}(\tau)\mathcal{S}^T(\tau')\rangle = \begin{pmatrix} 0 & 0 & 0 \\ 1 & 0 & -2\langle\hat{\sigma}^\dagger(\tau')\rangle_{\hat{\rho}_{st}} \\ -2\langle\hat{\sigma}(\tau')\rangle_{\hat{\rho}_{st}} & 0 & 2[1-\langle\hat{\sigma}^z(\tau')\rangle_{\hat{\rho}_{st}}] \end{pmatrix} \times \delta(\tau-\tau').$$

The formal solution of Eq. (E2) is

$$v(\tau) = e^{\Omega\tau}v + (e^{\Omega\tau}-1)\Omega^{-1}b + \int_0^\tau d\tau' e^{\Omega(\tau-\tau')}\mathcal{S}(\tau'). \tag{E3}$$

If we apply the limit $\tau \to \infty$ for Eq. (E3) we get the stationary states for $\hat{\sigma}$, $\hat{\sigma}^\dagger$, and $\hat{\sigma}^z$ which define the stationary density matrix

$$\hat{\rho}_{\rm st} = \begin{pmatrix} \frac{1+|\xi|^2}{1+2|\xi|^2} & \frac{\xi^*}{1+2|\xi|^2} \\ \frac{\xi}{1+2|\xi|^2} & \frac{|\xi|^2}{1+2|\xi|^2} \end{pmatrix}. \tag{E4}$$

If we now use the general solution [Eq. (E3)] together with the density operator in Eq. (E4) to calculate the diffusion coefficient [Eq. (E1)] we obtain

$$2D = \frac{(\hbar k)^2}{2} w\tan^2(kx)|\xi|^2 \left\{ 1 + \frac{2\left(\frac{\Delta_c}{\kappa/2}\right)^2|\xi|^2}{1+2|\xi|^2} - 2\frac{\left(\frac{\Delta_c}{\kappa/2}\right)^2}{1+\left(\frac{\Delta_c}{\kappa/2}\right)^2} \times \frac{|\xi|^2}{[1+2|\xi|^2]^2} \frac{5+\left(\frac{\Delta_c}{\kappa/2}\right)^2 + 4\left[\left(\frac{\Delta_c}{\kappa/2}\right)^2+1\right]|\xi|^2}{1+2|\xi|^2} \right\}. \tag{E5}$$

## APPENDIX F: DETAILED COMPARISON WITH THE RESULTS OF REF. [23]

An interesting example highlighting the complementarity of the two approaches is found by comparing the expectation value of population inversion. In the adiabatic limit (in the thermodynamic limit $Ng^2 = \text{const}$) the population inversion we calculate reads

$$\langle z\rangle \approx \left\langle \frac{1}{1+2|\xi(x)|^2} \right\rangle,$$

which implies that there is always population inversion $\langle z\rangle \geqslant 0$. Note that if all particles are in the excited state then $\langle z\rangle = 1$, thus $X = 0$ and the atoms are not synchronized. Hence synchronization requires a nonvanishing expectation value of the dipole. This is not the case for the parameters of Ref. [23], where the expectation value of the dipole vanishes at steady state.

We now show that also in Ref. [23] all particles are in the excited state if one takes the equations of motion there defined, neglects spontaneous emission and performs the limit $N \to \infty$ with $Ng^2 = \text{constant}$, taking $\kappa$ as the largest parameter. For this purpose we take the formula for the population inversion $z_N$ in Eq. (25) of Ref. [23], and report it using our notations giving

$$z_N = \frac{\kappa w + N\Gamma w - w\sqrt{[\kappa+N\Gamma]^2 - 4\kappa N\Gamma}}{2N\Gamma w}. \tag{F1}$$

We already neglected spontaneous emission $\gamma = 0$ and applied the limit $g^2 \propto N^{-1}$ with $N \to \infty$. In Eq. (F1) the frequency $\Gamma$ is the emission rate defined as $\Gamma = wg^2/(w^2+\Delta^2)$. From this expression one can verify that when $\kappa$ is chosen to be the largest frequency then $z_N = 1$.

[1] D. J. Wineland and W. M. Itano, Phys. Rev. A **20**, 1521 (1979).
[2] S. Chu, Rev. Mod. Phys. **70**, 685 (1998); C. N. Cohen-Tannoudji, *ibid.* **70**, 707 (1998); W. D. Phillips, *ibid.* **70**, 721 (1998).
[3] C. E. Wieman, D. E. Pritchard, and D. J. Wineland, Rev. Mod. Phys. **71**, S253 (1999).
[4] H. J. Metcalf and P. van der Straten, *Laser Cooling and Trapping* (Springer, New York, 1999).
[5] M. Aspelmeyer, T. J. Kippenberg, and F. Marquardt, Rev. Mod. Phys. **86**, 1391 (2014).
[6] A. Rayner, N. R. Heckenberg, and H. Rubinsztein-Dunlop, J. Opt. Soc. Am. B **20**, 1037 (2003).
[7] J. Eschner, G. Morigi, F. Schmidt-Kaler, and R. Blatt, J. Opt. Soc. Am. B **20**, 1003 (2003).
[8] T. Walker, D. Sesko, and C. Wieman, Phys. Rev. Lett. **64**, 408 (1990).
[9] S. Marksteiner, K. Ellinger, and P. Zoller, Phys. Rev. A **53**, 3409 (1996).
[10] Y. Castin, J. I. Cirac, and M. Lewenstein, Phys. Rev. Lett. **80**, 5305 (1998).
[11] J. I. Cirac, M. Lewenstein, and P. Zoller, Europhys. Lett. **35**, 647 (1996).
[12] S. Stellmer, B. Pasquiou, R. Grimm, and F. Schreck, Phys. Rev. Lett. **110**, 263003 (2013).
[13] P. Horak, G. Hechenblaikner, K. M. Gheri, H. Stecher, and H. Ritsch, Phys. Rev. Lett. **79**, 4974 (1997).
[14] V. Vuletic and S. Chu, Phys. Rev. Lett. **84**, 3787 (2000).
[15] H. Ritsch, P. Domokos, F. Brennecke, and T. Esslinger, Rev. Mod. Phys. **85**, 553 (2013).
[16] M. Hosseini, Y. Duan, K. M. Beck, Y.-T. Chen, and V. Vuletić, Phys. Rev. Lett. **118**, 183601 (2017).
[17] P. Domokos and H. Ritsch, Phys. Rev. Lett. **89**, 253003 (2002).
[18] J. K. Asbóth, P. Domokos, H. Ritsch, and A. Vukics, Phys. Rev. A **72**, 053417 (2005).
[19] S. Schütz and G. Morigi, Phys. Rev. Lett. **113**, 203002 (2014).
[20] S. Schütz, S. B. Jäger, and G. Morigi, Phys. Rev. A **92**, 063808 (2015).
[21] T. Salzburger and H. Ritsch, Phys. Rev. Lett. **93**, 063002 (2004).
[22] T. Salzburger, P. Domokos, and H. Ritsch, Phys. Rev. A **72**, 033805 (2005).
[23] T. Salzburger and H. Ritsch, Phys. Rev. A **74**, 033806 (2006).
[24] J. G. Bohnet, Z. Chen, J. M. Weiner, D. Meiser, M. J. Holland, and J. K. Thompson, Nature (London) **484**, 78 (2012).
[25] M. Xu, S. B. Jäger, S. Schütz, J. Cooper, G. Morigi, and M. J. Holland, Phys. Rev. Lett. **116**, 153002 (2016).
[26] D. Meiser, J. Ye, D. R. Carlson, and M. J. Holland, Phys. Rev. Lett. **102**, 163601 (2009).

[27] D. Meiser and M. J. Holland, Phys. Rev. A **81**, 033847 (2010).
[28] C. W. Gardiner and M. J. Collett, Phys. Rev. A **31**, 3761 (1985).
[29] S. Stenholm, Rev. Mod. Phys. **58**, 699 (1986).
[30] For details on the implementation of the stochastic differential equations in a similar setup see S. Schütz, H. Habibian, and G. Morigi, Phys. Rev. A **88**, 033427 (2013).
[31] C. Cohen-Tannoudij, J. Dupont-Roc, and G. Grynberg, *Atom-Photon Interactions* (Wiley, Toronto, 1992).
[32] A. Vukics, P. Domokos, and H. Ritsch, J. Opt. B: Quantum Semiclassical Opt. **6**, 143 (2004).
[33] D. A. Tieri, M. Xu, D. Meiser, J. Cooper, and M. J. Holland, arXiv:1702.04830.
[34] G. Nienhuis, P. van der Straten, and S.-Q. Shang, Phys. Rev. A **44**, 462 (1991).

Section 3.4

# Summary

In this chapter we studied the interplay between external and internal degrees of freedom for an ensemble of atoms in determining the emission properties into the mode of an optical cavity. Our objective was to analyze how the mechanical effects of light affect the dynamics of steady-state superradiance.

We introduced, in section 3.1, the model of steady-state superradiance in the regime where the cavity degrees of freedom can be eliminated. We reviewed the effect of steady-state superradiance and discussed analogies with synchronization.

In section 3.2 we derived a mean-field model for steady-state superradiance where we include the optomechanical effects. We showed that quantum fluctuations due to the recoiling atoms can give rise to dynamical superradiant phases that can lead to a dephasing or a chaotic emission of the collective dipole [125].

After that, in section 3.3, we studied the dynamics of the atoms by means of a semi-classical model in the regime where cooling of the atomic motion emerges from the optomechanical coupling. We demonstrated that collective emission gives rise to a speed of the cooling process [131]. Furthermore we analyzed the relaxation dynamics and the stationary state of the atoms where we observed limit cycles [132].

# Concluding remarks

In this thesis we investigated the optomechanical dynamics of an atomic vapor coupled to an optical cavity. We identified the regime, where one could observe the emergence of spatio-temporal patterns and when these patterns are stable.

These dynamics emerge from atom-atom interactions mediated by cavity photons. These interactions are long-range and their strength can be tuned by changing the frequency and the intensity of the driving lasers. Such setups are ideal to study the out-of-equilibrium dynamics of long-range interacting systems [23, 28].

One direction might be to use adiabatic changes of the interaction strength to transfer kinetic energy into potential energy and therefore efficiently lower the particles' temperature. This is similar to a retrap-release method [137] that has recently been used to laser-cool particles to quantum degeneracy [138]. For the systems considered in this thesis, however, the trapping of the particles would be due to cooperative effects.

Moreover the cavity is intrinsically lossy and therefore dissipation plays a crucial role in the dynamics of the particles. The presence of dissipation might for example increase or decrease the relaxation time of the atoms and therefore give rise to dissipation-assisted metastable states. Features of such states have been found in Ref. [22, 25] by quenching the laser parameters. Their dynamics is though still unexplored.

Another direction is the study of new phases of matter by coupling the atoms to several modes [26, 27, 96, 139]. This might also be interesting for building a quantum annealer that is able to simulate almost arbitrary spin models [98].

Spin systems can also be implemented in an optical resonator where the emission of the cavity photon gives rise to a change of the internal state, e.g. by Raman scattering. This allows one to study spin textures, spinor self-ordering, spin-glasses, and quantum magnetism with long-range interactions [103–107, 140].

In the absence of motion the coherent dynamics of atomic spins in a cavity has also been studied for squeezing of the collective spin [72, 141–144] and metastability in presence of interactions [134]. This is in particular of interest for advances in frequency and time standards. Further studies should include the particles' motion since thermal and quantum fluctuations might limit these effects and can give rise to new superradiant dynamical phases [125].

Finally, a quantum model for the atomic variables should allow to study dynamical quantum phase transitions [145] and other out-of-equilibrium effects. Furthermore it can be used to describe dissipative effects, such as cooling, in the regime where quantum fluctuations are important.

# Chapter A

# Appendix

In appendix A.1 we provide additional information about the adiabatic elimination of the cavity field and the derivation of Eq. (1.3.13) and Eq. (3.1.3). We also present the decomposition of the momentum basis into momentum families that is used in subsection 3.2.2 for the numerical simulation of the mean-field master equation (3.2.1). This is shown in appendix A.2.

Section A.1

# ELIMINATION OF THE CAVITY-FIELD MODE

In this appendix we want to show a systematic method to eliminate the cavity degrees of freedom in the case where the decay rate $\kappa$ and the detuning $\Delta = \omega_c - \omega_a$ determine the fastest timescales in the dynamics governed by Eq. (1.3.12) and Eq. (3.1.1).

We first rewrite the dynamics of the density matrix $\hat{\rho}$ in Eq. (3.1.1) as

$$\frac{\partial \hat{\rho}}{\partial t} = \mathcal{L}_F \hat{\rho} + \mathcal{L}_A \hat{\rho} + \mathcal{L}_c \hat{\rho},$$

the three terms take the forms

$$\mathcal{L}_F \hat{\rho} = \frac{1}{i\hbar}\left[\hbar\Delta \hat{a}^\dagger \hat{a}, \hat{\rho}\right] + \kappa \mathcal{L}[\hat{a}]\hat{\rho}, \tag{A.1.1}$$

$$\mathcal{L}_A \hat{\rho} = \frac{1}{i\hbar}\left[\sum_{j=1}^{N} \frac{\hat{p}_j^2}{2m}, \hat{\rho}\right] + \sum_{j=1}^{N} w \mathcal{L}[\hat{\sigma}_j^\dagger]\hat{\rho}, \tag{A.1.2}$$

$$\mathcal{L}_c \hat{\rho} = \frac{1}{i\hbar}\left[\sum_{j=1}^{N} \hbar \frac{g}{2} \cos(k\hat{x}_j)(\hat{a}^\dagger \hat{\sigma}_j + \hat{\sigma}_j^\dagger \hat{a}), \hat{\rho}\right]. \tag{A.1.3}$$

The Lindbladian $\mathcal{L}_F$ describes dynamics of the cavity degrees of freedom while $\mathcal{L}_A$ describes the dynamics of the external and internal degrees of freedom of the atoms. The last term $\mathcal{L}_c$ is a coupling between cavity and atomic degrees of freedom.

We define the projector $\mathcal{P}\hat{\rho} = |\text{vac}\rangle\langle\text{vac}|\hat{\rho}|\text{vac}\rangle\langle\text{vac}|$ on the vacuum state of the cavity field $|\text{vac}\rangle$ with $\hat{a}|\text{vac}\rangle = 0$ and the projector $\mathcal{Q} = 1 - \mathcal{P}$ to its orthogonal space. We define further the matrices $\hat{v} = \mathcal{P}\hat{\rho}$ and $\hat{w} = \mathcal{Q}\hat{\rho}$. Applying now these projectors onto the master equation we obtain two coupled equations for $\hat{v}$ and $\hat{w}$ that can be written

$$\frac{\partial \hat{v}}{\partial t} = \mathcal{P}\mathcal{L}_F \hat{w} + \mathcal{P}\mathcal{L}_A \hat{v} + \mathcal{P}\mathcal{L}_c \hat{w}, \tag{A.1.4}$$

$$\frac{\partial \hat{w}}{\partial t} = \mathcal{Q}\mathcal{L}_F \hat{w} + \mathcal{Q}\mathcal{L}_A \hat{w} + \mathcal{Q}\mathcal{L}_c (\hat{v} + \hat{w}). \tag{A.1.5}$$

We used here that $\mathcal{L}_F \hat{v} = 0$ and that $\mathcal{L}_A$ commutes with the corresponding projectors. The elimination of the cavity degrees of freedom can be done using a formal integration of Eqs. (A.1.4) and (A.1.5) and including effects of $\mathcal{L}_A$ and $\mathcal{L}_c$ only up to second order. That means that $\kappa, \Delta_c$ are much larger then the incoherent pumping rate $w$ and the Doppler shift $k\Delta p/m$ where $\Delta p$ is the single particle momentum width. All frequency are taken in reference to $\kappa, \Delta$ and thus we use that $\mathcal{L}_F$ is of zeroth order

$$\mathcal{L}_F \hat{\rho} \sim \mathrm{O}(1).$$

Using $\epsilon$ as the small parameter we may conclude that $\mathcal{L}_A$ is of first order such that

$$\mathcal{L}_A \hat{\rho} \sim \mathrm{O}(\epsilon),$$

where $\epsilon \sim k\Delta p/m/\kappa, w/\kappa$ is very small. If we furthermore assume that the coupling between cavity and atomic degrees of freedom is weak we may write

$$\mathcal{L}_c\hat{\rho} \sim \mathrm{O}(\epsilon).$$

Here we used that $\epsilon \sim g\sqrt{\bar{n}}/\kappa$ where $\bar{n}$ denotes the mean intracavity photon number. Hence a large photon number would break this assumption. We derive now a master equation for $\hat{v}$ that is correct up to order in $\epsilon^2$.

We formally integrate Eq. (A.1.5) over the interval $[t_0, t]$ and obtain

$$\hat{w}(t) = e^{\mathcal{Q}(\mathcal{L}_F+\mathcal{L}_A+\mathcal{L}_c)\Delta t}\hat{w}(t_0) + \int_0^{\Delta t} d\tau\, e^{\mathcal{Q}(\mathcal{L}_F+\mathcal{L}_A+\mathcal{L}_c)\tau}\mathcal{Q}\mathcal{L}_c\hat{v}(t-\tau). \tag{A.1.6}$$

We assume now that the timestep $\Delta t$ is sufficienlty long such that the cavity degrees already relaxed but sufficiently short such that the particles did not evolve. This means that the following inequalities need to be fulfilled

$$\kappa^{-1}, |\Delta|^{-1} \ll \Delta t \ll (k\Delta p/m)^{-1}, w^{-1}, (g\sqrt{\bar{n}})^{-1}. \tag{A.1.7}$$

Insert Eq. (A.1.6) in Eq. (A.1.4) and using the inequalities in (A.1.7) we obtain

$$\frac{\partial\hat{v}}{\partial t} \approx \mathcal{P}\mathcal{L}_A\hat{v}(t) + \mathcal{P}(\mathcal{L}_c+\mathcal{L}_F)\int_0^{\infty} d\tau\, e^{\mathcal{Q}(\mathcal{L}_F+\mathcal{L}_A+\mathcal{L}_c)\tau}\mathcal{Q}\mathcal{L}_c\hat{v}(t-\tau). \tag{A.1.8}$$

We observe that the integration over $\tau$ includes terms where $\hat{v}$ is evaluated at points in the past $(t-\tau)$. Since we assume that $\Delta t$ is essentially large such that $\kappa\Delta t \gg 1$ but small enough that $\hat{v}(t-\tau) \approx \hat{v}(t)$ [1] for $\tau \in [0, \Delta t]$ we may write

$$\mathcal{P}(\mathcal{L}_c+\mathcal{L}_F)\int_0^{\infty} d\tau\, e^{\mathcal{Q}(\mathcal{L}_F+\mathcal{L}_A+\mathcal{L}_c)\tau}\mathcal{Q}\mathcal{L}_c\hat{v}(t-\tau) \approx \mathcal{P}(\mathcal{L}_c+\mathcal{L}_F)\int_0^{\infty} d\tau\, e^{\mathcal{Q}(\mathcal{L}_F+\mathcal{L}_c)\tau}\mathcal{Q}\mathcal{L}_c\hat{v}(t).$$

Using this relation and applying the trace over the cavity degrees of freedom where we define $\hat{\rho}_N = \mathrm{Tr}_{\mathrm{cav}}(\hat{v})$ in Eq. (A.1.8) leads to the effective master equation that describes the evolution of the reduced density matrix $\hat{\rho}_N$ for the particles degrees of freedom.

[1] This is possible since the evolution corresponding to $\mathcal{L}_A$ is already of order $\epsilon$ and therefore $\hat{v}$ evolves slowly. A correction corresponding to the first derivative in the expansion $\hat{v}(t-\tau) = \hat{v}(t) - \tau\frac{\partial\hat{v}(t)}{\partial t} + ...$ would correspond to a third order in $\epsilon$ term.

Section A.2

# Decomposition of the momentum basis

In this section we want to show how we can simulate the dynamics of a thermal gas, that occupies many momentum states, efficiently. Since $\cos(k\hat{x})$ in Eq. (3.2.2) couples only momentum states $|p\rangle$ and $|p \pm \hbar k\rangle$ we can conclude that the Projectors

$$\hat{1}_q = \sum_{n\in\mathbb{Z}} |q + n\hbar k\rangle\langle q + n\hbar k| \tag{A.2.1}$$

for $-0.5 < q \leq 0.5$ are conserved quantities of the evolution governed by Eq. (3.2.5). The operators in Eq. (A.2.1) are a partition of unity that fulfill $\hat{1} = \int_{-0.5}^{0.5} dq\, \hat{1}_q$, where $\hat{1}$ is the unity and $\hat{1}_q\hat{1}_{q'} = \delta_{q,q'}\hat{1}_q$. The projectors $\hat{1}_q$ can be used to define projectors on a subspace of matrices by

$$\mathcal{P}_q\hat{\rho} = \hat{1}_q\hat{\rho}\hat{1}_q. \tag{A.2.2}$$

Using these projectors we can rewrite Eq. (3.2.5) as

$$\frac{\partial\mathcal{P}_q\hat{\rho}_1}{\partial t} = \mathcal{P}_q\mathcal{L}_{\mathrm{mf}}[\hat{\rho}_1]\mathcal{P}_q\hat{\rho}_1 \tag{A.2.3}$$

for every $-0.5 < q \leq 0.5$. The latter equations for different values of $q$ are not completely decoupled since $\mathcal{L}_{\mathrm{mf}}[\hat{\rho}_1]$ depends of $\hat{\rho}_1$ and every $\mathcal{P}_q\hat{\rho}_1$ couples to the mean field

$$X = \int_{-0.5}^{0.5} dq X_q \tag{A.2.4}$$

with

$$X_q = \mathrm{Tr}(\hat{\sigma}\cos(k\hat{x})\mathcal{P}_q\hat{\rho}_1). \tag{A.2.5}$$

# Bibliography


[1] W. C. Saslaw, *The distribution of the galaxies: gravitational clustering in cosmology* (Cambridge University Press, 2000).

[2] S. Camazine, J.-L. Deneubourg, N. R. Franks, J. Sneyd, E. Bonabeau, and G. Theraula, *Self-organization in biological systems*, Vol. 7 (Princeton University Press, 2003).

[3] J. J. Hopfield, Proc. Natl. Acad. Sci. USA **79**, 2554 (1982).

[4] R. H. Dicke, Phys. Rev. **93**, 99 (1954).

[5] M. Gross and S. Haroche, Phys. Rep. **93**, 301 (1982).

[6] M. Bajcsy, S. Hofferberth, V. Balic, T. Peyronel, M. Hafezi, A. S. Zibrov, V. Vuletic, and M. D. Lukin, Phys. Rev. Lett. **102**, 203902 (2009).

[7] H. Kogelnik and T. Li, Appl. Opt. **5**, 1550 (1966).

[8] D. F. Walls and G. J. Milburn, *Quantum optics* (Springer Science & Business Media, 2007).

[9] P. Domokos and H. Ritsch, Phys. Rev. Lett. **89**, 253003 (2002).

[10] A. T. Black, H. W. Chan, and V. Vuletić, Phys. Rev. Lett. **91**, 203001 (2003).

[11] D. Nagy, G. Szirmai, and P. Domokos, Eur. Phys. J. D **48**, 127 (2008).

[12] K. Baumann, C. Guerlin, F. Brennecke, and T. Esslinger, Nature **464**, 1301 (2010), article.

[13] H. Ritsch, P. Domokos, F. Brennecke, and T. Esslinger, Rev. Mod. Phys. **85**, 553 (2013).

[14] R. Bonifacio, M. M. Cola, N. Piovella, and G. R. M. Robb, Europhys. Lett. **69**, 55 (2005).

[15] R. Bonifacio, L. De Salvo, L. M. Narducci, and E. J. D'Angelo, Phys. Rev. A **50**, 1716 (1994).

[16] D. Kruse, C. von Cube, C. Zimmermann, and P. W. Courteille, Phys. Rev. Lett. **91**, 183601 (2003).

[17] C. von Cube, S. Slama, D. Kruse, C. Zimmermann, P. W. Courteille, G. R. M. Robb, N. Piovella, and R. Bonifacio, Phys. Rev. Lett. **93**, 083601 (2004).

[18] Y. Kuramoto, in *International symposium on mathematical problems in theoretical physics* (Springer, 1975) pp. 420–422.

[19] J. A. Acebrón, L. L. Bonilla, C. J. Pérez Vicente, F. Ritort, and R. Spigler, Rev. Mod. Phys. **77**, 137 (2005).

[20] W. Niedenzu, T. Grießer, and H. Ritsch, Europhys. Lett. **96**, 43001 (2011).

[21] T. Grießer, W. Niedenzu, and H. Ritsch, New J. Phys. **14**, 053031 (2012).

[22] S. B. Jäger, S. Schütz, and G. Morigi, Phys. Rev. A **94**, 023807 (2016).

[23] A. Campa, T. Dauxois, and S. Ruffo, Phys. Rep. **480**, 57 (2009).

[24] S. Schütz and G. Morigi, Phys. Rev. Lett. **113**, 203002 (2014).

[25] S. Schütz, S. B. Jäger, and G. Morigi, Phys. Rev. Lett. **117**, 083001 (2016).

[26] T. Keller, S. B. Jäger, and G. Morigi, J. Stat. Mech. **6**, 064002 (2017).

[27] T. Keller, V. Torggler, S. B. Jäger, S. Schütz, H. Ritsch, and G. Morigi, New J. Phys. **20**, 025004 (2018).

[28] S. Gupta and S. Ruffo, Int. J. Mod. Phys. A **32**, 1741018 (2017).

[29] P. Horak, G. Hechenblaikner, K. M. Gheri, H. Stecher, and H. Ritsch, Phys. Rev. Lett. **79**, 4974 (1997).

[30] V. Vuletić and S. Chu, Phys. Rev. Lett. **84**, 3787 (2000).

[31] S. Schütz, S. B. Jäger, and G. Morigi, Phys. Rev. A **92**, 063808 (2015).

[32] D. Meiser, J. Ye, D. R. Carlson, and M. J. Holland, Phys. Rev. Lett. **102**, 163601 (2009).

[33] J. G. Bohnet, Z. Chen, J. M. Weiner, D. Meiser, M. J. Holland, and J. K. Thompson, Nature **484**, 78 (2012).

[34] T. Keller, S. B. Jäger, and G. Morigi, preprint arXiv:1702.07653 (2017).

[35] H. J. Metcalf and P. Van der Straten, *Laser cooling and trapping* (Springer Science & Business Media, 2012).

[36] H. B. G. Casimir and D. Polder, Phys. Rev. **73**, 360 (1948).

[37] G. L. Klimchitskaya, U. Mohideen, and V. M. Mostepanenko, Rev. Mod. Phys. **81**, 1827 (2009).

[38] C. Gardiner, P. Zoller, and P. Zoller, *Quantum noise: a handbook of Markovian and non-Markovian quantum stochastic methods with applications to quantum optics*, Vol. 56 (Springer Science & Business Media, 2004).

[39] H. Carmichael, *An open systems approach to quantum optics: lectures presented at the Université Libre de Bruxelles, October 28 to November 4, 1991*, Vol. 18 (Springer Science & Business Media, 2009).

[40] J. J. Sakurai, *Advanced quantum mechanics* (Pearson, 1967).

[41] R. J. Glauber, Phys. Rev. **131**, 2766 (1963).

[42] J. D. Jackson, *Classical Electrodynamics* (Wiley, New York, 1962).

[43] R. Grimm, M. Weidemüller, and Y. B. Ovchinnikov, Adv. At. Mol. Opt. Phys., **42**, 95 (2000).

[44] V. Letokhov and V. Minogin, Phys. Rep. **73**, 1 (1981).

[45] S. Stenholm, Rev. Mod. Phys. **58**, 699 (1986).

[46] Y. Castin, J. Dalibard, and C. Cohen-Tannoudji, in *Light Induced Kinetic Effects on Atoms, Ions and Molecules* (ETS Editrice, Pisa, 1991).

[47] C. Tsallis, J. Stat. Phys. **52**, 479 (1988).

[48] E. Lutz, Phys. Rev. A **67**, 051402 (2003).

[49] P. Douglas, S. Bergamini, and F. Renzoni, Phys. Rev. Lett. **96**, 110601 (2006).

[50] T. Hänsch and A. Schawlow, Opt. Commun. **13**, 68 (1975).

[51] D. J. Wineland and H. Dehmelt, Bull. Am. Phys. Soc. **20**, 639 (1975).

[52] D. J. Wineland, R. E. Drullinger, and F. L. Walls, Phys. Rev. Lett. **40**, 1639 (1978).

[53] J. Dalibard and C. Cohen-Tannoudji, J. Opt. Soc. Am. B **6**, 2023 (1989).

[54] C. N. Cohen-Tannoudji, Rev. Mod. Phys. **70**, 707 (1998).

[55] S. Chu, Rev. Mod. Phys. **70**, 685 (1998).

[56] W. D. Phillips, Rev. Mod. Phys. **70**, 721 (1998).

[57] P. Maunz, T. Puppe, I. Schuster, N. Syassen, P. W. H. Pinkse, and G. Rempe, Nature **428**, 50 (2004).

[58] F. Brennecke, T. Donner, S. Ritter, T. Bourdel, M. Köhl, and T. Esslinger, Nature **450**, 268 (2007).

[59] H. Gothe, D. Sholokhov, A. Breunig, M. Steinel, and J. Eschner, Phys. Rev. A **99**, 013415 (2019).

[60] H. Gothe, T. Valenzuela, M. Cristiani, and J. Eschner, Phys. Rev. A **99**, 013849 (2019).

[61] P. Domokos, P. Horak, and H. Ritsch, J. Phys. B **34**, 187 (2001).

[62] G. Morigi, P. W. H. Pinkse, M. Kowalewski, and R. de Vivie-Riedle, Phys. Rev. Lett. **99**, 073001 (2007).

[63] D. R. Leibrandt, J. Labaziewicz, V. Vuletić, and I. L. Chuang, Phys. Rev. Lett. **103**, 103001 (2009).

[64] M. Hosseini, Y. Duan, K. M. Beck, Y.-T. Chen, and V. Vuletić, Phys. Rev. Lett. **118**, 183601 (2017).

[65] N. Kiesel, F. Blaser, U. Delić, D. Grass, R. Kaltenbaek, and M. Aspelmeyer, Proc. Natl. Acad. Sci. USA **110**, 14180 (2013).

[66] P. Asenbaum, S. Kuhn, S. Nimmrichter, U. Sezer, and M. Arndt, Nat. Commun. **4**, 2743 (2013).

[67] A. Angerer, K. Streltsov, T. Astner, S. Putz, H. Sumiya, S. Onoda, J. Isoya, W. J. Munro, K. Nemoto, J. Schmiedmayer, and J. Majer, Nat. Phys. **14**, 1168 (2018).

[68] M. Tavis and F. W. Cummings, Phys. Rev. **170**, 379 (1968).

[69] M. Tavis and F. W. Cummings, Phys. Rev. **188**, 692 (1969).

[70] Y. K. Wang and F. T. Hioe, Phys. Rev. A **7**, 831 (1973).

[71] K. Hepp and E. H. Lieb, Ann. Phys. (N.Y.) **76**, 360 (1973).

[72] M. A. Norcia, R. J. Lewis-Swan, J. R. K. Cline, B. Zhu, A. M. Rey, and J. K. Thompson, Science **361**, 259 (2018).

[73] C. Cohen-Tannoudji, B. Diu, and F. Laloe, *Quantum Mechanics Vol. 1* (Wiley-VCH, 1977).

[74] S. Schütz, H. Habibian, and G. Morigi, Phys. Rev. A **88**, 033427 (2013).

[75] J. Dalibard and C. Cohen-Tannoudji, J. Phys. B **18**, 1661 (1985).

[76] H. W. Chan, A. T. Black, and V. Vuletić, Phys. Rev. Lett. **90**, 063003 (2003).

[77] J. K. Asbóth, P. Domokos, H. Ritsch, and A. Vukics, Phys. Rev. A **72**, 053417 (2005).

[78] K. J. Arnold, M. P. Baden, and M. D. Barrett, Phys. Rev. Lett. **109**, 153002 (2012).

[79] F. Brennecke, S. Ritter, T. Donner, and T. Esslinger, Science **322**, 235 (2008).

[80] D. Nagy, G. Kónya, G. Szirmai, and P. Domokos, Phys. Rev. Lett. **104**, 130401 (2010).

[81] J. Keeling, M. J. Bhaseen, and B. D. Simons, Phys. Rev. Lett. **112**, 143002 (2014).

[82] I. Bloch, J. Dalibard, and W. Zwerger, Rev. Mod. Phys. **80**, 885 (2008).

[83] I. Bloch, J. Dalibard, and S. Nascimbène, Nat. Phys. **8**, 267 (2012).

[84] H. Habibian, A. Winter, S. Paganelli, H. Rieger, and G. Morigi, Phys. Rev. Lett. **110**, 075304 (2013).

[85] J. Klinder, H. Keßler, M. R. Bakhtiari, M. Thorwart, and A. Hemmerich, Phys. Rev. Lett. **115**, 230403 (2015).

[86] R. Landig, L. Hruby, N. Dogra, M. Landini, R. Mottl, T. Donner, and T. Esslinger, Nature **532**, 476 (2016).

[87] N. Dogra, F. Brennecke, S. D. Huber, and T. Donner, Phys. Rev. A **94**, 023632 (2016).

[88] B. Sundar and E. J. Mueller, Phys. Rev. A **94**, 033631 (2016).

[89] T. Flottat, L. d. F. de Parny, F. Hébert, V. G. Rousseau, and G. G. Batrouni, Phys. Rev. B **95**, 144501 (2017).

[90] J. Panas, A. Kauch, and K. Byczuk, Phys. Rev. B **95**, 115105 (2017).

[91] R. Liao, H.-J. Chen, D.-C. Zheng, and Z.-G. Huang, Phys. Rev. A **97**, 013624 (2018).

[92] A. E. Niederle, G. Morigi, and H. Rieger, Phys. Rev. A **94**, 033607 (2016).

[93] J. Léonard, A. Morales, P. Zupancic, T. Esslinger, and T. Donner, Nature **543**, 87 (2017).

[94] J. Lang, F. Piazza, and W. Zwerger, New J. Phys. **19**, 123027 (2017).

[95] J. Léonard, A. Morales, P. Zupancic, T. Donner, and T. Esslinger, Science **358**, 1415 (2017).

[96] V. D. Vaidya, Y. Guo, R. M. Kroeze, K. E. Ballantine, A. J. Kollár, J. Keeling, and B. L. Lev, Phys. Rev. X **8**, 011002 (2018).

[97] S. Krämer and H. Ritsch, Phys. Rev. A **90**, 033833 (2014).

[98] V. Torggler, S. Krämer, and H. Ritsch, Phys. Rev. A **95**, 032310 (2017).

[99] J. Klinder, H. Keßler, M. Wolke, L. Mathey, and A. Hemmerich, Proc. Natl. Acad. Sci. USA **112**, 3290 (2015).

[100] S. Gupta and L. Casetti, New J. Phys. **18**, 103051 (2016).

[101] L. Hruby, N. Dogra, M. Landini, T. Donner, and T. Esslinger, Proc. Natl. Acad. Sci. USA **115**, 3279 (2018).

[102] S. Wald, A. M. Timpanaro, C. Cormick, and G. T. Landi, Phys. Rev. A **97**, 023608 (2018).

[103] M. Landini, N. Dogra, K. Kroeger, L. Hruby, T. Donner, and T. Esslinger, Phys. Rev. Lett. **120**, 223602 (2018).

[104] F. Mivehvar, F. Piazza, and H. Ritsch, Phys. Rev. Lett. **119**, 063602 (2017).

[105] R. M. Kroeze, Y. Guo, V. D. Vaidya, J. Keeling, and B. L. Lev, Phys. Rev. Lett. **121**, 163601 (2018).

[106] F. Mivehvar, S. Ostermann, F. Piazza, and H. Ritsch, Phys. Rev. Lett. **120**, 123601 (2018).

[107] S. Ostermann, H.-W. Lau, H. Ritsch, and F. Mivehvar, New J. Phys. (2018).

[108] A. Pikovsky, S. Gupta, T. N. Teles, F. P. C. Benetti, R. Pakter, Y. Levin, and S. Ruffo, Phys. Rev. E **90**, 062141 (2014).

[109] T. N. Teles, F. P. d. C. Benetti, R. Pakter, and Y. Levin, Phys. Rev. Lett. **109**, 230601 (2012).

[110] D. Meiser and M. J. Holland, Phys. Rev. A **81**, 033847 (2010).

[111] D. Meiser and M. J. Holland, Phys. Rev. A **81**, 063827 (2010).

[112] Y. Kuramoto, *Chemical oscillations, waves, and turbulence* (Courier Corporation, 2003).

[113] B. Zhu, J. Schachenmayer, M. Xu, F. Herrera, J. G. Restrepo, M. J. Holland, and A. M. Rey, New J. Phys. **17**, 083063 (2015).

[114] K. Tucker, B. Zhu, R. J. Lewis-Swan, J. Marino, F. Jimenez, J. G. Restrepo, and A. M. Rey, New J. Phys. **20**, 123003 (2018).

[115] J. D. Crawford, J. Stat. Phys. **74**, 1047 (1994).

[116] E. A. Martens, E. Barreto, S. H. Strogatz, E. Ott, P. So, and T. M. Antonsen, Phys. Rev. E **79**, 026204 (2009).

[117] D. M. Abrams and S. H. Strogatz, Phys. Rev. Lett. **93**, 174102 (2004).

[118] T. Maier, S. Kraemer, L. Ostermann, and H. Ritsch, Opt. Express **22**, 13269 (2014).

[119] M. A. Norcia and J. K. Thompson, Phys. Rev. X **6**, 011025 (2016).

[120] M. A. Norcia, M. N. Winchester, J. R. K. Cline, and J. K. Thompson, Sci. Adv. **2** (2016).

[121] D. Tieri, M. Xu, D. Meiser, J. Cooper, and M. Holland, preprint arXiv:1702.04830 (2017).

[122] K. Debnath, Y. Zhang, and K. Mølmer, Phys. Rev. A **98**, 063837 (2018).

[123] Z. Gong, R. Hamazaki, and M. Ueda, Phys. Rev. Lett. **120**, 040404 (2018).

[124] F. Iemini, A. Russomanno, J. Keeling, M. Schirò, M. Dalmonte, and R. Fazio, Phys. Rev. Lett. **121**, 035301 (2018).

[125] S. B. Jäger, J. Cooper, M. J. Holland, and G. Morigi, preprint arXiv:1811.10467 (2018).

[126] S. Inouye, A. P. Chikkatur, D. M. Stamper-Kurn, J. Stenger, D. E. Pritchard, and W. Ketterle, Science **285**, 571 (1999).

[127] D. Schneble, Y. Torii, M. Boyd, E. W. Streed, D. E. Pritchard, and W. Ketterle, Science **300**, 475 (2003).

[128] N. Piovella, R. Bonifacio, B. McNeil, and G. Robb, Opt. Commun. **187**, 165 (2001).

[129] C. Emary and T. Brandes, Phys. Rev. E **67**, 066203 (2003).

[130] A. Lerose, J. Marino, B. Žunkovič, A. Gambassi, and A. Silva, Phys. Rev. Lett. **120**, 130603 (2018).

[131] M. Xu, S. B. Jäger, S. Schütz, J. Cooper, G. Morigi, and M. J. Holland, Phys. Rev. Lett. **116**, 153002 (2016).

[132] S. B. Jäger, M. Xu, S. Schütz, M. J. Holland, and G. Morigi, Phys. Rev. A **95**, 063852 (2017).

[133] Y. Levin, R. Pakter, F. B. Rizzato, T. N. Teles, and F. P. Benetti, Phys. Rep. **535**, 1 (2014).

[134] D. Barberena, R. J. Lewis-Swan, J. K. Thompson, and A. M. Rey, preprint arXiv:1812.02291 (2018).

[135] R. Horodecki, P. Horodecki, M. Horodecki, and K. Horodecki, Rev. Mod. Phys. **81**, 865 (2009).

[136] K. Huang, *Statistical mechanics* (Wiley, 1987).

[137] M. T. DePue, C. McCormick, S. L. Winoto, S. Oliver, and D. S. Weiss, Phys. Rev. Lett. **82**, 2262 (1999).

[138] J. Hu, A. Urvoy, Z. Vendeiro, V. Crépel, W. Chen, and V. Vuletić, Science **358**, 1078 (2017).

[139] A. Georgakopoulos, A. Sommer, and J. Simon, Quantum Sci. Technol. **4**, 014005 (2018).

[140] F. Mivehvar, H. Ritsch, and F. Piazza, Phys. Rev. Lett. **122**, 113603 (2019).

[141] M. Kitagawa and M. Ueda, Phys. Rev. A **47**, 5138 (1993).

[142] I. D. Leroux, M. H. Schleier-Smith, and V. Vuletić, Phys. Rev. Lett. **104**, 073602 (2010).

[143] J. Hu, W. Chen, Z. Vendeiro, A. Urvoy, B. Braverman, and V. Vuletić, Phys. Rev. A **96**, 050301 (2017).

[144] R. J. Lewis-Swan, M. A. Norcia, J. R. K. Cline, J. K. Thompson, and A. M. Rey, Phys. Rev. Lett. **121**, 070403 (2018).

[145] M. Heyl, Rep. Prog. Phys. **81**, 054001 (2018).

# Danksagung

Besonders möchte ich meiner Betreuerin Giovanna Morigi danken. Sie hat mich stets unterstützt, wissenschaftlich gefördert und es mir ermöglicht viele Orte zu besuchen und Bekanntschaften zu machen. Des Weiteren danke ich auch Roland Speicher, der es mir ermöglicht hat während meiner Zeit als Promotionsstudent meine Masterarbeit in Mathematik in seiner Gruppe zu schreiben. Mein besonderer Dank gilt meinen Kollaboratoren und Freunden an der UdS, Stefan Schütz, der mir schon während meiner Masterarbeit und auch während meiner Promotion eine sehr große Hilfe war und Tim Keller, mit dem ich eine sehr fruchtbare Zusammenarbeit hatte. Außerdem danke ich Helmut Ritsch und Valentin Torggler, mit dem ich bei seinen zwei Besuchen an der UdS einen hervorragenden Austausch hatte. Besonderer dank gilt auch Murray Holland, der es mir ermöglicht hat seine Gruppe am JILA Boulder für drei Wochen zu besuchen. Bei meinem Besuch hatte ich das Vergnügen mit Athreya Shankra und John Bartolotta Bekanntschaft zu machen und Jinx Cooper kennenzulernen, der mir eine große Inspiration ist.

Ich danke der hervorragenden Arbeit von Monika Francois, Ingeborg Michel und Susanna Trampert, die sich stets um alle bürokratischen Angelegenheiten kümmerten. Das Arbeiten in der AG Morigi war immer sehr angenehm, was an der professionellen Betreuung durch Giovanna Morigi, aber auch an dem sehr guten Gruppenklima lag. Deshalb bedanke ich mich bei den derzeitigen und ehemaligen Gruppenmitgliedern, dich ich kennenlernen durfte: Susanne Blum, Lukas Himbert, Sascha Wald, Tim Keller, Jonas Cassel, Peter-Maximilian Ney, Timo Holz, Oxana Mishina, Cecilia Cormick, Tristan Tentrup, Jens Baltrusch, Andreas Buchheit, Francesco Rosati, Luigi Giannelli, Frederic Folz, Florian Cartarius, Tom Schmitt, Alexey Konovalov, Stefan Schütz, Thomás Forgarty, Christian Arenz, Malte Henkel und Marc Bienert. Besonders hebe ich hierbei meine Bürokollegen hervor: Nahuel Freitas, Katharina Rojan, Rebecca Kraus, Shraddha Sharma und Ralf Betzholz, die ich wahrscheinlich besonders oft vom Arbeiten abgehalten habe und die mir auch als Freunde zur Seite standen.

Zuletzt gilt mein Dank meiner Familie und meinen Freunden. Meinen Großeltern, Emma Jäger und Rudolf Jäger sowie Lydia Lode und Waldemar Lode, die mich bei meinem Studium unterstützt haben, meinem Vater und meiner Stiefmutter, Johannes Jäger und Elke Jäger, sowie ganz besonders meiner Mutter, Sabine Jäger. Außerdem danke ich meinen Brüdern Jakob Jäger und Maximilian Frisch, die mir immer zur Seite standen. Ich danke meinen beständigen Studienkollegen und Freunden Marius Schöndorf und Michael Kaicher und zu guter Letzt meiner immer hilfsbereiten und unterstützenden Freundin Stefanie Stalter.